

DESIGN OF AN AEROELASTIC PASSIVE CONTROL
STRATEGY FOR A FIXED-PITCH HORIZONTAL-AXIS WIND
TURBINE

JORGE MARIO TAMAYO AVENDAÑO

UNIVERSIDAD PONTIFICIA BOLIVARIANA
SCHOOL OF ENGINEERING
PhD IN ENGINEERING
MEDELLÍN

2023

DESIGN OF AN AEROELASTIC PASSIVE CONTROL
STRATEGY FOR A FIXED-PITCH HORIZONTAL-AXIS WIND
TURBINE

JORGE MARIO TAMAYO AVENDAÑO

This thesis is submitted for the degree of

Doctor in Engineering

Tutors

JULIÁN SIERRA PÉREZ
PhD in Engineering

IVÁN DAVID PATIÑO ARCILA
PhD in Engineering

CÉSAR NIETO LONDOÑO
PhD in Engineering

UNIVERSIDAD PONTIFICIA BOLIVARIANA
SCHOOL OF ENGINEERING
PHD IN ENGINEERING
MEDELLÍN

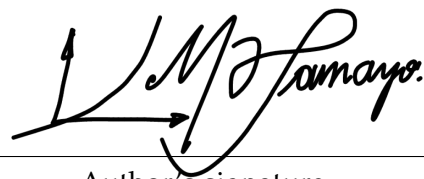
2023

DECLARACIÓN DE ORIGINALIDAD

June 13, 2023

Jorge Mario Tamayo Avendaño

“Declaro que este trabajo de grado no ha sido presentado con anterioridad para optar a un título, ya sea en igual forma o con variaciones, en esta o en cualquiera otra universidad”. Art 92, parágrafo, Régimen Estudiantil de Formación Avanzada.

A handwritten signature in black ink, reading "Jorge Mario Tamayo Avendaño". The signature is written in a cursive style with a large initial "J" and "M".

Author's signature

ABSTRACT

This work presents the evaluation of a wind turbine blade with bend-twist coupling induced by composite material anisotropy. Different sources in literature have been surveyed to identify the most relevant aspects concerning the use of this concept as a mechanism for passive control and its appeal to small wind technology. A theoretical approach is taken, based on the use of numerical analysis for the study of the wind turbine blade in different cases. A blade element momentum model is used to describe the aerodynamic loads of the rotor blade in a quick way, without disregarding important phenomena such as three-dimensional flow and dynamic stall. A finite-volume commercial solver is used to study the blade behavior in a more complete scenario, involving the modeling of turbulence and enabling the set-up of an FSI analysis, coupled to a finite-element simulation of the blade composite structure. The numerical results for validation and operation cases are compared with published experimental data, including the results from the unsteady aerodynamics experiment Phase VI. An insight into the validity of the use of bend-twist coupling shows positive results regarding the technical validity of the concept from the point of view of annual energy output and ultimate loads on the rotor blades.

ACKNOWLEDGMENTS

This work has been funded by the project *Estrategia de transformación del sector energético Colombiano en el horizonte de 2030*, financed by the World Bank and managed by *Minciencias* with the call for proposals 778-2017 *Ecosistema Científico*, with Contract Number: FP44842-210-2018. I thank deeply the institutional support provided by the project managers and researchers for the development of this work.

Likewise, I must thank my directors Julián and César for their constant and unconditional support during my doctoral studies, they have provided me with valuable advice from the first year up to the development of this thesis and have always procured my wellbeing as a student. Likewise, I would like to thank my advisor Iván for his patience, he dedicated numerous hours of his time to guide me through the path that has been this thesis and was of special help for a better understanding of numerical analysis.

CONTENTS

1	INTRODUCTION	1
1.1	OUTLINE	2
1.2	OBJECTIVES	3
2	LITERATURE REVIEW	4
2.1	BEND-TWIST COUPLING APPLICATIONS IN WIND ENERGY	4
2.2	NUMERICAL ANALYSIS OF WIND TURBINE BLADES WITH BEND-TWIST COUPLING	11
2.3	MAIN FINDINGS FROM THE LITERATURE REVIEW	13
3	THEORETICAL FRAMEWORK	20
3.1	AERODYNAMIC MODELS	23
3.1.1	Blade element momentum theory	23
3.1.2	RANS model and the Finite-Volume method	26
3.2	STRUCTURAL MODEL	37
3.2.1	Composite shell model	42
3.3	FLUID-STRUCTURE INTERACTION MODEL	51
3.3.1	Data transfer between non-matching meshes	51
3.3.2	Overview of the System Coupling workflow	56
3.3.3	Mesh update procedure	62
4	MATHEMATICAL MODELING	65
4.1	DYNAMIC INFLOW MODEL	67
4.2	STALL EFFECTS ON 3-D WIND TURBINE BLADE FLOWS	68
4.2.1	Lindenburt's centrifugal pumping correction model	68
4.2.2	Du-Selig's 3-D Stall delay correction model	69
4.2.3	Discussion on existing models	70
4.2.4	Dynamic stall modelling	72

4.3	PREDICTIONS OF TORQUE AND BLADE ROOT MOMENT FOR THE NREL PHASE VI WIND TURBINE	73
4.4	DYNAMIC SIMULATION WITH THE BLADE ELEMENT MOMENTUM MODEL	77
4.5	FINITE ELEMENT MODELING	79
4.5.1	Hollow beam structure with bend-twist coupling	79
4.5.2	Benchmarking for the structure model	81
4.6	IMPLEMENTATION OF A FLUID-STRUCTURE INTERACTION FRAMEWORK	82
4.6.1	Benchmarking for the fluid model	83
4.6.2	Benchmarking of the FSI environment	85
5	REFERENCE FE MODEL FOR THE NREL PHASE VI BLADE	95
5.1	THE NREL PHASE VI BLADE	96
5.2	DEFINITION OF AN EQUIVALENT STRUCTURAL MODEL	96
5.3	WIND TURBINE CONTROL WITH BEND-TWIST COUPLING	101
5.3.1	Maximum torsion from bend-twist coupling	101
5.3.2	Blade model with bend-twist coupling	103
6	RESULTS	105
6.1	SIMULATION CASES	105
6.1.1	Preliminary selection based on wind models	105
6.1.2	Steady operation	105
6.1.3	Extreme wind model (EWM)	106
6.2	ROBUST SIMULATION FRAMEWORK	106
6.2.1	Stability considerations	107
6.3	SIMPLIFIED SIMULATION FRAMEWORK	114
6.4	STEADY TORQUE CURVES	119
6.5	EXTREME WIND LOADING	133
	BIBLIOGRAPHY	140

LIST OF FIGURES

Figure 1.1	Baseline blade geometry (adapted from [1]).	2
Figure 2.1	Pitching motions of a wind turbine blade.	5
Figure 2.2	Blade planform with swept-back geometry towards the tip. . .	7
Figure 2.3	Concepts for mechanical unbalance in a typical biaxial laminate, adapted from [2].	8
Figure 2.4	Concepts for modeling of composite hollow structures.	12
Figure 3.1	Stream tube across an actuator disk	23
Figure 3.2	Velocity triangle at a blade element.	24
Figure 3.3	Balance for mass flow rates across the control volume boundaries (adapted from [3]).	27
Figure 3.4	Flow diagram for a general predictor-corrector procedure in pressure-velocity coupling.	34
Figure 3.5	Synchronized execution scheme for System Coupling and participant processes (Adapted from [4]).	58
Figure 3.6	Generation of mapping weights with shape functions (Adapted from [5]).	60
Figure 3.7	Example of input and output for shape function mapping (Adapted from [6]).	60
Figure 3.8	Example of input and output data for Intersect-Scatter-Gather mapping (adapted from [6]).	61
Figure 3.9	Example of input and output data for Intersect-Scatter-Gather mapping (adapted from [6]).	61
Figure 4.1	Sensitivity of torque and moment predictions with respect to variable and fixed-Reynolds corrections of airfoil coefficients. .	75
Figure 4.2	Steady-state prediction of integral rotor loads with the Blade Element Momentum (BEM) solver.	76
Figure 4.3	Torque predictions with the dynamic BEM model.	87
Figure 4.4	D-spar cross-sectional geometry.	88
Figure 4.5	Laminate orientation layout.	88

Figure 4.6	Laminate thickness contours.	88
Figure 4.7	Domain topology and boundary conditions.	89
Figure 4.8	D-spar analysis results.	90
Figure 4.9	Blade structural model geometry.	91
Figure 4.10	Modal analysis results.	91
Figure 4.11	Fluid simulation domain and mesh.	92
Figure 4.12	Aerodynamic force validation for the reference case.	93
Figure 4.13	Blade tip displacement prediction under base excitation conditions.	94
Figure 5.1	Structural concept of the NREL Phase VI experimental rotor blade.	96
Figure 5.2	Structural concept of the proposed numerical model.	97
Figure 5.3	Blade laminate groups and relative positions for one blade shell.	100
Figure 5.4	Structural properties for the baseline blade.	101
Figure 5.5	Off-axis fiber orientation for the tailored blade	102
Figure 5.6	Sensitivity analysis for the blade tip rotation.	103
Figure 5.7	Structural properties for the blade with coupling.	104
Figure 6.1	Fluid flow domain and mesh for the robust simulation framework.	108
Figure 6.2	Structural domain and mesh for the robust simulation framework.	108
Figure 6.3	Blade coordinate axis orientation.	109
Figure 6.4	Simplified blade section.	109
Figure 6.5	Mapping diagnostics for the transfer of displacements for Source (left) and Target (right) meshes.	111
Figure 6.6	Contours for the transfer of displacement data.	112
Figure 6.7	Mapping diagnostic for the transfer of forces.	113
Figure 6.8	Resulting contours for the transfer of forces.	114
Figure 6.9	Blade section rotation from bend-twist coupling.	115
Figure 6.10	Aerodynamic coefficients at 7 m/s.	116
Figure 6.11	Aerodynamic coefficients for the S809 airfoil at $Re = 1 \times 10^6$	117

Figure 6.12	Aerodynamic coefficients at 10 m/s.	118
Figure 6.13	Aerodynamic coefficients at 13 m/s.	119
Figure 6.14	Aerodynamic coefficients at 20 m/s.	120
Figure 6.15	Torque convergence history for the reference blade.	122
Figure 6.16	Torque convergence history for the coupled blade.	123
Figure 6.17	Pressure coefficient distributions for the robust framework co-simulations.	125
Figure 6.18	Blade-wise distributions of normal and tangential force coefficients.	127
Figure 6.19	Structural responses for reference and coupled blade.	129
Figure 6.20	Low speed shaft torque at different wind speeds.	130
Figure 6.21	Flap-wise bending moment at the blade root.	131
Figure 6.22	Edge-wise bending moment at the blade root.	131
Figure 6.23	Thrust curve comparison	132
Figure 6.24	Power curve comparison	132
Figure 6.25	Annual Energy Production (AEP) curve comparison.	133
Figure 6.26	Flap-wise and torsional displacement for the Extreme Wind Model (EWM).	135

LIST OF TABLES

Table 2.1	Main characteristics of relevant works.	16
Table 2.2	Key aspects of relevant works from the literature review.	18
Table 3.1	Boundary condition specification at the coupling interface.	52
Table 4.1	L-2 Relative error norm in percentage for the final “weighted Correction” results.	77
Table 4.2	Laminate mechanical properties for the validation case of a D-spar based on Ong et al. [7].	80
Table 5.1	Material properties for a 0.35 mm Carbon/Epoxy lamina, adopted from [8].	98
Table 5.2	Blade longitudinal segments.	99
Table 5.3	Laminate layup sequences.	99
Table 5.4	Laminate layup sequence for the sensitivity analysis model.	102
Table 5.5	Laminate layup sequences for a blade with bend-twist coupling.	103
Table 6.1	Simulation cases.	106
Table 6.2	Aerodynamic torque results for three mesh refinement levels.	107
Table 6.3	Torque prediction comparison between the proposed simulation frameworks.	133
Table 6.4	Load analysis at the blade root	134

LIST OF LISTINGS

Listing 6.1	Mapping diagnostics for displacement data transfer.	110
Listing 6.2	Coupling results for the incremental displacement data transfer.	111
Listing 6.3	Coupling results for the force data transfer.	113

ACRONYMS

ALE	Arbitrary Lagrangian-Eulerian
AMG	Algebraic Multi-Grid
AEP	Annual Energy Production
ACP	Ansys Composite Pre-Post
APDL	Ansys Parametric Design Language
BEM	Blade Element Momentum
BPE	Blade Property Extraction
BSP	Binary Space Partitioning
CLT	Classical Lamination Theory
CFD	Computational Fluid Dynamics
CFL	Courant-Friedrichs-Lewy
DSBT	Differential Stiffness Bend-Twist Coupling
ECG	Extreme Coherent Gust
EOG	Extreme Operating Gust
EWM	Extreme Wind Model
FEA	Finite-Element Analysis
FEM	Finite-Element Method
FVM	Finite-Volume Method
FSI	Fluid-Structure Interaction
GA	Genetic Algorithm
GCL	Geometric Conservation Law
IEC	International Electrotechnical Commission
NREL	National Renewable Energy Laboratory
PISO	Pressure-Implicit with Splitting of Operator
RANS	Reynolds-Averaged Navier-Stokes
SIMPLE	Semi-Implicit Method for Pressure Linked Equations
SIMPLEC	Semi-Implicit Method for Pressure Linked Equations-Consistent
UAE Phase VI	Unsteady Aerodynamics Experiment Phase VI

INTRODUCTION

As one of the current goals of the modern society, the transition towards cleaner and more sustainable sources of energy has permeated every aspect of the consumption chain, from large scale utility companies down to the small private consumers. Wind energy has a central role on this higher purpose as a complementary element to other forms of generation and storage. The *Energética 2030* program has been the driver behind this work through the project “Distributed generation from wind and photovoltaic energy”, in which several of the aspects treated here theoretically have been put to practice with the construction of a real scale prototype. The premise remains simple: exploring advanced technologies to improve the energy output of small wind turbines without increasing mechanical complexity.

From all the possible approaches to improve the energy output, the present work focuses on increasing the rotor power coefficient, by harnessing the potential for blade pitch actuation that is found in the behavior of composite materials under certain conditions, concerning both the composition of the laminates and the aerodynamic loads that the blades experience during their operation.

The main mechanism is known as bend-twist coupling and occurs when the torsional response of a wind turbine blade is coupled to the transverse deflection due to the aerodynamic loads. Such behavior is not exclusive to wind turbine blades since it is caused by the fiber orientation in the composite lay-up sequence. The high degree of customization, the mechanical simplicity and the instantaneous response between the coupled modes of displacement make this technology worth exploring as a suitable mean for the power output improvement of a wind turbine.

The analysis of the concept and the integration into a wind turbine blade is assessed with the aid of numerical analysis involving different models for describing the aerodynamic and structural response, and setting up a framework for the Fluid-Structure Interaction (FSI) analysis of the improved blade structure. The aerodynamic analysis is initially performed with a BEM solver, with an improved correction of 2-D airfoil coefficients and the implementation of a routine for the prediction of dynamic loads in the rotor blades. A more robust study is carried out with Computational Fluid Dynamics (CFD) by means of a commercial Finite-Volume Method (FVM) solver. The structural analysis is carried out with a commercial Finite-Element Method (FEM) solver capable of analyzing composite thin-walled structures in 3-D using shell elements. Because the scope of this thesis encompasses theoretical work only, the use of publicly available experimental data is presented along with the numerical results of the various analyses presented throughout this thesis. For this reason, the present work adopts the external blade geometry of the 10 m-diameter wind turbine used in the Unsteady Aerodynamics Experiment Phase VI (UAE Phase VI) and shown in Figure 1.1.

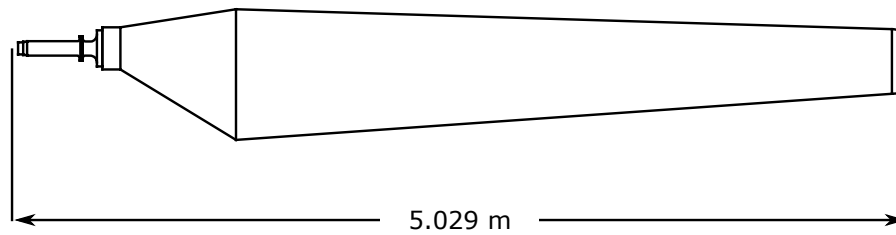


Figure 1.1: Baseline blade geometry (adapted from [1]).

1.1 OUTLINE

This thesis begins with a literature review in Chapter 2 of relevant works that have been published in the recent years and addressing the use of novel techniques for bend-twist coupling based control for wind turbine blades. Chapter 3 includes a description of the governing equations for the flow and structural physics, the basic aspects for the solution methods used in the solutions of the individual and coupled simulations and the theory behind a typical FSI coupling. Chapter 4 addresses the modeling of special effects pertaining to wind turbine operation along with the respective results; additionally, validation tasks for the simulation frameworks are carried out and presented along the error analysis. The definition of a blade structure in composite materials with negligible structural coupling is presented in Chapter 5 and a similar procedure is carried out for a blade with bend-twist coupling in Section 5.3. The Results for the simulation of the reference and coupled blade structures are presented and discussed in Chapter 6.

From a global perspective, the main tasks in this work involve the use of FSI simulations for the analysis of operation and proposal of a passive control mechanism based on the baseline blade geometry presented earlier. The FSI analysis involves the simulation of the fluid flow around the blade using a finite-volume solution of the Navier-Stokes equations and, the simulation of the structural response of the blade body using a finite-element solution of the first-order shear deformation model for laminated composite shell elements. The full coupling environment is defined using a commercial software for both solutions and for their mutual interfacing. Throughout the document several auxiliary simulation tasks are included, these have been devised to provide a validation for the numerical models. The tasks involve the aerodynamic modeling of the blade using both a fast BEM model implementation and a commercial finite-volume solver for the RANS equations. The structural model is validated entirely with a finite-volume analysis of a hollow beam with bend twist coupling and. The coupled simulation considering finite-volume and finite-element solutions for the flow and structure respectively is validates with the simulation of an industrial air conditioning fan blade with harmonic excitation at the base. The results presented in Chapter 6 are obtained from the full coupled simulations of the baseline blade, and are complemented with auxiliary computations of the aerodynamic loads using the BEM model, providing an additional reference for the turbulent flow solution.

1.2 OBJECTIVES

General objective

To develop a passive pitch control methodology for the power regulation of small horizontal axis wind turbines based on the bend-twist coupling of anisotropic layered composites using fluid-solid interaction numerical analysis.

Specific Objectives

1. To simulate the interaction between aerodynamic loads and blade deformations by means of an integrated FSI framework that includes the dynamic behavior of the drive train.
2. To determine the ideal twist distribution along the rotor blades, considering the expected torsional response by bend-twist coupling and the expected change in power output with respect to the baseline wind turbine.
3. To evaluate the structural response of the bend-twist coupled blade structure as an actuation mechanism on the local blade pitch angle, using a full FSI framework with the dynamic modeling of the drive train.
4. To assess the feasibility of a rotor with the bend-twist coupled blades by means of a numerical analysis of the structural integrity for the main components of the blade.

LITERATURE REVIEW

2.1 BEND-TWIST COUPLING APPLICATIONS IN WIND ENERGY

Some of the earlier works on wind energy applications for bend-twist coupling have a strong theoretical foundation on the quantification of the coupling phenomenon and the implications of potential aeroelastic instabilities. For example, to study the aeroelastic stability of a blade with bend-twist coupling, a FEM formulation was proposed by Lobitz and Veers [9] using beam elements. This approach is relatively simple; however, the authors have considered the key aspects of wind turbine blade operation, including bend-twist coupling and extension-twist to name two of the most relevant. Since the aerodynamic model that has been employed in this study relies on linear aerodynamics, stall flutter has not been studied, in this sense, only divergence and classical flutter are analyzed.

The work presented by Ong et al. [7], in which an experimental and numerical analysis is performed on a D-spar with bend-twist coupling, focuses on the application of this kind of materials for load mitigation and highlights the potential for overall aerodynamic improvement. The main hurdles before a successful application on wind turbines are identified in the fields of aeroelastic stability and feasibility of manufacture. Bend-twist coupling is found to depend strongly on material properties (i.e. torsional and bending stiffnesses), ply angle and relative proportion of anisotropic layers. Numerical predictions match experiments better when the model includes out-of-plane warping due to torsion.

By the end of the nineties, an interest on practical approaches to bend-twist coupling of wind turbine blades was evident from works subsequent to [7]. Not only the coupling is evaluated in terms of effectiveness but also in terms of feasibility. Such is the work of Ashwill et al. [10], in which bend-twist coupling capabilities are explored in wind turbine blade applications from three different perspectives. The results include a parametric analysis on a conventional wind turbine blade, exploring the effects of material anisotropy on the composition of main elements such as skins, spar caps and shear webs and including cost estimates for bend-twist enhanced blades. Additionally this study shows the effectiveness of braided preforms for manufacturing coupled blades and the use of swept blade geometries for the implementation of purely geometrical bend-twist coupling.

On a similar direction, the work of Veers et al. [11] discusses the use of bend-twist coupled blade structures, including the favorable behavior of coupled blades in terms of fatigue reduction. Besides being the first to explicitly establish the similitude between bend-twist and conventional pitch actuation mechanisms, the authors discuss the advantages of having a bend-twist coupling that pitches the blade into feather

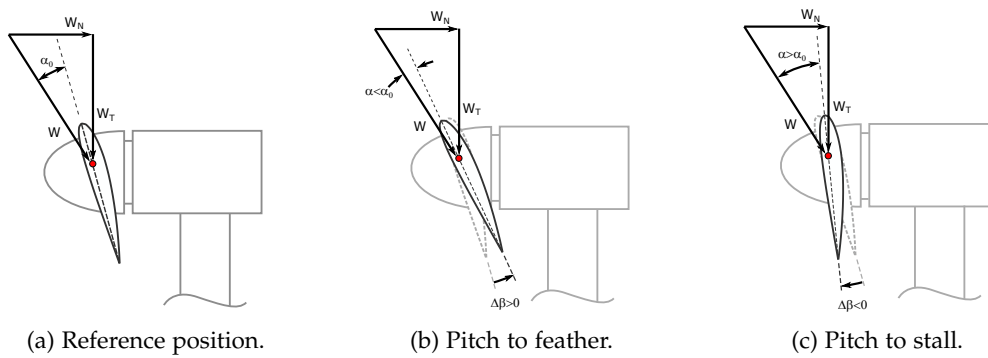


Figure 2.1: Pitching motions of a wind turbine blade.

instead of stall, as the former is better to avoid fatigue damage and stall flutter. A representation of both directions of inducing twist is shown in Figure 2.1, which also illustrates the associated change in the local angle of attack.

Griffin et al. [12] introduce the development of different blade prototypes, including a 9 m long model that incorporates bend-twist coupling; this very model is the subject of subsequent experiments on structural performance as presented by Ashwill [13]. The 9 m prototype, denominated “TX-100”, has a 20° ply-angle for the carbon fibers on the blade skins, while the spar caps are designed with conventional glass fiber laminates. According to the preliminary analyses in [12] the blade performs well under a turbulent wind inflow, resulting in up to 4° of twist and an acceptable tracking of flap-wise bending moment as shown by aeroelastic analyses. On the other hand, it is noted that the skins play a more important role in bearing the loads as compared to conventional blades, where an internal box structure is usually the single structurally relevant component, for these reasons the authors point the uncertainty on these changes from conventional blade configurations as they can have a significant impact on the overall blade performance.

Concerning aeroelastic stability, Lobitz [14] presents an analysis centered on flutter instabilities for a large wind turbine blade using Theodorsen’s theory for unsteady aerodynamics. A 12% reduction in flutter speed is predicted for a bend-twist blade with respect to its conventional counterpart. In this case, the flutter speed is determined in terms of angular speed. Furthermore, the author points, based on existing analyses that smaller stiffer blades tend to have higher flutter speeds when compared to larger blades, which tend to be less stiff.

Maheri et al. [15] present an algorithm for implementing bend-twist coupling into a baseline conventional rotor, seeking to increase the AEP. For a tip twist of 3° into feather, the authors report a 6% increase in AEP and 50% increase in maximum power output. The work includes subsequent modifications to the rotor chord distribution and radius, mainly as a mean to bound the root flap-wise moment and to maintain the maximum power at the rated value. These modifications yield an increase of AEP of 13% is observed, however, for this case the improvement is seen for a tip twist of 5.3° into stall.

To some extent, the work of Maheri et al. [15] shows the impact of controlling blade loads on the root bending moment when increasing power output. In addition, many works on bend-twist coupling are implemented on utility-scale wind turbines, with

blade lengths above 50 m for the 5 MW machines and even larger for the more recent 10 MW reference wind turbines. The tendency towards larger rotors implies higher demands on structural performance; therefore, the use of bend-twist coupling has been established as a plausible alternative for load alleviation as discussed by Thresher and Laxson [16] in a review of key technologies for wind turbines of increasing sizes. At this point the use of bend twist coupling can be associated with two design paradigms: increased power output and, load alleviation. It is also evident that the latter paradigm is particularly important for large scale rotors.

The work on tidal turbines by Nicholls-Lee and Turnock [17] considered bend-twist coupled blades on a numerical analysis, with the aim of mitigating loads and improving AEP. For this purpose, an artificial recreation of the structural coupling is adopted to effectively modify the aerodynamic performance. The approach taken in this work corresponds to an artificial prescription of the blade deformation as a function of wind speed, as opposed to the direct numerical modeling of the blade deformation response; since this treatment does not constitute an interaction problem from a strict perspective, the capability of predicting the time-response of the system, its instabilities or both, remains unclear.

The earlier works addressing effectiveness and feasibility of bend-twist coupled blades for different design applications tend to focus on what could be called a “classical” bend-twist coupling mechanism which depends on the anisotropy of composite materials and is usually known as material-based coupling or material-based morphing. When it comes to modern wind turbine design, the use of composite materials is still the main option for blades of different sizes. Likewise, the main mechanism for implementing bend-twist coupling still relies on composite material anisotropy for most of the reviewed works, with some innovations that allow a higher level of control over the induced twist; nevertheless, new concepts for bend-twist coupling which do not depend on material anisotropy have been proposed as evidenced by several works published within the last decade.

In the first half of a two-part study, Capuzzi et al. [18] carry out an exhaustive search optimization procedure based on BEM theory, for finding the optimal blade twist as a function of the radial location and the wind speed. Considering the classical pitch control of the analyzed wind turbine and the non-monotonic variation of ideal twist along the blade, the authors extend the analysis to define target twist distributions based on considerations of feasibility. Under these constraints the target twist curves are determined to induce twist towards feather over a partial length of the blade.

The continuation on the structural design and overall evaluation of the blade is presented by Capuzzi et al. [19] which analyses a blade modeled as the central box of the structure, with tow steered laminates in the spar caps. It must be mentioned that the aerodynamic analysis neglects blade deformations and considers the blade geometry as straight. This is important not only because of the flap-wise deformations but because the blade includes geometric sweep as a mechanism for bend-twist coupling. The adaptive blade combining anisotropy and geometric sweep is compared with baseline models optimized for maximum AEP and maximum production at rated conditions. The concept presented by the authors is proven as a viable alternative to conventional pitch actuation and is expected to see decreased loads due to the twist towards feather approach.

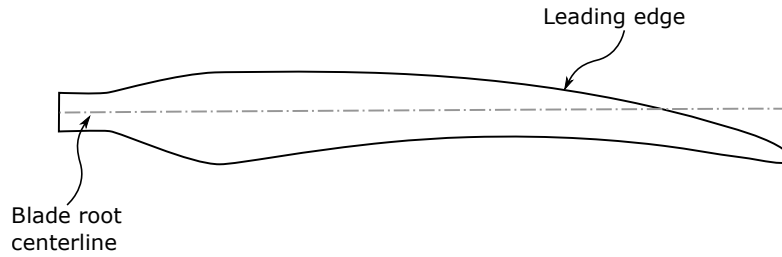


Figure 2.2: Blade planform with swept-back geometry towards the tip.

The structural design by Capuzzi et al. [20] for example, demonstrates the feasibility of a blade concept that incorporates bend-twist coupling by combining material anisotropy in the form of tow steered laminates with a curved blade planform swept towards the blade trailing edge as shown in Figure 2.2. Tow steering is used to induce a non-monotonic twist variation along the blade following the needs of an existing aerodynamic design. As part of the design procedure, the authors compare both linear and non-linear structural analysis, revealing that the latter exhibits an increased stiffness in out-of-plane deflections and in consequence, a slight reduction in induced twist.

A novel concept known as Differential Stiffness Bend-Twist Coupling (DSBT) is proposed by Herath et al. [21] as a mechanism to introduce bend-twist coupling on a blade structure; however, unlike conventional approaches relying on composite material anisotropy, the coupling is induced on the macro-scale level with structural stiffeners which are always subjected to pure bending but vary in stiffness in such a way that the overall structure exhibits the bend-twist coupling behavior.

Hayat and Ha [2] present a parametric analysis of a 5 MW wind turbine considering a bend-twist coupled blade in which the reduction of fatigue loads is proven. In this work, a classical coupling is considered, but the authors explore in detail the effects in which the lay-up parameters affect the overall coupling; these parameters are ply-angle, ply-thickness, and ply-material and determine the different categories of material-based coupling as shown in Figure 2.3. According to the authors the highest level of coupling is observed on a composite blade that includes a combination of all three parameters in the skin, for a ply orientation of 25° in a combination of carbon and glass reinforced epoxy.

Zahle et al. [22] present an optimization work with the DTU 10 MW reference wind turbine as the baseline, and the respective design loads as a constraint for the optimization procedure. The blade geometry, except for the radius, makes part of the design variables, along with the internal structure parameters and operating conditions. The resulting rotor has bend-twist coupling that acts to pitch the blade towards feather despite no material anisotropy being considered. This behavior is derived from a relative displacement of the spar caps dictated by the optimization procedure itself. The authors point that such coupling effectively alleviates the loads on the blade, resulting in a longer blade under the specified set of constraints. This increase in blade length allows an 8.7% increase in AEP with respect to the reference model, which reveals how bend-twist coupled blades can indirectly increase the performance of the wind turbine by allowing an increased rotor area for the same structural demand. Another work on the DTU 10 MW reference wind turbine is performed by Ståblein et al. [23], aiming to implement a pre-twist distribution on a blade with bend-twist coupling, modeled by

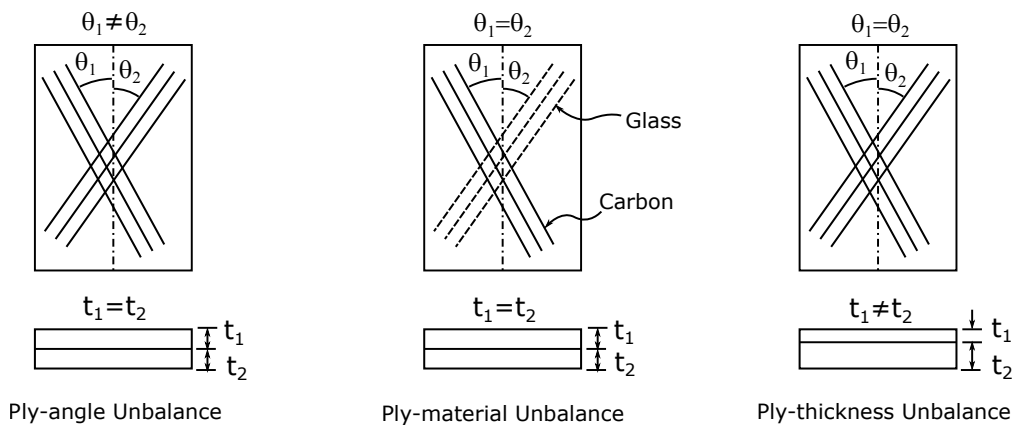


Figure 2.3: Concepts for mechanical unbalance in a typical biaxial laminate, adapted from [2].

means of coupling terms in the stiffness matrices of the blade elements. One of the key aspects of this work is to address the problematic that arises when the bend-twist coupling, initially conceived as a load alleviating mechanism, drives the efficiency of the rotor away from the optimal value by changing the angle of attack distribution in the below rated wind speed range. As a solution, the authors opt for a pre-twisted blade such that the coupling-induced twist is compensated for at a certain reference wind speed. This procedure demonstrates that the loss in [AEP](#) due to bend-twist coupling towards feather, can be reduced by pre-twisting the blade, in the most extreme case bringing the [AEP](#) relative difference from about -0.30% to less than -0.05% with respect to the uncoupled blade.

The work of Saverin et al. [24] is based on aeroelastic simulations built on the framework of the software FAST, making emphasis on aerodynamic modeling with a Lifting Line Free Wake Vortex model and presenting the respective benchmarking against a [BEM](#) solver and a Reynolds-Averaged Navier-Stokes ([RANS](#)) solver with turbulence modeling. Regarding the structural modeling, the authors consider a formulation based on geometrically exact beam theory (BeamDyn) and a modal-based solver (ElastoDyn). Both approaches are implemented in the aeroelastic framework, though the former is proven for the prediction of the blade behavior when bend-twist coupling is included, this is done by simulating different scenarios such as increasing wind speeds and a sudden turbine stop.

Scott et al. [25] present an analysis on the performance of bend-twist coupled blades for the National Renewable Energy Laboratory ([NREL](#)) 5 MW and DNV GL 7 MW reference wind turbines, evaluating the [AEP](#), load alleviation and pitch system performance. Wind turbine modal frequencies are decreased in general by bend-twist coupling. The only frequency showing an increase is the first torsional mode for the [NREL](#) 5 MW model with purely material coupling. In determining the adequate twist distribution for maximized [AEP](#), the authors aim for a rated-optimal twist, which is, attaining the optimal twist after induced torsional deformations at the rated operating conditions. The simulation case of Extreme Operating Gust ([EOG](#)) extends the results from Scott et al. [25] and shows that the DNV GL 7 MW blade with anisotropic coupling, experiences a reduction in blade root bending moment of 1.95% for the peak load and 12.03% for the amplitude. For the same wind turbine, the optimized bend twist cou-

pling results in an increased AEP with respect to the baseline model, by 1.91% for the anisotropic coupling and 2.41% for the combined anisotropic-geometric coupling. For turbulent wind simulations the annual energy yield in the 7 MW model is slightly reduced with respect to the baseline model, with the interaction between blade dynamics and active pitch controller being one of the probable causes. The implementation of bend-twist coupling on large rotors with variable pitch control has proven effective for load alleviation, but several works point to a reduction in power in the below-rated range. In a similar approach to that of Scott et al. [25], the work of Atalay and Kayran [26] presents a modified design of the NREL 5 MW rotor, implementing anisotropy-based bend-twist coupling in the spar caps. After aeroelastic simulations that include turbulent wind and a classical PD pitch control, a reduction in fatigue loads is found along with a reduction of power in the below rated range. Under the premise of reducing damage equivalent loads in metallic components at the blade root and drive train, the authors determine the laminate layups in such a way that the loads are mitigated in the below-rated wind speed regime without losses in power production.

Bagherpour et al. [27] present the analysis of the DTU 10 MW rotor including off axis laminates in the spar caps of the blade to implement bend-twist coupling. Aeroelastic simulations are carried out in hGAST and compared to other similar codes. The effectiveness of the coupling for load alleviation is demonstrated, obtaining a 10% reduction in fatigue flap-wise bending moment and 8% reduction in extreme flap-wise bending moment without reductions in power. This is achieved by implementing a laminate with 12.5° offset, which leads to a 4° torsional deformation at the tip towards feather.

The work of Riva et al. [28] explores the effects of bend-twist coupling on the aeroelastic stability of a modified version of the DTU 10 MW wind turbine by using both an aeroelastic multi body simulation and modal analysis tools. The analysis is performed over an isolated blade and over the fully assembled wind turbine. The results show a mild influence of coupling on the wind turbine modes, except for the tower forward-after and edge-wise collective modes which experience a reduction in damping.

Şener and Kayran [29] take the NREL 5MW rotor as the baseline for an analysis of bend-twist coupling as a mechanism for load mitigation, particularly for reducing damage equivalent loads in key wind turbine components at the drive train and blade root using a fatigue exponent of four, corresponding to metallic components. The coupling is achieved by aligning spar cap fibers at 15° towards the leading edge from the blade root, which results in an induced twist towards feather. For wind speeds around 10 m/s the damage equivalent root flap-wise moment is reduced by 15% with respect to the baseline blade.

Zhou et al. [30] implement bend-twist coupling on a 5 MW rotor with offset angle laminates at 25° and unbalanced ply thicknesses for the blade skins, in a series of design cases. Significant reductions in blade torsional stiffness are observed, with values of 6.6% and 7.5% for ply-angle unbalanced laminates and ply-thickness unbalanced laminates, respectively. Little change is seen in bending flap-wise and edgewise stiffnesses. These results are opposed to the ones in Riva et al. [28] for which bend-twist coupling is implemented in the spar caps alone; however, the work of Zhou et al. [30] does not provide information on the mirroring of the skin laminates with respect to the chord-wise plane which might be a key factor for this discrepancy. The results show that the limit angular velocity for flutter is above the rated angular velocity of

the wind turbine. The flutter limit found with non-linear flutter analysis is observed to be 23% below the same limit found with linear flutter analysis.

Ferede et al. [31] implemented bend-twist coupling on a 5 MW wind turbine as part of the demonstration of an optimization approach that uses aeroelastic simulations with a low fidelity approach for aerodynamics and preliminary structural analysis. Localized analysis of stresses and buckling is considered by extending the structural analysis to a 3D model based on a shell element formulation in the software NAS-TRAN. An interesting result is the optimization outcome for a blade with balanced laminates, for which the optimization procedure generates a displacement of the shear center towards the trailing edge aiming to replicate the bend-twist coupling exhibited by a similar blade with unbalanced laminates, this is similar to the results reported in Zahle et al. [22].

Further results from [31] indicate a 2% reduction on the cost of electricity for a blade with unbalanced laminates when compared to the balanced counterpart; nevertheless, such a reduction seems to be dominated by a reduction of initial capital costs due to a reduction in blade mass, as the AEP is also reduced for the unbalanced blade. In fact, the power for wind speeds below the rated point sees a slight reduction with respect to the baseline machine. In the light of the actual context, this work reveals that the presented optimization makes better use of bend-twist coupling at high wind speeds, for which the power is regulated at or near the rated value.

An optimization procedure presented by Barr and Jaworski [32] uses a robust FSI analysis under a partitioned approach with a RANS solver for the fluid and a shell-element based FEM solver. The most prominent aspect of their research is perhaps the use of variable angle tow for the constitution of the composite material, achieving specific values of induced twist at different sections of the blade span similar to the approach of Capuzzi et al. [20]. Furthermore, the authors opt for passive pitch actuation towards stall to maximize power at different wind speeds. Unlike most of the recent works, dealing with large turbines, the analysis presented by Masoudi and Pope [33] takes as a subject an NREL Phase VI turbine, modified to have a swept geometry towards the tip; in this sense, a purely geometric bend-twist coupling is implemented and studied at different conditions with a one way robust FSI analysis on commercial software. The magnitude of attained induced twist is modest, i.e. around 0.67° , however the power at specific wind speeds is increased to about 1.8%; this is a promising sign for the improvement in AEP. The effects of swept geometry on the distribution of relative velocity along the blade are left unexplored.

Miao et al. [34] present an FSI analysis on a wind turbine based on the NREL 5 MW model under extreme wind events; modifications to the blade design are added to account for bend-twist coupling via material anisotropy and geometric sweep. The authors find that the swept blade offers little advantage compared to the conventional blade with pure anisotropic coupling, due to the increased torsional moments that swept blades experience in order to achieve an induced twist.

On a recent design of a 3.4 MW wind turbine, Madsen et al. [35] proposed an increased rotor diameter with respect to the baseline, aiming for operations between 2 m/s and 13 m/s. The increase in AEP due to operation at lower speeds comes with increased rotor loads; in response, the authors opt for a design with gradient-based optimization in which the shear caps of the blade structure are located towards the

leading edge of the blade. A consequence of this structural design is a bend-twist coupling pitching the blades towards feather, resulting in an overall load alleviation.

Serafeim et al. [36] presented a re-design of the DTU 10 MW wind turbine considering a Genetic Algorithm (GA) procedure for optimization of laminate layup in a new bend-twist coupled blade. This resulted in a 10% reduction in blade mass and 5% reduction in blade root bending moment.

In terms of aerodynamic analysis, the work of Li et al. [37] explores the effects of bound vorticity on the aerodynamics of curved blade planform and shows that the curved bound vortex is essential for accurately predicting the loads on curved blades when using models based on the lifting-line formulation.

The works of Shakya et al. [38] and Shakya et al. [39] are some of the more recent studies on flutter stability for wind turbine blades using frequency-domain and time-domain aerodynamic analyses for each of the respective works. The work in [39] uses a BEM solver with dynamic inflow for describing the aerodynamics and is based on the use of bend-twist coupled laminates for increasing the flutter critical speed in several wind turbine models with rated power above 1.5 MW.

2.2 NUMERICAL ANALYSIS OF WIND TURBINE BLADES WITH BEND-TWIST COUPLING

Important aspects on blade structural modeling are highlighted by Veers et al. [11], particularly the limitations of section-based models (i.e. beam modeling) in contrast to full 3-D modeling. Despite its simplicity and popularity at early design stages, the basic 1-D beam models fail to describe phenomena such as local distortion and buckling, stress concentration and cross-sectional warping. Different “section-analysis” software tools are mentioned as they allow to extract equivalent section properties from full 3-D shell models for use in simpler yet detailed beam section formulations.

The analysis performed by Laird et al. [40] contemplates different element formulations, shown in Figure 2.4, including shell elements both node-centered and node-offset and compared them to results with full solid elements. Besides a significant error in torsional response of a wind turbine blade when off-set node shells are used, the authors also find errors in bending response when the wall thickness is large compared to the section curvature radius, revealing the need for special attention to blade areas such as the leading edge.

On a subsequent study, Maheri et al. [41] compare FSI analyses considering a so called “single-step” in one case and, a fully coupled simulation in the other. The authors conclude that bend-twist coupling strictly requires a fully coupled FSI interface since bending deformation is dependent on aerodynamics; extension-twist coupling is seen to depend solely on the mechanical modeling.

This and further works such as [42, 43], are carried out with the software developed by Maheri et al. [44], they explore the feasibility of simplifying structural calculations by using partly analytic calculations and the implementation of a dedicated aeroelastic wind turbine code for evaluations in optimization problems based on a genetic algorithm.

The work of Lee et al. [45] consists in the FSI analysis of the NREL Phase VI wind turbine with a computational set up involving CFD and FEM in a 2-way coupled simulation. The results of this work are used to feed a BEM model with correction of stall

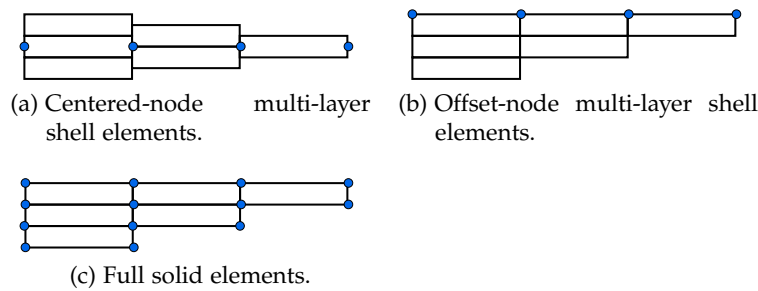


Figure 2.4: Concepts for modeling of composite hollow structures.

delay effects but more importantly, provide a direct reference model for the analysis of the wind turbine blade under study in the current work.

Paquette et al. [46] include different element formulations in their Finite-Element Analysis (FEA) of wind turbine blades with both neutral and bend-twist coupled structure. The authors find good agreement between the simulations using shell elements, with node-centered and node-offset formulations distancing from the findings in [40] which report discrepancies. Experimental validation of the torsional response is not fully demonstrated due to limitations in the experimental set up.

Fedorov et al. [47] predict bending and torsional response for a segment of a wind turbine blade using three standard FEA solvers in five different element formulations that include full shell and mixed shell/solid elements. The most significant discrepancies with respect to experimental tests are found in the torsional response of the blade, particularly those with node offset shell formulations which confirm the concerns presented in [40] with respect to the structural modeling accuracy of node-offset models.

The work of Lago et al. [48] addresses the aeroelastic analysis on a blade of the NREL 5MW reference wind turbine blade by means of a novel computational tool based on a beam-element structural model and the blade element momentum theory for the prediction of aerodynamic loads. The structural modeling in this work is based on a dimensional reduction technique, known also as the generalized Timoshenko beam theory, which accounts for preexisting deformations on the blade structure such as pre-bending, swept curvature or structural twist. The aerodynamic BEM solver on the other hand has been implemented with a correction for large blade deformations, under the concern that considerable deviations from the blade rigid geometry might result in incorrect representation of induced velocities and thrust force vectors on the sections of a deformed blade. It must be pointed that this work is the only to address this concern in the present review.

The structural analysis of bend-twist coupled blades has shown several topics that are usually addressed with a wider array of models (in comparison to aerodynamics for instance), mostly related to the inclusion of specific effects which tend to be simplified or neglected in the analysis of conventional blades. Those effects include:

- The treatment of warping in models based on beam-element formulations.
- The accuracy of torsional response with respect to full 3-D formulations based on shell-elements and solid elements.

- The validity of the assumption of small displacements and the effect on the requirements of the model (linear versus non-linear).

The modeling of aerodynamics on the other hand has been addressed with four different models: RANS formulations, vorticity-based formulations, Theodorsen's theory of unsteady aerodynamics and BEM theory. The only work that proposed a comparison between some of these models is that of Saverin et al. [24], in which reasonable agreement between the different methods is evidenced, except for operating conditions away from the design point.

The Review of Hansen et al. [49], mentions that besides the classical Glauert and Prandtl assumptions, the use of 2-D airfoil coefficients in the BEM model adds some uncertainty when neglecting rotational effects on the flow. Such effects can be mitigated by applying additional corrections on the input data. Besides, one of the critical limitations for the BEM theory is the lack of available airfoil data at high angles of attack which, coincide with the operating conditions at which notable differences were reported by Saverin et al. [24]. In addition, since the original BEM formulation is for a steady-state analysis, a considerable part of the modifications for transient problems involves dynamic models for individual phenomena such as time dependence in rotor inflow or dynamic stall.

The use of vortex-based methods and Theodorsen unsteady lift theory offers a better description of time-dependent phenomena but their accuracy is conditioned to the operating point, since these two models are also limited by the assumptions of attached boundary layer flow.

The use of RANS models represents one of the most versatile options but the typically high computation time limits their pertinence for interaction problems with a simplified set-up. This idea is supported by the fact that the Navier-Stokes solvers in the reviewed works are coupled at most with structural analysis modules, but not with complex wind models, i.e. aeroelastic models, or drive train dynamics.

2.3 MAIN FINDINGS FROM THE LITERATURE REVIEW

The earlier publications on bend-twist coupling applied to wind turbine blades show substantial amounts of effort directed towards a theoretical quantification of the phenomena. In one prominent case, this quantification is done in the form of the coupling coefficient, α , included in the expression:

$$g = \alpha \sqrt{(EIGK)} \quad (2.1)$$

where E and G represent Young and shear modulus respectively, while I and K represent the area moment of inertia and the polar moment of inertia respectively. This expression represents the coupling terms in the stiffness matrix, for the stress-strain relations as proposed by Lobitz and Veers [9] in their beam element formulation:

$$\begin{bmatrix} EI & -g \\ -g & GK \end{bmatrix} \begin{bmatrix} \frac{\partial \theta}{\partial x} \\ \frac{\partial \phi}{\partial x} \end{bmatrix} = \begin{bmatrix} M_b \\ M_t \end{bmatrix} \quad (2.2)$$

Here the vector of displacements involves the transverse angular displacement, θ and the torsional angular displacement, ϕ . The vector of generalized forces consists

of the bending moment M_b and the torsional moment M_t . For the stiffness matrix in Equation (2.2) to remain positive definite, the coupling coefficient is bounded by $-1 < \alpha < 1$.

It must be said also that dynamic stability of bend-twist coupled blades has been a topic of interest since the first applications for wind energy. Typical instabilities such as divergence, or flutter have been discussed and associated to changes in structural properties of coupled blades with respect to conventional designs. These phenomena can have a significant impact on the wind turbine service life; in consequence, the impact on economic performance is considerable and the topic has remained relevant in time.

The work of Lobitz and Veers [9] established a theoretical foundation for the quantification of bend-twist coupling in a FEM framework for beam elements. This has remained valid until today and is used within numerical analysis in which, bend-twist coupling can be included in a model without the strict need of defining any physical properties of the laminate. Some works such as that of Fedorov and Berggreen [50] make use of full 3-D models of the blade, including material and laminate lay-up specifications, for the sole purpose of determining mass and stiffness properties on discrete sections along the structure; these are used in the assembly of a beam model in which the numerical analysis is carried and the potential for aeroelastic coupling, represented by the coefficient α can be evaluated. In other cases, an abstract approach is taken, as the coupling can be simply prescribed by assigning desired and well-bounded values of α into the beam model without the need of a full 3-D model of the blade. Initially bend-twist coupling is conceived by deliberately altering the mechanical properties of composite materials used in the manufacture of wind turbine blades. This determines the first approach to bend-twist coupling based on material properties denominated here as coupling of type I, and can be subdivided into three categories as shown previously in Figure (2.3).

Ply-angle unbalance and ply-thickness unbalance are ways of introducing anisotropy by modifying the orientation or the thickness of individual plies with respect to the entire lay-up whereas material unbalance consist of a mixed composition of the laminate without unbalancing the angle or the thickness of the plies, for example by mixing carbon and glass fibers at opposite angles in plies of equal thickness. Additionally, combination of these types of unbalanced laminates can be implemented simultaneously.

Besides material coupling, other authors have proposed alternatives based on blade geometry regardless of the mechanical properties of the material. Geometry-coupling has been identified in two forms: a) swept blade geometry, denominated here coupling of type II, in which the blade is curved towards the trailing edge and b) displacement of the shear center, denominated as coupling of type III. The latter concept induces torsion because the mere distance between the aerodynamic force center and the shear center gives rise to a torsional moment.

A final category is contemplated in the work of Herath et al. [21], in which the bend-twist coupling is achieved on the structural level by using stiffening elements subjected to pure bending. This is a completely unique approach to bend-twist coupling, explored numerically in the cited work; furthermore, the resulting structural configuration is different from the conventional spar-cap and web designs that have been implemented so far. Having considered the principal areas of interest for the

application of bend-twist coupling and the main concepts for implementing this technology into wind turbine blades, a group of works has been collected and described in Table 2.1 which contains information on the coupling mechanism, the application and the approach for analysis. One of the most notable characteristics is that most works consist of numerical simulation with only a few of them including experimentation; this is expected however, since many of the cases are based on large machines. The works listed in Table 2.1 have been determined as relevant to the present project by judging the contributions to improving wind turbine energy capture by the implementation of bend-twist coupling.

It has been observed that the design paradigm of load alleviation can lead indirectly to improved energy capture, with the work of Zahle et al. [22] being the most prominent example. From the works in which twist towards feather is implemented with bend-twist coupling, it is common to observe that the main aim is load alleviation and it often comes with the consequence of power reductions in the below-rated range with respect to baseline models.

This is another case in which an objective of improving power is indirectly pursued as the bend-twist coupling for load alleviation in variable-pitch wind turbines tends to diminish power capture at low wind speeds. Consequently, utility-scale rotors with bend-twist coupling for load mitigation have been addressed with design modifications to preserve the blade geometrical optimality at the below-rated wind speed range.

One of the key characteristics of the work in Stäblein et al. [23], is precisely the modification to the blade twist distribution; however, this improvement is demonstrated at full for a single wind speed value, selected as the reference pre-twist wind speed. The work of Scott et al. [25] proposes a similar solution and is restricted to the specific wind speed for which the blade is optimized. Additionally, for both cases the wind turbine has a variable pitch control. Both Maheri et al. [15] and Atalay and Kayran [26] propose similar design solutions to maximize power output; however, Maheri et al. [15] contemplate what appears to be a stall regulated wind turbine.

This application for coupled blades has been implemented with large scale wind turbines, which are often equipped with robust control systems for optimum power capture in the below-rated range. From the previous appreciation two questions arise: in first place it seems that the twist towards feather is aimed at reducing the angle of attack causing a load reduction, even if the final angle of attack is inferior to the optimum; this might indicate that the twist actuation can point to two different objectives i.e. optimal power or reduced loads. In second place, it seems that, except for the work of Maheri et al. [15], stall regulated wind turbines have received less attention for analysis on how bend-twist coupling affects the rotor power capture in terms of the power coefficient at the different regions of the operating range.

The approach of Barr and Jaworski [32] concerning the direction of pitch actuation stands out from the majority of works in the sense that pitch towards stall is generally associated to higher risks of stall flutter and also to higher loads in the blade. Still, the declared goal of the authors is power maximization over reduction of loads. The study of Maheri et al. [15] also opts for twist towards stall, at least when presenting the maximum potential of the bend-twist concept introduced in their work. This approach can lead to different obstacles the first of which is fatigue performance; in second place is the difficulty for predicting the aerodynamic performance, as inducing the blades to

Coupling concept	Declared target	FSI interface	Structural modeling	Struc. Modeling tool	Aerodynamic modeling	Aero. modeling tool	source
I	Increase of AEP , power regulation	WTAB	FEM	TRIC	BEM	WTAero	[15]
Prescribed	Increase in AEP , reduction of loads.	N/A	N/A	N/A	BEM , Surface-Panel	Cwind, Palisupan	[17]
I, II	Structural design of blade with aeroelastic tailoring.	N/A	FEM	NASTRAN	BEM	Developed by the authors	[20]
I	Reduction of loads.	ADAMS	FEM	HyBlade	BEM , Generalized Dynamic Wake Model	AeroDyn	[2]
III	Optimization for max AEP .	HAWCStab2	FEM	HAWCStab2	BEM	HAWCStab2	[22]
Prescribed	Reduction of power losses.	HAWCStab2	FEM	HAWCStab2	BEM	HAWCStab2	[23]
I	Numerical modeling with vortex method.	FAST	FEM	BeamDyn	Lifting line free vortex wake	Qblade	[24]
I,II	Analysis of power performance, load alleviation and pitch actuation.	DNV GL Bladed	Multi-body dynamics, modal representation.	DNV GL Bladed, PreComp	BEM	DNV GL Bladed	[25]
I	Analysis of reduction of damage equivalent loads.	PHATAS	FEM	PHATAS	BEM	PHATAS	[26]
I	Optimization of tow orientation for maximized power output.	Partitioned, two-way	FEM	ABAQUS	RANS , $k-\epsilon$	CRUNCH CFD	[32]
I, II	Load alleviation	Partitioned, two-way	FEM	ABAQUS	RANS , $k-\omega$ SST	STAR-CCM+	[34]

Table 2.1: Main characteristics of relevant works.

stall leads to non-linear aerodynamics which are more complex to treat. In third place comes the risk of inducing aerodynamic instabilities which no matter how remote, always should be evaluated.

SUMMARY

A selected group of works is presented in Table 2.2 with general information on the aims and results that are relevant to this project. The highlighted rows represent those works which, in the author's criteria, align more closely to the aims and objectives of this proposal. Other works are included due to the relevance in the methodology and approach to the analysis of blades with bend twist-coupling. The most notable aspect in several of the cited works lies in the fact that the structural modeling is often over-simplified with respect to other elements in the overall analysis. In some cases, the structural response is not directly modeled but prescribed either by an artificial function of the wind speed or by parametrizing a normalized deformation mode and assuming it as the actual deformation behavior of the blade structure. Other works with promising results neglect secondary structural components such as the blade skins. Lastly, there is a clear focus towards wind turbines with relatively high rated wind speeds, often above 10 m/s, while the present work is intended to address the operation in low speed wind regimes.

Upon a review of state-of-the-art works in the implementation of bend-twist coupled blade structures in wind turbines, the present work can be justified considering that:

- Wind turbines in the small to medium size range have not been widely studied from the perspective of bend-twist coupling applications when compared to large wind turbines.
- The use of bend-twist coupling as a purely passive control strategy has been considered in applications that disregard the structural modeling of coupled blades and instead prescribe the torsional deformation. The present work contemplates the modeling of all modular components involved in FSI problems.
- The distance between the aerodynamic center and the shear center of a blade section can induce bend-twist coupling behavior to some extent, depending on the magnitude of aerodynamic loads and the bending and torsional stiffness. To the best of the author's knowledge this effect has not been computed directly, except for the related work in Couturier et al. [52]; instead, it is accounted for implicitly when the blade is simulated with an aeroelastic model. In this work, this effect is expected to be quantified prior to the design of a bend-twist coupled blade, this should result in an improved design without the need of an iterative procedure. Furthermore, if existing aeroelastic codes for wind turbine analyses, based on 1-D beam models neglect the torsional deformation of the blade, the aerodynamic twist of conventional blades can be an unattended phenomenon that impacts the performance of the turbine when deployed for operation.
- The application of bend-twist coupling in wind turbines operating at constant angular speeds and fixed-pitch has not been explored with the same detail as variable-pitch machines. This opens an opportunity for improvement to be ad-

Source	Aim	Improvement in AEP	Simplifications and differing aspects regarding the present work
Maheri et al. [15]	Increase of AEP and Power regulation.	13% incr. AEP (5.3° Twist to Stall), 6% Incr. AEP (3° Twist to Feather, with maximum power increased by 50% over the nominal value)	Assumed constant fiber angle, mechanical properties, and shell thickness along the span. The shape of the induced twist is not modeled but rather assumed from an external source. Chord distribution and blade radius can vary. Apparently constant speed, passive stall regulated WT
Nicholls-Lee and Turnock [17]	Increase in AEP and reduction of loads	2.65% incr. AEP (pitch+linear twist), 1.80% incr. AEP (linear twist)	Structural response is not simulated but artificially prescribed as a function of flow velocity. Variable pitch considered.
Capuzzi et al. [18]	Twist optimization for Power increase	-	Adaptive behavior is targeted to a very high rated wind speed (15 m/s). Performance near cut in wind speed is essentially unchanged.
Capuzzi et al. [19]	Structural design of an aeroelastically tailored blade	1.8% (variable-pitch, w.r.t. AEP optimized baseline), 2.8% (fixed-pitch, w.r.t. AEP optimized baseline)	The effect of the blade skins is neglected. WT with pitch control considered.
Capuzzi et al. [20]	Structural design of an aeroelastically tailored blade.	-	-
Hayat and Ha [2]	Evaluation of load mitigation capabilities.	-	-
Zahle et al. [22]	Optimization for max AEP	8.7% (via passive load alleviation resulting in a 9% longer blade)	Primary target is load alleviation in the above-rated range. WT with pitch control.
Stäblein [51]	Reduction of power losses	-	-
Scott et al. [25]	Analysis of power performance, load alleviation and pitch actuation.	-	-
Atalay and Kayran [26]	Analysis of reduction of damage equivalent loads.	-	-
Barr and Jaworski [32]	Optimization of tow orientation for maximized Power output.	14% incr. in power (for a cut-in optimized blade), 7% incr. in power (for a rated wind speed optimized blade)	Optimization based on both cut-in and rated wind speeds. A high cut-in wind speed is considered (4.4 m/s for a 5 MW machine). WT with pitch control.
Madsen et al. [35]	Load alleviation	40-45% increase in AEP (by increase of rotor diameter)	Design by gradient-based optimization. Pitch to feather due to class III bend-twist coupling. The rotor considers standard pitch controller.

Table 2.2: Key aspects of relevant works from the literature review.

dressed here, since fixed-pitch, constant angular speed rotors tend to generate power at sub-optimal C_p in a considerable portion of the operation range.

- To the best of the authors knowledge, no work has explored the potential for bend-twist coupling in pre-bended blades on which the flap-wise moment is caused by inertial loads. The analysis of starting behavior is expected to be carried out in this work by considering bend-twist coupling actuation by inertial loads on pre-bended blades.
- The review exercise reveals a lack of explicit interest for machines operating at low wind speeds; instead, the majority if not all the reviewed works contemplate wind turbines with high rated wind speeds, commonly beyond 10 m/s. In the present work, the analysis considers rated wind speeds below 10 m/s and a focus on starting behavior at cut-in wind speeds.

3

THEORETICAL FRAMEWORK

The present chapter includes the description of the mathematical models used in the setting of the simulation frameworks for the analysis of aerodynamics, structural response of a composite blade and the analysis of interaction between aerodynamic and structural solutions in a set of **FSI** simulations. The aerodynamic models consists of the computationally inexpensive **BEM** model and the more robust **FVM**. A set of basic governing equations is presented for each model. The structural analysis is performed with a robust **FEM** and the pertinent details about the governing equations and the transient formulations are included as well. The description of the **FSI** process is dedicated to the mesh treatment for deforming domains and the treatment of data mapping carried out at each coupling step.

NOMENCLATURE

a	Axial induction factor	F_t	Tangential force
A, A_R	Area, Rotor Area	\mathbf{I}	Identity Matrix
$area_f$	Surface of distributed resistance	J_f	Mass flux through the j -th cell face
$a_n b$	Linearized coefficient for the neighboring nodes	J'_f	Mass flux correction
a'	Tangential induction factor	J_f^*	Guessed mass flux
a_p	Linearized coefficient for the central node	k	Foundation stiffness
B	Number of blades in the rotor	$[K_e]$	Element stiffness matrix
$[B]$	Strain-displacement matrix	$[K]$	Structural stiffness matrix
c	Local blade chord	$[K_e^f]$	Element foundation stiffness matrix
$[C]$	Structural damping matrix	L	Lift force
C_d	Drag coefficient	$[M_e]$	Element mass matrix
C_l	Lift coefficient	$[M]$	Structural mass matrix
C_n	Normal force coefficient	n	Unit vector normal to the actuator disk
C_t	Tangential force coefficient	$[N_n]$	Matrix of shape functions for normal motion
C_T	Thrust coefficient	$[N]$	Matrix of shape functions
$[D]$	Stress-strain matrix	nb	neighboring cell index
dA	Area of an annular blade element	p	Pressure field
d_f	Flux correction factor	$\{p\}$	Pressure vector
dM	Differential moment for an annulus	p_{c0}, p_{c1}	Nodal pressure values around face f
dT	Differential thrust force for an annulus	p'	Pressure correction
F	Prandtl tip-loss factor	p^*	Guessed pressure field
f	Face index	r	Radial location
F_s	Spatial discretization term	R	Rotor radius
$\{F^a\}$	Acceleration force vector	R_{n+1}	Residual vector at time instant $n+1$
$\{F_e^{nd}\}$	Nodal forces acting on the element	S	Source term
$\{F_e^{th}\}$	Element thermal load vector	t	Time
$\{F_e^{pp}\}$	Element pressure vector	U	Strain energy
$F^a(t)$	External load vector	U_1	Strain energy
$F^i(t)$	Internal load vector	U_2	Surface tension strain energy
F_B	Body forces	$\{u\}$	Nodal displacement field
f_g	Glauert correction factor	$\{\ddot{u}\}$	Acceleration vector
F_n	Normal force	u_i	Velocity field in indicial notation

\mathcal{V}	Volume	Greek symbols	
V	External work		
V_1	External work	α	Local angle of attack
V_2	Pressure force work	α_m, α_f	HHT- α scheme parameters
V_3	Nodal force work	α_N, δ_N	Newmark's integration parameters
vol	Element volume	α_p	Pressure correction factor
V_∞	Free-stream wind speed	β	Local twist angle
v	Velocity field	γ	Amplitude decay factor
v_n	Normal velocity component at a cell face	δ	Virtual operator
V'	Relative velocity at the rotor plane in skewed flow	$\{\varepsilon\}$	mechanical strain vector
V_{rel}	Relative velocity at a blade element	$\{\varepsilon^{th}\}$	Thermal strain vector
W	Induced velocity at the actuator disk	ρ	Flow density
$\{w_n\}$	Component of motion normal to the wall	τ	Viscous stress tensor
$\{w\}$	Displacement vector	$\{\sigma\}$	Stress vector
W_1	Flow velocity far downstream of the actuator disk	ϕ	Local flow angle
W_n	Normal component of the induced velocity	φ	Scalar quantity
W_t	Tangential component of the induced velocity	ω	Rotor angular speed
W_θ	Rotational velocity component		

3.1 AERODYNAMIC MODELS

3.1.1 Blade element momentum theory

Under the description of Hansen [53], the BEM model uses a discretization in which each blade is treated as a series of mutually independent elements, each one sweeping an annular area around the center of the rotor. As the starting point of the model, the Momentum theory considers a blade, or blade element as an actuator disk, depicted in Figure 3.1. According to Newton's law of linear momentum, the wind speed reduction caused by the actuator disk is proportional to the axial fluid load experienced by the actuator. The change in speed as the air flows through the actuator disk is represented mathematically in terms of the axial induction factor, a , in the following way:

$$W = (1 - a) V_\infty \quad (3.1)$$

Here V_∞ represents free-stream wind speed, W represents the flow velocity at the location of the actuator disk, and its relative difference with respect to the freestream wind speed is given by a . Using Momentum theory, the annular area swept by a single blade element is treated as an actuator surface; for each one of these actuator surfaces there is an associated annular streamtube, an assumption that forbids the flow of air between adjacent actuator surfaces and which by extension, prevents radial flow to occur. Each annular surface experiences a differential thrust force defined in terms of the change in wind speed as it passes through:

$$dT = 4\pi r \rho V_\infty^2 a (1 - a) dr \quad (3.2)$$

likewise, the differential moment acting on the element is defined as:

$$dM = 4\pi r^3 \rho V_\infty \omega (1 - a) a' dr \quad (3.3)$$

The representation for torque given in Equation 3.3 is based on the axial induction factor, a , and the tangential induction factor, a' . The inclusion of a' allows to describe the change in angular velocity due to the momentum transferred from the rotating blade element into the airflow; in fact, tangential induction can be defined in terms of flow speed in the same way it is done for axial induction, defining an angular velocity component, W_θ , as:

$$W_\theta = 2a'\omega r \quad (3.4)$$

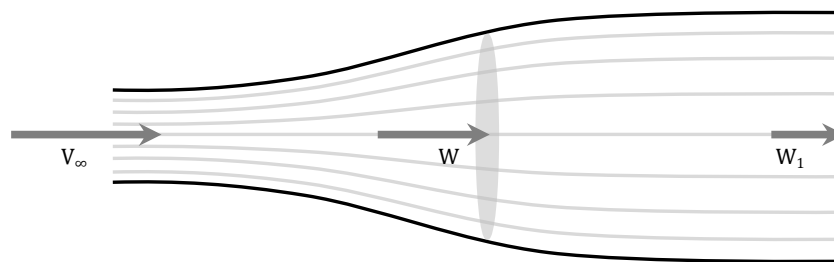


Figure 3.1: Stream tube across an actuator disk

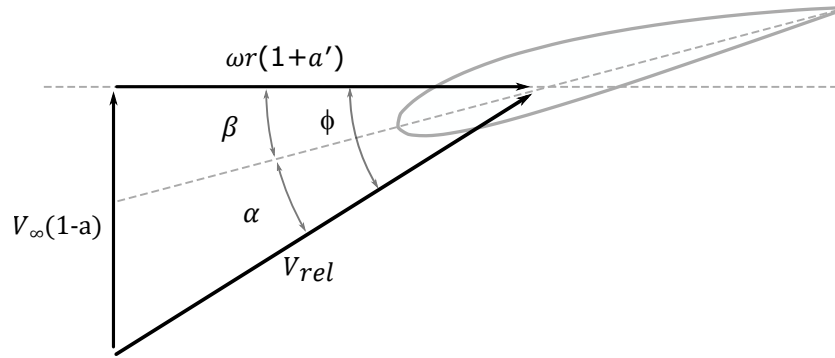


Figure 3.2: Velocity triangle at a blade element.

Additional expressions for differential thrust and moment are provided from [BEM](#) theory, based on airfoil lift and drag coefficients for the cross sectional shape of each blade element. Since dT is normal to the rotor plane and dM is contained in it, a corresponding projection for the airfoil force coefficients is established:

$$\begin{aligned} C_n &= C_l \cos(\phi) + C_d \sin(\phi) \\ C_t &= C_l \sin(\phi) + C_d \cos(\phi) \end{aligned} \quad (3.5)$$

This projection transforms lift and drag coefficients into normal and tangential force coefficients, and is nothing more than a rotation of axes by an angle ϕ , which is in fact the local flow angle for each blade element as illustrated in [Figure 3.2](#). A dimensional representation of normal and tangential forces per unit length is given by:

$$F_n = \frac{1}{2} \rho V_{rel}^2 c C_n \quad (3.6)$$

$$F_t = \frac{1}{2} \rho V_{rel}^2 c C_t \quad (3.7)$$

Now dT and dM can be defined in terms of normal and tangential forces:

$$dT = B F_n dr \quad (3.8)$$

$$dM = r B F_t dr \quad (3.9)$$

Where dr represents the span-wise length of each blade element and B represents the number of blades in the rotor. The remainder of the process in the [BEM](#) model consists of an iterative solution for a , based on the definitions for dT in [Equations 3.2](#) and [3.8](#) and, the definitions for dM in [Equations 3.3](#) and [3.9](#). Usually a steady-state computation is made with a fixed point iteration procedure, assuming $a = 1$ as an initial guess. After convergence, the final values for dT and dM are integrated along the blade radius to obtain total rotor thrust force and total rotor torque. The mechanical power delivered by the rotor can be expressed in terms of torque and angular speed as $P_R = T\omega$ and this is equivalent to the standard definition in terms of the dimensionless rotor power coefficient (C_P) according to:

$$P_R = \frac{1}{2} \rho V_\infty^2 A_R C_P \quad (3.10)$$

So far, the presented form is a basic formulation of the BEM model, and the underlying simplifications restrict this methodology to idealized cases. The first restriction requires that the blade tip loading is strictly two-dimensional, meaning that each blade is equivalent to an infinitely long wing and in consequence, the aerodynamic loads are higher than for a real blade, in which aerodynamic loads gradually reduce to zero at the tip of the blade. The second restriction requires that the rotor loads are small so that the momentum theory description of thrust force remains valid. This is necessary because in reality, the boundary of the streamtube of air passing through the turbine rotor becomes unstable when the rotor loads are too high; as a result, the flow downstream of the rotor becomes unsteady and the induction factor of momentum theory stops giving a correct description.

Regarding the first issue with the original BEM model, a popular correction for the blade tip loading is proposed in terms of the tip-loss factor, attributed to Prandtl and presented here in a compact form:

$$F = \frac{2}{\pi} \arccos \left[\exp \left(-\frac{B(R-r)}{2r \sin \phi} \right) \right] \quad (3.11)$$

This correction factor is then used to modify the expressions for dT and dM derived from momentum theory:

$$dT = 4\pi r \rho V_\infty^2 a (1-a) F dr \quad (3.12)$$

$$dM = 4\pi r^3 \rho V_\infty \omega (1-a) F a' dr \quad (3.13)$$

The second issue can be treated with an empirical correction for C_T , specified as a function of the axial induction factor, a :

$$C_T = \begin{cases} 4a(1-a)F & \text{for } a \leq 1/3 \\ 4a \left[1 - \frac{1}{4}(5-3a)a \right] F & \text{for } a > 1/3 \end{cases} \quad (3.14)$$

Note that the definition for C_T is based on the differential thrust force:

$$C_T = \frac{dT}{\frac{1}{2} \rho V_\infty^2 dA} \quad (3.15)$$

An extension of this formulation for a dynamic computation can be done by considering Bramwell's relationship for a rotor in forward flight:

$$W_n = \mathbf{n} \cdot \mathbf{W} = \frac{T}{2\rho A |V'|} \quad (3.16)$$

Where \mathbf{n} represents the unit vector of the thrust force in the reference frame of the rotation axis and $|V'| = |\mathbf{V}_\infty + \mathbf{n}(\mathbf{n} \cdot \mathbf{W})|$. In this relation the component of the induced velocity normal to the actuator disk is parallel to the thrust force. Expanding the expression for a representative area, the following is obtained for the normal induced velocity:

$$W_n = \frac{-BL \cos \phi}{4\pi\rho r F |V_\infty + f_g \mathbf{n} (\mathbf{n} \cdot \mathbf{W})|} \quad (3.17)$$

For the tangential component a similar relationship exists, proving that under the treatment of yaw misalignment given in Equation 3.16, only lift force affects the induced velocity through the rotor plane:

$$W_t = \frac{-BL \sin \phi}{4\pi\rho r F |V_\infty + f_g \mathbf{n} (\mathbf{n} \cdot \mathbf{W})|} \quad (3.18)$$

3.1.2 RANS model and the Finite-Volume method

The solution method used in the simulation of the fluid flow field is presented next. Its presentation in the context of this work begins with a recount of the governing equations for the flow of a viscous and transient fluid. In subsequent chapters the work is restricted to an incompressible flow; however the model presented next is given for a fluid of arbitrary density.

Governing equation of conservation of mass

The governing equation for conservation of mass of a three-dimensional flow in the cartesian coordinate system can be derived by considering a small volume of fluid, with an hexahedral shape of dimensions Δx , Δy , and Δz and considering fluid flow components u , v , and w in x , y and z directions respectively. Mass conservation requires that the change in mass within the control volume equals the net mass flow rate crossing the boundary of the control volume, known as the control surface. Using the control volume shown in Figure 3.3, the mass flow rate can be expressed at the faces of the control surface as a set of first-order Taylor series expanded around the center of the control volume where the flow field is known. Assuming that the mass flow out of the volume is positive, the total flow mass balance contains six terms, one for each face of the control surface:

$$\begin{aligned} & \left[\rho u + \frac{\partial(\rho u)}{\partial x} \frac{\Delta x}{2} \right] \Delta y \Delta z + \left[\rho v + \frac{\partial(\rho v)}{\partial y} \frac{\Delta y}{2} \right] \Delta x \Delta z - \left[\rho u - \frac{\partial(\rho u)}{\partial x} \frac{\Delta x}{2} \right] \Delta y \Delta z \\ & - \left[\rho v - \frac{\partial(\rho v)}{\partial y} \frac{\Delta y}{2} \right] \Delta x \Delta z + \left[\rho w + \frac{\partial(\rho w)}{\partial z} \frac{\Delta z}{2} \right] \Delta x \Delta y - \left[\rho w - \frac{\partial(\rho w)}{\partial z} \frac{\Delta z}{2} \right] \Delta x \Delta y \end{aligned}$$

This, according to the principle of conservation of mass, must equal to the rate of change of mass within the control volume:

$$-\frac{\partial \rho}{\partial t} \Delta x \Delta y \Delta z$$

Both expressions are equated and divided by the total volume $\Delta x \Delta y \Delta z$ to obtain:

$$\frac{\partial \rho}{\partial t} + \frac{\partial}{\partial x} (\rho u) + \frac{\partial}{\partial y} (\rho v) + \frac{\partial}{\partial z} (\rho w) = 0 \quad (3.19)$$

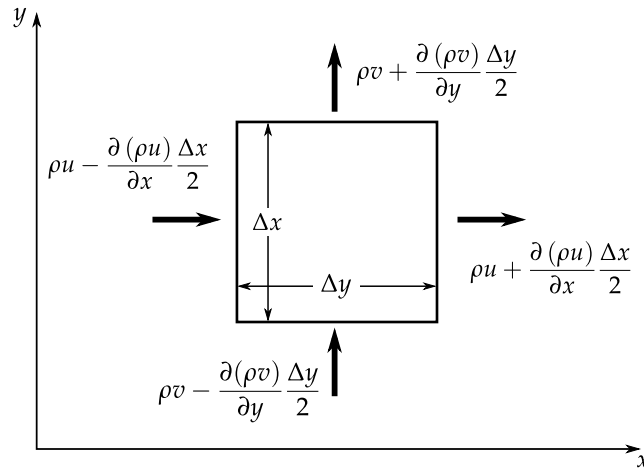


Figure 3.3: Balance for mass flow rates across the control volume boundaries (adapted from [3]).

Which represents the conservation of mass in its most generic form, for a control volume of arbitrary size, and a fluid flow of density ρ .

Equation of conservation of linear momentum

Viewed as a statement of Newton's second law for a fluid particle, the equation of conservation of linear momentum relates the sum of all external forces acting on the fluid particle to the time rate of change of its linear momentum. With this in mind, the total acceleration of a fluid particle can be expressed as the substantial derivative of the velocity field, which is defined as the sum of the local acceleration and the convective acceleration:

$$\frac{d\mathbf{V}}{dt} = \frac{\partial \mathbf{V}}{\partial t} + u \frac{\partial \mathbf{V}}{\partial x} + v \frac{\partial \mathbf{V}}{\partial y} + w \frac{\partial \mathbf{V}}{\partial z} = \frac{\partial \mathbf{V}}{\partial t} + (\mathbf{V} \cdot \nabla) \mathbf{V} \quad (3.20)$$

The equation above is a vector equation which represents in compact form the total acceleration for each one of the three scalar components of the velocity field. When paying attention to the forces acting on a fluid particle, it is common to classify them into: a) body forces, which act directly on the mass of the fluid, and b) surface forces, which act directly on the surface of the fluid particle. The body forces in x can be expressed in terms of a body force per unit mass f_x , as $f_x \rho \Delta x \Delta y \Delta z$. The surface forces are calculated at the different faces of the control surface in terms of the components of the stress tensor τ_{ij} which, using the known values at the center of a reference control volume, can be expressed at the faces of the control surface with a first-order Taylor series expansion:

$$\begin{aligned}
& \rho f_x \Delta x + \left[\tau_{xx} + \frac{\partial}{\partial x} (\tau_{xx}) \frac{\Delta x}{2} \right] \Delta y \Delta z - \left[\tau_{xx} - \frac{\partial}{\partial x} (\tau_{xx}) \frac{\Delta x}{2} \right] \Delta y \Delta z \\
& \left[\tau_{yx} + \frac{\partial}{\partial y} (\tau_{yx}) \frac{\Delta y}{2} \right] \Delta x \Delta z - \left[\tau_{yx} - \frac{\partial}{\partial y} (\tau_{yx}) \frac{\Delta y}{2} \right] \Delta x \Delta z \\
& \left[\tau_{zx} + \frac{\partial}{\partial z} (\tau_{zx}) \frac{\Delta z}{2} \right] \Delta x \Delta y - \left[\tau_{zx} - \frac{\partial}{\partial z} (\tau_{zx}) \frac{\Delta z}{2} \right] \Delta x \Delta y \\
& = \rho f_x \Delta x \Delta y \Delta z + \frac{\partial}{\partial x} (\tau_{xx}) \Delta x \Delta y \Delta z + \frac{\partial}{\partial y} (\tau_{yx}) \Delta x \Delta y \Delta z + \frac{\partial}{\partial z} (\tau_{zx}) \Delta x \Delta y \Delta z \quad (3.21)
\end{aligned}$$

Following the definition of the conservation of linear momentum, the x -component of the total particle acceleration described in Equation 3.20 times the mass must be equal to the x -component of the total forces acting over the fluid particle which is represented by the control volume. When written, this equation takes the form:

$$ma_x = \rho \Delta x \Delta y \Delta z \frac{du}{dt} = \rho \Delta x \Delta y \Delta z \left[\frac{\partial u}{\partial t} + (\mathbf{V} \cdot \nabla) u \right] = F_x \quad (3.22)$$

Now, a more explicit form of the equation can be obtained by substituting Equation 3.21 into the tem F_x and dividing the resulting expression by the volume of the control volume itself :

$$\rho \left[\frac{\partial u}{\partial t} + (\mathbf{V} \cdot \nabla) u \right] = \rho f_x + \frac{\partial \tau_{xx}}{\partial x} + \frac{\partial \tau_{yx}}{\partial y} + \frac{\partial \tau_{zx}}{\partial z} \quad (3.23)$$

The conservation equations for y and z linear momentum are obtained following the same procedure for the total acceleration and the totale external forces acting in those directions. The resulting equations are:

$$\rho \left[\frac{\partial v}{\partial t} + (\mathbf{V} \cdot \nabla) v \right] = \rho f_y + \frac{\partial \tau_{xy}}{\partial x} + \frac{\partial \tau_{yy}}{\partial y} + \frac{\partial \tau_{zy}}{\partial z} \quad (3.24)$$

$$\rho \left[\frac{\partial w}{\partial t} + (\mathbf{V} \cdot \nabla) w \right] = \rho f_z + \frac{\partial \tau_{xz}}{\partial x} + \frac{\partial \tau_{yz}}{\partial y} + \frac{\partial \tau_{zz}}{\partial z} \quad (3.25)$$

The relationship between the motion of the fluid and the stresses acting on it can be established in terms of the strain rates. With this purpose Bertin and Cummings [3] summarize very well the necessary assumptions for establishing a suitable definition for stress components. In first place, the fluid is assumed to be Newtonian which means that transverse velocity gradients are related to shear stresses by means of the viscosity coefficient μ , according to the relationship $\tau = \mu (\partial u / \partial y)$. A so called second viscosity coefficient appears in the description of normal stress components, this is necessary in flows of variable density and is defined according to the Stoke's hypothesis as $\lambda = -2/3\mu$. In second place, the stress-strain relationships are assumed to be invariant with respect to the coordinate system. Finally, in third place if all the velocity gradients vanish, then the stress components reduce to the hydrostatic pressure, p . Following the previous considerations, the components of the stress tensor are defined as:

$$\begin{aligned}
\tau_{xx} &= -p - \frac{2}{3}\mu\nabla \cdot \mathbf{V} + 2\mu\frac{\partial u}{\partial x} \\
\tau_{yy} &= -p - \frac{2}{3}\mu\nabla \cdot \mathbf{V} + 2\mu\frac{\partial v}{\partial y} \\
\tau_{zz} &= -p - \frac{2}{3}\mu\nabla \cdot \mathbf{V} + 2\mu\frac{\partial w}{\partial z} \\
\tau_{xy} &= \tau_{yx} = \mu\left(\frac{\partial u}{\partial y} + \frac{\partial v}{\partial x}\right) \\
\tau_{xz} &= \tau_{zx} = \mu\left(\frac{\partial u}{\partial z} + \frac{\partial w}{\partial x}\right) \\
\tau_{yz} &= \tau_{zy} = \mu\left(\frac{\partial v}{\partial z} + \frac{\partial w}{\partial y}\right)
\end{aligned} \tag{3.26}$$

After substituting the definitions for the stress components into Equations 3.23 to 3.25, the final version of the coservation of linear momentum in the x , y and z directions is given by:

$$\rho\frac{\partial u}{\partial t} + \rho(\mathbf{V} \cdot \nabla)u = \rho f_x - \frac{\partial p}{\partial x} + \frac{\partial}{\partial x}\left(2\mu\frac{\partial u}{\partial x} - \frac{2}{3}\mu\nabla \cdot \mathbf{V}\right) + \frac{\partial}{\partial y}\left[\mu\left(\frac{\partial u}{\partial y} + \frac{\partial v}{\partial x}\right)\right] + \frac{\partial}{\partial z}\left[\mu\left(\frac{\partial u}{\partial z} + \frac{\partial w}{\partial x}\right)\right] \tag{3.27}$$

$$\rho\frac{\partial v}{\partial t} + \rho(\mathbf{V} \cdot \nabla)v = \rho f_y + \frac{\partial}{\partial x}\left[\mu\left(\frac{\partial u}{\partial y} + \frac{\partial v}{\partial x}\right)\right] - \frac{\partial p}{\partial y} + \frac{\partial}{\partial y}\left(2\mu\frac{\partial v}{\partial y} - \frac{2}{3}\mu\nabla \cdot \mathbf{V}\right) + \frac{\partial}{\partial z}\left[\mu\left(\frac{\partial v}{\partial z} + \frac{\partial w}{\partial y}\right)\right] \tag{3.28}$$

$$\rho\frac{\partial w}{\partial t} + \rho(\mathbf{V} \cdot \nabla)w = \rho f_z + \frac{\partial}{\partial x}\left[\mu\left(\frac{\partial u}{\partial z} + \frac{\partial w}{\partial x}\right)\right] + \frac{\partial}{\partial y}\left[\mu\left(\frac{\partial v}{\partial z} + \frac{\partial w}{\partial y}\right)\right] - \frac{\partial p}{\partial z}\left(2\mu\frac{\partial w}{\partial z} - \frac{2}{3}\mu\nabla \cdot \mathbf{V}\right) \tag{3.29}$$

An additional step required for the closure of the governing equations along with the turbulence model consists in defining the individual components of velocity in terms of an average component and a turbulent component; for instance, the instantaneous x -component of the velocity is defined as $u = \bar{u} + u'$. Subsequently, the Navier-Stokes equations are averaged such that whole system is given in terms of the average components \bar{u} , \bar{v} , and \bar{w} and the momentum equations gain an additional term called the Reynolds turbulent stress components, represented in indicial notation as $\rho\overline{u'_i u'_j}$; for a two dimensional flow, where u'_k represents the turbulent components of velocity. These are the so-called RANS equations, the derivation is omitted for the sake of brevity. Finally, it can be said that the turbulent Reynolds stresses are the link between the governing equations for the flow and the equations for the turbulent model, to be introduced later.

Governing equations for a moving mesh

One of the most important aspects of FSI in terms of accuracy and stability is the treatment given to the conservation equations in the context of a moving mesh for the fluid flow domain. The formulation of the equations for the conservation of mass and linear momentum in a moving mesh is known as the Arbitrary Lagrangian-Eulerian (ALE) formulation. As mentioned by van Zuijlen [54], van Zuijlen et al. [55], the use of this format introduces the Geometric Conservation Law (GCL) into the flow equations, this is crucial because a moving mesh implies not only translation of the cells and its nodes, but also that the motion can stretch or compress the cells, thus changing the local volume. The theory presented next has been adopted from published literature [54, 55]; the relevance of this step on the stability of the coupled solution has been stressed by other authors working on coupled analyses of wind turbine blades such as Lee et al. [45] and Bazilevs et al. [56, 57, 58].

The standard formulation for the Navier-Stokes equations in three dimensions are represented by Equation 3.19 and by Equations 3.23 to 3.25 in terms of the stress tensor τ_{ij} . To succinctly illustrate the ALE formulation, the Navier-Stokes equations are presented in compact form as:

$$\frac{\partial \mathbf{W}}{\partial t} + \frac{\partial \mathbf{E}}{\partial x} + \frac{\partial \mathbf{F}}{\partial y} + \frac{\partial \mathbf{G}}{\partial z} = \mathbf{J} \quad (3.30)$$

where the unknowns are represented by \mathbf{W} , all the non-linear functions of \mathbf{W} are included in \mathbf{E} , \mathbf{F} and \mathbf{G} and the source terms are included in \mathbf{J} :

$$\begin{aligned} \mathbf{W} &= \begin{bmatrix} \rho \\ \rho u \\ \rho v \\ \rho w \end{bmatrix} & \mathbf{E} &= \begin{bmatrix} \rho u \\ \rho u^2 + p - \tau_{xx} \\ \rho uv - \tau_{xy} \\ \rho uw - \tau_{xz} \end{bmatrix} \\ \mathbf{F} &= \begin{bmatrix} \rho v \\ \rho uv - \tau_{xy} \\ \rho v^2 + p - \tau_{yy} \\ \rho vw - \tau_{yz} \end{bmatrix} & \mathbf{G} &= \begin{bmatrix} \rho w \\ \rho uw - \tau_{xz} \\ \rho vw - \tau_{yz} \\ \rho w^2 + p - \tau_{zz} \end{bmatrix} \\ \mathbf{J} &= \begin{bmatrix} 0 \\ \rho f_x \\ \rho f_y \\ \rho f_z \end{bmatrix} \end{aligned} \quad (3.31)$$

Next the differential form in Equation 3.30 is integrated over a fixed control volume:

$$\frac{\partial}{\partial t} \int_{V_{\text{fix}}} \mathbf{W} dV + \int_{S_{\text{fix}}} [\mathbf{E}(\mathbf{W}), \mathbf{F}(\mathbf{W})] \cdot \mathbf{n} dS = \int_{V_{\text{int}}} \mathbf{J} dV \quad (3.32)$$

This results in the standard Navier-Stokes equations, which unfortunately are no longer valid when the control volume of interest is moving and deforming. The reason is that the time derivative in the first term of Equation 3.32 cannot be pushed out of the volume integral for a moving volume since in such a case, the volume is a function

of time. This reveals a conflict with the very definition of the total derivative, in which the transient term is defined specifically for a fixed point in space. For this reason the equation must be integrated over a moving control volume instead:

$$\int_{V_{\text{mov}}} \frac{\partial \mathbf{W}}{\partial t} dV + \int_{S_{\text{mov}}} [\mathbf{E}, \mathbf{F}] \cdot \mathbf{n} dS = \int_{V_{\text{mov}}} \mathbf{J} dV \quad (3.33)$$

At this point, the conservation equations present no visible change other than the volume of integration. In order to incorporate the GCL the change of \mathbf{W} in time for a moving volume must be defined. This can be done by assigning the symbol $\dot{\mathbf{x}}$ for the general mesh velocity and results in:

$$\int_{V_{\text{mov}}} \frac{\partial \mathbf{W}}{\partial t} dV = \frac{\partial}{\partial t} \int_{V_{\text{mov}}} \mathbf{W} dV - \int_{S_{\text{mov}}} \mathbf{W} \dot{\mathbf{x}} \cdot \mathbf{n} dS \quad (3.34)$$

which is a statement indicating that the integral time variation of \mathbf{W} over the control volume at a given instant equals the time variation of the integral of \mathbf{W} over the moving volume minus the apparent flux of \mathbf{W} crossing the boundaries of the control volume as a result of the mesh motion which derives in a motion of the boundary itself. When Equation 3.34 is inserted into Equation 3.33, the ALE formulation of the Navier-Stokes equations is obtained:

$$\frac{\partial}{\partial t} \int_{V_{\text{mov}}} \mathbf{W} dV + \int_{S_{\text{mov}}} ([\mathbf{E}, \mathbf{F}] \cdot \mathbf{n} - \mathbf{W} \dot{\mathbf{x}} \cdot \mathbf{n}) dS = \int_{V_{\text{mov}}} \mathbf{J} dV \quad (3.35)$$

From the second term, it is possible to observe that the role of the ALE formulation in FSI is to account for the apparent fluxes that arise from the motion of the faces of the control volume.

Discretization

The governing equations of the fluid model to be solved via the FVM describe the motion of incompressible, viscous fluid flow. The set of equations derived in the previous section, known also as the Navier-Stokes equations, describe the conservation of mass and momentum and are presented again for a transient case in integral form:

$$\int \frac{\partial \rho}{\partial t} d\mathcal{V} + \int \rho \mathbf{v} \cdot d\mathbf{A} = 0 \quad (3.36)$$

$$\int \frac{\partial \rho \mathbf{v}}{\partial t} d\mathcal{V} + \int \rho \mathbf{v} (\mathbf{v} \cdot d\mathbf{A}) = - \int p \mathbf{I} \cdot d\mathbf{A} + \int \boldsymbol{\tau} \cdot d\mathbf{A} + \int \mathbf{F}_B d\mathcal{V} \quad (3.37)$$

Following the formulation of Ansys[®] Fluent [59], the momentum equation (eq. 3.37) is integrated over a single control volume which results in:

$$\frac{\partial \rho \mathbf{v}}{\partial t} \mathcal{V} + \sum_f^{N_{\text{faces}}} \rho v_f (\mathbf{v}_f \cdot \mathbf{n} A_f) = - \sum_f^{N_{\text{faces}}} p_f \mathbf{n} A_f \cdot \mathbf{I} + \sum_f^{N_{\text{faces}}} \boldsymbol{\tau}_f A_f + \mathbf{F}_B \mathcal{V} \quad (3.38)$$

Addressing the steady-state portion only and adopting index notation for the components of velocity (u_i), the final linearized form of the momentum conservation equation for a node p centered at the volume centroid, is written as:

$$a_P u_i = \sum_{nb} a_{nb} u_{i,nb} + \sum p_f \mathbf{n} A_f \cdot \mathbf{e}_i + S \quad (3.39)$$

where a_P and a_{nb} and the subscript nb represents the values at the neighboring center nodes of the node P .

The steady-state discretized form of the continuity equation is:

$$\sum_f^{N_{faces}} J_f A_f = 0 \quad (3.40)$$

where the mass flux through the j -th face is computed as $J_f = \rho v_n$.

Pressure-velocity coupling

From the list of available algorithms in Ansys® Fluent [59], one can observe either of two general approaches: coupled or segregated. A common segregated algorithm for treating pressure-velocity coupling is the Semi-Implicit Method for Pressure Linked Equations (SIMPLE) and consists of a predictor-corrector procedure, in which a pressure field is obtained while mass conservation is simultaneously enforced. In other sources such as Ferziger and Perić [60] this kind of correction is known as a projection method, and consists of a velocity estimation which is later modified to satisfy continuity by applying a pressure correction.

The SIMPLE algorithm starts from a guessed pressure field p^* used to compute a guess of the cell-face mass flux involved in the discretized continuity equation:

$$J_f^* = \hat{J}_f^* + d_f (p_{c0}^* - p_{c1}^*) \quad (3.41)$$

This prediction step results in a face flux J_f^* which does not necessarily satisfies the continuity equation. To find a flux J_f that fulfills mass conservation, J_f^* is corrected by an amount J_f' :

$$J_f = J_f^* + J_f' \quad (3.42)$$

The correction is stated in terms of a pressure correction, p' , according to:

$$J_f' = d_f (p'_{c0} - p'_{c1}) \quad (3.43)$$

So far, this correction depends on d_f which is a function of \bar{a}_p , an average of the linearized coefficients a_p for the discrete momentum equation. This results from an approach in which cell face velocities are weighted with the a_p coefficients from the momentum equation instead of using linear interpolation; this procedure, similar to the one in [61] is done to prevent checkerboarding or unphysical oscillations of the pressure solution. The final form of the corrected flux J_f written in terms of p' is used in the discretized equation for mass conservation. The result of using mass fluxes computed in terms of a pressure gradient to evaluate the continuity equation is a Poisson-type equation for the pressure correction at each cell whose discrete form can be written as:

$$a_P p' = \sum_{nb} a_{nb} p'_{nb} + b \quad (3.44)$$

The net flow rate into the cell is represented by the source term:

$$b = \sum_f^{N_{faces}} J_f^* A_f \quad (3.45)$$

The solution of Equation 3.44 is followed by the correction of pressure and face mass flux which in fact satisfies the mass conservation equation:

$$p = p^* + \alpha_p p' \quad (3.46)$$

$$J_f = J_f^* + d_f (p'_{c0} - p'_{c1}) \quad (3.47)$$

For an accelerated convergence, a variation of the previous procedure known as Semi-Implicit Method for Pressure Linked Equations-Consistent (SIMPLEC) algorithm can be used; in this case the correction equation for the face fluxes (Equation 3.43) has a new definition for d_f , which is now a function of $\overline{a_p - \sum_{nb} a_{nb}}$. The overall procedure for correcting the pressure field can be observed in Figure 3.4 which is valid for the SIMPLE, SIMPLEC and PISO coupling schemes.

Turbulence model

Considering that for the cases under analysis in this work, the Reynolds number on the wind turbine blades can exceed the value of 500,000, it can be safely assumed that the flow past the blade surfaces eventually becomes turbulent. For this reason a suitable model is required to be coupled with the solution of the Navier-Stokes equations that have been previously introduced. From the wide spectrum of available models for turbulence modelling, the present work is built around the group of so-called two-equation models, and more specifically the k - ω turbulence model. All of the two-equation models as well as the one-equation Spalart-Allmaras turbulence model is based on the Boussinesq hypothesis which defines the Reynolds stresses in terms of the mean velocity gradients. The main advantage of this approach is the low computational cost as the resulting model involves a transport equation for the turbulent kinetic energy k , and one transport equation for the specific dissipation rate ω .

The Baseline k - ω turbulence model is proposed by Menter [62, 63] and is well known to predict turbulent flows with adverse pressure gradients as is the case of the flow past a wind turbine blade. As mentioned above, the model consists of a transport equation for k :

$$\frac{\partial}{\partial t} (\rho k) + \frac{\partial}{\partial x_i} (\rho k u_i) = \frac{\partial}{\partial x_j} \left(\Gamma_k \frac{\partial k}{\partial x_j} \right) + G_k - Y_k - S_k + G_k \quad (3.48)$$

and a transport equation for ω :

$$\frac{\partial}{\partial t} (\rho \omega) + \frac{\partial}{\partial x_i} (\rho \omega u_i) = \frac{\partial}{\partial x_j} \left(\Gamma_\omega \frac{\partial \omega}{\partial x_j} \right) + G_\omega - Y_\omega + D_\omega - S_\omega + G_\omega \quad (3.49)$$

Where the production of turbulence kinetic energy is given by

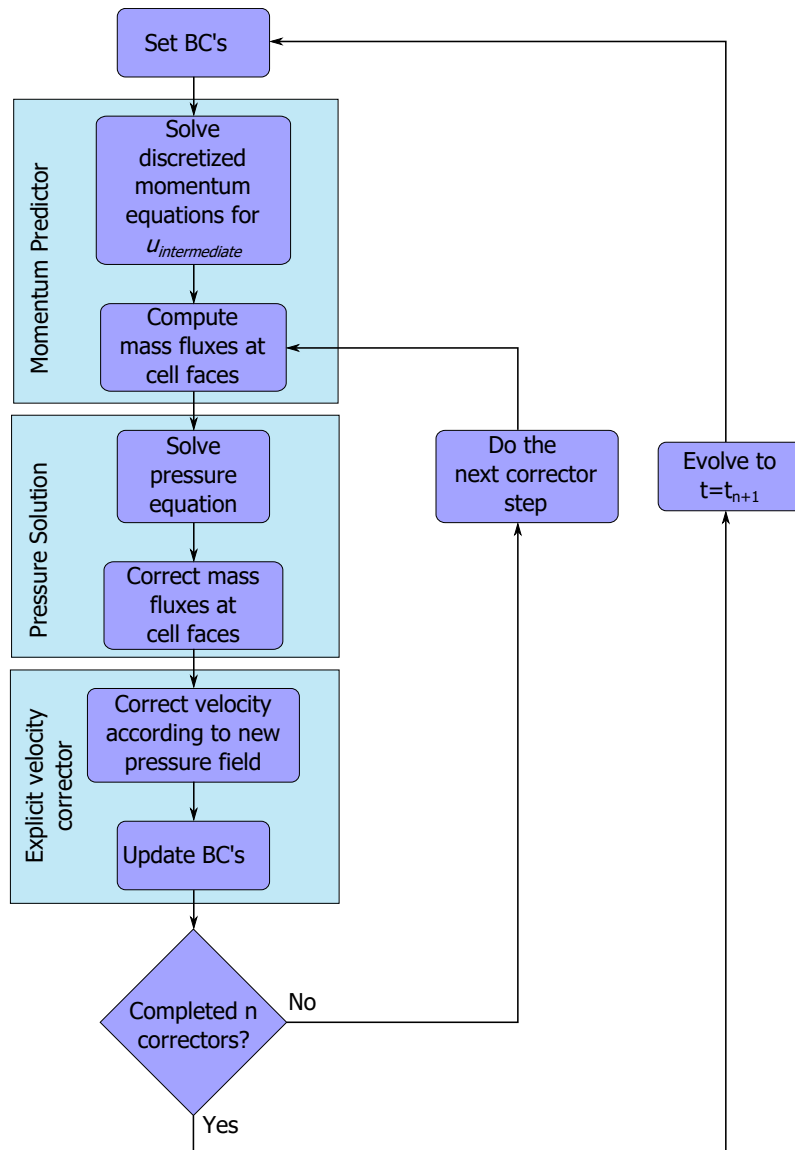


Figure 3.4: Flow diagram for a general predictor-corrector procedure in pressure-velocity coupling.

$$G_k = \mu_t S^2 \quad (3.50)$$

where μ_t is the turbulent viscosity and S is the modulus of the mean rate-of-strain tensor defined as $S \equiv \sqrt{2S_{ij}S_{ij}}$.

The generation of ω is defined as

$$G_\omega = \frac{\alpha\alpha^*}{\nu_t} G_k \quad (3.51)$$

The effective diffusivity for k and ω is given by Γ_k and Γ_ω respectively and are defined by:

$$\Gamma_k = \mu + \frac{\mu_t}{\sigma_k} \quad (3.52)$$

$$\Gamma_\omega = \mu + \frac{\mu_t}{\sigma_\omega} \quad (3.53)$$

where the turbulent Prandtl numbers for k and ω are represented by σ_k and σ_ω and. The coefficient α^* is the low-Reynolds number correction.

The dissipation of k and ω due to turbulence is represented by Y_k and Y_ω respectively, defined as:

$$Y_k = \rho\beta^*k\omega \quad (3.54)$$

$$Y_\omega = \rho\beta f_\beta\omega^2 \quad (3.55)$$

The cross diffusion term is represented by D_ω and defined by:

$$D_\omega = 2(1 - F_1)\rho \frac{1}{\omega\sigma_{\omega,2}} \frac{\partial k}{\partial x_j} \frac{\partial \omega}{\partial x_j} \quad (3.56)$$

S_k and S_ω represent source terms, whereas G_b and $G_{\omega b}$ represent the terms associated to the effects of buoyancy.

The Shear-Stress Transport (SST) k - ω turbulence model is built upon the baseline model considering a different definition for the turbulent viscosity that accounts better for the transport of the turbulent shear stress using a limiter as follows:

$$\mu_t = \frac{\rho k}{\omega} \frac{1}{\max\left[\frac{1}{\alpha^*}, \frac{SF_2}{\alpha_1\omega}\right]} \quad (3.57)$$

F_2 is given by:

$$F_2 = \tanh(\Phi_2^2) \quad (3.58)$$

$$\Phi_2 = \max\left[2\frac{\sqrt{k}}{0.09\omega y}, \frac{500\mu}{\rho y^2\omega}\right] \quad (3.59)$$

The model constants are:

$$\alpha_\infty^* = 1, \alpha_\infty = 0.52, \beta_\infty^* = 0.09, \beta_i = 0.072, R_\beta = 8$$

$$R_k = 6, R_\omega = 2.95, \zeta^* = 1.5, M_{t0} = 0.25, R_\beta = 8$$

$$\sigma_{k,1} = 1.176, \sigma_{\omega,1} = 2.0, \sigma_{k,2} = 1.0, \sigma_{\omega,2} = 1.168$$

$$a_1 = 0.31, \beta_{i,1} = 0.075, \beta_{i,2} = 0.0828$$

A crucial aspect in the modeling of turbulence lies in the fact that an inaccurate discretization scheme may result in non-physical dispersion, thus hindering the effort in describing the natural diffusion of turbulence throughout the fluid flow. The spatial discretization schemes used for this case are defined according to this criterion, and are consequently chosen to be second order accurate. When it comes to discretization in time the solution stability restrictions become a relevant criterion which is addressed next. As for the accuracy of the turbulence model in terms of the discretization error, the work of Menter [62] is used as a reference in the first place, to justify the selection of the SST version of the k - ω model over the original formulation, highly sensitive to free-stream conditions and over the baseline (BSL) version which does not account for the proportionality relationship between the turbulent kinetic energy and the transport of turbulent shear-stress. In second place, it is used to justify the selection of second order accurate discretization in space for the turbulence model transport equations, which in this work is the same as for the Navier-Stokes equations and the selection of first order time discretization. According to Menter [62], the sensitivity of the k - ω SST turbulence model to the discretization is not as heavily affected by the discretization schemes as is by the discretization of the fluid flow equations.

Time advancement scheme

The time advancement of the solution in Ansys[®] is done with an implicit discretization which for the governing equation (3.37) consists in approximating the terms for convection, diffusion and sources, with the field at the future time instant $n + 1$:

$$\int \frac{\partial \rho v}{\partial t} d\mathcal{V} + \int \rho v^{n+1} (v^{n+1} \cdot d\mathbf{A}) = - \int p^{n+1} \mathbf{I} \cdot d\mathbf{A} + \int \boldsymbol{\tau}^{n+1} \cdot d\mathbf{A} + \int \mathbf{F}_B^{n+1} d\mathcal{V} \quad (3.60)$$

Here the transient term is discretized with a second-order scheme which results in a truncation error $\mathcal{O}(\Delta t^2)$. The discretization in time introduces the first source of error, and the second one is introduced by the segregated solution of the different equations, the so called splitting error. The way the splitting error is treated depends on the selected scheme for advancing the solution in time. The implementation in Ansys[®] Fluent follows an implicit scheme in which the solution is advanced from one time to the next using an iterative solution, referred to as “outer iterations”. This procedure can treat the non-linearities and the coupling of equations, eliminating the splitting error from the scheme.

The discretization of the transient term in the transport equation can be done using a first or second order method. The first order method approximates the time derivative according to the implicit backward Euler method, in which the scalar at the new time level is expressed as:

$$\varphi^{n+1} = \varphi^n + \Delta t F_s \left(\varphi^{n+1} \right) \quad (3.61)$$

As observed, φ^{n+1} , is solved in terms of the solution at the old time step, and the terms involved in the spatial discretization evaluated at the new time level. Despite the first order truncation error in time, this method is simple and what is more important, is unconditionally stable for any time step size, which means a large step size can be adopted when needed. The second available method in Ansys[®] Fluent, is formulated for variable time step sizes, but for a constant value can be written as:

$$\frac{3\varphi^{n+1} - 4\varphi^n + \varphi^{n-1}}{2\Delta t} = F_s \left(\varphi^{n+1} \right) \quad (3.62)$$

This method is built on a quadratic backward approximation in time and fully implicit since the spatial discretization term, F_s , is again evaluated at the new time step. As pointed by Ferziger and Perić [60, page 150], it is second order accurate and unconditionally stable; however, if very large time steps are used, the method may result in oscillatory solutions. Considering the computational demand for the simulation cases of this work, the use of large time steps can be expected, at least when compared to similar works. Given the implications of this constraint over solution stability, the second order scheme is disregarded from this work, while adopting the first order scheme in all simulations.

Solution of linear systems

For the linear solution of the scalar equations, Ansys[®] relies on a point implicit Gauss-Seidel solver; given the size of the problem for the current research and for any case of interest in practical applications, the use of direct solvers is ruled out. To improve solution convergence and reduce the computational cost, a point implicit Gauss-Seidel solution is used along with an Algebraic Multi-Grid (AMG) method. The latter aspect of this approach is more than justified when considering for example the observations of Ferziger and Perić [60], who state that if the solution error is a smooth function of the spatial discretization, then for a 3-D problem, the iterative solution for a mesh twice as coarse costs 1/8 of the effort needed for the original mesh.

3.2 STRUCTURAL MODEL

The FEM model derivation follows the procedure for determining the system matrices as explained in the Ansys[®] Mechanical APDL Theory Reference [64]. The model is built upon the principle of virtual work, in which the strain energy, U , and external work, V , are related through the virtual operator δ :

$$\delta U = \delta V \quad (3.63)$$

In this equation the strain energy is stated in terms of strain energy and surface tensions as: $U = U_1 + U_2$, and the external work is stated in terms of external work, pressure force work and nodal forces as: $V = V_1 + V_2 + V_3$. The definition of the virtual strain energy is given as:

$$\delta U_1 = \int_{vol} \{\delta \varepsilon\} \{\sigma\} d(vol)^T \quad (3.64)$$

where $\{\varepsilon\}$ represents the strain vector, $\{\sigma\}$ represents the stress vector and vol represents the volume of the element. If a linear material and a linear geometry are assumed, the strain-stress relationship can be described by $\{\sigma\} = [D] \{\varepsilon^{el}\}$, then the virtual strain energy is rewritten:

$$\delta U_1 = \int_{vol} (\{\delta \varepsilon\}^T [D] \{\varepsilon\} - \{\delta \varepsilon\}^T [D] \{\varepsilon^{th}\}) d(vol)^T \quad (3.65)$$

Note that the strain is defined as the sum of the mechanical $\{\varepsilon\}$ and thermal $\{\varepsilon^{th}\}$ components, and the work of the thermal stresses is negative to account for compressive strains from a positive change in temperature. Additionally, the relationship between the strain $\{\varepsilon\}$ and the nodal displacement $\{u\}$ is given through the strain-displacement matrix $[B]$:

$$\{\varepsilon\} = [B] \{u\} \quad (3.66)$$

The final definition for virtual strain energy in the global Cartesian reference frame is given by

$$\delta U_1 = \{\delta u\}^T \int_{vol} [B]^T [D] [B] d(vol) \{u\} - \{\delta u\}^T \int_{vol} [B]^T [D] \{\varepsilon^{th}\} d(vol) \quad (3.67)$$

The contribution of surface tractions to the strain energy is represented by:

$$\delta U_2 = \int_{area_f} \{\delta w_n\}^T \{\sigma\} d(area_f) \quad (3.68)$$

where $\{w_n\}$ is the component of motion normal to the wall, $\{\sigma\}$ is the surface stress and $area_f$ is the surface of the distributed resistance. The normal motion at each point and the nodal displacements are related through the matrix of shape functions for normal motion with respect to the surface:

$$\{w_n\} = [N_n] \{u\} \quad (3.69)$$

An expression for stresses can be built as $\{\sigma\} = k \{w_n\}$; with k representing the foundation stiffness, with dimensions of force per unit length per unit area. With this, the final expression for δU_2 becomes:

$$\delta U_2 = \{\delta u\}^T k \int_{area_f} [N_n]^T [N_n] d(area_f) \{u\} \quad (3.70)$$

The external virtual work is expressed by:

$$\delta V_1 = - \int_{vol} \{\delta w\}^T \frac{\{F^a\}}{vol} d(vol) \quad (3.71)$$

where $\{w\}$ is the displacement vector and $\{F^a\}$ is the acceleration force vector. From Newton's second law, the displacement vector is related to the acceleration force vector:

$$\frac{\{F^a\}}{vol} = \rho \frac{\partial^2}{\partial t^2} \{w\} \quad (3.72)$$

The relationship between nodal displacements and the displacement field within each element is given by $\{w\} = [N] \{u\}$, where the matrix of shape functions is represented by $[N]$. With this, δV_1 can be rewritten as:

$$\delta V_1 = -\{\delta u\}^T \rho \int_{vol} [N]^T [N] d(vol) \frac{\delta^2}{\delta t^2} \{u\} \quad (3.73)$$

The virtual work associated to a pressure-force vector can be written in terms of the pressure vector $\{P\}$ and the area where the force is applied, $\{area_p\}$:

$$\delta V_2 = \int_{area_p} \{\delta w_n\}^T \{P\} d\{area_p\} \quad (3.74)$$

or, considering the relationship between element internal displacements and node displacements, the pressure virtual work is rewritten as:

$$\delta V_2 = \{\delta u\}^T \int_{area_p} [N_n]^T \{P\} d\{area_p\} \quad (3.75)$$

Finally, the virtual work associated to the nodal forces acting on the element, $\{F_e^{nd}\}$ can be written as:

$$\delta V_3 = \{\delta u\}^T \{F_e^{nd}\} \quad (3.76)$$

Then, equating the sum of all contributions of internal work to the sum of all contributions of external work according to the principle of virtual work, the following is obtained:

$$\begin{aligned} & \{\delta u\}^T \int_{vol} [B]^T [D] [B] d(vol) \{u\} - \{\delta u\}^T \int_{vol} [B]^T [D] \{\varepsilon^{th}\} d(vol) + \{\delta u\}^T k \int_{area_f} [N_n]^T [N_n] d(area_f) \{u\} \\ &= -\{\delta u\}^T \rho \int_{vol} [N]^T [N] d(vol) \frac{\delta^2}{\delta t^2} \{u\} + \{\delta u\}^T \int_{area_p} [N_n]^T \{P\} d\{area_p\} + \{\delta u\}^T \{F_e^{nd}\} \end{aligned} \quad (3.77)$$

Considering that the factor $\{\delta u\}^T$ is common to all terms, the principle of virtual work can only be satisfied, as stated above, if the following relationship is fulfilled:

$$([K_e] + [K_e^f]) \{u\} - \{F_e^{th}\} = [M_e] \{\ddot{u}\} + \{F_e^{pr}\} + \{F_e^{nd}\} \quad (3.78)$$

Time advancement scheme

Following the guidelines for the time integration methods available in the Ansys® APDL theory reference [64], the current model is illustrated first by considering the semi-discrete form of the equation of motion:

$$[M] \{\ddot{u}(t)\} + [C] \{\dot{u}(t)\} + \{F^i(t)\} = \{F^a(t)\} \quad (3.79)$$

Here the internal load vector is represented implicitly, and depending on its nature, the second-order differential equation can be used to describe a linear system, in which the internal loads are linear with respect to the internal nodal displacements through the constant structural stiffness matrix $[K]$. In contrast, for the representation of a non-linear system through Equation 3.79, the internal loading vector is no longer linear with respect to nodal displacements, as the structural stiffness matrix becomes a function of displacements.

Assuming the second case, the solution of the non-linear set of algebraic equations represented by Equation 3.79 should involve not only the time integration, but a Newton-Raphson iterative approach. From the methods incorporated in the APDL structural solver for non-linear structures, there are two common ones: Newmark's scheme (Newmark [65]) and the HHT- α scheme (Hilber et al. [66]).

For the Newmark method, Equation 3.79 can be written for a time instant t_{n+1} as:

$$[M]\{\ddot{u}_{n+1}\} + [C]\{\dot{u}_{n+1}\} + \{F_{n+1}^i(\{u_{n+1}\})\} = \{F_{n+1}^a\} \quad (3.80)$$

As part of the method, the updates for nodal velocities and displacements are given by equations:

$$\{\dot{u}_{n+1}\} = \{\dot{u}_n\} + [(1 - \delta_N)\{\dot{u}_n\} + \delta_N\{\ddot{u}_{n+1}\}] \Delta t \quad (3.81)$$

$$\{u_{n+1}\} = \{u_n\} + \{\dot{u}_n\} \Delta t + \left[\left(\frac{1}{2} - \alpha_N \right) \{\dot{u}_n\} + \alpha_N \{\ddot{u}_{n+1}\} \right] \Delta t^2 \quad (3.82)$$

The relevance of the integration parameters α_N and δ_N lies in their role over the method's stability, for the parameter δ_N controls the numerical algorithm dissipation and, when fulfilling the following conditions:

$$\begin{aligned} \delta_N &\geq \frac{1}{2} \\ \alpha_N &\geq \frac{1}{4} \left(\frac{1}{2} + \delta_N \right)^2 \end{aligned} \quad (3.83)$$

the entire family of Newmark's methods may be unconditionally stable as stated in [64]. Additionally, by using the amplitude decay factor $\gamma \geq 0$, unconditional stability can be obtained for the Newmark's method if the following conditions are met:

$$\begin{aligned} \delta_N &\geq \frac{1}{2} + \gamma \\ \alpha_N &\geq \frac{1}{4} (1 + \gamma)^2 \\ \gamma &\geq 0 \end{aligned} \quad (3.84)$$

Now Equation 3.80 can be re-written in terms of the residual vector $\{R_{n+1}(\{u_{n+1}\})\}$ as:

$$\{R_{n+1}(\{u_{n+1}\})\} = \{F_{n+1}^a\} - \{F_{n+1}^i(\{u_{n+1}\})\} - [M]\{\ddot{u}_{n+1}\} - [C]\{\dot{u}_{n+1}\} \quad (3.85)$$

From the residual, a linearized time integration operator can be obtained using the Newton-Rhapson method:

$$\{R_{n+1}(\{u_{n+1}^k\})\} + \frac{\partial\{R_{n+1}(\{u_{n+1}^k\})\}}{\partial\{u_{n+1}^i\}}\{\Delta u_{n+1}^k\} = \{0\} \quad (3.86)$$

Equation 3.85 is then written as:

$$[(a_0[M] + a_1[C]) + [K_{n+1}^T(\{u_{n+1}^k\})]]\{\Delta u_{n+1}^k\} = \{R_{n+1}(\{u_{n+1}^k\})\} \quad (3.87)$$

The coefficients for mass and damping matrices are defined as $a_0 = 1/\alpha_N \Delta t^2$ and $a_1 = \delta_N/\alpha_N \Delta t$. The term $[K_{n+1}^T(\{u_{n+1}^k\})]$ represents the tangent stiffness matrix at the future time instant t_{n+1} .

In addition to Newmark's scheme, Ansys[®] Ansys Parametric Design Language (APDL) offers the generalized HHT- α method, which starts by considering the semi-discrete form of the motion equation as:

$$[M]\{\ddot{u}_{n+1-\alpha_m}\} + [C]\{\dot{u}_{n+1-\alpha_f}\} + \{F_{n+1}^i(\{u_{n+1-\alpha_f}\})\} = \{F^a(t_{n+1-\alpha_f})\} \quad (3.88)$$

The definition for the external and internal load vectors in terms of the time operator is given by:

$$\{F_{n+1}^i(\{u_{n+1-\alpha_f}\})\} = (1 - \alpha_f)\{F_{n+1}^i(\{u_{n+1}\})\} + \alpha_f\{F_n^i(\{u_n\})\}$$

$$\{F^a(t_{n+1-\alpha_f})\} = (1 - \alpha_f)\{F_{n+1}^a\} + \alpha_f\{F_n^a\}$$

Once more, a residual vector is defined in terms of Equation 3.88 according to:

$$\{R_{n+1}(\{u_{n+1}\})\} = \{F^a(t_{n+1-\alpha_f})\} - \{F_{n+1}^i(\{u_{n+1-\alpha_f}\})\} - [M]\{\ddot{u}_{n+1-\alpha_m}\} - [C]\{\dot{u}_{n+1-\alpha_f}\} \quad (3.89)$$

The corresponding time integrator operator is also obtained from the Newton-Rhapson method as defined in Equation 3.86; the residual and internal load vectors however, are defined as:

$$R_{n+1}(\{u_{n+1}^k\}) = \{F^a(t_{n+1-\alpha_f})\} - \{F_{n+1}^i(\{u_{n+1-\alpha_f}^k\})\} - [M]\{\ddot{u}_{n+1-\alpha_m}\} - [C]\{\dot{u}_{n+1-\alpha_f}\}$$

$$\{F_{n+1}^i(\{u_{n+1-\alpha_f}^k\})\} = (1 - \alpha_f)\{F_{n+1}^i(\{u_{n+1}^k\})\} + \alpha_f\{F_n^i(\{u_n\})\}$$

Finally, from the Newton-Rhapson time advancement operator, the following is obtained:

$$[(a_0[M] + a_1[C] + (1 - \alpha_f)[K_{n+1}^T(\{u_{n+1}^k\})]]\{\Delta u_{n+1}^k\} = \{R_{n+1}(\{u_{n+1}^k\})\} \quad (3.90)$$

with coefficients $a_0 = (1 - \alpha_m)/\alpha_N \Delta t^2$ and $a_1 = (1 - \alpha_f) \delta_N/\alpha_N \Delta t$.

As stated in [64], the HHT- α method is unconditionally stable and second order accurate if the scheme parameters fulfill the conditions

$$\begin{aligned}\delta_N &\geq \frac{1}{2} - \alpha_m + \alpha_f \\ \alpha_N &\geq \frac{1}{2}\delta_N \\ \alpha_m &\leq \alpha_f \leq \frac{1}{2}\end{aligned}\tag{3.91}$$

In these conditions $\alpha_m \leq 0$ and $0 \leq \alpha_f \leq \frac{1}{2}$. Again, by introducing the amplitude decay factor, numerical damping can be controlled by establishing the following relationship between the parameters:

$$\begin{aligned}\alpha_N &\geq \frac{1}{4}(1 + \gamma)^2 \\ \delta_N &\geq \frac{1}{2} + \gamma \\ \alpha_f &= \frac{1 - \gamma}{2} \\ \alpha_m &= \frac{1 - 3\gamma}{2}\end{aligned}\tag{3.92}$$

3.2.1 Composite shell model

The FEM model in APDL can be set to describe different problems in terms of the structural element type. The structure of the NREL Phase VI wind turbine blade are layered composites with a thick dimension which is small compared with the overall in-plane dimensions; in fact, this is common for many composite structures which tend to be two-dimensional objects similar to a plate. As defined by Liu and Quek [67], a shell structure is also characterized by a predominantly two-dimensional geometry, just as a plate, but is special in the sense that it can experience loads in-plane and normal to the plane and can in consequence experience bending, twisting and in-plane deformations.

The condition described above corresponds to the general load state acting on the skin of a wind turbine blade and can be described in APDL using the four-node SHELL181 element. According to the documentation [68], the default version of the element has six degrees of freedom corresponding to three translations in x , y and z and three rotations about the x , y and z axes. The formulation of this element is based on the assumption of small changes in curvature for a given time increment and is based on the First-Order Shear-deformation theory, also known in literature as the Reissner-Mindlin shell theory [69, 70].

First-order shear-deformation theory

The first-order shear-deformation theory lies is built upon the assumption that the transverse normal lines to the neutral plane do not remain perpendicular after the shell has been deformed; therefore, transverse shear strain is accounted for at the

same time that the deformation w is assumed constant along the thickness direction (z).

The displacement field (u, v, w) is defined according to:

$$\begin{aligned} u(x, y, z, t) &= u_0(x, y, z, t) + z\phi_x(x, y, z, t) \\ v(x, y, z, t) &= v_0(x, y, z, t) + z\phi_y(x, y, z, t) \\ w(x, y, z, t) &= w_0(x, y, z, t) \end{aligned} \quad (3.93)$$

where the mid-plane displacements are represented by (u_0, v_0, w_0) . The rotations of the transverse normals around the $-x$ and $-y$ axes are represented by (ϕ_y, ϕ_x) respectively and can be defined as:

$$\frac{\partial u}{\partial z} = \phi_x, \quad \frac{\partial v}{\partial z} = \phi_y \quad (3.94)$$

When the characteristic in-plane dimension to thickness ratio is around 50 or greater the rotations ϕ_x and ϕ_y approach the slopes of the actual transverse deflections:

$$\phi_x = -\frac{\partial w_0}{\partial x}, \quad \phi_y = -\frac{\partial w_0}{\partial y} \quad (3.95)$$

The non-linear strains are given in terms of the displacement field according to:

$$\begin{aligned} \varepsilon_{xx} &= \frac{\partial u_0}{\partial x} + \frac{1}{2} \left(\frac{\partial w_0}{\partial x} \right)^2 + z \frac{\partial \phi_x}{\partial x} \\ \gamma_{xy} &= \left(\frac{\partial u_0}{\partial y} + \frac{\partial v_0}{\partial x} + \frac{\partial w_0}{\partial x} \frac{\partial w_0}{\partial y} \right) + z \left(\frac{\partial \phi_x}{\partial y} + \frac{\partial \phi_y}{\partial x} \right) \\ \varepsilon_{yy} &= \frac{\partial v_0}{\partial y} + \frac{1}{2} \left(\frac{\partial w_0}{\partial y} \right)^2 + z \frac{\partial \phi_y}{\partial y} \\ \gamma_{xz} &= \frac{\partial w_0}{\partial x} + \phi_x, \quad \gamma_{yz} = \frac{\partial w_0}{\partial y} + \phi_y, \quad \varepsilon_{zz} = 0 \end{aligned} \quad (3.96)$$

The strains shown above are derived from the general Green-Lagrange non-linear strain tensor for an anisotropic elastic solid, assuming small rotations and sufficiently small displacement gradients such that their squares are negligible. According to Equation 3.96 the strains ε_{xx} , ε_{yy} and γ_{xy} are linear with respect to the z -direction whereas the transverse shear strains γ_{xz} and γ_{yz} remain constant. This is an assumption with respect to the real stress field which shows a quadratic variation in the thickness dimension. Arranged in matrix form, the strains can be written as:

$$\begin{pmatrix} \varepsilon_{xx} \\ \varepsilon_{yy} \\ \gamma_{yz} \\ \gamma_{xz} \\ \gamma_{xy} \end{pmatrix} = \begin{pmatrix} \varepsilon_{xx}^{(0)} \\ \varepsilon_{yy}^{(0)} \\ \gamma_{yz}^{(0)} \\ \gamma_{xz}^{(0)} \\ \gamma_{xy}^{(0)} \end{pmatrix} + z \begin{pmatrix} \varepsilon_{xx}^{(1)} \\ \varepsilon_{yy}^{(1)} \\ \gamma_{yz}^{(1)} \\ \gamma_{xz}^{(1)} \\ \gamma_{xy}^{(1)} \end{pmatrix} = \begin{pmatrix} \frac{\partial u_0}{\partial x} + \frac{1}{2} \left(\frac{\partial w_0}{\partial x} \right)^2 \\ \frac{\partial v_0}{\partial y} + \frac{1}{2} \left(\frac{\partial w_0}{\partial y} \right)^2 \\ \frac{\partial w_0}{\partial y} + \phi_y \\ \frac{\partial w_0}{\partial x} + \phi_x \\ \frac{\partial u_0}{\partial y} + \frac{\partial v_0}{\partial x} + \frac{\partial w_0}{\partial x} \frac{\partial w_0}{\partial y} \end{pmatrix} + z \begin{pmatrix} \frac{\partial \phi_x}{\partial x} \\ \frac{\partial \phi_y}{\partial y} \\ 0 \\ 0 \\ \frac{\partial \phi_x}{\partial y} + \frac{\partial \phi_y}{\partial x} \end{pmatrix} \quad (3.97)$$

where the upperscript (0) is used to denote the membrane strains and the upperscript (1) is used to denote the bending strains also known as curvatures.

Governing equations of motion

Following the description of Reddy [71] for the first-order shear-deformation theory, the governing equations are obtained from the principle of virtual displacements in its dynamic formulation:

$$0 = \int_0^T (\delta U + \delta V - \delta K) dt \quad (3.98)$$

The definitions of the virtual strain energy, δU , the virtual work done by external forces, δV , and the virtual kinetic energy, δK , are given by:

$$\delta U = \int_{\Omega_0} \left\{ \int_{-\frac{h}{2}}^{\frac{h}{2}} \left[\sigma_{xx} \left(\delta \varepsilon_{xx}^{(0)} + z \delta \varepsilon_{xx}^{(1)} \right) + \left(\delta \varepsilon_{yy}^{(0)} + z \delta \varepsilon_{yy}^{(1)} \right) + \sigma_{xy} \left(\delta \gamma_{xy}^{(0)} + z \delta \gamma_{xy}^{(1)} \right) \right. \right. \\ \left. \left. + \sigma_{xz} \delta \gamma_{xz}^{(0)} + \sigma_{yz} \delta \gamma_{yz}^{(0)} \right] dz \right\} dx dy \quad (3.99)$$

$$\delta V = - \int_{\Omega_0} [(q_b + q_t) \delta w_0] dx dy - \int_{\Gamma_\sigma} \int_{-\frac{h}{2}}^{\frac{h}{2}} [\hat{\sigma}_{nn} (\delta u_n + z \delta \phi_n) + \hat{\sigma}_{ns} (\delta u_s + z \delta \phi_s) \\ + \hat{\sigma}_{nz} \delta w_0] dz ds \quad (3.100)$$

$$\delta K = \int_{\Omega_0} \int_{-\frac{h}{2}}^{\frac{h}{2}} \rho_0 [(\dot{u}_0 + z \dot{\phi}_x) (\delta \dot{u}_0 + z \delta \dot{\phi}_x) + (\dot{v}_0 + z \dot{\phi}_y) (\delta \dot{v}_0 + z \delta \dot{\phi}_y) + \dot{w}_0 \delta \dot{w}_0] dz dx dy \quad (3.101)$$

The term q_b in the definition of δV represents a distributed transverse force applied at the bottom surface of the layered shell corresponding to $z = h/2$; similarly, the term q_t represents the distributed transverse force acting over the top surface of the laminate corresponding to $z = -h/2$. The definition of δV contains also the stresses $\hat{\sigma}_{nn}$, $\hat{\sigma}_{ns}$, and $\hat{\sigma}_{nz}$, representing stress components on a portion Γ_σ of the domain boundary Γ , δu_{0n} and δu_{0s} represent virtual displacements along the normal and tangential directions of the boundary Γ . The density of the plate materials is given by ρ_0 .

After substitution of the definitions into the statement of the principle of virtual displacements and

$$\begin{aligned}
0 = \int_0^T \left\{ \int_{\Omega_0} \left[N_{xx} \delta \varepsilon_{xx}^{(0)} + M_{xx} \delta \varepsilon_{xx}^{(1)} + N_{yy} \delta \varepsilon_{yy}^{(0)} + M_{yy} \delta \varepsilon_{yy}^{(1)} + N_{xy} \delta \gamma_{xy}^{(0)} + M_{xy} \delta \gamma_{xy}^{(1)} \right. \right. \\
+ Q_x \delta \gamma_{xz}^{(0)} + Q_y \delta \gamma_{yz}^{(0)} - q \delta w_0 - I_0 (\dot{u}_0 \delta \dot{u}_0 + \dot{v}_0 \delta \dot{v}_0 + \dot{w}_0 \delta \dot{w}_0) \\
- I_1 (\dot{\phi}_x \delta \dot{u}_0 + \dot{\phi}_y \delta \dot{v}_0 + \delta \dot{\phi}_x \dot{u}_0 + \delta \dot{\phi}_y \dot{v}_0) - I_2 (\dot{\phi}_x \delta \dot{\phi}_x + \dot{\phi}_y \delta \dot{\phi}_y) \left. \right] dx dy \\
- \int_{\Gamma_\sigma} (\hat{N}_{nm} \delta u_n + \hat{N}_{ns} \delta u_s + \hat{M}_{nm} \delta \phi_n + \hat{M}_{ns} \delta \phi_s + \tilde{Q}_n \delta w_0) ds \left. \right\} dt \quad (3.102)
\end{aligned}$$

This equation introduces the in-plane force resultants per unit length N_{xx} , N_{yy} , N_{xy} , the moment resultants per unit length M_{xx} , M_{yy} , M_{xy} , the transverse distributed force $q = q_t + q_b$ and the mass moments of inertia I_0 , I_1 , I_2 which along with the in-plane forces and moments are defined from the integration of the stresses across the thickness direction. Additionally the transverse force resultants are defined as:

$$\begin{Bmatrix} Q_x \\ Q_y \end{Bmatrix} = \int_{-\frac{h}{2}}^{\frac{h}{2}} \begin{Bmatrix} \sigma_{xz} \\ \sigma_{yz} \end{Bmatrix} dz \quad (3.103)$$

The current definition for the shear transverse strains show a constant behavior with respect to the thickness direction, this implies that transverse shear stresses are also constant along the thickness. A discrepancy is then evident between the first-order shear-deformation theory and the real variation of transverse shear stresses which is at least quadratic. For this reason a shear correction factor K is used to solve the difference by multiplying the shear stresses at the computation of the resulting transverse shear forces:

$$\begin{Bmatrix} Q_x \\ Q_y \end{Bmatrix} = K \int_{-\frac{h}{2}}^{\frac{h}{2}} \begin{Bmatrix} \sigma_{xz} \\ \sigma_{yz} \end{Bmatrix} dz \quad (3.104)$$

Citing the description made by Reddy [71] K is dependent on the properties of the laminae and the lamination sequence. It is usually computed equating the strain energy due to transverse shear stresses with the strain energy associated to the transverse stresses predicted with the three-dimensional elasticity theory.

Taking now Equation 3.102 and substituting the virtual strains in terms of the resultant forces and moments, an equivalent expression is obtained in terms of resulting forces, moments and mass moments of inertia:

$$\begin{aligned}
0 = & \int_0^T \int_{\Omega_0} [-(N_{xx,x} + N_{xy,y} - I_0 \ddot{u}_0 - I_1 \ddot{\phi}_y) \delta u_0 \\
& - (N_{xy,x} + N_{yy,y} - I_0 \ddot{v}_0 - I_1 \ddot{\phi}_x) \delta v_0 \\
& - (M_{xx,x} + M_{xy,y} - Q_x - I_2 \ddot{\phi}_x - I_1 \ddot{u}_0) \delta \phi_x \\
& - (M_{xy,x} + M_{yy,y} - Q_y - I_2 \ddot{\phi}_y - I_1 \ddot{v}_0) \delta \phi_y \\
& - (Q_{x,x} + Q_{y,y} + \mathcal{N}(w_0) + q - I_0 \ddot{w}_0) \delta w_0] dx dy \\
& + \int_0^T \int_{\Gamma} [(N_{nn} - \hat{N}_{nn}) \delta u_n + (N_{ns} - \hat{N}_{ns}) \delta u_s + (Q_n - \hat{Q}_n) \delta w_0 \\
& + (M_{nn} - \hat{M}_{nn}) \delta \phi_n + (M_{ns} - \hat{M}_{ns}) \delta \phi_s] ds dt \tag{3.105}
\end{aligned}$$

where

$$\mathcal{N}(w_0) = \frac{\partial}{\partial x} \left(N_{xx} \frac{\partial w_0}{\partial x} + N_{xy} \frac{\partial w_0}{\partial y} \right) + \frac{\partial}{\partial y} \left(N_{xy} \frac{\partial w_0}{\partial x} + N_{yy} \frac{\partial w_0}{\partial y} \right) \tag{3.106}$$

$$\mathcal{P}(w_0) = \left(N_{xx} \frac{\partial w_0}{\partial x} + N_{xy} \frac{\partial w_0}{\partial y} \right) n_x + \left(N_{xy} \frac{\partial w_0}{\partial x} + N_{yy} \frac{\partial w_0}{\partial y} \right) n_y \tag{3.107}$$

The transverse normal rotations ϕ_x and ϕ_y are expressed in terms of the rotations of normal and tangential lines ϕ_n, ϕ_s at a point in the shell boundary:

$$\phi_x = n_x \phi_n - n_y \phi_s, \quad \phi_y = n_y \delta \phi_n + n_x \delta \phi_s \tag{3.108}$$

Finally when the coefficients of $\delta u_0, \delta v_0, \delta w_0, \delta \phi_x$ and $\delta \phi_y$ from the latter statement of the virtual displacement principle are set to zero for the boundary portion Ω_0 the Euler-Lagrange equations are obtained:

$$\begin{aligned}
\delta u_0 : \quad & \frac{\partial N_{xx}}{\partial x} + \frac{\partial N_{xy}}{\partial y} = I_0 \frac{\partial^2 u_0}{\partial t^2} + I_1 \frac{\partial^2 \phi_x}{\partial t^2} \\
\delta v_0 : \quad & \frac{\partial N_{xy}}{\partial x} + \frac{\partial N_{yy}}{\partial y} = I_0 \frac{\partial^2 v_0}{\partial t^2} + I_1 \frac{\partial^2 \phi_y}{\partial t^2} \\
\delta w_0 : \quad & \frac{\partial Q_x}{\partial x} + \frac{\partial Q_y}{\partial y} + \mathcal{N}(w_0) + q = I_0 \frac{\partial^2 w_0}{\partial t^2} \\
\delta \phi_x : \quad & \frac{\partial M_{xx}}{\partial x} + \frac{\partial M_{xy}}{\partial y} - Q_x = I_2 \frac{\partial^2 \phi_x}{\partial t^2} + I_1 \frac{\partial^2 u_0}{\partial t^2} \\
\delta \phi_y : \quad & \frac{\partial M_{xy}}{\partial x} + \frac{\partial M_{yy}}{\partial y} - Q_y = I_2 \frac{\partial^2 \phi_y}{\partial t^2} + I_1 \frac{\partial^2 v_0}{\partial t^2} \tag{3.109}
\end{aligned}$$

For the natural boundary conditions the coefficients of $\delta u_n, \delta u_s, \delta w_0, \delta \phi_n$ and $\delta \phi_s$ are set to zero over the boundary Γ :

$$\begin{aligned}
N_{nn} - \hat{N}_{nn} = 0 \quad , \quad N_{ns} - \hat{N}_{ns} = 0 \quad , \quad Q_n - \hat{Q}_n = 0 \\
M_{nn} - \hat{M}_{nn} = 0 \quad , \quad M_{ns} - \hat{M}_{ns} = 0 \tag{3.110}
\end{aligned}$$

where

$$Q_n \equiv Q_x n_x + Q_y n_y + \mathcal{P}(w_0) \quad (3.111)$$

Primary variables of the first-order shear-theory are u_n , u_s , w_0 , ϕ_n , ϕ_s whereas the secondary variables are N_{nn} , N_{ns} , Q_n , M_{nn} , M_{ns} . The initial conditions of the problem comprise both the values of displacements as well as the first derivatives over the boundary Ω_0 :

$$\begin{aligned} u_n &= u_n^0, \quad u_s = u_s^0, \quad w_0 = w_0^0, \quad \phi_n = \phi_n^0, \quad \phi_s = \phi_s^0 \\ \dot{u}_n &= \dot{u}_n^0, \quad \dot{u}_s = \dot{u}_s^0, \quad \dot{w}_0 = \dot{w}_0^0, \quad \dot{\phi}_n = \dot{\phi}_n^0, \quad \dot{\phi}_s = \dot{\phi}_s^0 \end{aligned} \quad (3.112)$$

Laminate constitutive equations

The constitutive equations for a laminate are defined here assuming that each lamina is orthotropic and follows Hooke's law. These equations relate the force and moment resultants to the strains on the laminate. Since each k -th lamina may have different mechanical properties, the stresses are variable despite the strains being continuous; for this reason the constitutive equations involve lamina-wise integration. The force resultants are described by:

$$\begin{pmatrix} N_{xx} \\ N_{yy} \\ N_{xy} \end{pmatrix} = \sum_{k=1}^N \int_{z_k}^{z_{k+1}} \begin{pmatrix} \sigma_{xx} \\ \sigma_{yy} \\ \sigma_{yz} \end{pmatrix} dz = \sum_{k=1}^N \int_{z_k}^{z_{k+1}} \begin{bmatrix} \bar{Q}_{11} & \bar{Q}_{12} & \bar{Q}_{16} \\ \bar{Q}_{12} & \bar{Q}_{22} & \bar{Q}_{26} \\ \bar{Q}_{16} & \bar{Q}_{26} & \bar{Q}_{66} \end{bmatrix}^{(k)} \begin{pmatrix} \varepsilon_{xx}^{(0)} + z\varepsilon_{xx}^{(1)} \\ \varepsilon_{yy}^{(0)} + z\varepsilon_{yy}^{(1)} \\ \gamma_{yz}^{(0)} + z\gamma_{yz}^{(1)} \end{pmatrix} dz$$

$$\begin{pmatrix} N_{xx} \\ N_{yy} \\ N_{xy} \end{pmatrix} = \begin{bmatrix} A_{11} & A_{12} & A_{16} \\ A_{12} & A_{22} & A_{26} \\ A_{16} & A_{26} & A_{66} \end{bmatrix} \begin{pmatrix} \varepsilon_{xx}^{(0)} \\ \varepsilon_{yy}^{(0)} \\ \gamma_{yz}^{(0)} \end{pmatrix} + \begin{bmatrix} B_{11} & B_{12} & B_{16} \\ B_{12} & B_{22} & B_{26} \\ B_{16} & B_{26} & B_{66} \end{bmatrix} \begin{pmatrix} \varepsilon_{xx}^{(1)} \\ \varepsilon_{yy}^{(1)} \\ \gamma_{yz}^{(1)} \end{pmatrix} \quad (3.113)$$

$$\begin{pmatrix} M_{xx} \\ M_{yy} \\ M_{xy} \end{pmatrix} = \sum_{k=1}^N \int_{z_k}^{z_{k+1}} \begin{pmatrix} \sigma_{xx} \\ \sigma_{yy} \\ \sigma_{yz} \end{pmatrix} z dz = \sum_{k=1}^N \int_{z_k}^{z_{k+1}} \begin{bmatrix} \bar{Q}_{11} & \bar{Q}_{12} & \bar{Q}_{16} \\ \bar{Q}_{12} & \bar{Q}_{22} & \bar{Q}_{26} \\ \bar{Q}_{16} & \bar{Q}_{26} & \bar{Q}_{66} \end{bmatrix}^{(k)} \begin{pmatrix} \varepsilon_{xx}^{(0)} + z\varepsilon_{xx}^{(1)} \\ \varepsilon_{yy}^{(0)} + z\varepsilon_{yy}^{(1)} \\ \gamma_{yz}^{(0)} + z\gamma_{yz}^{(1)} \end{pmatrix} z dz$$

$$\begin{pmatrix} M_{xx} \\ M_{yy} \\ M_{xy} \end{pmatrix} = \begin{bmatrix} B_{11} & B_{12} & B_{16} \\ B_{12} & B_{22} & B_{26} \\ B_{16} & B_{26} & B_{66} \end{bmatrix} \begin{pmatrix} \varepsilon_{xx}^{(0)} \\ \varepsilon_{yy}^{(0)} \\ \gamma_{yz}^{(0)} \end{pmatrix} + \begin{bmatrix} D_{11} & D_{12} & D_{16} \\ D_{12} & D_{22} & D_{26} \\ D_{16} & D_{26} & D_{66} \end{bmatrix} \begin{pmatrix} \varepsilon_{xx}^{(1)} \\ \varepsilon_{yy}^{(1)} \\ \gamma_{yz}^{(1)} \end{pmatrix} \quad (3.114)$$

In the relations above $Q^{(k)}$ are the lamina stiffnesses, A represents extensional stiffnesses, D represents the bending stiffnesses, and B the bending-extension coupling stiffnesses. These are related by:

$$(A_{ij}, B_{ij}, D_{ij}) = \sum_{k=1}^N \int_{z_k}^{z_{k+1}} Q_{ij}^{(k)}(1, z, z^2) dz \quad (3.115)$$

In addition to this constitutive relations which are valid for any laminated plate, the first-order shear-deformation theory considers the additional relationship for transverse stresses:

$$\begin{Bmatrix} \sigma_{yz} \\ \sigma_{xz} \end{Bmatrix}^{(k)} = \begin{bmatrix} \bar{Q}_{44} & \bar{Q}_{45} \\ \bar{Q}_{45} & \bar{Q}_{55} \end{bmatrix}^{(k)} \begin{Bmatrix} \gamma_{yz}^{(0)} \\ \gamma_{xz}^{(0)} \end{Bmatrix} \quad (3.116)$$

and the relation between the lamina stiffnesses and the laminae angle orientation:

$$\begin{aligned} \bar{Q}_{44} &= Q_{44} \cos^2 \theta + Q_{55} \sin^2 \theta \\ \bar{Q}_{45} &= (Q_{55} - Q_{44}) \cos \theta \sin \theta \\ \bar{Q}_{55} &= Q_{44} \sin^2 \theta + Q_{55} \cos^2 \theta \end{aligned} \quad (3.117)$$

The relationships for the resultant transverse shear forces are given by:

$$\begin{aligned} \begin{Bmatrix} Q_x \\ Q_y \end{Bmatrix} &= K \sum_{k=1}^N \int_{z_k}^{z_{k+1}} \begin{Bmatrix} \sigma_{yz} \\ \sigma_{xz} \end{Bmatrix} dz \\ \begin{Bmatrix} Q_x \\ Q_y \end{Bmatrix} &= K \begin{bmatrix} A_{44} & A_{45} \\ A_{45} & A_{55} \end{bmatrix} \begin{Bmatrix} \gamma_{yz}^{(0)} \\ \gamma_{xz}^{(0)} \end{Bmatrix} \end{aligned} \quad (3.118)$$

The respective extensional stiffnesses are computed as:

$$(A_{44}, A_{45}, A_{55}) = \int_{-\frac{h}{2}}^{\frac{h}{2}} (\bar{Q}_{44}, \bar{Q}_{45}, \bar{Q}_{55}) dz \quad (3.119)$$

$$= \sum_{k=1}^N \int_{z_k}^{z_{k+1}} (\bar{Q}_{44}^{(k)}, \bar{Q}_{45}^{(k)}, \bar{Q}_{55}^{(k)}) dz \quad (3.120)$$

$$= \sum_{k=1}^N (\bar{Q}_{44}^{(k)}, \bar{Q}_{45}^{(k)}, \bar{Q}_{55}^{(k)}) (z_{k+1} - z_k) \quad (3.121)$$

Disregarding thermal and piezoelectric effects on load state of the laminate, the relations for force and moment resultants as well as for are given by:

$$\begin{Bmatrix} N_{xx} \\ N_{yy} \\ N_{xy} \end{Bmatrix} = \begin{bmatrix} A_{11} & A_{12} & A_{16} \\ A_{12} & A_{22} & A_{26} \\ A_{16} & A_{26} & A_{66} \end{bmatrix} \begin{Bmatrix} \frac{\partial u_0}{\partial x} + \frac{1}{2} \left(\frac{\partial w_0}{\partial x} \right)^2 \\ \frac{\partial v_0}{\partial x} + \frac{1}{2} \left(\frac{\partial w_0}{\partial y} \right)^2 \\ \frac{\partial u_0}{\partial y} + \frac{\partial v_0}{\partial x} + \frac{\partial w_0}{\partial x} \frac{\partial w_0}{\partial y} \end{Bmatrix} + \begin{bmatrix} B_{11} & B_{12} & B_{16} \\ B_{12} & B_{22} & B_{26} \\ B_{16} & B_{26} & B_{66} \end{bmatrix} \begin{Bmatrix} \frac{\partial \phi_x}{\partial x} \\ \frac{\partial \phi_y}{\partial y} \\ \frac{\partial \phi_x}{\partial x} + \frac{\partial \phi_y}{\partial y} \end{Bmatrix} \quad (3.122)$$

$$\begin{Bmatrix} M_{xx} \\ M_{yy} \\ M_{xy} \end{Bmatrix} = \begin{bmatrix} B_{11} & B_{12} & B_{16} \\ B_{12} & B_{22} & B_{26} \\ B_{16} & B_{26} & B_{66} \end{bmatrix} \begin{Bmatrix} \frac{\partial u_0}{\partial x} + \frac{1}{2} \left(\frac{\partial w_0}{\partial x} \right)^2 \\ \frac{\partial v_0}{\partial x} + \frac{1}{2} \left(\frac{\partial w_0}{\partial y} \right)^2 \\ \frac{\partial u_0}{\partial y} + \frac{\partial v_0}{\partial x} + \frac{\partial w_0}{\partial x} \frac{\partial w_0}{\partial y} \end{Bmatrix} + \begin{bmatrix} D_{11} & D_{12} & D_{16} \\ D_{12} & D_{22} & D_{26} \\ D_{16} & D_{26} & D_{66} \end{bmatrix} \begin{Bmatrix} \frac{\partial \phi_x}{\partial x} \\ \frac{\partial \phi_y}{\partial y} \\ \frac{\partial \phi_x}{\partial x} + \frac{\partial \phi_y}{\partial y} \end{Bmatrix} \quad (3.123)$$

$$\begin{Bmatrix} Q_x \\ Q_y \end{Bmatrix} = K \begin{bmatrix} A_{44} & A_{45} \\ A_{45} & A_{55} \end{bmatrix} \begin{Bmatrix} \frac{\partial w_0}{\partial y} + \phi_y \\ \frac{\partial w_0}{\partial x} + \phi_x \end{Bmatrix} \quad (3.124)$$

If the force and moment resultants in Equation 3.109 are expressed in terms of the displacements u_0 , v_0 , w_0 , ϕ_x and ϕ_y the equations of motion for a layered shell of homogeneous laminae are written as:

$$\begin{aligned} & A_{11} \left(\frac{\partial^2 u_0}{\partial x^2} + \frac{\partial w_0}{\partial x} \frac{\partial^2 w_0}{\partial x^2} \right) + A_{12} \left(\frac{\partial^2 v_0}{\partial y \partial x} + \frac{\partial w_0}{\partial y} \frac{\partial^2 w_0}{\partial y \partial x} \right) + \\ & A_{16} \left(\frac{\partial^2 u_0}{\partial y \partial x} + \frac{\partial^2 v_0}{\partial x^2} + \frac{\partial^2 w_0}{\partial x^2} \frac{\partial w_0}{\partial y} + \frac{\partial w_0}{\partial x} \frac{\partial^2 w_0}{\partial y \partial x} \right) + \\ & B_{11} \frac{\partial^2 \phi_x}{\partial x^2} + B_{12} \frac{\partial^2 \phi_y}{\partial y \partial x} + B_{16} \left(\frac{\partial^2 \phi_x}{\partial x \partial y} + \frac{\partial^2 \phi_y}{\partial x^2} \right) + \\ & A_{16} \left(\frac{\partial^2 u_0}{\partial x \partial y} + \frac{\partial w_0}{\partial x} \frac{\partial^2 w_0}{\partial x \partial y} \right) + A_{26} \left(\frac{\partial^2 v_0}{\partial y^2} + \frac{\partial w_0}{\partial y} \frac{\partial^2 w_0}{\partial y^2} \right) + \\ & A_{66} \left(\frac{\partial^2 u_0}{\partial y^2} + \frac{\partial^2 v_0}{\partial x \partial y} + \frac{\partial^2 w_0}{\partial x \partial y} \frac{\partial w_0}{\partial y} + \frac{\partial w_0}{\partial x} \frac{\partial^2 w_0}{\partial y^2} \right) + \\ & B_{16} \frac{\partial^2 \phi_x}{\partial x \partial y} + B_{26} \frac{\partial^2 \phi_y}{\partial y^2} + B_{66} \left(\frac{\partial^2 \phi_x}{\partial y^2} + \frac{\partial^2 \phi_y}{\partial y \partial x} \right) - \\ & = I_0 \frac{\partial^2 u_0}{\partial t^2} + I_1 \frac{\partial^2 \phi_x}{\partial t^2} \end{aligned} \quad (3.125)$$

$$\begin{aligned}
& A_{16} \left(\frac{\partial^2 u_0}{\partial x^2} + \frac{\partial w_0}{\partial x} \frac{\partial^2 w_0}{\partial x^2} \right) + A_{26} \left(\frac{\partial^2 v_0}{\partial y \partial x} + \frac{\partial w_0}{\partial y} \frac{\partial^2 w_0}{\partial y \partial x} \right) + \\
& A_{66} \left(\frac{\partial^2 u_0}{\partial y \partial x} + \frac{\partial^2 v_0}{\partial x^2} + \frac{\partial^2 w_0}{\partial x^2} \frac{\partial w_0}{\partial y} + \frac{\partial w_0}{\partial x} \frac{\partial^2 w_0}{\partial y \partial x} \right) + \\
& B_{16} \frac{\partial^2 \phi_x}{\partial x^2} + B_{26} \frac{\partial^2 \phi_y}{\partial y \partial x} + B_{66} \left(\frac{\partial^2 \phi_x}{\partial x \partial y} + \frac{\partial^2 \phi_y}{\partial x^2} \right) + \\
& A_{12} \left(\frac{\partial^2 u_0}{\partial x \partial y} + \frac{\partial w_0}{\partial x} \frac{\partial^2 w_0}{\partial x \partial y} \right) + A_{22} \left(\frac{\partial^2 v_0}{\partial y^2} + \frac{\partial w_0}{\partial y} \frac{\partial^2 w_0}{\partial y^2} \right) + \\
& A_{26} \left(\frac{\partial^2 u_0}{\partial y^2} + \frac{\partial^2 v_0}{\partial x \partial y} + \frac{\partial^2 w_0}{\partial x \partial y} \frac{\partial w_0}{\partial y} + \frac{\partial w_0}{\partial x} \frac{\partial^2 w_0}{\partial y^2} \right) + \\
& B_{12} \frac{\partial^2 \phi_x}{\partial x \partial y} + B_{22} \frac{\partial^2 \phi_y}{\partial y^2} + B_{26} \left(\frac{\partial^2 \phi_x}{\partial y^2} + \frac{\partial^2 \phi_y}{\partial x \partial y} \right) - \\
& = I_0 \frac{\partial^2 v_0}{\partial t^2} + I_1 \frac{\partial^2 \phi_y}{\partial t^2} \tag{3.126}
\end{aligned}$$

$$\begin{aligned}
& KA_{55} \left(\frac{\partial^2 w_0}{\partial x^2} + \frac{\partial \phi_x}{\partial x} \right) + KA_{45} \left(\frac{\partial^2 w_0}{\partial y \partial x} + \frac{\partial \phi_y}{\partial y} \right) + \\
& KA_{45} \left(\frac{\partial^2 w_0}{\partial x \partial y} + \frac{\partial \phi_x}{\partial y} \right) + KA_{44} \left(\frac{\partial^2 w_0}{\partial y^2} + \frac{\partial \phi_y}{\partial y} \right) + \\
& N(w) + q = I_0 \frac{\partial^2 w_0}{\partial t^2} \tag{3.127}
\end{aligned}$$

$$\begin{aligned}
& B_{11} \left(\frac{\partial^2 u_0}{\partial x^2} + \frac{\partial w_0}{\partial x} \frac{\partial^2 w_0}{\partial x^2} \right) + B_{12} \left(\frac{\partial^2 v_0}{\partial y \partial x} + \frac{\partial w_0}{\partial y} \frac{\partial^2 w_0}{\partial y \partial x} \right) + \\
& B_{16} \left(\frac{\partial^2 u_0}{\partial y \partial x} + \frac{\partial^2 v_0}{\partial x^2} + \frac{\partial^2 w_0}{\partial x^2} \frac{\partial w_0}{\partial y} + \frac{\partial w_0}{\partial x} \frac{\partial^2 w_0}{\partial y \partial x} \right) + \\
& D_{11} \frac{\partial^2 \phi_x}{\partial x^2} + D_{12} \frac{\partial^2 \phi_y}{\partial y \partial x} + D_{16} \left(\frac{\partial^2 \phi_x}{\partial x \partial y} + \frac{\partial^2 \phi_y}{\partial x^2} \right) + \\
& B_{16} \left(\frac{\partial^2 u_0}{\partial x \partial y} + \frac{\partial w_0}{\partial x} \frac{\partial^2 w_0}{\partial x \partial y} \right) + B_{26} \left(\frac{\partial^2 v_0}{\partial y^2} + \frac{\partial w_0}{\partial y} \frac{\partial^2 w_0}{\partial y^2} \right) + \\
& B_{66} \left(\frac{\partial^2 u_0}{\partial y^2} + \frac{\partial^2 v_0}{\partial x \partial y} + \frac{\partial^2 w_0}{\partial x \partial y} \frac{\partial w_0}{\partial y} + \frac{\partial w_0}{\partial x} \frac{\partial^2 w_0}{\partial y^2} \right) + \\
& D_{16} \frac{\partial^2 \phi_x}{\partial x \partial y} + D_{26} \frac{\partial^2 \phi_y}{\partial y^2} + D_{66} \left(\frac{\partial^2 \phi_x}{\partial y^2} + \frac{\partial^2 \phi_y}{\partial y \partial x} \right) - \\
& KA_{55} \left(\frac{\partial w_0}{\partial x} + \phi_x \right) - KA_{45} \left(\frac{\partial w_0}{\partial y} + \phi_y \right) - \\
& = I_2 \frac{\partial^2 \phi_x}{\partial t^2} + I_1 \frac{\partial^2 u_0}{\partial t^2} \tag{3.128}
\end{aligned}$$

$$\begin{aligned}
& B_{16} \left(\frac{\partial^2 u_0}{\partial x^2} + \frac{\partial w_0}{\partial x} \frac{\partial^2 w_0}{\partial x^2} \right) + B_{26} \left(\frac{\partial^2 v_0}{\partial y \partial x} + \frac{\partial w_0}{\partial y} \frac{\partial^2 w_0}{\partial y \partial x} \right) + \\
& B_{66} \left(\frac{\partial^2 u_0}{\partial y \partial x} + \frac{\partial^2 v_0}{\partial x^2} + \frac{\partial^2 w_0}{\partial x^2} \frac{\partial w_0}{\partial y} + \frac{\partial w_0}{\partial x} \frac{\partial^2 w_0}{\partial y \partial x} \right) + \\
& D_{16} \frac{\partial^2 \phi_x}{\partial x^2} + D_{26} \frac{\partial^2 \phi_y}{\partial y \partial x} + D_{66} \left(\frac{\partial^2 \phi_x}{\partial x \partial y} + \frac{\partial^2 \phi_y}{\partial x^2} \right) + \\
& B_{12} \left(\frac{\partial^2 u_0}{\partial x \partial y} + \frac{\partial w_0}{\partial x} \frac{\partial^2 w_0}{\partial x \partial y} \right) + B_{22} \left(\frac{\partial^2 v_0}{\partial y^2} + \frac{\partial w_0}{\partial y} \frac{\partial^2 w_0}{\partial y^2} \right) + \\
& B_{26} \left(\frac{\partial^2 u_0}{\partial y^2} + \frac{\partial^2 v_0}{\partial x \partial y} + \frac{\partial^2 w_0}{\partial x \partial y} \frac{\partial w_0}{\partial y} + \frac{\partial w_0}{\partial x} \frac{\partial^2 w_0}{\partial y^2} \right) + \\
& D_{12} \frac{\partial^2 \phi_x}{\partial x \partial y} + D_{22} \frac{\partial^2 \phi_y}{\partial y^2} + D_{26} \left(\frac{\partial^2 \phi_x}{\partial y^2} + \frac{\partial^2 \phi_y}{\partial x \partial y} \right) - \\
& KA_{45} \left(\frac{\partial w_0}{\partial x} + \phi_x \right) - KA_{44} \left(\frac{\partial w_0}{\partial y} + \phi_y \right) - \\
& = I_2 \frac{\partial^2 \phi_y}{\partial t^2} + I_1 \frac{\partial^2 v_0}{\partial t^2}
\end{aligned} \tag{3.129}$$

3.3 FLUID-STRUCTURE INTERACTION MODEL

Before describing the settings of the coupled framework in Ansys[®], a description of the basic coupling aspects is provided here, including the data interpolation between solvers and the treatment of mesh deformation for the flow solution. The first of the elements to be addressed, the data transfer, is a necessary step derived from the partitioned approach to FSI, in which the solution of the participating models is performed from separate programs and usually have non-matching discretizations at the common interface. Secondly, the mesh deformation problem is discussed in its main characteristics in Subsection 3.3.3.

3.3.1 Data transfer between non-matching meshes

For the case of a wind turbine blade the participant solutions are the fluid flow solution on one side and the structural solution on the other. The wet surface of the blade is the interface between the meshes of each numerical domain. Since the discretizations of the two models are non-matching at the interface, a transformation procedure is required. The basic characteristics are discussed in this section, but before it is worth mentioning the data to be transferred from one domain to the other. The work of van Zuijlen [54] makes an appropriate description of the overall concept of an FSI problem, describing it as a three-field problem, because the solution involves three instances of mathematical modeling as shown in Table 3.1.

Field problem	Solution method	Boundary condition at the interface	Boundary condition provided by
Fluid Flow Solution	FVM	No-slip and no-through condition for velocity (Dirichlet)	N/A, Fixed by definition ($u, v, w = 0$ m/s at the blade surface)
Structural Solution	FEM	Pressure or Force per unit area (von Neumann)	Fluid Flow Solution
Mesh deformation	FVM	Mesh velocity at the boundary (Dirichlet)	Structural Solution

Table 3.1: Boundary condition specification at the coupling interface.

The interface is the contact region between the flow and structure domains, and the difference in discretization for each model can be exemplified by recalling that a turbulent flow solution usually requires much finer meshes compared to structural solutions. The characteristics of a desirable interpolation are explored in depth by de Boer et al. [72], whose work points out the importance of conservative coupling schemes, which ensure that the energy is conserved through the interface. In FSI the quantities to be transferred or interpolated from one domain to the other are pressure, p , and displacement, u , meaning that for a typical coupled problem, two data transfer procedures are required. de Boer et al. [72] mention that if both transfers are carried out under a conservative scheme, and using the same transformation matrix for both cases, the transfer of pressure to the structure side is likely to show fictitious oscillations. The use of different transformation matrices helps to avoid unphysical oscillations for pressure, which constitutes a consistent coupling. From a general perspective this summarizes the approaches to data transfer for coupled physics problems: conservative coupling and consistent coupling [72, 73]. The mathematical derivations proposed by de Boer et al. [72] are presented next as the basis for the coupling to be executed within a commercial software package.

The first step of a numerical coupling can be established by the coupling conditions:

$$\mathbf{u}_f = \mathbf{u}_s \quad \text{on } \Gamma \quad (3.130)$$

$$p_s \mathbf{n}_s = p_f \mathbf{n}_f \quad \text{on } \Gamma \quad (3.131)$$

where the kinematic condition states the equivalence between the displacement fields of the flow \mathbf{u}_f and the solid \mathbf{u}_s at the interface Γ and the dynamic condition states the equivalence between the pressure field on the structure surface p_s and the pressure field of the flow p_f at the interface Γ . In the dynamic condition \mathbf{n}_f and \mathbf{n}_s represent the normal vectors pointing outwards of the flow and structure sides of the interface respectively.

As pointed in [72], the coupling conditions are a general statement and regardless of the particular interpolation method used, the data transfer procedure always results in a set of matrix equations for the discrete coupling conditions:

$$\mathbf{U}_f = H_{sf} \mathbf{U}_s \quad (3.132)$$

$$\mathbf{P}_s = H_{fs} \mathbf{P}_f \quad (3.133)$$

where H_{sf} is the transformation matrix from flow to structure and H_{fs} is the transformation matrix from the structure to the flow. Additionally the continuous displacement and pressure fields are defined:

$$\mathbf{u}(\mathbf{x}) = \sum_{i=1}^{n^u} N^i(\mathbf{x}) \mathbf{U}_i \quad (3.134)$$

$$p(\mathbf{x}) \mathbf{n}(\mathbf{x}) = \sum_{j=1}^{n^p} D^j(\mathbf{x}) \mathbf{P}_j \quad (3.135)$$

where n^u and n^p represent the number of unknowns for the displacement and pressure respectively across the interface, $N(\mathbf{x})$ is a function depending on the spatial discretization for diaplacements and in a similar way, $D(\mathbf{x})$ is a function depending on the discretization used for the pressure.

At this point it is worth mentioning that if the transformation represented by Equations 3.132 and 3.133 is consistent, constant values must be interpolated exactly and in consequence the row-sums of the matrix H must be equal to one. For the conservative approach the energy must be conserved across the boundary as was mentioned earlier; in this sense, de Boer et al. [72] state the conservation of virtual work concerning coupling for small time-steps in order to establish the conservation of energy:

$$\int_{\Gamma_f} \mathbf{u}_f \cdot p_f \mathbf{n}_f ds = \int_{\Gamma_s} \mathbf{u}_s \cdot p_s \mathbf{n}_s ds \quad (3.136)$$

When the left hand side is expanded using Equations 3.134 and 3.135:

$$\begin{aligned} \int_{\Gamma_f} \mathbf{u}_f \cdot p_f \mathbf{n}_f ds &= \int_{\Gamma_f} \left[\sum_{j=1}^{n_f^u} N_f^j(\mathbf{x}) \mathbf{U}_{fj} \right] \left[\sum_{i=1}^{n_f^p} D_f^i(\mathbf{x}) \mathbf{P}_{fi} \right] ds \\ &= \sum_{i=1}^{n_f^p} \left[\sum_{j=1}^{n_f^u} \int_{\Gamma_f} D_f^i N_f^j ds \mathbf{U}_{fj} \right] \mathbf{P}_{fi} = [M_{ff} \mathbf{U}_f]^T \mathbf{P}_f \end{aligned} \quad (3.137)$$

A similar development can be done for the right hand side of Equation 3.136 resulting in:

$$\int_{\Gamma_s} \mathbf{u}_s \cdot p_s \mathbf{n}_s ds = [M_{ss} \mathbf{U}_s]^T \mathbf{P}_s \quad (3.138)$$

with the matrices M_{ff} and M_{ss} defined as:

$$M_{ff}^{ij} = \int_{\Gamma_f} D_f^i N_f^j ds, \quad M_{ss}^{ij} = \int_{\Gamma_s} D_s^i N_s^j ds \quad (3.139)$$

When Equations 3.137 and 3.138 are substituted into the statement of conservation of energy (Equation 3.136) it follows that pressure transferred while ensuring a global conservation of energy over the interface:

$$P_s = H_{fs}P_f \quad (3.140)$$

with the matrix H_{fs} defined as:

$$H_{fs} = \left[M_{ff}H_{sf}M_{ss}^{-1} \right]^T \quad (3.141)$$

For the transformation to be consistent, that is, ensuring that constant values are interpolated exactly, the row-sums of H_{sf} as well as the row sums of $H_{fs} = \left[M_{ff}H_{sf}M_{ss} \right]^T$ must be one. As mentioned earlier this does not happen to be the case for a general transformation, instead it depends on the specific interpolation method being used.

Coupling with the Weighted Residual Method

This method, presented in earlier works from several authors [74, 75, 72] is built upon the weak form of the conservation for displacements and pressures over the interface. For the sake of generality, the two sides of the interface are represented by A and B and, the coupling conditions introduced earlier are written in compact form as:

$$w_B(x) = w_A(x) \quad \text{on } \Gamma \quad (3.142)$$

With the displacement and pressure fields included in the definition $w = \{u, pn\}$. With the goal of finding a transformation that satisfies the coupling conditions approximately, both sides of Equations 3.142 by a set of weight functions represented by ϕ_k , subsequently both sides are integrated over the interface:

$$\int_{\Gamma} \phi_k w_B(x) dx = \int_{\Gamma} \phi_k w_A(x) dx \quad (3.143)$$

Just as introduced in the general transformation at the beginning of the section, the continuous form of the transformed fields are represented in terms of the discrete values W_A and W_B defined at the interface of meshes A and B respectively:

$$w_B(x) = \sum_{i=1}^{n_B} N_B^i(x) W_{B_i}, \quad w_A(x) = \sum_{j=1}^{n_A} N_A^j(x) W_{A_j} \quad (3.144)$$

here N_A and N_B represent the basis functions for the meshes A and B respectively, whereas n_A and n_B represent the number of unknowns at the interface. These two definitions are substituted into the integral equation of the coupling conditions:

$$\int_{\Gamma} \phi_k \sum_{i=1}^{n_B} N_B^i(x) W_{B_i} dx = \int_{\Gamma} \phi_k \sum_{j=1}^{n_A} N_A^j(x) W_{A_j} dx \quad (3.145)$$

Using a Galerkin method, the weight functions ϕ_k can be defined using the basis functions of the flow or the basis functions of the structure. In general terms the integration can be stated as:

$$\sum_{i=1}^{n_B} \left[\int_{\Gamma} N_{\alpha}^k N_B^i dx \right] \mathbf{W}_{B_i} = \sum_{j=1}^{n_A} \left[\int_{\Gamma} N_{\alpha}^k N_A^j dx \right] \mathbf{W}_{A_j} \quad (3.146)$$

where α represents the choice of basis functions, which are side A or side B . From this relationship the following matrices are defined:

$$C_{\alpha B}^{ki} = \int_{\Gamma} N_{\alpha}^k N_B^i dx, \quad C_{\alpha A}^{kj} = \int_{\Gamma} N_{\alpha}^k N_A^j dx \quad (3.147)$$

from which the transformation can be expressed in a more compact form:

$$C_{\alpha B} \mathbf{W}_B = C_{\alpha A} \mathbf{W}_A \quad (3.148)$$

where $C_{\alpha B}$ is a $n_{\alpha} \times n_B$ matrix and $C_{\alpha A}$ is a $n_{\alpha} \times n_A$ matrix.

The transformation that has been outlined so far corresponds to a transformation from side A to side B ; this implies that w_A is known beforehand and that the solution for this transformation yields the values on mesh B , that is w_B . Under this circumstances, the system can only be solved if the weight functions are assigned the basis functions of side B : $\alpha = B$, which results in:

$$\mathbf{W}_B = C_{BB}^{-1} C_{BA} \mathbf{W}_A \quad (3.149)$$

from which the transformation matrix H , mentioned at the beginning of the section, results to be defined as:

$$H_{AB} = C_{BB}^{-1} C_{BA} \quad (3.150)$$

In summary, this represents the transformation from side A of the interface to side B , using a weighted residual interpolation complemented with the Galerkin method. Now, the transformation can be treated depending on the desired approach with respect to the given requirements of conservativeness or consistency. When a consistent approach is pursued, it is known that the transformation outlined in Equation 3.149 must interpolate constant values exactly, this can be mathematically represented by the transformation:

$$C_{BB} \beta_B = C_{BA} \beta_A \quad (3.151)$$

where β_A and β_B are vectors of length n_A or n_B with a constant value of β . Now, if the Galerkin method is used again, the transformation matrices above can be developed accordingly:

$$\sum_{i=1}^{n_B} \left[\int_{\Gamma} N_B^k N_B^i dx \right] \beta = \sum_{j=1}^{n_A} \left[\int_{\Gamma} N_B^k N_A^j dx \right] \beta \quad \text{for } k = 1, \dots, n_B \quad (3.152)$$

Considering that $\sum_{k=1}^{n_{\alpha}} N_{\alpha}^k = 1$ and $\int_{\Gamma_{\alpha}} N_{\alpha}^k dx = 1$, the left-hand side of Equation 3.152 can be modified:

$$\sum_{i=1}^{n_B} \left[\int_{\Gamma} N_B^k N_B^i dx \right] \beta = \beta \int_{\Gamma} N_B^k \left[\sum_{i=1}^{n_B} N_B^i \right] dx = \beta \int_{\Gamma} N_B^k dx = \beta \quad (3.153)$$

Similarly, the right-hand side is modified to:

$$\sum_{j=1}^{n_A} \left[\int_{\Gamma} N_B^k N_A^j dx \right] \beta = \beta \int_{\Gamma} N_B^k \left[\sum_{j=1}^{n_A} N_A^j \right] dx = \beta \int_{\Gamma} N_B^k dx = \beta \quad (3.154)$$

Since both members of Equation 3.152 result in the exact value of the constant field, β , the transformation is consistent.

If instead of a consistent transformation, the coupling requires the conservation of energy across the boundary, a conservative approach should be pursued. For the weighted residual method, the conservative transformation of pressure has an impact on the overall consistency, which is explored next. As a starting point, the transformation matrix resulting from the weighted residual method is:

$$H_{sf} = C_{ff}^{-1} C_{fs} \quad (3.155)$$

from which the coupling condition for pressure is written as:

$$\mathbf{P}_s = \left[M_{ff} C_{ff}^{-1} C_{fs} M_{ss}^{-1} \right]^T \mathbf{P}_f \quad (3.156)$$

Using the same discretization for the pressure and displacements on the flow side, then $N_f = D_f$ and $n_f^u = n_f^p$ it turns out that $M_{ff} = C_{ff}$, in consequence the pressure transformation becomes:

$$\mathbf{P}_s = [C_{fs} M_{ss}^{-1}]^T \mathbf{P}_f \quad \text{or} \quad M_{ss} \mathbf{P}_s = C_{sf} \mathbf{P}_f \quad (3.157)$$

Recalling the definition of consistency, an exact interpolation of constant pressure can only be achieved when $M_{ss} \beta_s = C_{sf} \beta_f$ with β_s and β_f representing a vector of length n_s or n_f . For this case, it can be shown that:

$$\int_{\Gamma_s} N_s^k dx = \int_{\Gamma_f} N_s^k dx \quad (3.158)$$

In conclusion, the only way pressure is transformed both consistently and conservatively, is when the meshes are matching, that is $\Gamma_f = \Gamma_s$.

3.3.2 Overview of the System Coupling workflow

The main framework for the FSI wind turbine blade analysis is defined within the commercial package of Ansys[®], and more specifically with the use of the System Coupling module, which is in charge of controlling the interaction between Ansys[®] Fluent and Ansys[®] Mechanical's APDL. Chimakurthi et al. [4] present the characteristics of the System Coupling framework within the broader context of multi-physics simulations, addressing different aspects such as the adoption of a partitioned approach, the amount of executable files and processes as well as the existing approaches to mapping, data transfer convergence and instabilities.

Regarding the nature of the framework itself, System Coupling follows a "Partitioned" approach in which the participant solutions for the fluid, structural and other models take place as separate processes and are governed by different programs. This creates a need for the transfer of data between the solvers, in addition to the need to solve secondary issues that arise from this procedure. In any case, a partitioned ap-

proach is flexible and is a logical choice for setting up a cooperative simulation with already existing and validated individual physics solvers.

In the alternative case all solution participants exist as a single solution procedure in what is known as a “Monolithic” approach to multi-physics simulations. Because of its nature, in a monolithic solution all physics models are solved simultaneously with their governing equations assembled into a single matrix system. As pointed by Chimakurthi et al. [4], this may result in ill-conditioned systems for cases with large disparities between system stiffnesses for each model. This is despite of the obvious advantage of having all solution information directly accessible by all participants, thus requiring no data transfers.

The architecture of System Coupling from a computational point of view, consists of several executable programs and several processes. This means that multiple executable files are used for each participant solution and for each one of those, at least one process is created. The counterpart to this system consists of a single executable file to govern all participant solutions as a single process. For a framework in which the participant solutions are existing commercial programs, the most flexible option is to use multiple executable files, this way the need to intervene the programming of participant solvers is minimal.

Coupling management

System coupling manages the interaction between the participant solvers within the coupled solution scheme. The data transfer between “source” and “target” participants may occur in either one or two directions, this defines the one-way coupled analysis and the two-way coupled analysis. In a two-way FSI analysis both the fluid and structural solvers act as source and target participants along the evolution of the coupled problem. System coupling manages all communications between processes using a low-level TCP/IP based architecture, whereas all the high-level communication processes are handled with application programming interfaces (API's) for the tasks of process synchronization, data transfers and managing convergence.

System Coupling ensures that all processes associated to each participant advance synchronously through the coupled solution process, for this a 5-step sequence with corresponding verification points at which all processes must be completed before the next step is executed as shown in Figure 3.5. These steps are: initial synchronization, analysis initialization, solution, check convergence and shut down. The solution stage, at which the participant solvers advance in time are also synchronized between the start and beginning of the coupling step. Within this time lapse the solvers advance iteratively with the possibility of splitting the time advancement into sub-iterations or sub-steps.

Data mapping

Essential to the process of data transfer between the participant physics solvers, the process of data mapping consists of two separate stages as implemented in the System Coupling: the first one is associating the source and target meshes and the second is to generate data for the target location. These two steps are together known as mapping and are followed by a series of supplemental tasks such as the reconstruction of data

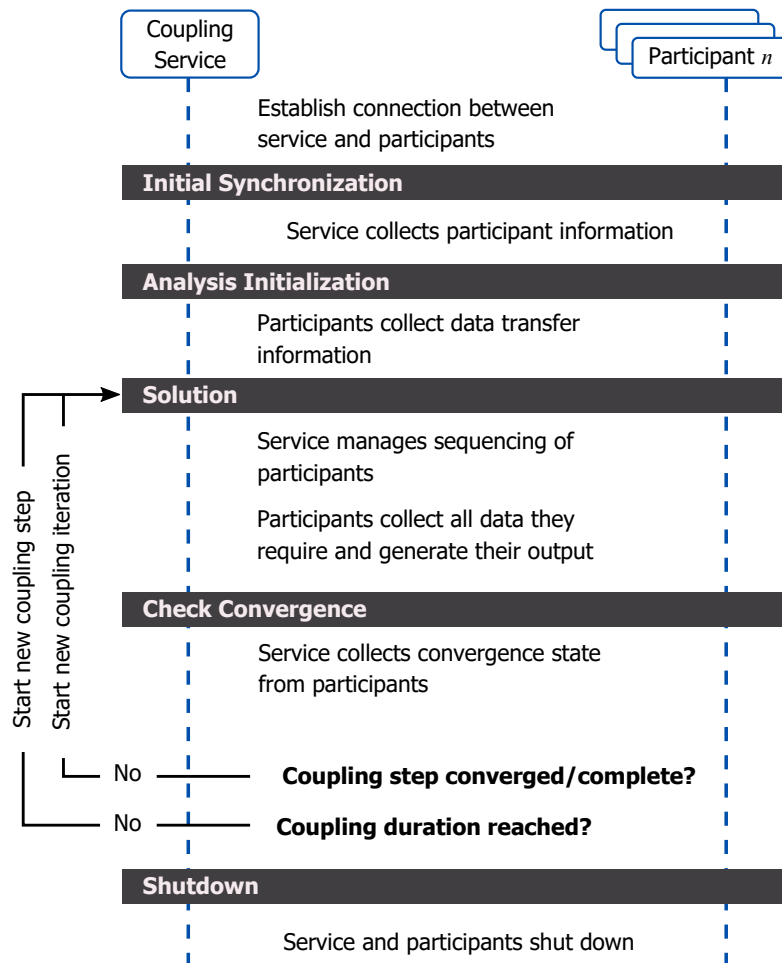


Figure 3.5: Synchronized execution scheme for System Coupling and participant processes (Adapted from [4]).

at mesh locations, the use of ramping or under-relaxation factors, the application of unit conversion and the implementation of a quasi-Newton stabilization.

Since Ansys[®] is a general purpose software, it can be tailored to treat a wide array of problems and such flexibility is reflected in the different ways mapping algorithms are defined. The first distinction is done with respect to the type of variable being transferred, in this sense profile-preserving mapping and conservative mapping are defined. According to System Coupling's documentation [6], a profile-preserving mapping aims to minimize the difference of the data profile after the transfer and is used for treating intensive scalar quantities such as temperature, heat transfer coefficient and convection reference temperature and intensive vector quantities, specifically incremental displacement. It must be noted that the transferred profile is as accurate as the least-resolved topology between the source and target meshes. Conservative mapping minimizes the difference between the sum of the transferred data at local and global levels; it is used for extensive quantities of scalar nature such as mass flow rate and heat transfer rate and of vector nature, specifically force quantities. For a typical FSI problem the variables being transferred are force and displacement. Since force is transferred per unit area, a conservative mapping is used, this ensures that the force per unit area acting on an interface surface is kept the same. For displacements the intention is to maintain the distribution across the mapping regions therefore a profile-preserving mapping algorithm is selected.

Association of source and target locations

Before the mapping procedure is carried out, System Coupling must identify the mesh locations that are going to serve as the source and the target for the data transfer. This is done with a Binary Space Partitioning (BSP) search algorithm and precedes the generation of mapping weights. These are subsequently used in the generation of transferred data for target locations and are defined with the use of a specific method depending on the topology of the source-target location pair. Depending on the involved mesh topologies, a specific association method is used:

- Projection association, used for surface-to-surface mapping
- Coincident association, used for volume-to-volume mapping
- Extrusion association, used for volume-to-planar surface and for planar surface-to-volume mapping

The interface between the fluid flow and the structure in a typical wind turbine blade analysis is a surface that corresponds exactly to the blade outer skin; thus a 2D-to-2D method is used for the generation of mapping weights, denominated as a "projection".

Generation of target data

The generation of mapping weights is necessary for interpolating data between source and target locations, according to the official documentation [6], the method for generating mapping weights is specific to the type of mapping: shape functions used for profile-preserving surface-to-surface mapping and an Intersect-Scatter-Gather method for conservative surface-to-surface mapping. A graphical representation for the generation of mapping weights and the input and output of data between source and target

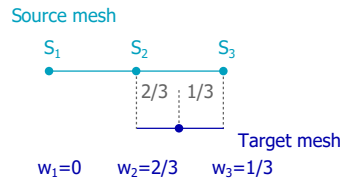


Figure 3.6: Generation of mapping weights with shape functions (Adapted from [5]).

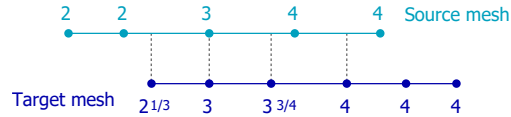


Figure 3.7: Example of input and output for shape function mapping (Adapted from [6]).

meshes can be observed in Figures 3.6 and 3.7. The specific shape functions used by System Coupling depend on the order of the source mesh being mapped, linear shape functions for linear elements and quadratic shape functions for quadratic elements. The 2-way interaction problem analyzed here considers a profile-preserving mapping for incremental displacement, for which the source mesh corresponds to the structural model of Ansys[®] Mechanical APDL. In consequence the assumed shape functions are those specified for a SHELL181 element according to APDL's documentation [64]:

$$u = \frac{1}{4} [u_I (1 - s) (1 - t) + u_J (1 + s) (1 - t) + u_K (1 + s) (1 + t) + u_L (1 - s) (1 + t)] \quad (3.159)$$

The shape function in Equation 3.159 describes the variation of x -translation (u) within an element with corner nodes denoted by I, J, K and L and with dimensionless in-plane internal coordinates s and t . This equation is the same for all three translation and rotation degrees of freedom.

For conservative mapping between like-topologies such as the present case, System Coupling uses the Intersect-Scatter-Gather algorithm to generate interpolation weights. As shown in Figure 3.8 the Intersect-Scatter-Gather mapping is based on an intersection of source and target elements and the value of each weight is determined by the size of the source-target element intersection relative to the size of the intersected source element. A typical input and output for Intersect-Scatter-Gather conservative mapping between like topologies is shown in Figure 3.9.

Supplemental processing algorithms

These algorithms are used for preprocessing and postprocessing data around the mapping procedure itself. The available algorithms are: data reconstruction, ramping, under-relaxation and quasi-Newton stabilization.

The Data reconstruction algorithm is used in the preinterpolation and postinterpolation stages of the data transfer process; here data is created at mesh locations from already known data, for example, generating data at mesh nodes from known data at face centroids. Data reconstruction is necessary when the source participant provides data at locations other than those required by the mapping process or when the

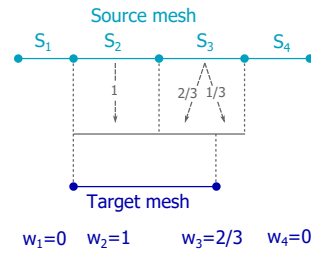


Figure 3.8: Example of input and output data for Intersect-Scatter-Gather mapping (adapted from [6]).

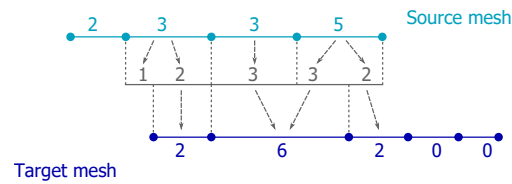


Figure 3.9: Example of input and output data for Intersect-Scatter-Gather mapping (adapted from [6]).

mapping process provides data at locations other than those required by the target participant. Conservative algorithms are always used, as data reconstruction is only required for extensive variables such as force or heat rate.

System coupling implements ramping algorithms to improve convergence, this is achieved by “slowing down” the application of source data on the target locations. According to system coupling documentation, the ramping is applied for transfer data locations where the condition $i \leq N_{\min}$ is true, as determined by:

$$\phi_{\text{Ramped}} = \phi_{\text{Reference}} + \frac{i}{N_{\min}} (\phi_{\text{Raw}} - \phi_{\text{Reference}}) \quad (3.160)$$

where ϕ_{Ramped} is the ramped target-side value, $\phi_{\text{Reference}}$ is the reference target-side value, ϕ_{Raw} is the raw target-side value obtained from interpolation, i is the coupling iteration number within the coupling step and N_{\min} is the minimum number of coupling iterations per coupling step.

Similarly, the use of under-relaxation aims to improve convergence of the overall analysis by limiting substantial changes of target-side data between successive coupling iterations. For each nodal location, the under-relaxation is applied according to the equation:

$$\phi_{\text{Relaxed}} = \phi_{\text{Reference}} + \omega (\phi_{\text{Raw}} - \phi_{\text{Reference}}) \quad (3.161)$$

where ϕ_{Relaxed} is the relaxed target-side value, $\phi_{\text{Reference}}$ is the reference target-side value, ϕ_{Raw} is the raw target-side value obtained from interpolation or from mapping directly and ω is the under relaxation factor.

Finally, the application of the quasi-Newton stabilization and acceleration method is yet another option for improving the convergence of the coupling procedure, aimed specifically at certain issues of two-way interaction problems. For FSI cases in particular, strongly coupled physics may experience instabilities as a small change in deformation may cause a large change in fluid forces or vice versa. Such issues may occur when

the solid body is slender or when the solid density is comparable or smaller than the fluid density. This method of stabilization can require problem specific tuning and works by applying an approximate Newton iteration to the data at the coupling interface. Subsequently, the inverse Jacobian-vector products associated with the residual of interface data are approximated using a least-squares model.

The implementation of the full coupling framework includes Quasi-Newton stabilization for the data transfers of pressure and incremental displacement only at the initial simulations. All the results obtained with the robust simulation framework omit the implementation of stabilizing algorithms after observing that in all cases the coupling converges satisfactorily at the third iteration.

3.3.3 Mesh update procedure

During a coupled simulation in the Ansys[®] environment, the mesh is updated for each coupling step with different options for modeling the deformation and performing remeshing as needed according to the simulation type and characteristics. There are two available procedures for updating the mesh during each coupling iteration, the first is known as *smoothing* and consists in deforming the mesh by modeling the displacement of the inner nodes subject to the displacement of one or several moving boundaries. The second available procedure is a *remeshing* of either a fraction or the entire fluid domain after the motion of the boundary is applied.

Diffusion-based smoothing

The mesh smoothing procedure can be treated with different models, the first of them is based on a diffusion model based on the governing equation

$$\nabla \cdot (\gamma \nabla \vec{u}) = 0 \quad (3.162)$$

where \vec{u} represents the mesh displacement velocity and γ represents the diffusion coefficient. This model requires a numerical solution, which might imply higher computational cost but providing better mesh quality with respect to other methods which do not model the deformation with a differential equation solution. When the flow mesh contains polyhedral cells, as happens to be the present case, the mesh smoothing is solved at the cell centroids using a finite-volume discretization and the displacement is then interpolated to the nodes. The smoothing takes a Dirichlet type boundary condition, which consists in the velocity specified at the FSI interface, corresponding to the wet surface of the blade. Since the output of the structural solution through System Coupling is an incremental displacement, the Dirichlet boundary condition is computed with the initial and final positions for each time step, and a similar inverse procedure is used to update the position of the mesh nodes:

$$\vec{x}_{new} = \vec{x}_{old} + \vec{u} \Delta t \quad (3.163)$$

The definition of γ can be based on the distance to the moving boundary or based on cell volume. In the first approach, the diffusion coefficient is defined according to:

$$\gamma = \frac{1}{d^\alpha} \quad (3.164)$$

where α is the diffusion parameter and d is the normalized distance to the moving boundary wall.

At this point it is useful to note that for a diffusion based smoothing, the node displacement is uniform across the mesh if γ is constant; if on the contrary diffusivity is variable in space as described by Equation 3.164, the nodes in a region with high γ should tend to move with little relative displacement, which is equivalent to a more rigid deformation. The distance based approach to a diffusion model for smoothing offers a convenient method for restricting the mesh deformation near the moving boundary, therefore it is relevant to the present work because the fluid mesh in the near wall regions is of special consideration due to the requirements for the modeling of turbulence and for mesh quality. The alternate definition of diffusivity is based on a normalized cell volume according to:

$$\gamma = \frac{1}{V^\alpha} \quad (3.165)$$

In this case, the diffusivity is larger for larger volumes, which means that the model preserves the shape of the smaller cells in the mesh and transmits the motion to the larger volumes instead.

Spring-based smoothing

This option for mesh smoothing assumes that the edges connecting adjacent node pairs behave in the same way as a spring element. In this sense, the fictitious force caused by the displacement of boundary nodes acts on the springs connected to those nodes and can be described by Hooke's law:

$$\vec{F}_i = \sum_j^{n_i} k_{ij} (\Delta \vec{x}_j - \Delta \vec{x}_i) \quad (3.166)$$

here $\Delta \vec{x}_i, \Delta \vec{x}_j$ represent the displacements of node i and its neighbor node j , n_i represents the number of neighbor nodes to node i and k_{ij} represents the spring constant stiffness for the element connecting nodes i and j .

The stiffness of the spring elements is defined in terms of an input parameter k_{fac} known as the spring constant factor:

$$k_{ij} = \frac{k_{fac}}{\sqrt{|\vec{x}_i - \vec{x}_j|}} \quad (3.167)$$

The spring constant factor is restricted to $0 \leq k_{fac} \leq 1$; a value of 0 means that the springs have little damping and thus the boundary nodes transmit more of their displacement to interior nodes whereas a value of 1 imposes the default damping introduced by the model. As stated in [59], the model assumes that the undeformed mesh corresponds to the equilibrium state, from which the following iterative relation is proposed:

$$\Delta \vec{x}_i^{m+1} = \frac{\sum_j^{n_i} k_{ij} \Delta \vec{x}_j^m}{\sum_j^{n_i} k_{ij}} \quad (3.168)$$

In this equation m represents the iteration number and it can be solved for Δx_i from the known displacements at the boundaries at each position update. The resulting value is used for updating the mesh deformation from step n to step $n + 1$ as given by:

$$\vec{x}_i^{n+1} = \vec{x}_i^n + \Delta \vec{x}_i^{\text{converged}} \quad (3.169)$$

The specified solution method in Ansys[®] Fluent is a Jacobi Sweep, performed for Δx_i until convergence is obtained for all interior nodes in the mesh. In terms of usability, it is worth recalling that the method is built on the concept of springs joining node pairs; while this is a good idea for triangular or tetrahedral cells depending on the problem, the Ansys[®]Fluent user's guide [76] indicates that use of such model in non-tetrahedral cells is suitable only if the problem has boundaries that move in one direction predominantly and if the motion is normal to said boundaries. When such conditions are not met for non-tetrahedral cells, the method may result in highly skewed meshes after deformation. Therefore, the model presents the option of affecting mesh zones with tetrahedral cells only. This would be a very convenient strategy for boundary layer meshes with tetrahedral or triangular cells in the zones away from the wall boundaries, but the expected deflection on either a fan blade or a wind turbine blade, makes strictly necessary that the boundary layer mesh also deforms to conform to the characteristic curved deflection of this type of slender bodies.

Linearly elastic solid-based model

This model is the third available option for the present work and assumes that the fluid mesh deforms as a solid with linear elastic behavior according to the governing equations:

$$\nabla \cdot \sigma(\vec{y}) = 0 \quad (3.170)$$

$$\sigma(\vec{y}) = \lambda(\text{tr}\varepsilon(\vec{y}))I + 2\mu\varepsilon(\vec{y}) \quad (3.171)$$

$$\varepsilon(\vec{y}) = \frac{1}{2}(\nabla \vec{y} + (\nabla \vec{y})^T) \quad (3.172)$$

where the stress and strain tensors are represented by σ and ε and the mesh deformation is represented by \vec{y} . The shear modulus, μ , and the Lamé's first factor are related through the Poisson's modulus which is the input of the model, and is restricted by $-1.0 \geq \nu \geq 0.5$. The solution procedure for the linear elastic solid method involves the boundary deformation as the boundary conditions of a FEM discretization, later processed with a conjugate gradient method with additional options for improving stability. When the motion of the boundary involves rotation or the geometry has sharp edges, the method may result in bad quality cells, making the diffusion based method a better choice.

4

MATHEMATICAL MODELING

The present chapter contains a description of the mathematical modeling for special flow effects that complement the baseline models introduced in section 3. These aspects are taken into consideration to cover issues that are neglected or simplified in the baseline models, for example: stall delay effects, the modeling of dynamic stall or the [FEM](#) modeling of anisotropic composite materials.

4.1 DYNAMIC INFLOW MODEL

The contents of the present section as well as the next section (4.2) are devoted to describe the most critical phenomena in the modelling of wind turbine performance with the BEM model. The current work contemplates the implementation of a computationally low cost framework based on the accurate yet fast BEM computations of rotor aerodynamic loads. However, the standard BEM model can hardly compete against a full finite-volume solution of the Navier-Stokes equations unless stall delay and dynamic stall phenomena are included in the model.

As the loads acting over the rotor blades change, so does the inflow or induced velocity at the rotor plane. These changes in loads may be caused by an unsteady wind input, an actuation of the blade pitch angle or a change in wind direction. A correct description of this time-dependent change is crucial in the formulation of a dynamic BEM method. One common model for dynamic inflow is proposed by Schepers and Snel [77] and Snel and Schepers [78] and, presented in Hansen's formulation of the dynamic BEM model [53]. This dynamic approach, originally formulated by Øye [79] from the Technical University of Denmark, describes the dynamic behavior of induced velocity in terms of a quasi-steady induced velocity, W_{qs} , computed from the standard steady-state BEM model and an intermediate induced velocity, W_{int} :

$$W_{int} + \tau_1 \frac{dW_{int}}{dt} = W_{qs} + k\tau_1 \frac{dW_{qs}}{dt} \quad (4.1)$$

$$W + \tau_2 \frac{dW}{dt} = W_{int} \quad (4.2)$$

The dynamic inflow model allows to compute a filtered induced velocity W , with a time behavior that lags behind the change in rotor loads in accordance with the differential Equations 4.1 and 4.2. The model constant is set to $k = 0.6$ while the time constants are defined according to:

$$\tau_1 = \frac{1.1}{1 - 1.3a} \frac{R}{V_\infty} \quad (4.3)$$

$$\tau_2 = \left[0.39 - 0.26 \left(\frac{r}{R} \right)^2 \right] \tau_1 \quad (4.4)$$

The dynamic inflow model proposed by Pitt and Peters [80] and included in the works of Schepers and Snel [77] and Snel and Schepers [78] describes the variation of induced velocity at the rotor plane with a differential equation formulated in terms of the axial induction factor, a :

$$\kappa \dot{a} + 4Fa (1 - f_g a) = hC_T \quad (4.5)$$

It is important to note that the factors for the Prandtl tip and root losses are included in this differential equation for dynamic inflow; after all, the term in which they appear is in fact the definition for the momentum theory representation of thrust coefficient, C_T , for an annulus. Since the explicit solution of Equation 4.5 requires C_T to be known at the previous time instant, the blade-element theory definition is used:

$$C_T = \frac{dT}{\frac{1}{2}\rho V_\infty^2 dA} \quad (4.6)$$

Under the formulation outlined in Chapter 3, the definition for the thrust of an element is $dT = Bp_z dr$ whereas the area of an annulus swept by that element is $dA = 2\pi r dr$. The model constants are defined as:

$$\kappa = \frac{16 (R_2^3 - R_1^3)}{3\pi V_\infty (R_2^2 - R_1^2)} \quad (4.7)$$

$$h = \frac{\sigma V^2}{V_\infty^2} \quad (4.8)$$

where R_1, R_2 are the bounding radii for each blade element.

4.2 STALL EFFECTS ON 3-D WIND TURBINE BLADE FLOWS

The operation of a wind turbine blade at certain conditions may result in high angles of attack along the blade span, either partially or fully. Along with a high angle of attack condition comes the well known phenomenon of flow separation, which is detrimental for blade lift and drag coefficients and in consequence, for the mechanical torque output. The rotating motion of a wind turbine blade imposes a challenge on the way stall is understood and predicted, because this phenomenon occurs differently over a rotating wing. The current section explores the mechanisms that affect the behavior of stall for rotating blades and includes them on the current BEM implementation to provide a better prediction of wind turbine torque and blade root moment.

4.2.1 *Lindenburt's centrifugal pumping correction model*

This correction model proposed by Lindenburt [81] is based on the centrifugal pumping mechanism, responsible for the apparent delay of stall over the suction surface of a rotating blade; this phenomenon starts as the tendency of air to flow outwards over the suction side of the blade in the radial direction. This affects pressure gradients and therefore the flow separation behavior over the suction surface. Lindenburt's model is based on the flow separation occurring from the trailing edge, for which the separated mass of air is acted upon by the centrifugal loading due to the blade rotation. The length of the separated flow region which is the same as the distance between the trailing edge and the separation point in the chordwise direction is expressed by the separation parameter, f :

$$f = \left[2\sqrt{\frac{C_n}{\alpha - \alpha_0} \left(\frac{\partial C_{n,0}}{\partial \alpha} \right)^{-1} - 1} \right]^2 \quad (4.9)$$

which is obtained from the Kirchhoff-Helmholtz model for the normal force coefficient, C_n , over a flat plate. In the expression above $C_{n,0}$ and α_0 denote the normal force coefficient and the angle of attack, both at zero-lift conditions respectively. Because the separation parameter is based on the normal force coefficient, the final correction modifies the values of both lift and drag; this is an interesting approach with respect

to other works which only correct lift, considering that stall affects both coefficients and that both coefficients have a direct effect on the blade torque and loads. Having defined f from the original airfoil coefficients, the set of modified angles of attack, α_{rot} , is given by

$$\alpha_{\text{rot}} = \alpha_{\text{non-rot}} + \frac{0.3\text{rad}}{2\pi} 1.5(1-f) \frac{c}{r} \left(\frac{\Omega r}{V_{\text{eff}}} \right)^2 \quad (4.10)$$

Where the empirical factor 0.3 rad corresponds to Lindenburg's fitting to the measurements of the NREL Phase VI rotor. The expressions for corrected lift and drag coefficients are given by:

$$C_{l,\text{rot}} = C_{l,\text{non-rot}} + 1.5 [\cos(\alpha_{\text{rot}}) + 0.3 \cos(\alpha_{\text{rot}} - \alpha_0)] (1-f) \frac{c}{r} \left(\frac{\Omega r}{V_{\text{eff}}} \right)^2 \quad (4.11)$$

$$C_{d,\text{rot}} = C_{d,\text{non-rot}} + 1.5 \sin(\alpha_{\text{rot}}) (1-f) \frac{c}{r} \left(\frac{\Omega r}{V_{\text{eff}}} \right)^2 \quad (4.12)$$

4.2.2 Du-Selig's 3-D Stall delay correction model

The correction model presented by Du and Selig [82] is built on the analysis of the integral boundary layer equations for a rotating reference frame, from which an expression for the length of the separation point is obtained as a function of the local speed ratio. Like Lindenburg's model, this one is also applied to drag coefficients in addition to lift coefficients, which is one of the reasons why both models can be regarded as more physically consistent among existing works, as some of them perform corrections for lift data only. The model contemplates two functions for the lift and drag corrections based on the modelling of the flow separation point, these functions, named f_l and f_d are defined as follows:

$$f_l = \frac{1}{2\pi} \left[\frac{1.6(c/r) a_d - (c/r) \frac{d}{\Lambda} \frac{R}{r}}{0.1267 b + (c/r) \frac{d}{\Lambda} \frac{R}{r}} - 1 \right] \quad (4.13)$$

$$f_d = \frac{1}{2\pi} \left[\frac{1.6(c/r) a_d - (c/r) \frac{d}{2\Lambda} \frac{R}{r}}{0.1267 b + (c/r) \frac{d}{2\Lambda} \frac{R}{r}} - 1 \right] \quad (4.14)$$

The modified tip-speed ratio is defined as $\Lambda = \Omega R / \sqrt{V_\infty^2 + (\Omega R)^2}$ while a_d , b and d are empirical factors which for the present work take the values of $a_d = 1$, $b = 1$ and $d = 1.5$. This correction is similar in nature to that of Lindenburg, in the sense that there is a dependence on the tip-speed ratio and the local blade element geometry and position, as expressed by the factor c/r . The final correction for lift and drag coefficients is given by:

$$C_{l,3D} = C_{l,2D} + f_l (C_{l,p} - C_{l,2D}) \quad (4.15)$$

$$C_{d,3D} = C_{d,2D} - f_d (C_{d,2D} - C_{d,0}) \quad (4.16)$$

These correction equations depend on the potential-flow approximation for the lift curve, given by $C_{l,p} = 2\pi(\alpha - \alpha_0)$ and the drag coefficient at an angle of attack of zero degrees, $C_{d,0} = C_{d,2D}(0)$.

4.2.3 Discussion on existing models

Throughout the rest of this work, the prediction of wind turbine aerodynamics is compared to the measurements of the [UAE Phase VI](#), using published data from [NREL \[1\]](#). The experimental campaigns of the [NREL Phase VI](#) work addresses different aspects of wind turbine aerodynamics under unsteady conditions, some of which are directly applicable to the numerical predictions presented in this work.

The results from Lindenburg [\[81\]](#) are compared with the Sequence H measurements [\[83\]](#) of the [UAE Phase VI](#) (Up-wind turbine, zero-yaw misalignment and 3° blade pitch), revealing that the correction of rotational effects on 2-D airfoil coefficients has an evident impact on the quasi-steady torque predictions. The authors show that uncorrected 2-D coefficients result in underpredicted torque values for stalled conditions (12 m/s and above). The opposite is found when the 2-D data is corrected for rotational effects, for which large overestimations are attributed to ignoring the dependence of stall delay on local tip speed ratio and extending the decay of the correction to a high angle (i.e., 50° instead of 45°).

In Lindenburg's comparison of torque predictions with airfoil coefficients from different sources [\[81\]](#), the authors noticed that the calculations for wind speeds between 14 and 20 m/s show considerable discrepancies between sets of coefficients, most likely related to the stall behavior for angles of attack around 20° which tend to occur for the mentioned speed range.

The work of Syed Ahmed Kabir and Ng [\[84\]](#) explores existing formulations for stall delay effects due to blade rotation, including the correction models of Snel et al. [\[85\]](#), Du and Selig [\[82\]](#), Chaviaropoulos and Hansen [\[86\]](#) and Lindenburg [\[81\]](#). The comparison between power curve predictions and the experimental results of the [NREL Phase VI](#) experiment corroborates the prevailing trend: power is underestimated when 2-D airfoil coefficients are used and, when corrections for stall delay are implemented, a good match is found at low speeds whereas for medium and high wind speeds, the torque is notably overestimated. This situation is attributed to an underprediction of drag coefficients from correction models, especially at high wind speeds.

Breton et al. [\[87\]](#) implements different stall delay corrections on a lifting line vortex model for a wind turbine and compared their results to the [NREL Phase VI](#) measurements. Their power curve predictions shows good agreement at wind speeds of up to 10 m/s. For higher wind speeds the power is overpredicted by most correction models, with a considerable amount of dispersion among them. The authors point out that the overprediction of the blade tip loads is a key factor for the overestimation of loads and thus power at high wind speeds. The explored models tend to produce large lift coefficient values at the tip of the blades, while from experimental results, rotational effects on stall delay are predominant on inboard and middle blade sections.

Hamlaoui et al. [\[88\]](#) present a novel model for stall delay corrections on 2-D airfoil coefficients, formulated for the specific case of the test wind turbine of the [NREL Phase VI](#) experiment; their work involves a correction on lift coefficient alone for subsequent calculations in a [BEM](#) solution method, which results in outstanding torque predic-

tions with respect to similar works that use alternative models for treating stall delay. The predicted torque curve shows good agreement with the experimental data as no extreme overpredictions are observed around wind speeds of 10 m/s or 25 m/s.

Zhong et al. [89] propose a tip-loss correction for the BEM model, based on the premise that blade rotation also contributes to tip losses in the load distribution, a hypothesis that is discussed also by Breton et al. [87] in their review of stall delay correction models. The authors compare their results for the loads of the 95% blade section to the NREL Phase VI measurements, finding a satisfactory match for the loads at the operating conditions of the linear portion of the C_l vs α curve. However, the results for operation at stall and deep-stall regimes show clear discrepancies. The authors do not present torque or power curve predictions, but a degraded performance of their correction model is observed at flow regimes with stall; additionally, no comparison is provided for the 30% blade section.

A remarkably well adjusted set of results are presented by Lanzafame and Messina [90] who reproduce the power curve for the NREL Phase VI wind turbine by applying an original stall delay correction on the aerodynamic coefficients of the NREL S809 airfoil. The correction of [90] increases lift coefficients for $20^\circ < \alpha < 45^\circ$ in a smoothed curve that blends with the values for the pre-stall regime. The authors present a good prediction for the power curve, but these results are based on the assumption of a constant Reynolds number of 500,000 along the blade span.

As discussed earlier in Chapter 2, Lee et al. [45] present an FSI analysis on the NREL Phase IV wind turbine in which a BEM approach is used to predict the aerodynamic loads on the rotor blades. In their work, the authors are fully aware of the disadvantages of the BEM model and its assumptions, particularly those associated to the stall delay phenomenon. For this reason, the authors predict the aerodynamic coefficients at the sections of the blades from full 3-D CFD simulations of the rotor, thus ensuring that these special effects are captured and transferred into the BEM modeling. The accuracy in the torque predictions for seven values of wind speeds between 5 and 15 m/s show a remarkable match with experimental results.

The work of Tang et al. [91] consists in a BEM computation of the power curve for the NREL Phase VI wind turbine, using a hybrid approach for the correction of aerodynamic coefficients and resulting in close power predictions with respect to the experimental data. The corrections in this work blend corrected 2-D coefficients from wind tunnel measurements, with 3-D coefficients recovered from 3-D CFD simulations.

An alternative to obtain adequate power predictions using 2-D wind tunnel data is presented by Tangler [92] in one of the earliest works with respect to the publication of the UAE Phase VI measurements. In this approach, no formal correction for rotational effects is applied over the original 2-D coefficients; instead, a set of C_l measurements up to $\alpha = 20^\circ$ is used and extended to higher angles with flat plate theory. In this extrapolation two different data sets are produced assuming no sudden lift drop (from $\alpha = 16^\circ$) and assuming sudden lift drop ($\alpha = 20^\circ$). The most attractive results are obtained by averaging both data sets.

The approach of Tangler [92] offers good results and has two aspects that deserve closer attention: in first place, by assuming two different kinds of behavior in the construction of the final lift characteristics (i.e., soft versus sudden stall), there is no certainty on the accuracy of the 2-D input data as such, and an inconsistency appears with respect to different measurements available in literature. In second place the av-

eraging technique relies on two extreme scenarios which modify the values of lift but leave drag coefficients unchanged, this makes sense for the case of assuming no sudden loss of lift (extrapolation from $\alpha = 16^\circ$) as one would expect a smooth transition between attached and detached flow regimes but, when considering sudden loss of lift (extrapolation from $\alpha = 20^\circ$), the task of justifying unchanged drag values becomes a difficult one.

4.2.4 Dynamic stall modelling

In Hansen's version of the dynamic BEM model [53] the role of the dynamic stall model is to provide a description of the evolution of flow separation over the blade surface, as the local angle of attack changes with time and, to avoid the computation of non-physical vibrations resulting from step changes in the local angle of attack. Such instabilities are of numerical nature and are enough drive the results away from the real behavior of the system. The dynamic stall model considers trailing edge separation through the parameter f_s which describes the degree of separation over the airfoil section surface and forms the basis for the definition of the lift coefficient in the following way:

$$C_l = f_s C_{l,p}(\alpha) + (1 - f_s) C_{l,f_s}(\alpha) \quad (4.17)$$

In the expression above, $C_{l,p}$ can be known by extrapolating the linear portion of the static lift curve. The time dependency is modeled for the parameter f_s according to:

$$\frac{df_s}{dt} = \frac{f_s^{st} - f_s}{\tau} \quad (4.18)$$

The model constant for the time variation is defined as $\tau = 4c/V_{rel}$, f_s^{st} represents the value of f_s necessary to reproduce the static lift curve with the Equation 4.17; according to Hansen [53] the differential equation represents the tendency of the dynamic value to "chase" the static value at all times. The determination of both C_{l,f_s} and f_s^{st} is outlined by Hansen et al. [93]. In their model, f_s^{st} represents the amount of separated flow for trailing edge stall and is determined from the expression for lift over flat plate in a potential Kirchhoff flow:

$$C_l^{st} = C_{l,\alpha} \left(\frac{1 + \sqrt{f_x^{st}(\alpha)}}{2} \right)^2 (\alpha - \alpha_0) \quad (4.19)$$

Here, C_l^{st} is the static lift coefficient and α_0 the angle of attack for zero-lift. Because the separation function is defined as the dimensionless location of the separation point, $f_x = x/c$, it can take values between $f_x = 0$ for fully separated flow and $f_x = 1$ for fully attached flow. The slope of the lift curve in the linear portion, $C_{l,\alpha}$ is determined from:

$$C_{l,\alpha} = \max \{ C_l^{st}(\alpha) / (\alpha - \alpha_0) \} \quad (4.20)$$

The angles of attack $\alpha^{\pm f_s}$ for which the flow is completely separated from the airfoil surface can be determined from the relationship:

$$\left| C_l^{st}(\alpha^{\pm f^s}) \right| = \left| \frac{C_{l,\alpha}(\alpha^{\pm f^s} - \alpha_0)}{4} \right| \quad (4.21)$$

For all angles of attack greater than α^{+f^s} or smaller than α^{-f^s} the value of the separation function is manually set to $f^{st} = 0$. If the lift for static conditions, which corresponds to the input in a steady-state BEM calculation is then described in terms of fully attached and fully separated lift coefficients, with the separation factor f^{st} playing the role of an interpolation factor:

$$C_l^{st} = C_{l,\alpha}(\alpha - \alpha_0) f^{st} + C_l^{fs}(\alpha)(1 - f^{st}) \quad (4.22)$$

then an expression for fully separated lift coefficient can be established:

$$C_l^{fs} = \frac{C_l^{st} - C_{l,\alpha}(\alpha - \alpha_0) f^{st}}{1 - f^{st}} \quad (4.23)$$

To avoid undefined operations in the computation of C_l^{fs} when $f^{st} = 1$, its value is manually set to $C_l^{fs} = C_l^{st}/2$, which is the correct result in the limit of $f^{st} \rightarrow 1$ when Equation 4.19 is solved for f^{st} and then substituted into Equation 4.23.

4.3 PREDICTIONS OF TORQUE AND BLADE ROOT MOMENT FOR THE NREL PHASE VI WIND TURBINE

The current validation of blade load prediction has been performed using a classical BEM code, with the standard Glauert correction for highly loaded blades and the Prandtl tip and root correction for losses at the ends of the blade. Although the computations are made in a transient formulation of the BEM method, in which the time change of induction is described by an empirical model, the following calculations are representative of steady-state values for wind speed varying between 5 m/s and 25 m/s, constant angular velocity of 72 RPM and, with the assumption of fully rigid blades set to a tip-pitch angle of 3° as configured for the Sequence H [83] from the UAE Phase VI [1]. Here the steady wind velocity input and the steady setting of the pitch angle ensure that the torque output behaves steadily; similarly, the presented experimental data is representative of steady state operation as each experimental torque is an average of 30 s continuous measurements with constant operation parameters, with the error in yaw and pitch angles and in angular velocity being responsible for an oscillation with is assumed to vary around average values in the long term. The prediction and assessment of transient rotor loads is addressed in a subsequent section, using the corresponding experimental measurements for unsteady rotor operation.

Most data sets from the UAE Phase VI experiment are measured at a constant angular velocity of 72 RPM, this means that the nominal tip-speed ratio takes typical values below four when the wind speed increases beyond 10 m/s. Considering the geometry of the velocity triangle at an average section of the blade (Figure 3.2), an increase in free-stream wind speed equals an increase in angle of attack; therefore the rotor blades are expected to operate under partial or full stall, or even deep stall for the higher wind speeds where the tip speed ratio decreases below two. Considering this, accurate stall

predictions become crucial as well as the inclusion of blade rotation effects on flow separation.

The contents of the previous section present an overview of existing models for stall delay correction, a measure of their accuracy and in some cases the key underlying principles. The current implementation of the BEM method considers two models for stall delay correction: Du and Selig [82] and Lindenburg [81]. This pair of works are relevant because: a) in both formulations the independent variable c/r can be set constant or variable along the blade span, b) unlike the models of Tangler [92] or Lanzafame and Messina [90], the lift and drag coefficients vary with the Reynolds number and still provide acceptable results with respect to the experimental values and c) The current formulation can be applied without the need for previous computations in 3-D RANS environments or experimentation other than the obtention of pure 2-D airfoil coefficients. In terms of dissimilarities, the correction models of Lindenburg and Du-Selig have a notorious difference in the way torque is predicted with respect to wind speed; for instance, at high wind speeds, the model of Lindenburg does a good prediction while the model of Du-Selig fails notoriously and at low wind speeds, the model of Du-Selig has a better prediction than Lindenburg's.

Figure 4.1a shows the torque predictions performed in this work with the model of Lindenburg [81] with variable Reynolds (between 300,000 and 1 million) and with constant Reynolds of 1 million. The difference between data sets is small and most notorious around the peak torque (at 11 m/s). The model can replicate the general shape of the experimental curve but overpredicts torque around 11 m/s while showing considerable underpredictions at higher wind speeds.

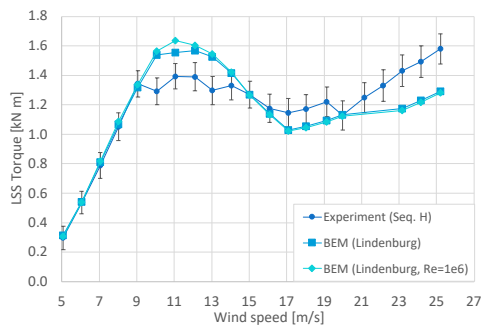
The prediction of blade root bending moment in the flap-wise direction with the current implementation of Lindenburg's model presented in Figure 4.1b, shows a notable overprediction for wind speeds of up to 16 m/s; for higher wind speeds the prediction is close to the experimental results. The same set of calculations but performed with the model of Du and Selig [82] is shown in Figures 4.1c and 4.1d. The rotor torque is highly overpredicted for wind speeds above 8 m/s while the blade root flap-wise bending moment is overpredicted with a smaller maximum error but for the entire range of wind speeds.

Considering that the correction of Du and Selig [82] follows the general shape of the results with non-corrected data, an alternative for better predicting the torque around peak nominal values (around 11 m/s) is to use a new prediction based on a moderate correction of the original 2-D coefficients. At this point the current work proposes an improvement on this correction, obtained by blending the aerodynamic coefficients corrected with the Du-Selig model, with the original 2-D coefficients, this approach is named here as "Moderate Du-Selig". The definition of the airfoil coefficients under this proposed scheme is:

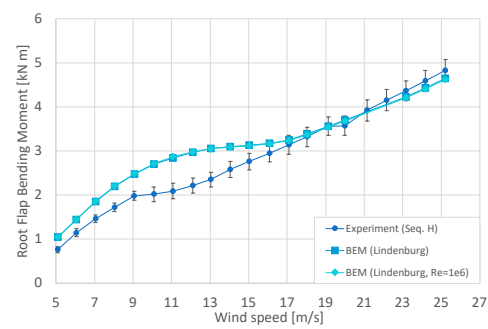
$$C_{l,\text{mod}} = w_1 C_l + (1 - w_1) C_{l,DS} \quad (4.24)$$

$$C_{d,\text{mod}} = w_1 C_d + (1 - w_1) C_{d,DS} \quad (4.25)$$

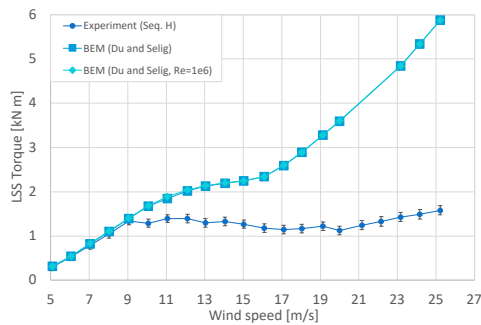
The resulting coefficients of this moderate correction, $C_{l,\text{mod}}$ and $C_{d,\text{mod}}$, are obtained with a weight factor of $w_1 = 0.8$, which for the current work is being proposed arbitrarily as a proof of concept. The current implementation of this correction for the



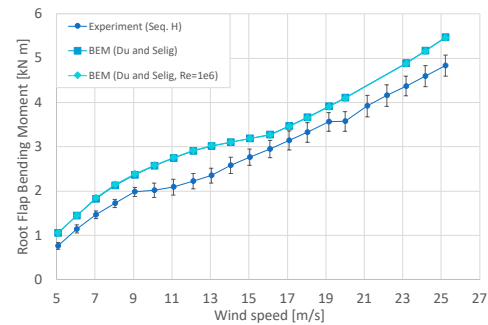
(a) Low speed shaft torque, predicted here with the model of Lindenburg [81].



(b) Blade root flap bending moment predicted here with the model of Lindenburg [81].



(c) Low speed shaft torque predicted here with the model of Du and Selig [82].



(d) Blade root flap bending moment predicted here with the model of Du and Selig [82].

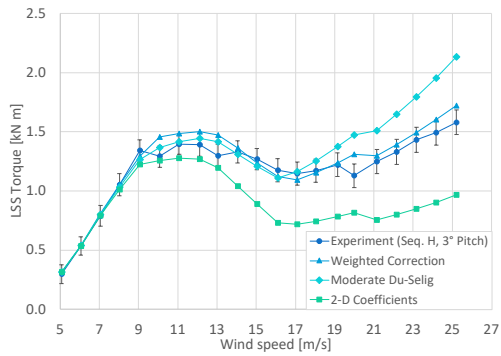
Figure 4.1: Sensitivity of torque and moment predictions with respect to variable and fixed-Reynolds corrections of airfoil coefficients.

rotor load prediction is shown in Figure 4.2, which reflects an improved match for wind speeds up to 18 m/s, 16 m/s and 19 m/s for the three considered cases of pitch (i.e., 3° , 0° and 6°). The drawback of this blending is evident from the results, as both torque and bending moment values are overpredicted for higher wind speeds. Noting that such overprediction coincides with the underpredicted values of the model of Lindenburg, a second sequential blending is proposed to adjust the final prediction evenly over the entire range of wind speeds. This second improvement also operates in the form of a blending, this time between the moderate correction discussed earlier (Equations 4.24 and 4.25) and the correction with the model of Lindenburg:

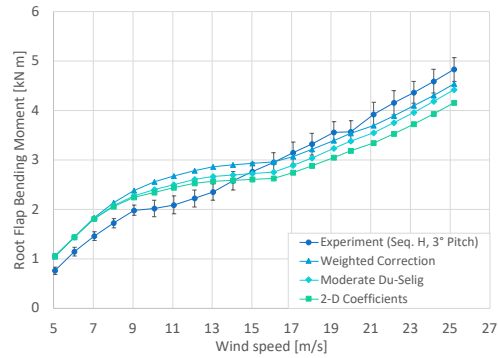
$$C_{l,cor} = w_2 C_{l,mod} + (1 - w_2) C_{l,LN} \quad (4.26)$$

$$C_{d,cor} = w_2 C_{d,mod} + (1 - w_2) C_{d,LN} \quad (4.27)$$

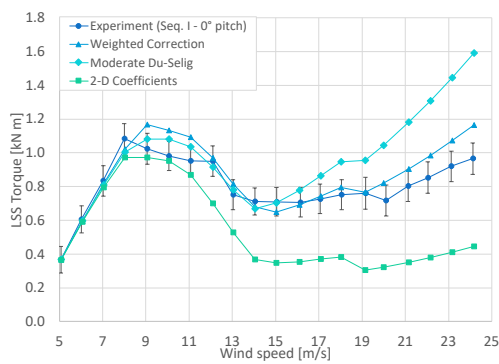
In its general form, the blending of Lindenburg and moderate Du-Selig models as presented in Equations 4.26 and 4.27 takes the form of a weighted average. By using a weight of $w_2 = 0.5$ for this second blending, an arithmetic average between moderate Du-Selig and Lindenburg corrections is obtained. Again it must be mentioned that the weights are selected arbitrarily to demonstrate the concept. At this point it is important to mention that the selected models for assembling the weighted average are compat-



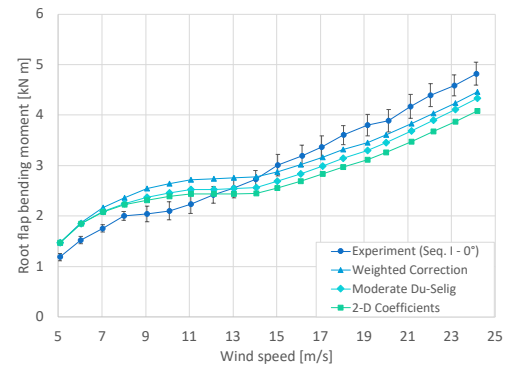
(a) Low-speed shaft torque, pitch= 3°.



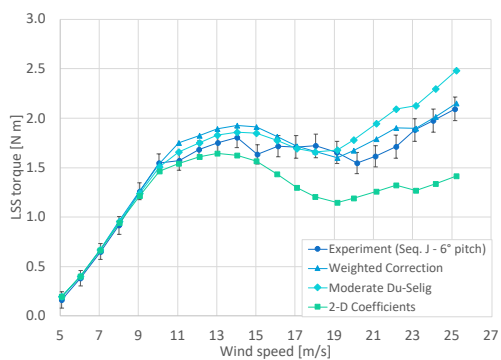
(b) Blade-root flap-wise bending moment, pitch= 3°.



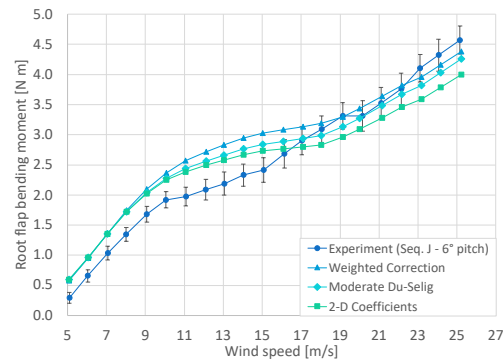
(c) Low-speed shaft torque, pitch= 0°.



(d) Blade-root flap-wise bending moment, pitch= 0°.



(e) Low-speed shaft torque, pitch= 6°.



(f) Blade-root flap-wise bending moment, pitch= 6°.

Figure 4.2: Steady-state prediction of integral rotor loads with the BEM solver.

Case	LSS torque		Blade root flap-wise moment	
	2-D data	Corrected data	2-D data	Corrected data
Sequence H [83]	29.5 %	7.2 %	13.9 %	11.1 %
Sequence I [94]	39.3 %	11.5 %	15.4 %	10.8 %
Sequence J [95]	22.1 %	7.3 %	12.7 %	13.6 %

Table 4.1: L-2 Relative error norm in percentage for the final “weighted Correction” results.

ible to each other in the sense that they are not built upon contradicting assumptions. Both models are based on the quantification of the separation point over the upper blade surface, meaning that the description of drag is based on trailing edge stall; furthermore, in both cases a dependency on the blade geometry is maintained through the parameter c/r . The model of Du-Selig is based on the boundary layer equations considering 2-D flow for the convective terms while keeping the 3-D terms associated to centrifugal and coriolis loads acting on a volume of fluid. The Du-Selig correction is dependent on the blade geometry but also on the effects of rotation, considered through a localized version of the tip-speed ratio parameter. The Lindenburg model is also proposed on the proportionality of the separation length over the blade surface to the effects of radial flow and coriolis acceleration; however only c/r is considered as the main geometrical parameter of this correction. The only defined difference between both corrections is the fact that the Du-Selig model applies the correction over C_l and C_d directly whereas the Lindenburg model applies the correction over the normal force coefficient C_n .

All predictions for rotor torque show a good agreement with the measurements as observed in the series “Weighted Correction” in Figure 4.2, especially for blade pitch angles of 3° and 6° . The L-2 relative error norm defined in Equation 4.28 is calculated for all predictions and presented in Table 4.1.

$$\|\text{Error}\|_2 = \sqrt{\frac{\sum_{i=1}^n \left(T_{\text{LSS}}^{i,\text{num}} - T_{\text{LSS}}^{i,\text{exp}} \right)^2}{\sum_{i=1}^n \left(T_{\text{LSS}}^{i,\text{exp}} \right)^2}} \quad (4.28)$$

The values of blade root flap-wise bending are overpredicted for wind speeds between 5 and 17 m/s for the worst case (pitch of 6°). The remaining two cases also show similar overpredictions in bending moment but at lower wind speeds. The bending moment at higher wind speeds is underpredicted in all three cases but the values are within the standard deviation of the measurements (pitch of 3° and 6°) or close to the lower limit (pitch of 0°).

4.4 DYNAMIC SIMULATION WITH THE BLADE ELEMENT MOMENTUM MODEL

The implementation of the dynamic formulation of the BEM model, including the models for stall delay and dynamic stall is compared with the experimental results of the NREL Phase VI sequence Q [96] which considers dynamic inflow in different cases. From these experiments, the present work considers four cases in which the wind tur-

bine operates at a 0° -yaw, with constant wind speed and rotational speed of 72 RPM but, including step variations of blade pitch angle as follows:

- Sequence at 5 m/s, pitch variation between 10° and -6° .
- Sequence at 8 m/s, pitch variation between 18° and 0° .
- Sequence at 10 m/s, pitch variation between 24° and 6° .
- Sequence at 15 m/s, pitch variation between 36° and 18° .

To assess the performance of the implemented models, the low-speed shaft torque is predicted and compared with the corresponding experimental values. The results shown in Figure 4.3 compare the numerical torque values obtained in this work to the experimental time histories for each one of the cases listed above. In general, the predictions match well with the experimental values, showing an even better match for cases with smaller wind speeds ($V=5$ m/s) and smaller pitch angles.

Another notorious discrepancy between experimental and numerical values is perhaps the oscillatory behavior of the NREL measurements, presented under the label “Experimental” for all plots in Figure 4.3. Numerical predictions of torque appear to stabilize after the change in blade pitch for each sequence, some of them with small amplitude oscillations but without the large amplitude oscillations present in the experimental values. This is because the simulations with the dynamic formulation of the BEM model consider completely uniform flow without turbulence, the yaw angle is exactly 0° and there is no motion of the rotor hub due to tower deflection in the forward-aft and side-side directions. The motion of the tower can be expected to cause the large amplitude oscillation on rotor loads as it causes an oscillatory change in local wind speed with a frequency proportional to both the rotor angular frequency and the number of blades. The visible oscillatory output on the numerical results happens because the input angular velocity is set as the real value measured in the experimental campaigns, thus including an inherent error.

Paying attention to the results in Figure 4.3, the predictions with the model of Øye described by Equations 4.1 and 4.2, and with the model of Pitt and Peters described by equation 4.5, appear to have a noticeable discrepancy. This difference in torque prediction appears to be well correlated to the pitch angle for at least the first three of the four measurements presented in Figure 4.3. It must be considered that the pitch angles for each sequence as listed at the beginning of this section follow a convention for pitch actuation signs which establish that negative pitch angles denote pitch towards feather, thus reducing the angle of attack, whereas positive pitch angles denote pitch towards stall, thus increasing the angle of attack. Since high angles of attack result in separated flow; it is harder to predict experimental behavior using the present models. This is observed for example in Figure 4.3a in which torque predictions before $t = 15$ s and after $t = 30$ s differ mutually due to the high pitch angle of 10° . On the contrary, the predictions between $t = 15$ s and $t = 30$ s show a good match since the negative pitch angle means a small angle of attack and thus, attached flow over the blade. This tendency is observed again in Figures 4.3b and 4.3c as the torque prediction for the smaller rotor loading (i.e. small pitch setting) is predicted with consistency by both dynamic models. On the contrary, the results at the higher pitch setting show larger

differences as the blade aerodynamic state is taken towards stall, a condition in which the BEM model tends to fail. The results in Figure 4.3d are a special case because the difference between numerical predictions is more or less consistent throughout the time history, regardless of the pitch angle setting. The reason for this behavior might be related to the high wind speed of 15 m/s, since increasing wind speed while maintaining the rotor angular velocity is another way of having large angles of attack, resulting in stall or deep stall conditions due to the mere geometry of the velocity triangle.

At this point it is worth mentioning that the model of Øye is designed as a pair of filters working in series precisely to include both the near wake influence and the far wake influence on the dynamic response of the induced velocity at the rotor plane. The model of Pitt and Peters has a simpler formulation in the sense that it contemplates one single differential equation which does not involve constants to be fitted with auxiliary models or experimental measurements. Besides the challenging conditions for torque prediction at stabilized conditions, each model reveals a different evolution profile just after the sudden change in blade pitch.

4.5 FINITE ELEMENT MODELING

4.5.1 *Hollow beam structure with bend-twist coupling*

This section contains the validation exercise for the FEM model to be used as the main analysis tool in the structural component of the project. The general approach in this case consists in using the analysis subject of Ong et al. [7] as a conceptual approximation for the structure of a wind turbine blade under the following considerations: the structure is conformed by the external shells only, is assembled from thin composite laminates, may exhibit bend-twist coupling behavior and, is subject to a steady state load at the tip. All wind turbine blades in modern applications have a tapered geometry, that is, a cross section varying in size with the radial location; however, the constant cross-sectional geometry of the beam used in the reference case is still relevant because of its “D” shape. Such shape is representative of the typical geometry of the load carrying members in wind turbine blades, which for the NREL Phase VI blade coincides with the blunt edge geometry that is found between the middle of the cross section and the leading edge point.

The validation considers a 1.828 m long spar, with the cross section geometry shown in Figure 4.4. The reference prototype is manufactured with an epoxy reinforced hybrid carbon/glass laminate; the mechanical properties for each type of ply are shown in Table 4.2. Because the laminate is designed to induce bend-twist coupling on the spar, the fiber orientation must be symmetrical with respect to the neutral plane of the beam; therefore, fiber discontinuity is inevitable at the union lines of the upper and lower surfaces. To obtain the required fiber orientation while achieving a balanced laminate across the wall thickness direction, Ong et al. [7] propose an intricate ply layup sequence using combinations of plies at 20° and 70°. The virtual model of the beam has been assembled using the “Pre” module of Ansys Composite Pre-Post (ACP). The ply angle orientation for the resulting structure is shown in Figure 4.5 while the thickness distribution is shown in Figure 4.6.

Because the geometry is simple, a mesh with rectangular SHELL181 elements could be easily implemented. According to the documentation for Ansys® APDL, the SHELL181

Property	Graphite/Epoxy	Glass/Epoxy
E_x [GPa]	120.66	38.61
E_y [GPa]	8.96	8.27
E_s [GPa]	5.52	4.55
ν_x	0.3	0.3

Table 4.2: Laminate mechanical properties for the validation case of a D-spar based on Ong et al. [7].

element type consists in a four-node shell element, selected in the first place because of the geometry of the beam, whose thickness is substantially smaller than any of the other dimensions. Besides, this element type offers flexibility in the sense that it works well within a range of thin to moderately thick structures. In second place, both large-rotations and large-deflections can be handled using this element type. In third place, the SHELL181 element can be used to describe layered materials, enabling the solver to handle composite structures without which, the bend-twist coupling could be hardly tailored for usefull applications. All elements are defined from the set up using the general shell option, which enables six degrees of freedom: translations in the x, y and z directions and rotations about the x, y and z axes.

The geometry of the blade is split into five longitudinal segments with the purpose of using the resulting lines as locations for remote points where torsional rotations can be retrieved for later comparison with the reference measurements. The resulting domain topology is shown in Figure 4.7 along with the defined boundary conditions: a fixed support on one end and a vertical force on the other. The force is applied on lower half of the free end, and this is done with the deliberate purpose of avoiding unrealistic gradients on the local deformation field. With the purpose of comparing results directly, the numerical data sampling is done over the upper spar surface. If the load is applied on the upper surface as well, the appearance of localized deformation gradients results in an unrealistic deformation field when compared with the measurements, since the experimental load is applied over the spar using a finite-thickness string, thus providing a smooth load distribution over the composite surface.

The results from steady loading on the free end of the D-spar are compared to the reference data using the static deformation of the beam, longitudinal strain and torsional deformation. Each variable is sampled along the upper or tensile surface of the beam, over a straight line that splits the top rectangular face in half. The experimental cases include also a numerical computation with 1-D beam elements (Ong and Tsai [97]), those are presented for vertical deflection in Figure 4.8a, along with their reported experimental measurements and the numerical prediction developed in the current work. Judging the quality of the results, it is observed that the general shape of the vertical deflection is consistent with the expected shape and the reference data; no discontinuities appear and the L-2 norm based on the relative error with respect to the experiment from [97] is 5.6%, reflecting a satisfactory solution from the finite-element shell model used in the present work.

When observing the plot for longitudinal strain (ϵ_1) in Figure 4.8b, the results from the present analysis again show a good match with the reference experimental data, compared to either of the results that are reported for 1-D FEM analysis. The L-2 er-

ror norm for the three sampling points where measured data is available is found to be 0.76%, revealing a satisfactory prediction from the current numerical analysis. Nevertheless, the values of strain at the free end of the beam appear distorted when compared to the trends given by 1-D results. In this case, further inspection of the strain contours over the tension surface of the beam revealed the presence of gradients near the corners and the curved wall of the beam. During the replication of the analysis, the clamping and load application could not be fully known, because of this, the simplified boundary conditions described earlier are the best approximation possible; additionally, the strains for the end locations are averaged values for the corresponding lines over the tension surface. With the previous considerations, the present results closely follow those of the reference case.

The final and most relevant comparison is that of the torsional deformation because it shows that the SHELL181 FEM model provides a fair prediction of bend-twist coupling in a composite structure. Concerning the modelling of composite structures with bend-twist coupling the present validation is not re-iterated any further with additional cases, considering that the work of Ong and Tsai [97] is the only known published work that allows for a complete reproduction of both the numerical model and the experimental set-up. Two main findings can be derived from the plots in Figure 4.8c: in first place, the present results are bounded by the reported 1-D numerical predictions from the reference case in a similar way as for the previous two variables and, in second place, the present results confirm the monotonic increase in twist angle with the longitudinal coordinate, contrary to the results from experiments. Regarding the experimental results reported by Ong et al. [7] and Ong and Tsai [97], it must be said that the twist angles in their work do not correspond to the same load but rather to a linear regression for multiple measurements with different load magnitudes. The dispersion in the data results in the unexpected behavior reported by the authors which measure the rotation at two locations only and take the respective averages, for this reason the “Experimental” series in Figure 4.8c should not be considered a distribution in a strict sense. Besides, the method for measuring the rotations in the experiment uses a set of linear displacement gauges on auxiliary bars attached to the upper surface of the beam. This last variable shows the greatest relative error with 18.8%; nevertheless, the numerical prediction can be still considered valid since the reported measurements are actually averages from a series of measurements, with an inherent dispersion due to experimentation error.

4.5.2 Benchmarking for the structure model

Prior to the validation of the structural solution, an auxiliary exercise is done to ensure that the structural model for the condenser fan blade has the same characteristics as the real blade in terms of eigenfrequencies and also to ensure solution stability due to the fact that this is the only instance of the present work in which a multi-block solid mesh is used. With this purpose a model for the fan blade is assembled in the Ansys[®] environment by creating a multi-block domain; an approach that follows the suggestion of Peters et al. [98] in the sense that the domain blocks are strategically delimited for obtaining a high quality structural mesh. Because the blade geometry (Figure 4.9a) is split into different parts, appropriate contact definitions are required between the blocks of the blade body. It is important to recall that the blade body is

made of aluminum and the holding plates and bolt are made of steel. With this context, the workflow for defining the contacts begins by verifying the geometry regions at which the physical contact occurs and that they are correctly scoped by the program. Subsequently the Augmented Lagrange formulation is assigned for all contact interfaces through the CONTA178 3-D node-to-node contact element [64]. The penetration from a contact target into a contact source is determined by the equation:

$$F_n = k_n x_p + \lambda \quad (4.29)$$

where F_n represents the contact force, defined as normal to the source surface, x_p represents the amount of penetration from one surface to the other, k_n represents the contact stiffness and λ represents the Lagrange multiplier force term, responsible for reducing the sensibility of the contact to the magnitude of k_n . The premise of the contact model is that a smaller penetration x_p between adjacent bodies is the desired, more physically accurate scenario. This can be achieved with a higher stiffness k_n but unfortunately at the cost of a numerically unstable solution. Following the guidelines from the program documentation, the contact stiffness is defined by trial and error to a value that ensures a sufficiently small penetration while avoiding an unstable solution. The contact penetration tolerance is verified to be at 1×10^{-6} m and the penetration behavior is checked visually at different contact points to ensure it matches this or greater values. The solution stability is ensured first by obtaining full solutions with no fails and then by obtaining stabilization times of less than 1 s after the initial transients, using a transient simulation with a point load in vacuum applied to the free end of the blade. During this process, an amplitude decay factor of 0.03 is set manually to ensuring that the transient oscillations at the beginning of the simulation settle into a stabilized condition at which the blade tip displacement oscillates solely due to the base excitation, the absence of aerodynamic damping in a vacuum simulation. The contact stiffness is then manually set to $k_n = 0.1$ and the first verification of the structural model with the mesh shown in Figure 4.9b, is made with a modal analysis in vacuum with a fixed boundary condition at the base of the steel bolt.

Each one of the first four modes is depicted in Figure 4.10, where it can be seen that the first eigenfrequency of 11.34 Hz, corresponding to the first flap-wise mode (Figure 4.10a), is verified against the frequency reported by Peters et al. [98] with a negligible difference. This results serve as a verification over the contact definition in Ansys® and the model as a whole, but also provide a mean of determining the required time step for the transient analyses.

4.6 IMPLEMENTATION OF A FLUID-STRUCTURE INTERACTION FRAMEWORK

This section presents an implementation of a FSI set-up based on the study performed by Peters et al. [98] on an industrial fan blade, considering a vibrating boundary condition at the base. Unlike the case of interest for this thesis, the reference work for this section considers a blade made of isotropic materials and a relatively simple geometry from an aerodynamic standpoint. However, its results are relevant because a two-way FSI interface is established between a transient FEM model and a fully turbulent fluid flow analysis with turbulence models of varying complexity. The structural analysis of the FSI benchmark case is simple because the material is isotropic; hopefully, a more

complete picture can be given when adding the validation case of the D-spar in which a thin-walled composite structure is used. The work layout for the assembly of the coupled simulation is based on the individual benchmarking of the fluid and solid solutions and a subsequent solution of both systems as a fully coupled **FSI** framework.

4.6.1 Benchmarking for the fluid model

A validation of the fluid flow solution has been proposed by replicating the analysis of Peters et al. [98]. The geometry of the fan blade and the domain were replicated as shown in Figures 4.11a and 4.9a. As seen also in Figure 4.11b, the domain is decomposed into 9 blocks to facilitate the application of mesh controls for hexahedral elements in all blocks, with the exception of the central block, where the blade geometry is enclosed. Within this central block, the domain is discretized with tetrahedral elements; this is a requirement when using the inflation option in the mesh module of Ansys[®] Fluent. The details of the tetrahedral and near wall mesh can be appreciated in Figure 4.11c.

The transient solution of the fluid flow around the blade is performed every 2° for $0^\circ < \alpha < 8^\circ$, which amounts to five different cases already studied by Peters [99] and compared to experimental results from Riegels [100]. Because the domain topology aims to replicate the geometry of a wind tunnel section, the velocity orientation at the inlet could not be changed between cases and the blade geometry was manually rotated and re-meshed for each one of the simulations instead. The boundary conditions are specified as velocity-inlet/pressure-outlet sets, because they provide solution stability for incompressible flows; the magnitude of the inlet velocity is set to 20.45 m/s which for the flow conditions reported in the reference work corresponds to a flow regime of $Re = 157,000$. The lateral faces in the domain are set to “symmetry” type boundary conditions whereas the blade surface is defined as a no-slip wall boundary condition.

Peters et al. [98] validate their own fluid model with steady state computations of the lift and drag coefficients; the present work also reproduces the results for the same conditions using steady state simulations with the **SIMPLEC** solver, using second-order upwind discretization schemes. Because a time-dependent solution is to be implemented in the final **FSI** simulation framework, a single case with $\alpha = 6^\circ$ is simulated using the solver **SIMPLEC** in transient mode. A second order time discretization scheme is used and, because the computations are initially done with the Pressure-Implicit with Splitting of Operator (**PISO**) solver, the time step is defined to ensure the Courant-Friedrichs-Lewy (**CFL**) condition for stable computations with $dt = 3.5 \times 10^{-5}$ s; this is the resulting time step size for a free-stream flow speed of 20.45 m/s and minimum mesh dimension of 8×10^{-4} m. This single case for the transient simulation was performed with an angle of attack of 6° to assess the convergence and accuracy of the solution in a flow condition with substantial flow separation. The steady and transient simulations are done with fully turbulent flow with the $k - \omega$ SST model. For the given flow conditions the height of the wall-adjacent cells is set to 8×10^{-4} m, resulting in $y^+ \geq 30$ for the wall adjacent cells. With this conditions, the turbulence model is expected to activate the use of wall functions for modeling the boundary layer flow and provide adequate results on a mesh of modest size. The use of two-equation turbulence models is a common practice in applied **CFD**, this is the model employed in the

works used as reference for the validation of the present CFD model set up and it is no surprise since two-equation models offer a good balance between computational cost and solution accuracy. A sufficiently accurate simulation of turbulence with the available computation resources is the most important criterion for the present work, the prediction of both turbulence and flow regime transition adds extra complexity, is ruling out this last option due to the restriction of computational time. The feasible models are thus restricted to the two-equation models also known as $k - \varepsilon$ and $k - \omega$. Among these two models, the $k - \omega$ SST version is considered for the development of the present work, because on top of the advantages in terms of computation cost, is a capable model when it comes to the prediction of flow in challenging scenarios such as highly curved flow fields and adverse pressure gradients as discussed in Chapter 3. The boundary conditions for turbulence at the inlet and outlets of the domain are set to a free-stream turbulent intensity of 5% and a free-stream turbulent viscosity ratio of 10. At the walls the turbulent kinetic energy is set to zero whereas the specific dissipation rate is imposed to a value of $18.16 \times 10^3 \text{ s}^{-1}$ following the guidelines in [63].

An important aspect of the solution process is the observed difficulty for the mass residual to fall below the specified tolerance of 1×10^{-6} , for both steady and transient solutions. In any case the monitored force coefficients and net mass flow rate reach steady behavior before the solutions are reported. During the meshing procedure a small amount of highly skewed cells is found, coinciding with an inappropriate orthogonal quality for those mesh regions. The solution process with a quality-sensitive solver such as PISO quickly fails and for this reason, the selection of the SIMPLEC solver, as recommended by the authors in the reference work, is fully justified, especially considering that the intricacy of the blade geometry details prevents an acceptable quality to be attained for the 100% of cells unless a very large cell count can be permitted.

Reflecting a satisfactory solution, the steady state results for C_L shown in Figure 4.12a match those of Peters et al. [98]. The presented plots include the results for the full blade geometry with the label "Present", the results for a version of the blade without the bolt at the base, labelled as "Present (clean)", the reference results provided by Peters [99] and the reference results for a flat plate from Riegels [100], additionally, the results for a transient solution at 6° are also included with the label "Transient". This transient solution case is computed from an initial condition in which the fluid flow is initialized to the free-stream wind speed at all locations; the reported results correspond to the stabilized solution past the initial transients in lift and drag coefficients. The numerical predictions are satisfactory for all angles of attack, with the exception of $\alpha = 6^\circ$ and $\alpha = 8^\circ$ which reveal a relatively small difference. The experimental solution, presented by Peters et al. [98] from the data in Riegels [100] keeps for most of the cases, the same proportion with respect to the present numerical results and, as explained by Peters et al. [98], the discrepancy might be due to the fact that the experimental study is performed on a 2-D wind tunnel set up whereas the numerical cases reproduce a 3-D scenario where the blade tip is freely exposed to the incoming flow. The transient solution for $\alpha = 6^\circ$ matches the steady state calculations despite underpredicting lift; however, the transient computation is acceptable considering that the flow conditions at this angle of attack might involve a degree of separated flow near the trailing edge, a permanent challenge in terms of accuracy for the implemented turbulence model.

From the sets of calculated coefficients, it can be observed that one of them is labeled as “Present (clean)” and it can also be observed that the difference is unnoticeable as far as the C_L values concern (see Figure 4.12a). Instead, it is by observing Figure 4.12b that a difference between both sets becomes evident: the simulation labeled “Present” shows a mostly sustained overprediction of C_D with respect to the reference data. Because the root assembly of the fan blade is not expected to contribute to lift, being constituted by an axisymmetric cylinder and two flat plates, a second set of simulations with a “clean” blade geometry is proposed; confirming the initial premise, the computed lift is not affected by this change while the computed drag gets closer to the reference for both steady and transient cases. The evident difference between experimental and numerical C_D might signal that the presence of drag due to lift in the 3-D case is responsible for the underestimation when compared to the experimental C_D .

4.6.2 Benchmarking of the FSI environment

A validation of the FSI solution environment has been done following the model set-up from [98, 99] and considering the experimental results published earlier by Basson [101]. The validation work presented here adopts three reference cases where the blade is fixed at a 9° angle while the inlet wind speed is set to 20.05 m/s, 15.033 m/s and 10.717 m/s respectively. An oscillation boundary condition is employed at the base of the blade, exciting the first flap-wise mode of the blade with an amplitude of 2 mm. The experimental work of Basson [101] consists of 50 instantaneous measurements of the blade tip displacement with the base excitation mechanism on; these measurements are random in nature, thus, an average value for each simulation case is computed and used as the reference for comparison with the experimental results. The time history of the numerical blade tip displacement is shown in Figure 4.13 spanning approximately four oscillation cycles at constant amplitude and excluding the initial transients for each data set, these are labeled “Numerical”. In addition to the instantaneous tip displacement, the average is also presented under the label “Ave. Numerical”, and compared directly to the average of the experimental data reported by Basson [101] under the label “Ave. (Basson 2015)”. Before looking into the results, it is worth mentioning that the experimental measurements reported in literature are not obtained as a time history of the tip displacement; instead, the data is collected as a series of 50 random measurements and, for this reason, the present analysis proposes a comparison between the average values.

The first case, corresponding to the simulation with an inlet wind speed of 20.05 m/s, is presented in Figure 4.13a and shows that the average numerical tip displacement closely matches the experimental data. The average experimental values are enclosed within the amplitude of the oscillation whereas the numerical prediction average deviates from the experimental value by 5.6%. The remaining two cases are also simulated at a 9° angle also and the same oscillation applied to the base of the blade. As observed in Figures 4.13b and 4.13c, the average numerical tip displacement is relatively close to the average experimental value, with relative error measurements of 11.2% at 15.03 m/s and 13.2% at 10.72 m/s.

The validation exercise for the FSI interface has resulted in a satisfactory outcome because the relative error for the analyzed cases is small. However, there is a clear increase in the relative error when the inlet wind speed is reduced from 20 m/s to

10 m/s. It is important to recall that the current simulations are performed on a modestly sized fluid mesh, of about 1.5 million cells and the modeling of turbulence is performed with the $k-\omega$ SST model with $y^+ \geq 30$ for all the wall adjacent nodes. Additionally, from the computational analysis performed by Peters [99] and Peters et al. [98] it is clear that the blade deformation is highly dependent on the excitation frequency in the vicinity of the first flap-wise eigenfrequency. The presented simulations assume an excitation frequency of 11.2 Hz as an approximation of the frequency for peak motion transmissibility but, the simulation of the whole frequency range was omitted due to computing time constraints.

There is a correlation between inlet wind speed and the error for the average tip displacement indicating that a higher free-stream wind speed results in more accurate predictions of the average tip displacement. There is at least two reasons that can be thought of as responsible for this behavior, the first of them is the Reynolds number, because the change in wind speed from 10 m/s to 20 m/s implies a change in the Reynolds number by one order of magnitude, considering air at standard conditions and a blade chord of 0.12 m. The smaller wind speed of 10 m/s results in $Re = 8.2 \times 10^4$, a scenario which might be less affected by turbulent boundary layer and more affected by early separation due to the thin plate geometry of the blade and the small Reynolds; if this is the case for the experiment, then the numerical prediction, based on the assumption of fully turbulent flow might not be as appropriate as for the cases with higher wind speeds, where the assumption of fully turbulent flow is closer to the reality. The second and perhaps most likely reason for the observed correlation between error and inlet wind speed is still related to the flow separation phenomena, because the observed angle of attack at a given section of the fan blade is the result of the combination of two perceived components of velocity: the inlet flow velocity and the relative vertical velocity due to the oscillatory displacement. The geometrical relationship between the inlet and vertical velocities dictates that the angle of attack for a given blade section should be larger when the inlet wind speed is smaller, this could be understood by imagining that for a smaller horizontal velocity, the resultant wind velocity should be more inclined with respect to the horizon line that coincides with the blade chord direction; therefore, a larger angle of attack can be expected. The current assumptions on the turbulence modelling added to the thin plate and sharp leading edge geometry of the fan blade, can result in poor predictions for the portion of flow that becomes detached from the suction surface of the blade, which in this case alternates between both sides as the blade vibrates due to the base excitation.

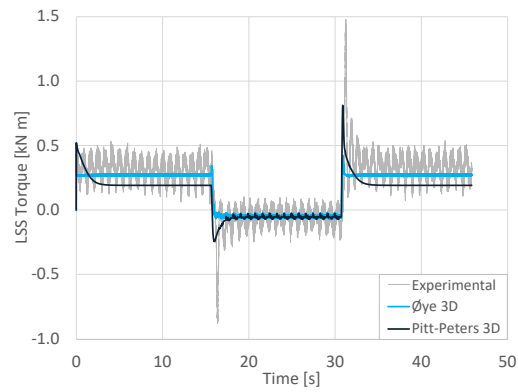
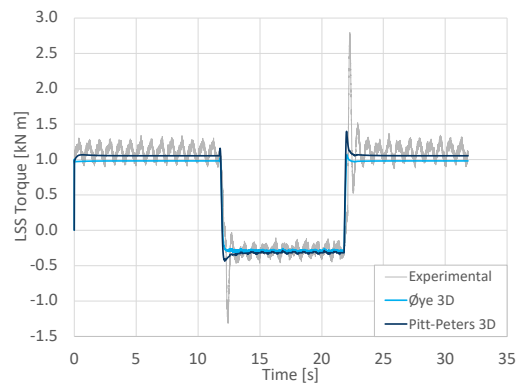
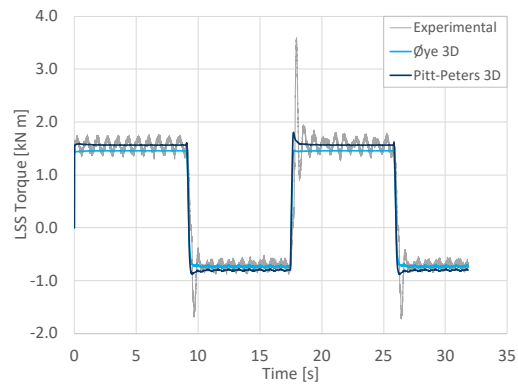
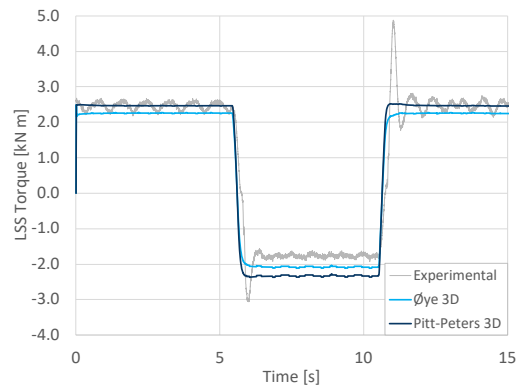
(a) $V_\infty = 5 \text{ m/s}$.(b) $V_\infty = 8 \text{ m/s}$.(c) $V_\infty = 10 \text{ m/s}$.(d) $V_\infty = 15 \text{ m/s}$.

Figure 4.3: Torque predictions with the dynamic BEM model.

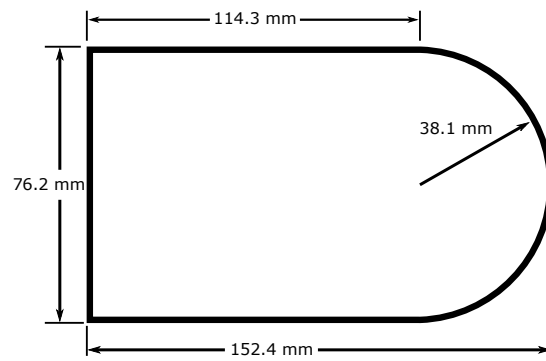


Figure 4.4: D-spar cross-sectional geometry.

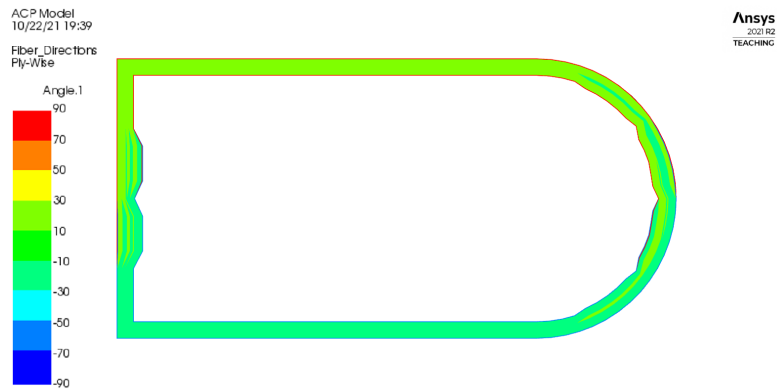


Figure 4.5: Laminate orientation layout.

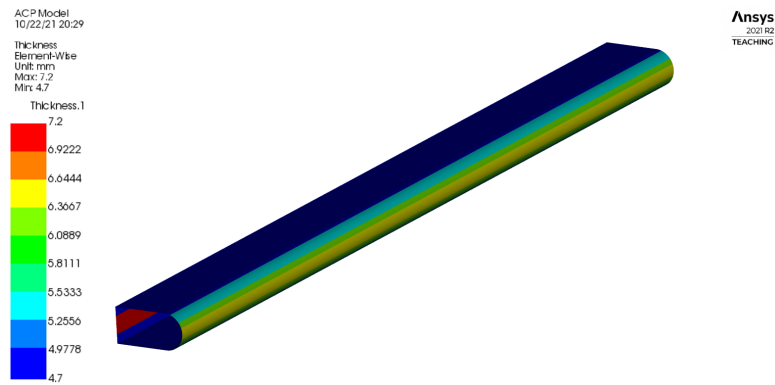


Figure 4.6: Laminate thickness contours.

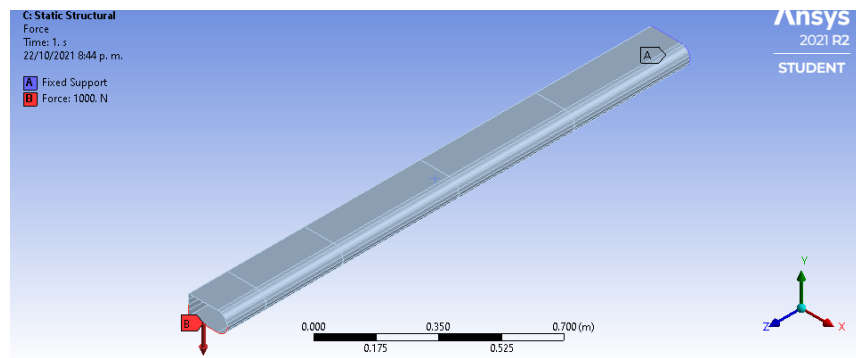
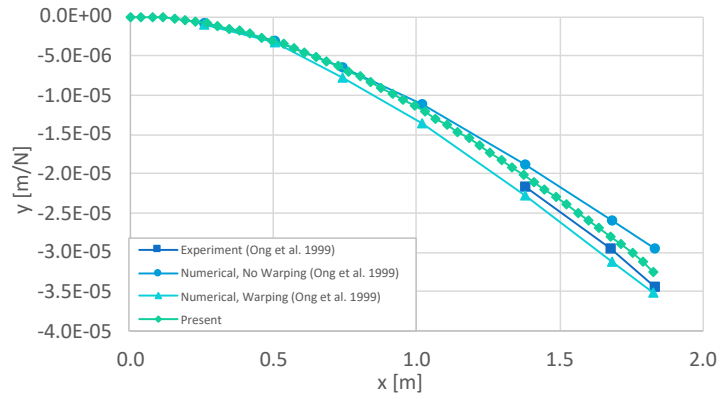
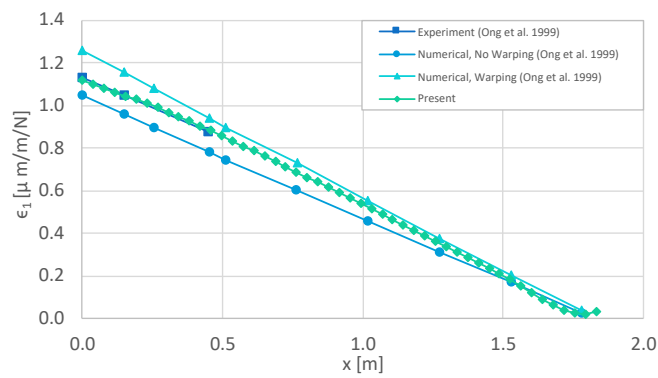


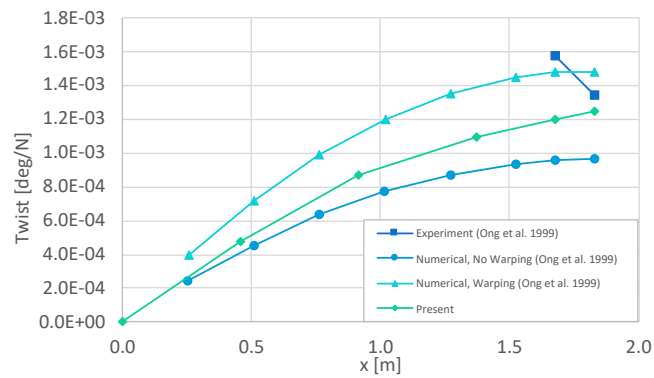
Figure 4.7: Domain topology and boundary conditions.



(a) Static deflection in the vertical direction.



(b) Longitudinal strain.



(c) Twist distribution.

Figure 4.8: D-spar analysis results.

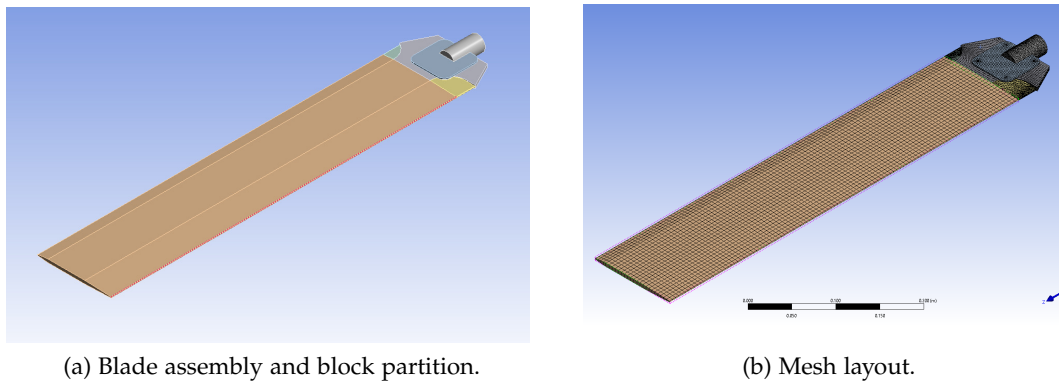


Figure 4.9: Blade structural model geometry.

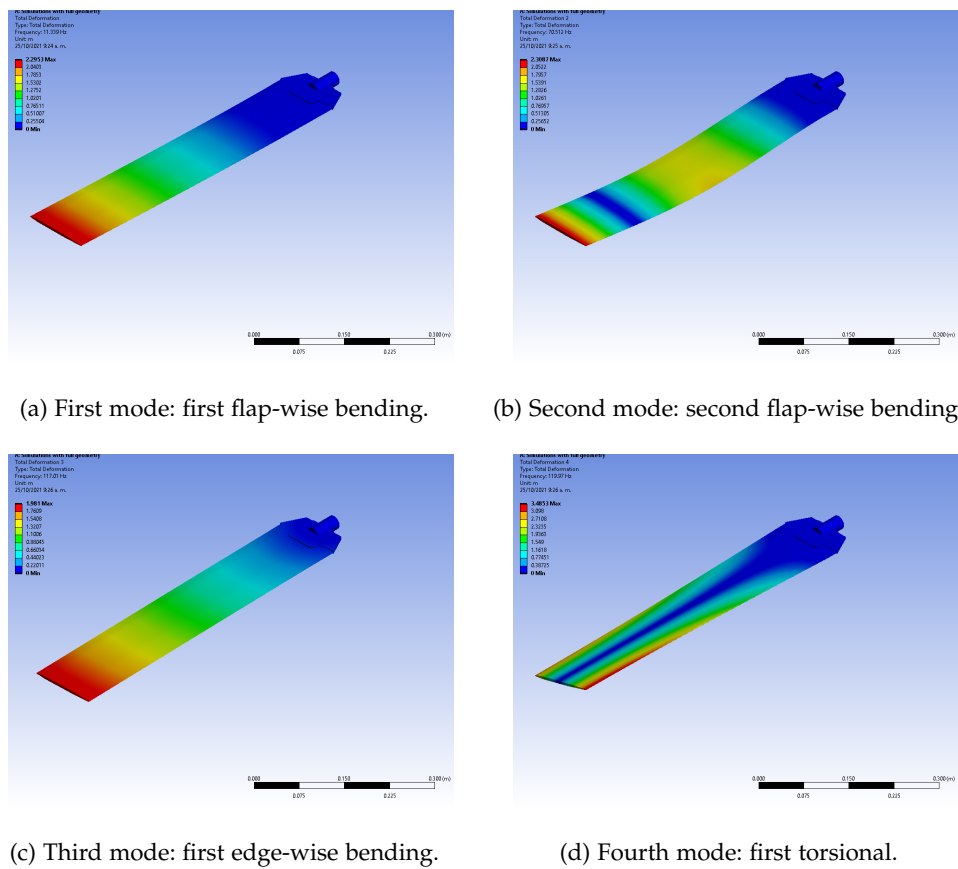
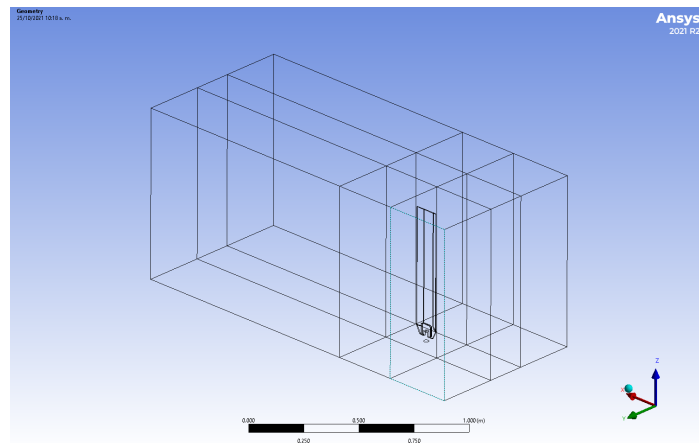
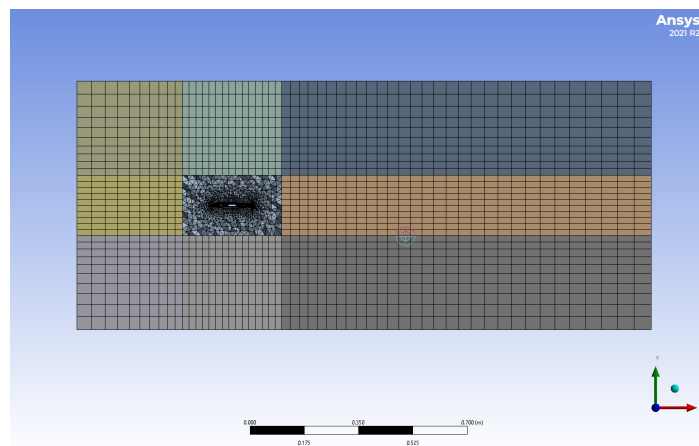


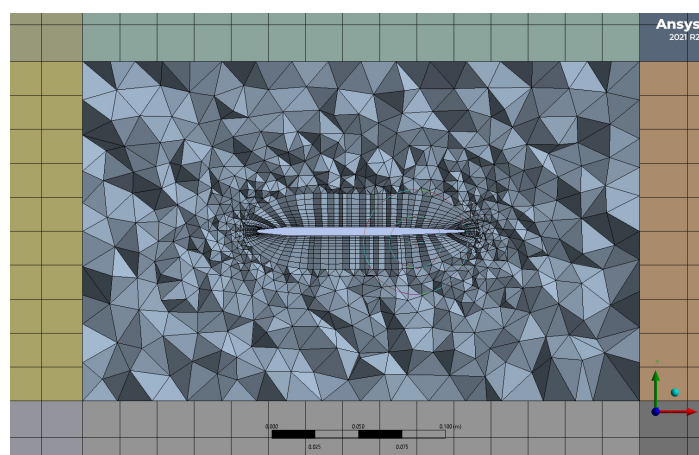
Figure 4.10: Modal analysis results.



(a) Overview of the simulation domain.



(b) View of the general mesh layout.



(c) View of the mesh around the blade and the near wall region.

Figure 4.11: Fluid simulation domain and mesh.

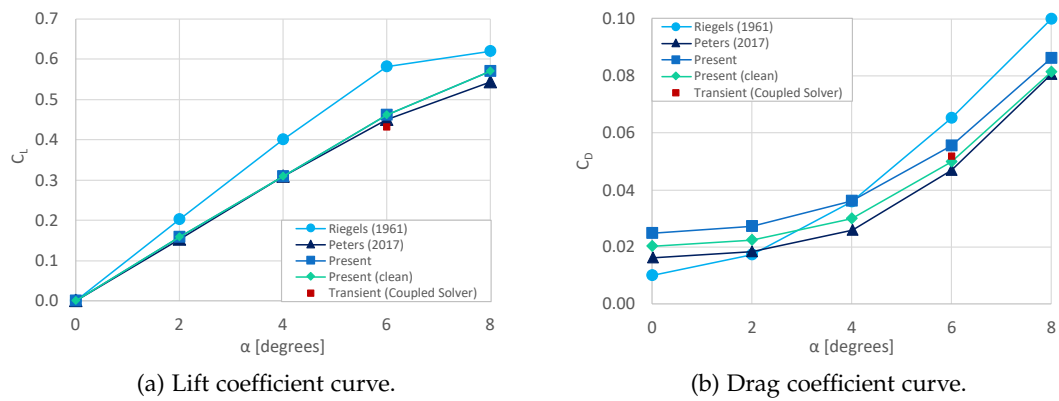


Figure 4.12: Aerodynamic force validation for the reference case.

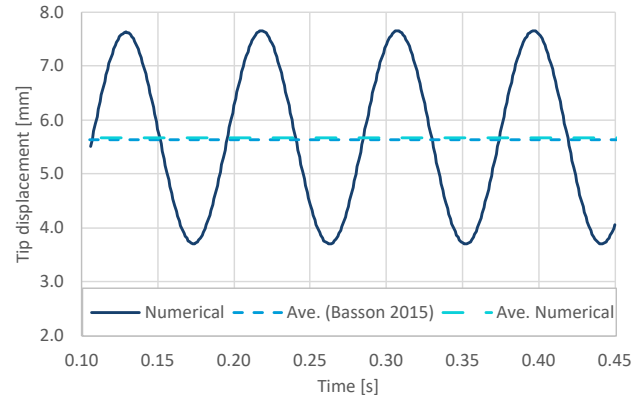
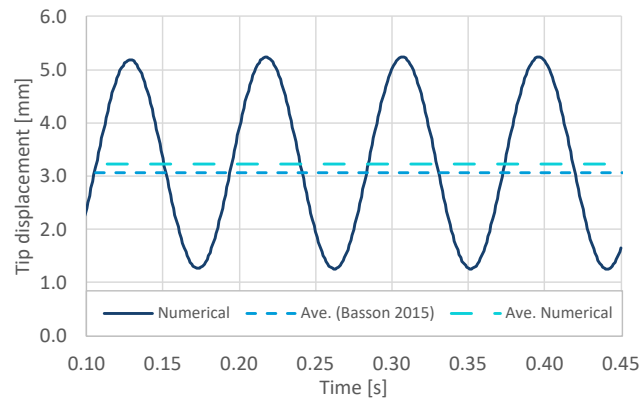
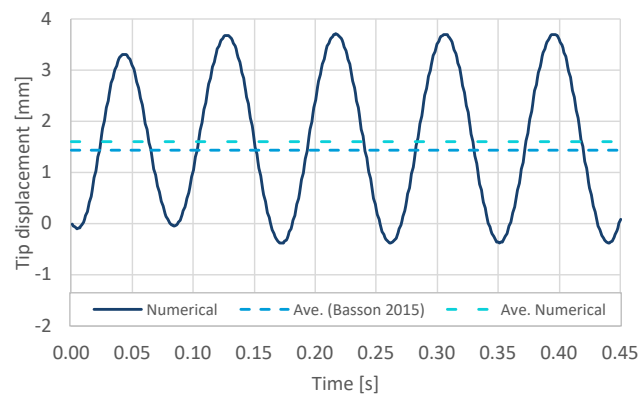
(a) $V_\infty = 20 \text{ m/s}$.(b) $V_\infty = 15.03 \text{ m/s}$.(c) $V_\infty = 10.72 \text{ m/s}$.

Figure 4.13: Blade tip displacement prediction under base excitation conditions.

5

REFERENCE FE MODEL FOR THE NREL PHASE VI BLADE

Constructing a numerical model for the [NREL](#) Phase VI turbine blade has become a necessity for the execution of the present work for purposes of verification of the numerical solution and for having a baseline case in the analyses of subsequent chapters. The first step consists in the definition of a suitable blade geometry, representative of the aerodynamic properties of the real blade: given in terms of the 2-D section coefficients and also in terms of the finite-volume turbulence model configuration. Such tasks have been included in Chapter 4. This chapter documents the second step for constructing the numerical model: the definition of a structural representation of the blade while ensuring, to the extent of possible, equivalent structural properties with respect to the experimental blade by using an adequate specification of the blade geometry, adopting adequate mechanical properties for the constituent materials and determining a logical layup sequence for the composite laminate.

NOMENCLATURE

θ	Ply fiber angle
E_x	Elastic modulus in the primary direction
E_y	Elastic modulus in the secondary direction
E_z	Elastic modulus in the out-of-plane direction
G_{xy}	In-plane shear modulus
G_{zx}, G_{yz}	Out-of-plane shear moduli
ν_{xy}	In-plane Poisson ratio
ν_{xz}, ν_{yz}	Out-of-plane Poisson ratios

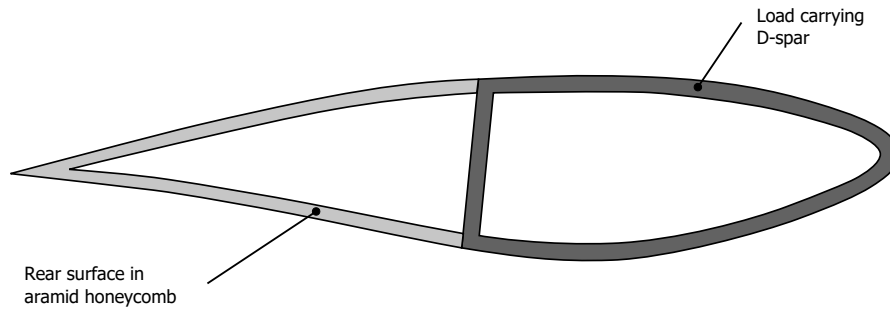


Figure 5.1: Structural concept of the NREL Phase VI experimental rotor blade.

5.1 THE NREL PHASE VI BLADE

As described by the report of Hand et al. [1], the [UAE Phase VI](#) is performed on a two bladed wind turbine. Different blade tip attachments are considered depending on the measurement campaign. The results of interest to the present work correspond to a blade with the standard tip and with a tip radius of 5.029 m. From a total rotor mass of 577.3 kg, the set of two blades amounts to approximately 120.4 kg, or 60.2 kg each. The center of gravity for each blade is located at 2.266 m, measured from the center of rotation.

The load-carrying member of the blade structure is a D-spar, formed by a shear web at 40% of the chord length and the remaining leading edge section. This part is manufactured with unidirectional carbon with $\pm 45^\circ$ interwoven glass fibers. The rear section of the experimental blade is formed by two aramid honeycomb panels, that merge at the trailing edge. A drawing of a representative blade section is shown in [Figure 5.1](#).

Since the present work explores the potential for a blade with bend-twist coupling with the same geometry as the [NREL Phase VI](#) blade, any change in performance should be compared against the original blade as a reference; hence the interest on defining a numerical model, analog to the experimental blade, including the original structural properties.

The machine description from the experimental set up in [1] gives no further detail on the composition of the blade structure (i.e. laminate lay-up and mechanical properties); therefore, by knowing the overall structural characteristics of the experimental blade, the following section covers the definition of a model with sufficient detail and equivalent structural properties.

5.2 DEFINITION OF AN EQUIVALENT STRUCTURAL MODEL

An estimation of the structural properties at different stations along the blade of reference is published in the experiment description [1], including the distributions of mass and stiffness as a function of the blade length. As mentioned before, there is an interest in obtaining a laminate sequence with comparable structural properties, in terms of flap-wise bending stiffness, axial stiffness and mass distribution. A composite wind turbine blade can be designed in an infinity of material and laminate layup combinations; therefore, the present work does not pretend to match exactly the properties

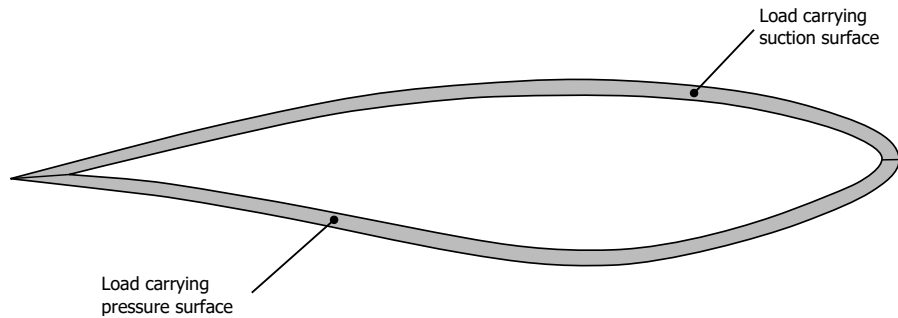


Figure 5.2: Structural concept of the proposed numerical model.

of the experimental subject; instead, an approximate structure is pursued as a mean to establish a reference for assessing the effect of coupled laminate materials.

Because the bend-twist coupling phenomenon manifests itself when the blade undergoes a flap-wise deformation due to aerodynamic loading, the first property of interest is the flap-wise stiffness distribution. The second property of interest is the mass, which should also resemble to the distribution in the experimental model, considering the relevance of rotor inertia for starting behavior characteristics at least. Finally the third relevant property is the distribution of axial stiffness, to ensure an adequate response to inertial loads from a safety point of view, because even though the present work is completely theoretical, it is still important to demonstrate the viability of a coupled blade structure while also maintaining the structural integrity of the blade and the turbine rotor as a whole.

A work with similar goals as the current task has been carried out by Chujutalli et al. [8]. They propose a set of laminate mechanical properties and layup sequence to obtain a 3-D equivalent numerical model of the NREL Phase VI blade. On a similar analysis, centered also on the entire turbine assembly, Lee et al. [102] develop a finite element model of the NREL Phase VI wind turbine and replicate the mass and axial stiffness distributions for the entire blade. Their approach involves a simplified assumption in which isotropic materials are considered, in a series of different cases, each one with a different level of fidelity with respect to the experimental model.

It must be pointed that the blade structure proposed by the present work differs from the structure of the experimental blade in the sense that only the outer skins are conceived as the load carrying members, resulting in the simpler structure shown in Figure 5.2.

This is justified by the emphasis of the present work on small wind turbines, for which simplified blade structures are often the rule, and aiming also to validate the feasibility of bend-twist coupling by modification of the composite laminates in the skins of the blade and no other components (i.e. shear webs).

A set of nine material properties required for defining an orthotropic lamina are listed in Table 5.1, these are representative of an unidirectional prep-reg carbon/epoxy lamina to be used as the basic constituent element of the blade composite structure. The present modeling of the blade structure uses shell elements, under the assumption of negligible out-of-plane deformations. For such cases, only the in-plane material constants are required but the present work adopts also the out-of-plane properties as a required input for a subsequent analysis on the structural properties across several blade stations.

Property	Magnitude
ρ [kg/m ³]	1621
E_x [GPa]	74.035
E_y [GPa]	9.376
E_z [GPa]	9.376
G_{xy} [GPa]	4.863
G_{yz} [GPa]	3.500
G_{xz} [GPa]	4.863
ν_{xy}	0.35
ν_{yz}	0.34
ν_{xz}	0.35

Table 5.1: Material properties for a 0.35 mm Carbon/Epoxy lamina, adopted from [8].

Following the typical thickness distribution of the skin of a wind turbine blade, the number of laminae must decrease towards the tip of the blade. Such decrease in blade skin thickness must be gradual; therefore, following the work of Chujutalli et al. [8], the definition of five segments along the blade span, in which a series of laminate drop-offs are placed according to the desired thickness and mass distributions is adopted. The upper limits for each one of the blade segments (S1 to S5) are given in Table 5.2 and are measured from the center of rotation. The laminate ply sequence is fairly similar to that of Chujutalli et al. [8] in terms of the proportion of plies in each segment, but the amount of plies and the orientation varies. For this work, the entire structure is constituted of carbon/epoxy, orientations other than 0° are considered and a higher number of plies per section is proposed. The laminates are separated into seven groups (G1 to G7), each one with a different amount of plies and laminate sequence as shown in Table 5.3. One of the critical aspects when defining the laminate sequences for each ply group is to avoid coupling from a macromechanical standpoint. This is verified by inspecting the terms in the stiffness matrices of resulting force and moment equations where the bend-twist coupling terms, D_{16} and D_{26} , must be zero. A computational implementation of the Classical Lamination Theory (CLT), is used to verify the coupling condition for the presented laminate sequences. For further detail the reader is referred to the book of Jones [103].

The disposition of the laminate groups as described by Table 5.3 is depicted in Figure 5.3. The drop-offs between adjacent laminate groups are specified in terms of the relation between laminate groups and blade segments, resulting in the expected reduction of blade mass towards the tip of the blade. An important characteristic of this layout is that the drop-offs between adjacent plies are not being considered.

A verification of the structural properties for the present numerical model of the NREL Phase VI blade, in which the load-carrying components are the aerodynamic surfaces alone, is performed using the software NuMAD [104]. The resulting mass, flap-wise and axial stiffness distributions are obtained and compared to the experimental properties of the real blade. The extraction of blade section properties is done with the

Blade Segment	r_{upper} [m]
S1	1.257
S2	2.012
S3	3.018
S4	4.023
S5	5.029

Table 5.2: Blade longitudinal segments.

Ply group	Ply count	Laminate sequence
G1	8	$[0^\circ / -45^\circ / 0^\circ / 45^\circ / -45^\circ / 0^\circ / 45^\circ / 0^\circ]$
G2	1	$[0^\circ / 0^\circ]$
G3	1	$[0^\circ / 0^\circ]$
G4	32	$[\pm 45^\circ / 0^\circ / 90^\circ / \mp 45^\circ / 0^\circ / 0^\circ / \mp 45^\circ / 0^\circ / 90^\circ / \pm 45^\circ / 0^\circ / 0^\circ]_s$
G5	1	$[0^\circ / 0^\circ]$
G6	1	$[0^\circ / 0^\circ]$
G7	8	$[0^\circ / -45^\circ / 0^\circ / 45^\circ / -45^\circ / 0^\circ / 45^\circ / 0^\circ]$

Table 5.3: Laminate layup sequences.

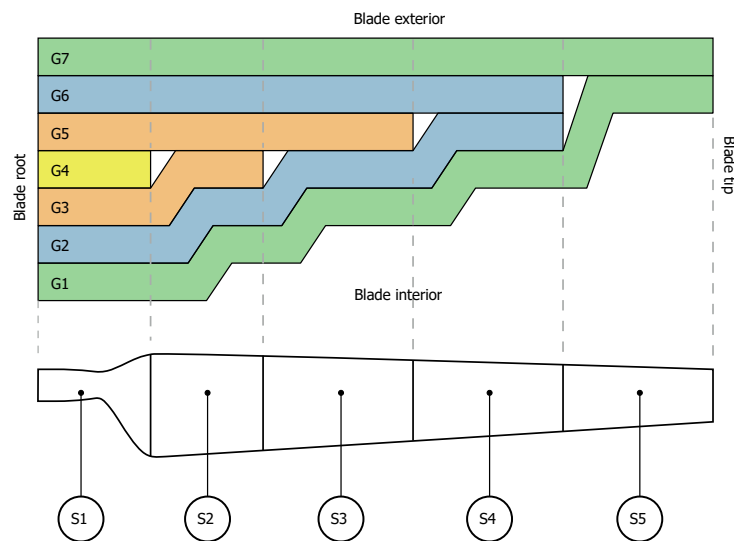


Figure 5.3: Blade laminate groups and relative positions for one blade shell.

Blade Property Extraction (BPE) application; further information on this methodology can be found in [105].

The mass distribution of the present blade corresponds purely to the mass of the composite materials for each blade surface; this must be emphasised because the experimental model has a series of extra elements adding to the total blade mass. Having no active role on the blade structure, this kind of elements are omitted from the present numerical model. A resulting distribution for cumulative mass, shown in Figure 5.4a, reveals a close match between the proposed blade model and the experimental one. The total mass is around 60 kg, as described for the experimental blade in the official documentation [1].

The distribution of flap-wise stiffness, seen in Figure 5.4b, shows a similar match between the proposed and experimental blade models for most of the blade length except for the root sections. The material of the proposed model may be thicker at these location than in the real blade. This discrepancy is rather unavoidable, recalling that the official experiment description provides little detail on the blade manufacture. The flap-wise stiffness for mid and outer blade sections is close enough to the desired values which is good, since the flap-wise deformations that will eventually exert a coupled twist, occur because of the deflection of the outer sections.

When observing the resulting distribution for axial stiffness in Figure 5.4c, an over-estimation of the experimental axial stiffness along the entire blade span can be easily identified; however, this situation is not expected to compromise the validity of the proposed model, since the torsional deformation response of a bend-twist coupled structure is not as affected by an axial deformation as it is by a bending deformation in the flap-wise direction. The discrepancy though, is not surprising, given the departures of the present model from the experimental and the numerical reference in [8], for example, the proposed blade increases the chord-wise extension of the structural elements, replacing the load carrying D-spar that spans only 40% of the chord length, with a pair of load carrying aerodynamic surfaces, comprising the entire blade section or 100% of the chord length. Additionally, the present design also extends the use of carbon/epoxy to the whole structure, following the changes in the structural elements.

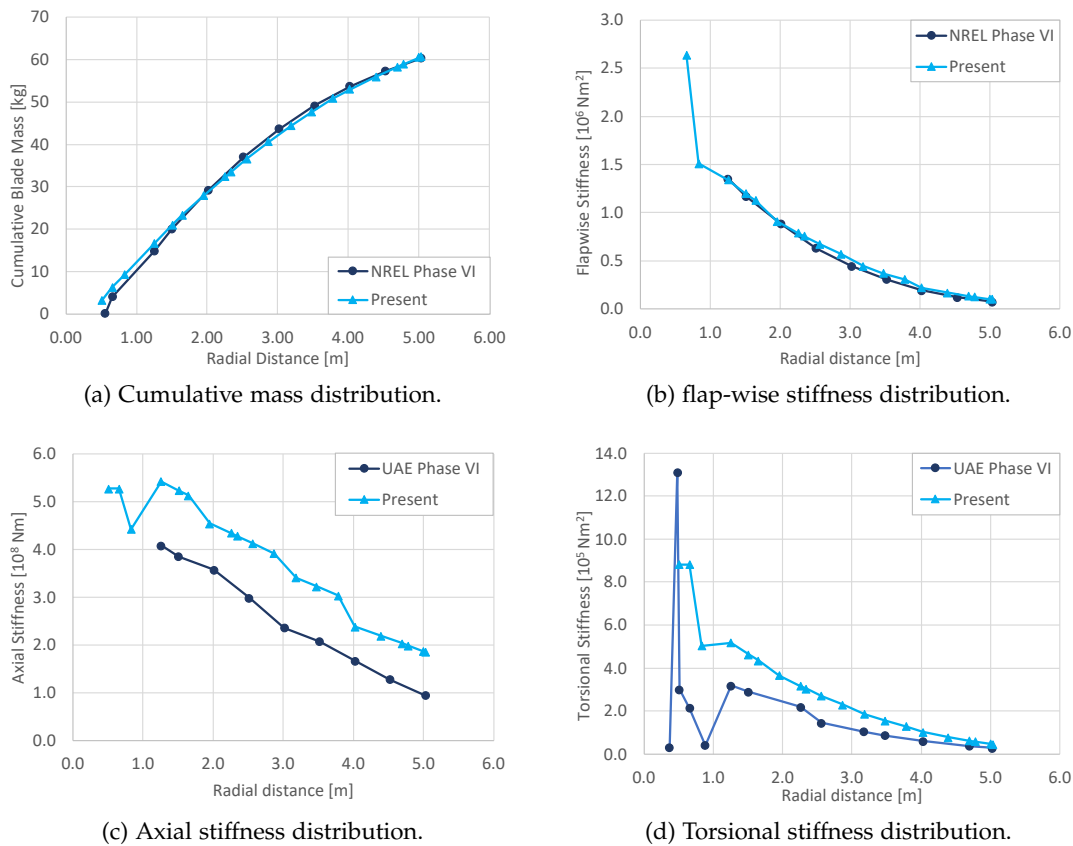


Figure 5.4: Structural properties for the baseline blade.

In summary, the resulting blade is composed by a stiffer material, on a greater extent of the blade section and therefore a higher axial stiffness is obtained.

5.3 WIND TURBINE CONTROL WITH BEND-TWIST COUPLING

Using the blade geometry from the [NREL Phase VI](#) rotor and an approximate structure as a reference, this section introduces an aeroelastically tailored counterpart. Since the matrix-reinforcement is kept the same as in [Chapter 5](#), the mechanical properties for a single lamina remain the same as well. The general layout of the chapter consists of a description of the preliminary sensitivity analysis, the proposal for a laminate with bend-twist coupling in replacement of the reference structure and the verification of the structural properties for the new coupled blade.

5.3.1 *Maximum torsion from bend-twist coupling*

It is known from the findings of the literature review in [Chapter 2](#) that bend-twist coupling can be attained by different means, i.e. induced by the layup fiber orientation, by using a swept blade planform geometry or by taking advantage of the aerodynamic moment. The first of the mentioned options is explored here initially to define a fiber orientation that maximizes the expected effect of the bend-twist coupling.

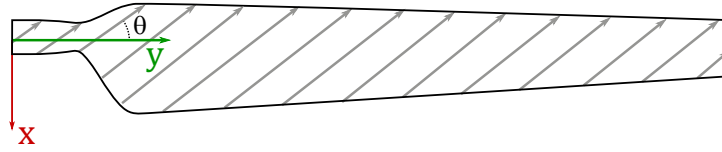


Figure 5.5: Off-axis fiber orientation for the tailored blade

Ply group	Ply count	Laminate sequence
G1	8	$[0^\circ/\theta/0^\circ/\theta/\theta/0^\circ/\theta/0^\circ]$
G2	1	$[0^\circ]$
G3	1	$[0^\circ]$
G4	32	$[\pm 45^\circ/0^\circ/90^\circ/\mp 45^\circ/0^\circ/0^\circ/\mp 45^\circ/0^\circ/90^\circ/\pm 45^\circ/0^\circ/0^\circ]_s$
G5	1	$[0^\circ]$
G6	1	$[0^\circ]$
G7	8	$[0^\circ/\theta/0^\circ/\theta/\theta/0^\circ/\theta/0^\circ]$

Table 5.4: Laminate layup sequence for the sensitivity analysis model.

Accordinging also to the findings of the literature review, a pitching actuation towards the feather position throughout the blade length is the preferred scenario. When a wind turbine blade rotates towards the feather position, the angle of attack along the blade span is decreased, in consequence the aerodynamic behavior of the blade cross sections leans towards a linear and more stable regime from the point of view of the lift coefficient. In order to obtain the required nose-down rotation at each section, the general arrangement of the off-axis fibers must be as shown in Figure 5.5, bearing in mind that the laminates of the suction side must mirror those of the pressure side. This requires that, for a coordinate system consistently oriented outwards for all blade surfaces, the off-axis fiber orientation of the suction side must have the same magnitude but opposite sign as that of the pressure side.

Using a simplified version of the blade structure from chapter 5 in a series of 1-way FSI simulations and taking the off-axis fiber orientation, θ , as a free parameter, a sensitivity analysis of the blade tip rotation is assembled; in this analysis, the 45° fibers were replaced by off-axis fibers in all laminates except for the group G4 (see Table 5.6). The results are shown in Figure 5.6 and indicate clearly that the maximum tip rotation occurs when the off-axis fibers are oriented at 20° with respect to the longitudinal axis. This finding is subject to a set of basic assumptions that are held throughout the subsequent analyses: the blade structure consists only of the suction and pressure side skins, known as shells, the joint of both shells is assumed ideal despite representing a discontinuity in the orientation of the off-axis plies, the blade is fixed at the root and, rotations and displacements are retrieved at virtual locations at the center of each section.

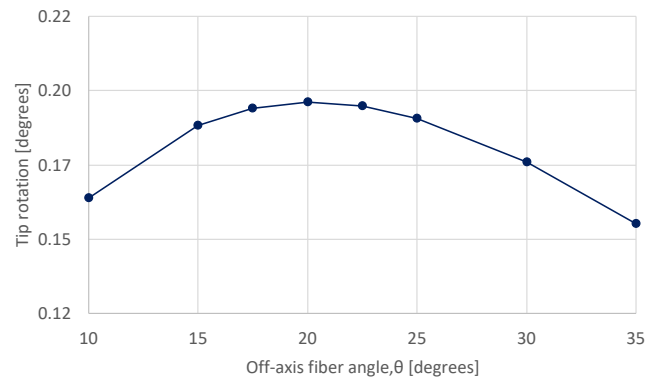


Figure 5.6: Sensitivity analysis for the blade tip rotation.

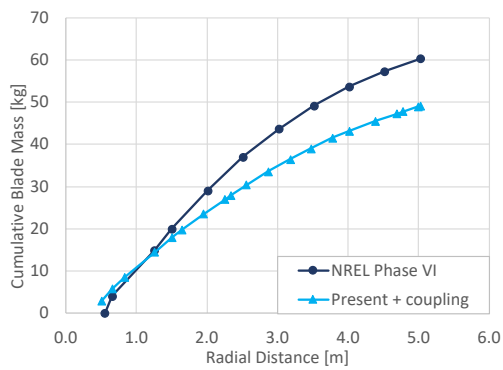
Ply group	Ply count	Laminate sequence
G1	6	$[\theta/0^\circ/\theta/\theta/0^\circ/\theta]$
G2	1	$[\theta]$
G3	1	$[\theta]$
G4	32	$[\theta_2/0^\circ/90^\circ/\theta_6/0^\circ/90^\circ/\theta_4]_s$
G5	1	$[\theta]$
G6	1	$[\theta]$
G7	6	$[\theta/0^\circ/\theta/\theta/0^\circ/\theta]$

Table 5.5: Laminate layup sequences for a blade with bend-twist coupling.

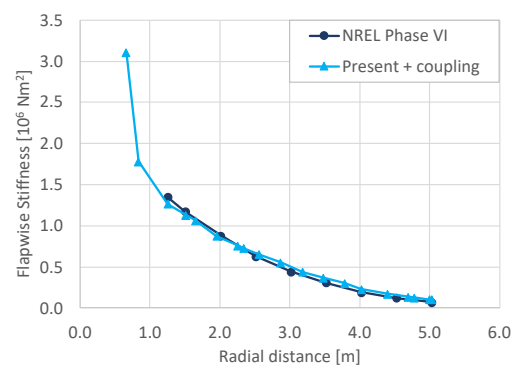
5.3.2 Blade model with bend-twist coupling

The second and final laminate sequence is described in Table 5.5 and has three important changes with respect to the sequence used for the sensitivity analysis: the ply orientation for bend-twist coupling is extended to the laminates in group G4, the plies at 0° in groups G2, G3, G5 and G6 are changed to off-axis plies, and two plies at 0° are removed from laminate groups G1 and G7. The first of these changes aims to increase the overall blade rotation by enabling the effect to take place throughout the entire laminate thickness, whereas both the second and third changes, are done to increase the proportion of off-axis plies in the whole laminate considering the findings of Hayat and Ha [2] relating the effects of ply proportion and the amount of coupling that can be achieved.

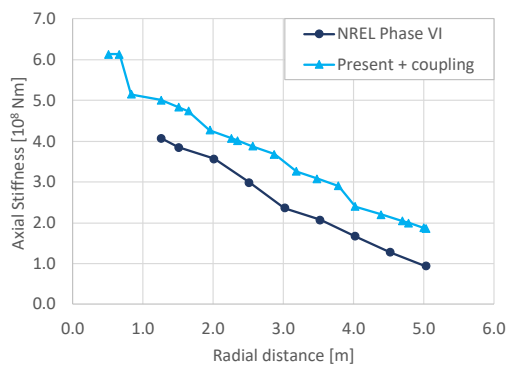
A similar procedure to the one in Chapter 5 is performed on the blade with bend-twist coupling to determine the lengthwise distribution of relevant mechanical properties and to determine in a preliminary form, the rotational response of the final blade structure. From the set of relevant properties, most of them remain close to the properties of the NREL Phase VI experimental blade or to the properties of the baseline structural design presented in the previous chapter. The cumulative mass distribution in Figure 5.7a shows a lighter blade by approximately 11.6 kg, mainly due to the reduction in 0° plies with respect to the reference blade. The flap-wise bending stiffness



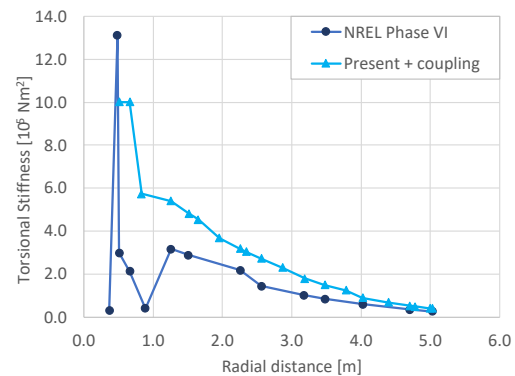
(a) Cumulative mass distribution.



(b) flap-wise bending stiffness distribution.



(c) Axial stiffness distribution.



(d) Torsional stiffness distribution.

Figure 5.7: Structural properties for the blade with coupling.

(Figure 5.7b) is significantly closer to the reference properties in comparison to the other results and this is precisely one of the key points from the present task, considering that the desired blade rotation is occurring from a bending displacement in the flap-wise direction. The results for axial and torsional stiffness in Figures 5.7c and 5.7d reveal a stiffer blade design with respect to the experimental blade but fairly close to the mechanical properties of the baseline design.

6

RESULTS

This chapter presents an overview of the simulation frameworks and results for the fluid-structure interaction analyses, considering the blade designs presented in Section 5 and following the simulation plan outlined next.

6.1 SIMULATION CASES

This Section introduces the proposed simulation plan for assessing the wind turbine blade with bend-twist coupling. A general description of the mathematical model for the wind conditions along with the implementation in each one of the cases is included. Each case is accompanied by a justification of its relevance and a description on the software in which it is implemented.

6.1.1 *Preliminary selection based on wind models*

The cases of interest are listed in Table 6.1 and all of them, contemplate a transient wind input, except for the last one, which proposes the calculation of steady torque curves. The adopted cases from the International Electrotechnical Commission (IEC) 61400-2 Standard [106], known as “Design Load Cases” are considered along with the pertinent wind models, covering different operational scenarios that are relevant to the present research.

6.1.2 *Steady operation*

The steady operation cases correspond to the computation of rotor torque and power curves for a defined set of operating wind speeds between V_{in} and V_{out} . Because there is no need to assess the dynamic change in loads as the wind speed changes, this simulation case is performed as a series of steady-state calculations. Assuming a perfectly aligned flow facilitates the implementation of finite-volume computations in the Ansys® environment besides the implementation in the BEM environment. Since the operating envelope for wind speed is defined based on the already established structural considerations, the primary aim behind the implementation of this case is not to assess loading conditions, but rather to determine the torque and power production as an indicator in itself and an input for the computation of the AEP.

Description	IEC design load Case	Wind Model	Reference In IEC 61400-2	Framework
Steady operation	-	-	-	BEM/Ansys®
Normal operation	1.3	EOG ₅₀	Extreme operating gust	BEM
	1.5	Extreme Coherent Gust (ECG)	Extreme coherent gust	BEM
Extreme wind loading	5.1	EWM	Extreme wind model	BEM/Ansys®

Table 6.1: Simulation cases.

6.1.3 Extreme wind model (EWM)

By assuming a Class III small wind turbine, the reference wind speed V_{ref} , equivalent to 37.5 m/s is chosen for calculating the 50 and one year extreme wind speeds. The respective magnitudes are $V_{e50} = 52.5$ m/s and $V_{e1} = 39.4$ m/s. This work assumes the magnitude of the extreme wind models in IEC 61400-2 “Small wind turbines”, but disregards the influence of the vertical wind profile on the rotor loads by considering a perfectly uniform magnitude across the turbine swept area.

The computations with an extreme wind loading model aim to assess the response of rotor torque and blade root moment under an extreme wind speed for a recurrence period of 50 and one years and under steady conditions. The magnitude of the extreme wind speed is based on the reference wind speed, V_{ref} , defined according to the corresponding wind turbine class. The corresponding wind speeds, V_{e50} and V_{e1} , are computed according to:

$$\begin{aligned}
 V_{e50} &= 1.4V_{ref} \left(\frac{z}{z_{hub}} \right)^{0.11} \\
 V_{e1} &= 0.75V_{e50}
 \end{aligned} \tag{6.1}$$

6.2 ROBUST SIMULATION FRAMEWORK

The robust simulation framework is implemented in Ansys® System Coupling which is an interface that couples the Ansys® Fluent and Ansys® Mechanical APDL solvers, in the simulation of a two-way and non-linear problem. As usual, Ansys® Fluent performs the solution of the fluid flow field properties, using the FVM whereas Ansys® Mechanical APDL is assigned.

The fluid flow solver performs a pressure-based, transient solution of the RANS equations, considering the $k - \omega$ SST turbulence model. The domain and mesh for the fluid flow solution participant is shown in Figure 6.1. Given the number of blades of the

Mesh	Cell count	Torque [N m]
Coarse	4,929,538	359.52
Medium	7,602,176	339.37
Fine	8,729,681	338.71

Table 6.2: Aerodynamic torque results for three mesh refinement levels.

NREL Phase VI wind turbine, the fluid flow domain for the stand-alone CFD simulations and for the system coupling simulations is based on a geometry with a periodicity of 180° emulating a wind tunnel with a circular section and an equivalent area to that of the NASA Ames $80\text{ ft} \times 120\text{ ft}$ ($24.4\text{ m} \times 36.6\text{ m}$) wind tunnel. The transient solution is set on a moving, dynamic mesh domain with tetrahedral elements and an inflation layer around the wind turbine blade. The rest of the domain is meshed with hexahedral elements. The elements of the nacelle are omitted; instead, a free-slip wall is defined in the inner surface coinciding with the blade root and for the outer domain wall. A formal mesh independence analysis is not carried out due to time constraints; instead, a set of three cases is considered for the calculation of aerodynamic torque. The cases are run with an inlet wind speed of 7 m/s and an angular speed of 72 RPM shown in Table 6.2. The relative difference in integral torque between the coarse and Medium mesh is about 5.6% whereas the difference between the Medium and Fine meshes reduces to 0.2% but the computational time increases from 7 to 30 days. Assuming the 5.6% difference as acceptable, the 4.9 million mesh is used for the entire analysis.

The structural response is obtained from a transient solution of the FEM derived from the principle of virtual work and using the formulation for a layered composite shell element, outlined in Chapter 4. A general view of the structure domain and mesh is shown in Figure 6.2, the observed discretization has 3242 elements and 3266 nodes and is created by splitting the blade into 64 segments in the spanwise direction and 25 segments in the cordwise direction per side. The time dependent solution is based on the HHT- α scheme, with a time step size that is governed by the system coupling process. The numerical model of the blade structure is formed by shell elements, derived from the fluid-flow domain geometry. Taking advantage of the topology for each blade surface, a fully structured mesh is defined, using shell elements with orthotropic properties. The material properties are defined using the ACP Pre module in the workbench environment.

An overview of the blade local reference frame is given by Figure 6.3, which shows the turbine rotation axis (z), the freestream wind direction ($-z$) and the principal axes for blade torsion (y) and blade flap-wise deformation (z) and edge-wise displacement (x).

6.2.1 Stability considerations

The interaction between the blade structure and the aerodynamic loads due to the surrounding fluid flow constitute an aeroelastic interaction scenario which, under the right conditions, can result in several instabilities. In theory, three instabilities may arise when considering the interaction problem associated to a wind turbine blade

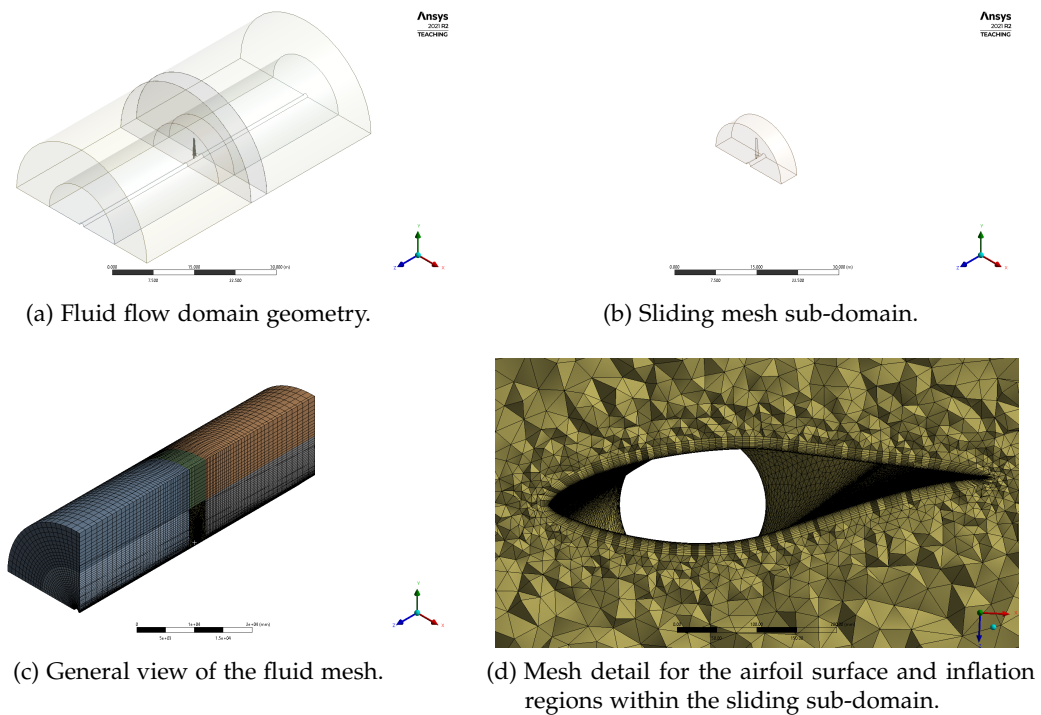


Figure 6.1: Fluid flow domain and mesh for the robust simulation framework.

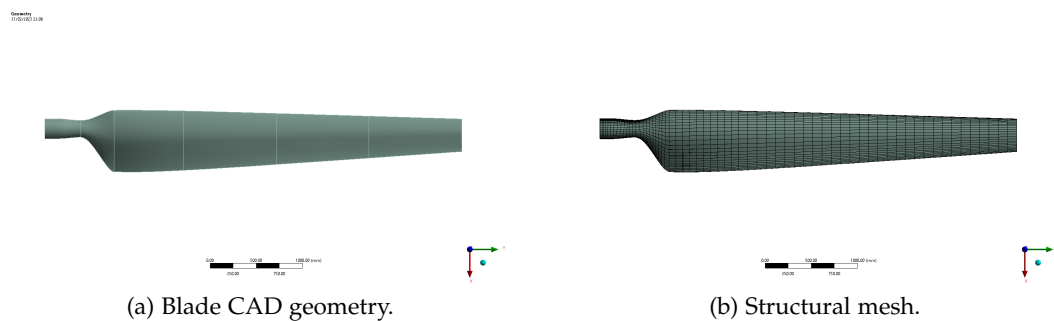


Figure 6.2: Structural domain and mesh for the robust simulation framework.

and to a wing in more general terms, these are: a) stall-induced flutter, b) classical flutter and c) divergence.

In general, flutter is a instability in which the flapping and torsion modes are coupled together in an oscillation that grows with time causing a sudden failure on the wing, it is caused by the interaction between the elastic oscillation of the blade and the deep-stall lift forces acting on the blade section. The analysis of stall-induced flutter is often challenging because it involves the non-linear aerodynamics of the stall flow regime; nevertheless, this problem has not been reported for wind turbine blades mentioned by Holierhoek [107] and Lobitz [14, 108].

The case of classical flutter is similar because it consists in a growing oscillation of the coupled flapping and torsion modes but is not associated to stall conditions; instead, as described by Holierhoek [107], it occurs at small angles of attack, high tip velocities, a relatively small torsional rigidity and a center of gravity located behind

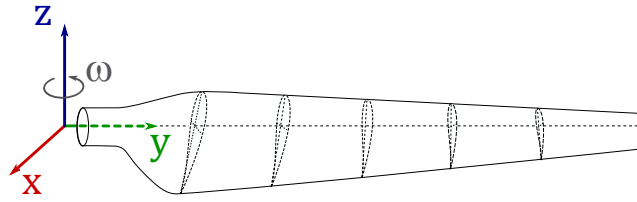


Figure 6.3: Blade coordinate axis orientation.

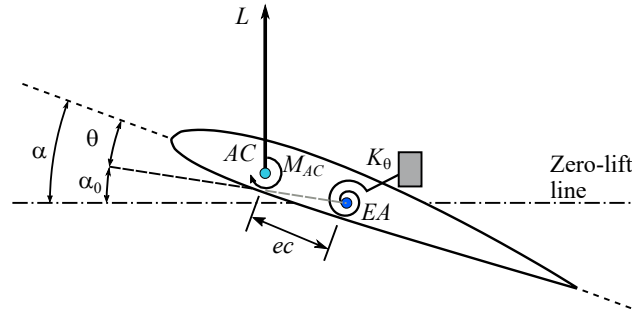


Figure 6.4: Simplified blade section.

the aerodynamic center. The analysis presented by Lobitz and Veers [9] explores aeroelastic instabilities on a wind turbine blade with bend twist coupling which can deform between -3° and 10° and concludes that for a small-sized wind turbine the angular speed for flutter is about six times greater than the operational speed of 72 RPM. Despite noting that an extreme amount of bend twist coupling can reduce the threshold rotational speed for flutter, it is pointed that smaller wind turbine blades tend to have higher stiffnesses and in consequence, are unaffected by stability problems of this kind. In fact Lobitz [108] and Holierhoek [107] converge in the notion that aeroelastic instabilities are a concern for wind turbine blades of increasing size. Lobitz [108] illustrates this point very well with the analysis of a 70 m diameter wind turbine for which the flutter rotational speed is above twice the operational speed and reduces 12% after including bend-twist coupling. From the analysis of a small wind turbine in Lobitz and Veers [9] flutter occurs at six times the operational speed whereas for a mid-sized wind turbine the flutter speed drops to twice the operational speed.

To explore the tendency of the present coupled blade to divergence, an idealized section is considered as depicted in Figure 6.4. Here the lift force L and the aerodynamic moment M_{AC} are applied at the point AC , located approximately at 25% of the chord length measured from the leading edge. The elastic axis is located at the point EA , located behind AC at a distance of approximately 20% of the chord length c which means that $e = 0.2$. the torsional spring stiffness is given by $K_\theta = GJ/L$. At an equilibrium condition, the angle of attack is α_0 and after a torsional deformation it becomes $\alpha = \alpha_0 + \theta$ with respect to the line for zero lift.

Assuming a torsional stiffness GJ of $1 \times 10^5 \text{ Nm}^2$ at a blade radius of 4 m and a blade length of 3.5 m, the resulting torsional spring stiffness is 28571.4 Nm/rad. Considering a representative blade chord of 0.45 m at $r = 4 \text{ m}$ the reference area is $S = 1.58 \text{ m}^2$. By defining positive moments in the clock-wise direction, the sum of all moments acting about EA can be written as:

$$\sum M_{EA} = [C_{L\alpha} (\alpha_0 + \theta) e + C_{M_{AC}}] cqS - K_\theta$$

where $C_{L\alpha}$ represents the C_l versus α curve slope, $C_{M_{AC}}$ is the aerodynamic moment coefficient around AC and q represents the dynamic pressure. The torsion angle θ for equilibrium conditions can be known by solving for $\sum M_{EA} = 0$ from which the following expression is obtained:

$$\theta = \frac{cqS [C_{L\alpha}\alpha_0 e + C_{M_{AC}}]}{K_\theta \left[1 - \frac{C_{L\alpha} ecqS}{K_\theta} \right]} \tag{6.2}$$

As can be observed, the torsion angle about EA can grow unbounded when the torsional stiffness approaches $K_\theta = C_{L\alpha} ecqS$. A stable condition for the torsional deformation can be defined according to $\partial M / \partial \theta \leq 0$ which means that for a small perturbation in the angle of torsion, the system reacts with a restoring moment of opposite sign. This condition results in:

$$1 - \frac{C_{L\alpha} ecqS}{K_\theta} \geq 0 \tag{6.3}$$

or in terms of the dynamic pressure q :

$$q \leq \frac{K_\theta}{C_{L\alpha} ecS} \tag{6.4}$$

Considering linear aerodynamics the lift curve slope is $C_{L\alpha} = 2\pi$. Finally, if a standard air density is assumed, the equation above indicates a flutter speed of 264 m/s. The present blade is operated at 72 RPM, therefore the maximum relative wind speed acting on the blade occurs at 25 m/s and has a magnitude of 39.2 m/s. This shows that torsional divergence is unlikely for the given conditions.

Displacement mapping procedure.

As explained in Chapter 3, the coupling method relies on the mapping procedure for a successful transfer of data between participant solutions; therefore the diagnostics for both transfers are discussed in this part of the work. The co-simulation procedure has a single interface that consists of the blade surface. This surface is identical for both solvers and is used for the transference of displacement and force between solutions. Displacement information is transferred from Mechanical APDL or Side 1 to Fluent or Side 2 and for both solvers, this data is stored at nodal locations. The mapping summary for the displacement transfer named as "Data Transfer" is shown in the Listing 6.1:

Listing 6.1: Mapping diagnostics for displacement data transfer.

+	-----		+
	MAPPING SUMMARY		
+	-----		+
		Source Target	

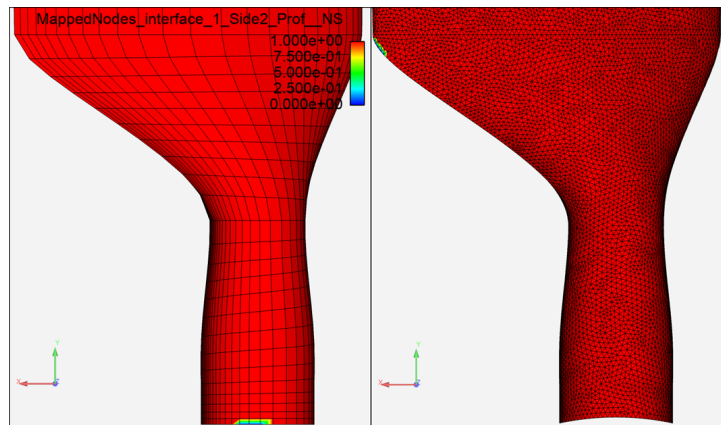


Figure 6.5: Mapping diagnostics for the transfer of displacements for Source (left) and Target (right) meshes.

+-----+-----+		
interface-1		
Data Transfer		
Mapped Area [%]	>99	100
Mapped Elements [%]	>99	100
Mapped Nodes [%]	>99	>99
Data Transfer 2		
Mapped Area [%]	100	>99
Mapped Elements [%]	100	>99
Mapped Nodes [%]	100	>99
+-----+-----+		

The relevant diagnostics for the mapping is that in terms of area, more than 99% of the source mesh is mapped whereas 100% of the target mesh area is successfully mapped. When it comes to the nodes, more than 99% of the source mesh nodes, corresponding to Mechanical APDL's mesh is successfully mapped to send data to the target mesh. From the target mesh in Fluent more than 99% of the nodes are mapped and receive data from the source mesh.

Figure 6.5 shows another perspective of the mapping diagnostics for displacement. For instance, on mechanical, the Source side, more than 99% of the nodes map to and send values to the target. Several nodes at the base of the blade are shown to be unmapped because the same region of the blade is removed from the Fluent mesh during the construction of the inner slip surface of the wind tunnel geometry. This could be solved by intersecting the structural geometry with the inner slip surface. On the target side, corresponding to Fluent, more than 99% of the nodes map to and receive values from the source. Some nodes appear unmapped in the transition region at the trailing edge, and this happens because the coarse mesh in the source cuts-off the rounded corner, and the source geometry appears truncated with respect to the much more refined mesh in the target side. The weighted average values shown in the Listing 6.2, are mutually similar for the source and target sides of the "Data transfer" mapping of incremental displacements between Mechanical APDL and Fluent.

Listing 6.2: Coupling results for the incremental displacement data transfer.

+=====+

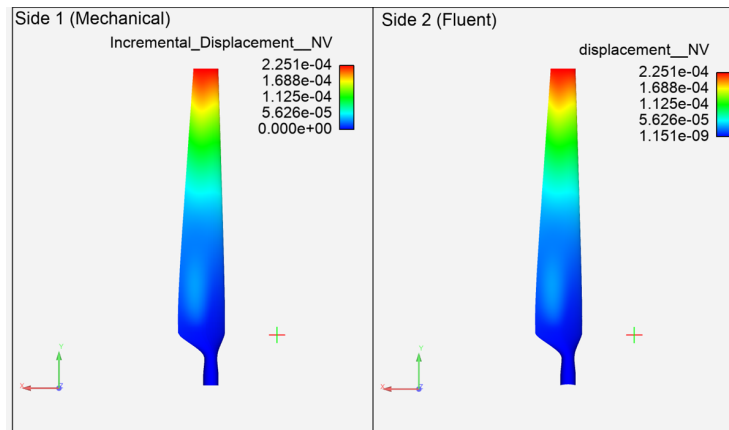


Figure 6.6: Contours for the transfer of displacement data.

COUPLING STEP = 1539		SIMULATION TIME = 5.66500E+00 [s]	
+-----+			
...			
+-----+			
COUPLING ITERATION = 3			
+-----+			
...			
fluid			
Interface: interface-1			
Data Transfer		Converged	
RMS Change		1.79E-03	1.99E-03
Weighted Average x		-2.39E-05	-2.39E-05
Weighted Average y		1.65E-06	1.65E-06
Weighted Average z		4.44E-05	4.44E-05
+-----+			

The displacement data transfer results in Figure 6.6, show that the transferred values near the root sections of the blade are small and approach to zero at the very bottom. Unmapped regions at both the source and target sides of the transfer are located at this area; therefore the effect of the missing nodal information during the transfer process is not relevant to the overall solution.

Force mapping procedure

Force data transfer takes place between Fluent at the Side 2 of the co-simulation and Mechanical APDL at the Side 1. In this case nodal information is no longer the sole concern as Fluent stores data at the Element locations instead of the nodes. In mechanical however, force is still stored at nodal locations. The mapping diagnostic for the transfer of force data under the name “Data Transfer 2” is included in the Listing 6.1, which shows that 100% of the area is mapped on fluent and more than 99% of the area is mapped on mechanical. The results indicate that 100% of the elements in the source mesh are successfully mapped whereas more than 99% of the elements in the target mesh are mapped. The successful mapping of node locations is similar, with 100% of the nodes in Fluent mapping to the target mesh and sending data to it and, more than

99% of the nodes in Mechanical being successfully mapped to the source mesh and receiving information from it.

The results from these diagnostic are now shown as a visualization in Figure 6.7, in which the left hand side shows some of the unmapped nodes in mechanical and the right hand side shows the fluent nodes being 100 % mapped. The Figure is centered around the root area because it is precisely at this location where unmapped nodes appear for the Side 1 solver of the cooperative simulation, and from comparing both geometries, the projected cylinder at the bottom of the Side 2 mesh is responsible for the unsuccessfully mapped nodes in mechanical. Such cylindrical projection is a feature of the Fluent mesh that corresponds to the intersection between the blade root and the slip wall surface in the fluid flow domain. This mismatch between geometries is minor, and is expected to barely affect the overall solution since at least the displacement of the neighboring nodes are limited by the applied fixed support boundary condition in the Mechanical side of the coupling.

The overall summary of the force data transfer at the last coupling iteration per time step is shown in the Listing 6.3 with the corresponding convergence indicators for the transfer procedure.

Listing 6.3: Coupling results for the force data transfer.

```

+=====+
| COUPLING STEP = 1539                               SIMULATION TIME = 5.66500E+00 [s] |
+-----+
|                               | Source      Target      |
| . . .                         |            |            |
+-----+
|                               |            |            |
|                               |            |            |
|                               |            |            |
|                               |            |            |
|                               |            |            |
|                               |            |            |
|                               |            |            |
|                               |            |            |
|                               |            |            |
|                               |            |            |
+-----+
| Transient Structural          |            |            |
| Interface: interface-1       |            |            |
| Data Transfer 2              |            |            |
| RMS Change                   | 3.93E-04  | 3.56E-04  |
| Sum x                        | 4.88E+01  | 4.88E+01  |
| Sum y                        | 3.01E+00  | 3.00E+00  |
| Sum z                        | 1.53E+02  | 1.53E+02  |
+-----+

```

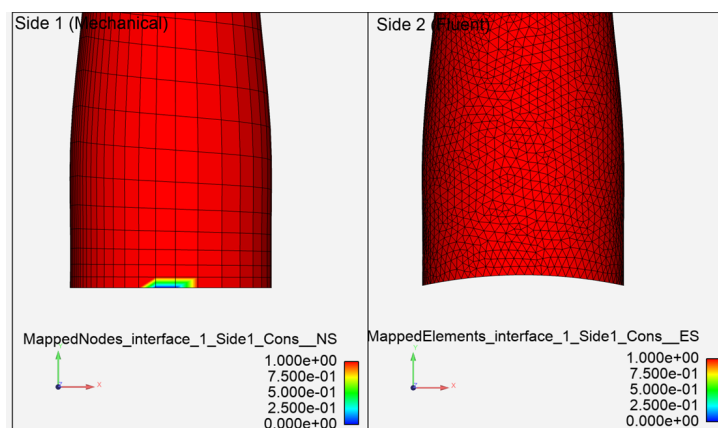


Figure 6.7: Mapping diagnostic for the transfer of forces.

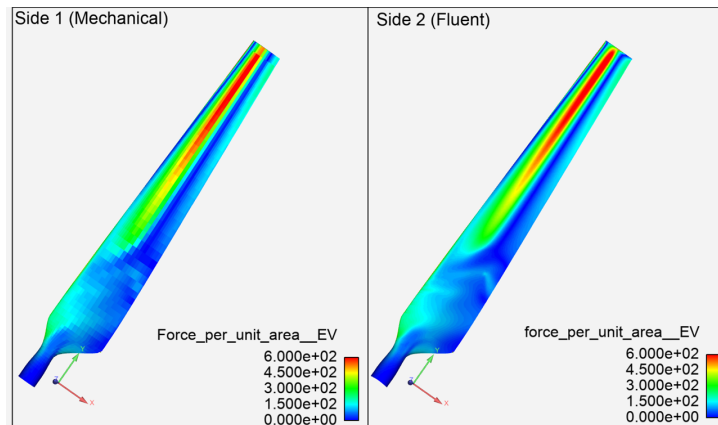


Figure 6.8: Resulting contours for the transfer of forces.

It shows that the rms residual values and the x , y and z sums for source and target sides of the force data transfer closely match one another. A visualization of the force transfer can be observed in Figure 6.8 where the data is presented in the form of force per unit area, to facilitate the comparison of the information between meshes with elements of different sizes. In general the profiles of the force in Side 2 seem to be preserved well on the contours for Side 1.

6.3 SIMPLIFIED SIMULATION FRAMEWORK

This framework considers a simplified aerodynamic solution based on the blade element momentum model with added models for stall delay and dynamic stall phenomena. The structural solution in this case is emulated from a 1-way steady state interaction analysis and, is capable to reproduce bend-twist coupling. The torsional deformation due to flap-wise bending is recorded as a function of blade radial position and wind speed; then, the local torsional deformation along the blade is interpolated inside the BEM model implementation.

Considering a wind speed range from 5 to 25 m/s an analysis with steady CFD and 1-Way FSI is carried out with the sole purpose of building a representation of the torsional deformation response as a function of wind speed and blade radial location. These results are used as an auxiliary computation to the main simplified framework analysis to be introduced subsequently. The data is shown as a series of plots in Figure 6.9 and revealing a maximum tip rotation of 0.44° at the maximum wind speed of 25%. In fact, the rotations at all locations appear to increase in direct proportion to the wind speed magnitude, indicating that drag forces associated to the high wind speed regimes for fixed-speed and fixed-pitch wind turbines play an important role on the overall bending deformation of the wind turbine blades. Similarly, this results show a favorable scenario in which the control action of pitching the blade towards feather can be executed at operation regimes in which stall onset and deep stall occur. The situation at smaller wind speeds shows that blade rotations are consistently smaller throughout the entire blade length. From a general perspective, the blade section rotation is linear with respect to the wind speed in the range between 5 and 15 m/s but for higher the wind speeds of 20 m/s and 25 m/s the respective rotations stop showing

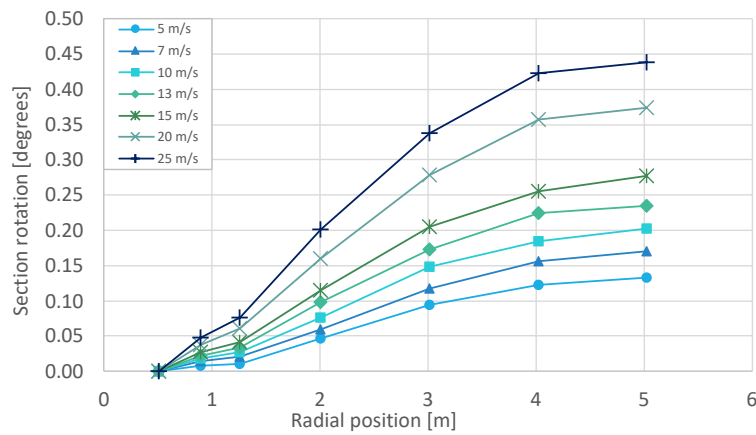
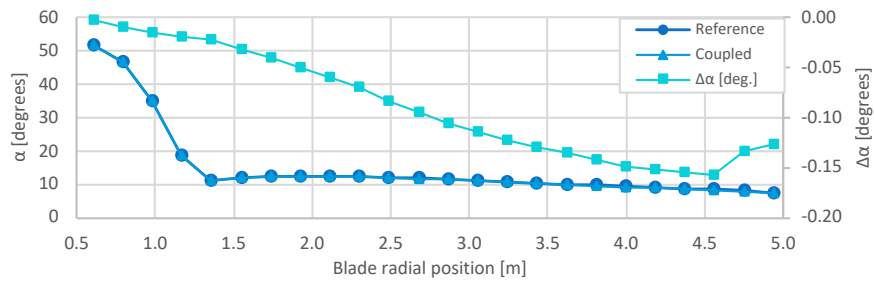


Figure 6.9: Blade section rotation from bend-twist coupling.

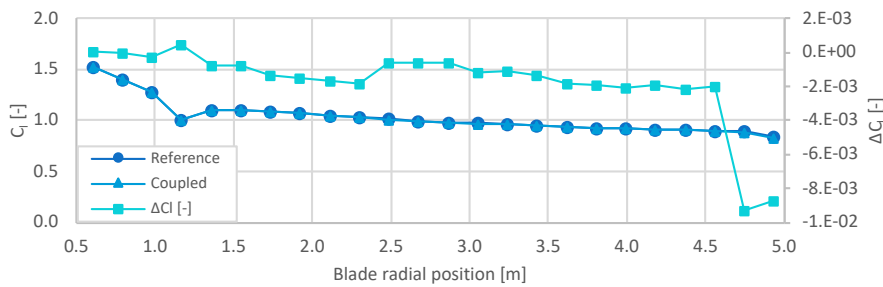
a clear proportionality with respect to wind speed, besides being notably higher in magnitude.

A more insightful view of the blade aerodynamic state as predicted with the BEM model is given by the results to the simulation case of steady operation from Table 6.1, particularly by checking the blade longitudinal distribution for the angle of attack (α) and the respective distributions of lift (C_l) and drag coefficients (C_d). This data is recovered from stabilized transient calculations using the same approach as for the torque curves of Chapter 4, this way, fully converged and stabilized aerodynamic coefficients are organized at 7, 10, 13 and 20 m/s and, providing also the comparison between the reference blade and the coupled blade. The results for the slowest wind speed, at 7 m/s are shown in Figure 6.10 and reveal that α , C_l and C_d have fairly smooth variations with blade length. Some of the noticeable features are the dip in C_l near the root of the blade, and the higher C_d also in the blade root region. The concurrence of blunt airfoil shapes due to the transition between the blade root and inboard sections and high angles of attack are the most likely causes for this variations. As a direct representation of the effect of bend-twist coupling over the blade aerodynamics, the change in angle of attack, $\Delta\alpha$, lift coefficient ΔC_l , and drag coefficient, ΔC_d , are presented along with the distributions of the base variables. First of all, a decrease in α is evident and also expected from the torsion towards feather that the coupling induces on the blade. Due to the small wind speed and according to the displacement profiles from Figure 6.9, the change in α remains small along the blade for the 7 m/s case, this in turn, results in C_l reductions of order 1×10^{-3} and C_d reductions of order 1×10^{-4} .

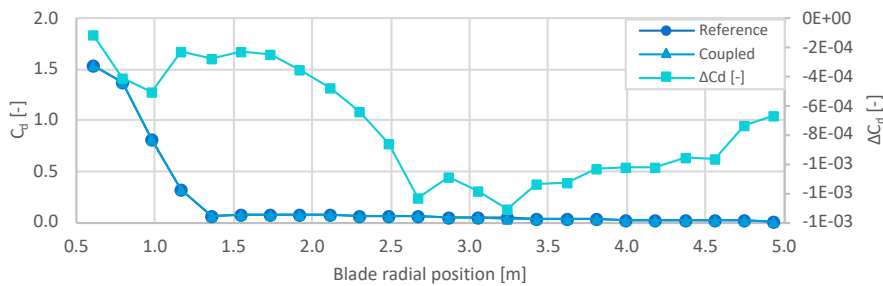
According to Figure 6.12, the change in α at 10 m/s is negative everywhere and decreases along the blade radial position. Both of these outcomes are expected, although, the decrease in α appears to have a small dip around the 4 m mark on the horizontal axis; an interesting feature since the respective changes in C_l and C_d appear to have peaks around the same blade sections where α has a dip. The general trend for the change in C_l shows a decrease in magnitude for most of the blade length, except for the blade stations between 3 m and 4.5 m, where the change in C_l is positive, meaning an increase in lift. The respective change in C_d is similar because it is uniformly negative for most of the blade length but still shows a region between 3 m and 3.5 m, where the drag decrease is one order of magnitude greater than for the rest of the blade lo-



(a) Angle of attack.



(b) Lift coefficient.



(c) Drag coefficient.

Figure 6.10: Aerodynamic coefficients at 7 m/s.

cations. As a possible explanation for the blade aerodynamics at 10 m/s it is worth observing that at the same location where the change in α has a slight dip, the nominal values for the angle of attack are between 10° and 20° ; therefore, it is likely that the bend-twist induced torsion is bringing the angle of attack at those locations out of the deep stall regime and into the stall on-set regime, where considerable increments in C_l tend to coincide with high C_d .

A look on the C_l vs α and C_d vs α curves in Figure 6.11 shows that the deep stall regime starts right before 20° ; it is just at this point where the C_l curve shows a change in slope, dividing the attached and fully separated flow regions. Lift coefficients appear to decrease after the maximum for α values between 15° and 20° ; a decrease in α below 20° should inevitably result in the observed increase in lift for the 10 m/s case. The C_d values show a change of slope right before 20° as well, and appear to have a very steep variation at this point; this might help in understanding why a small negative change in angle of attack could derive in the sudden decreases in drag that are observed in Figure 6.12.

Seeing the changes in α for a wind speed of 13 m/s one can identify the expected tendency by which the effect of bend-twist coupling is consistently stronger at greater wind speeds. At least for the torsion mechanism that is being proposed in this work, the flap-wise deflection is being driven by the axial force acting on the blade, and such force increases as a direct consequence of the increase in angle of attack, which now increases due to the change in the velocity triangle when free-stream wind speed increases while angular speed is kept fixed. There is value to this simple approach, because it is at the deep stall regimes, associated to small tip speed ratios, at which a torsion towards feather could improve the blade performance by reducing the angle of attack. In this scenario, the torsion by bend-twist coupling serves the purpose of mitigating the deep stall on the blade. However, the question on how much torsion can be attained remains open since the laminate sequence for the coupled blade has been defined with an ingredient of uncertainty on the exact ply sequence of the reference experimental blade, leaving room for optimization of the proposed design.

The changes in α for the 13 m/s case in Figure 6.13 show the same tendency to the previous cases at 7 and 10 m/s: there is a reduction in angle of attack, growing in magnitude with the blade radius and reaching a larger maximum with respect to the 10 m/s case, which is consistent with the trends discussed above. In contrast, the change in C_l shows an irregular profile because in two locations for $r > 3.5$ m the change in lift is positive. The change for C_d for example, follows a smooth variation and is smaller than -5×10^{-3} for most of the blade.

The results shown in Figure 6.14 show that at 20 m/s, the effect of bend-twist coupling is the strongest from all of the four cases explored in this section, the variation in α along the blade span follows the expected profile, which is similar to the profile in torsional displacement shown earlier in Figure 6.9. The distribution of α shows that almost all blade sections are operating between 30° and 50° except for the root region where α is naturally very high and for the last 0.5 m which are slightly below 30° . When observing again the C_l vs. α curve in Figure 6.11 one can see that the variation in C_l is smooth around 30° and beyond for the original 2-D coefficients and for the set of coefficients treated with the Lindenburg stall delay correction model; therefore, the observed increments in α which are smooth and continuous result in similarly smooth and continuous reductions in lift for most of the blade stations. Between 4 and 4.5 m there is a sudden drop in C_l that takes place at the same point at which the distribution

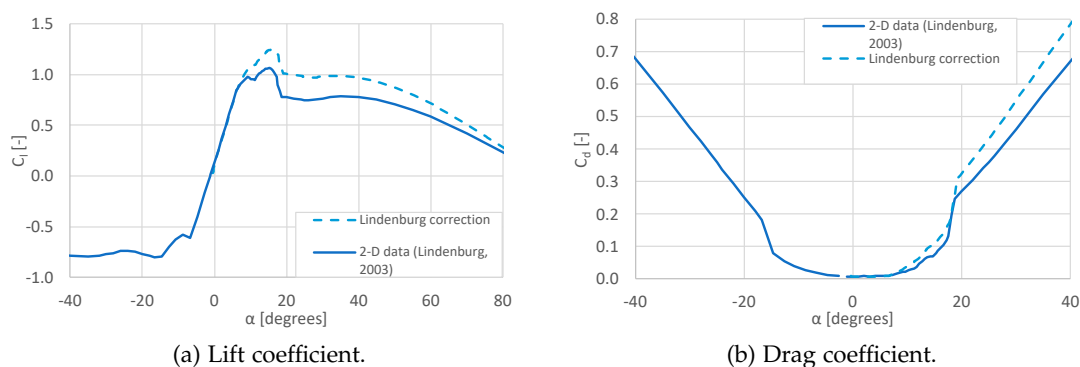
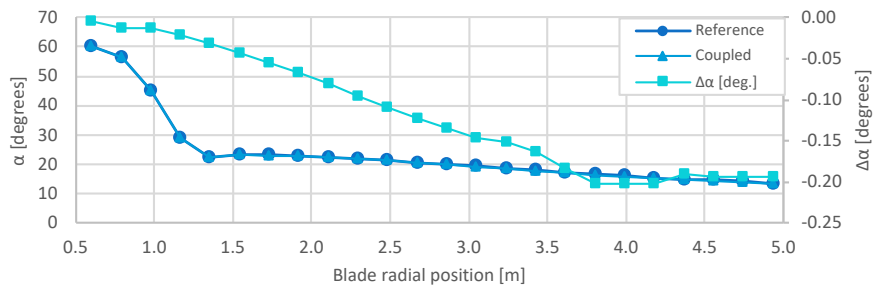
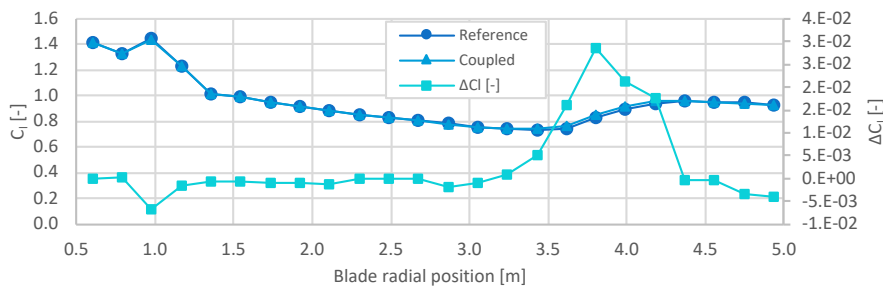


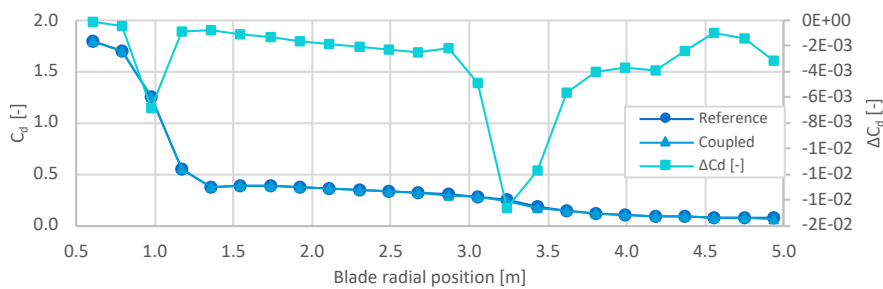
Figure 6.11: Aerodynamic coefficients for the S809 airfoil at $Re = 1 \times 10^6$.



(a) Angle of attack.



(b) Lift coefficient.

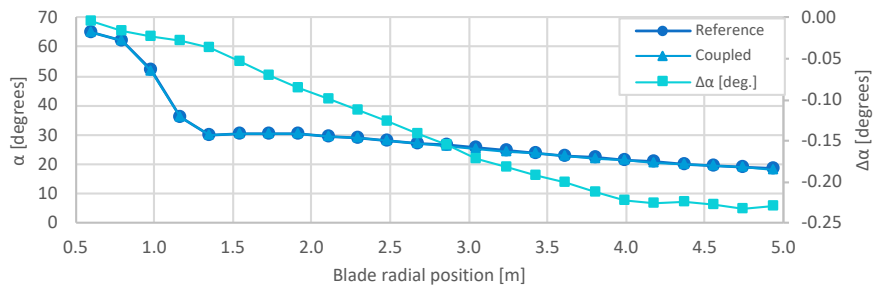


(c) Drag coefficient.

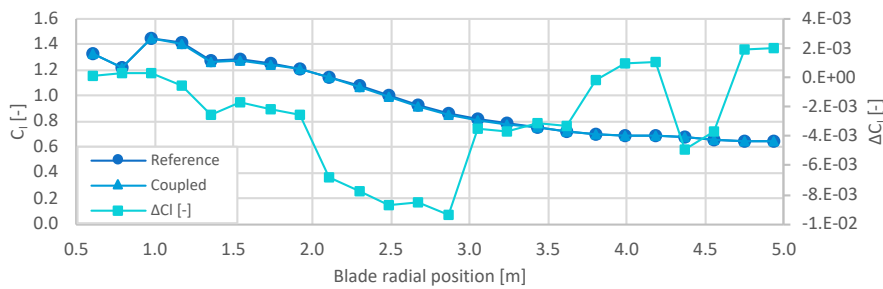
Figure 6.12: Aerodynamic coefficients at 10 m/s.

in α crosses the 30° mark. Paying closer attention to the series for C_l treated with the Lindenburg correction model in Figure 6.11, a small dip between 20° and 30° can be observed; here, a small deviation in α below 30° may cause a larger drop in C_l , instead of the relatively small decrease that prevails everywhere else along the blade length.

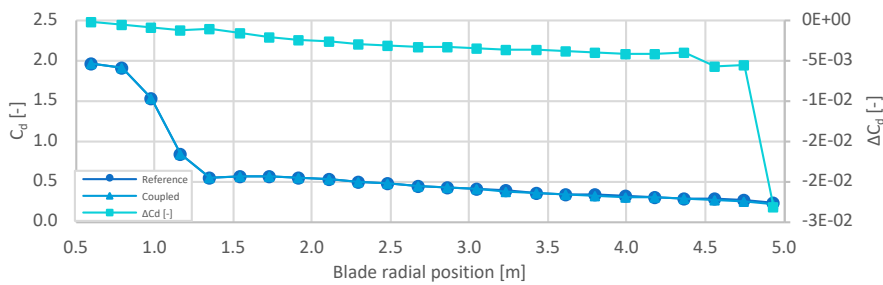
The slope of the C_d vs. α curve is fairly regular for $\alpha > 30^\circ$, for this reason it is no surprise that the changes in α along the blade, give as a result a smooth variation profile for drag. For all the blade stations, except two at the root, there is a reduction in C_d as a result of the induced torsion; the largest magnitude is observed at the tip of the blade, where the reduction in α causes a drop in C_d by 8×10^{-3} . For comparison, the reduction in C_l is smaller than 7×10^{-3} for most of the blade length, except for the blade stations at $r > 4$ m at which lift sees a reduction of order 1×10^{-2} . This means that for roughly 80% of the blade span, the reduction in C_d is greater than the reduction in C_l ; in the context of a wind turbine blade this is a favorable situation for increasing mechanical torque, since the only force opposing to the generation of torque is being reduced by a greater extent than the force driving it. In other words, the lift-to-drag



(a) Angle of attack.



(b) Lift coefficient.



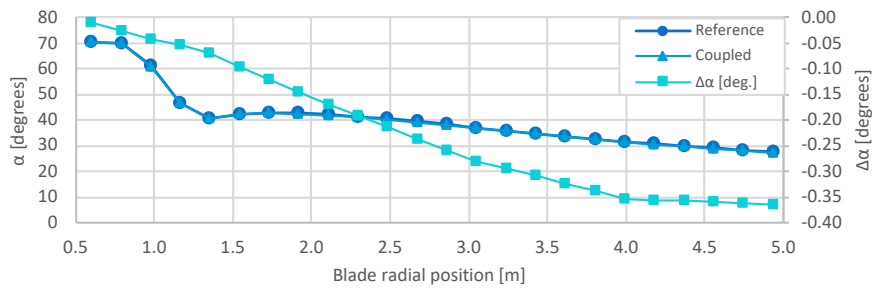
(c) Drag coefficient.

Figure 6.13: Aerodynamic coefficients at 13 m/s.

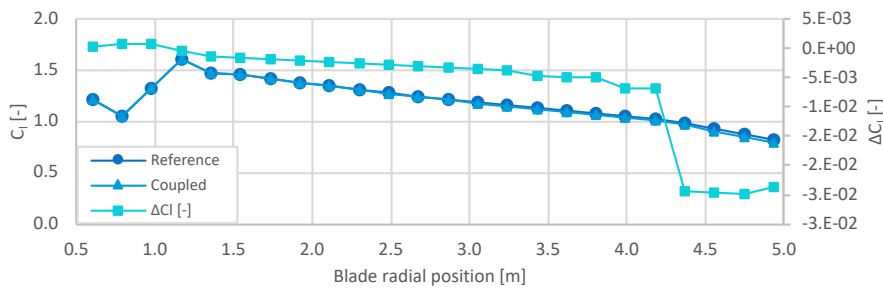
ratio or L/D which is in a way, an indicator of the aerodynamic efficiency of the blade, sees an overall gain.

6.4 STEADY TORQUE CURVES

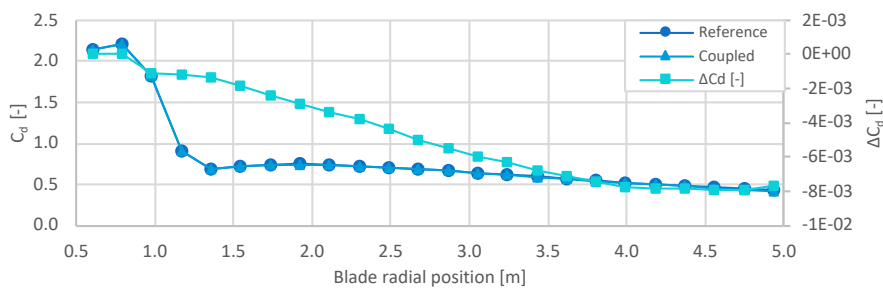
According to the simulation plan established in Section 6.1, the first of the simulation cases to consider for the neutral and coupled blade structures is that of the torque curve with a sequence of cases in steady state operation. Due to computation time constraints, the numerical torque is predicted at four specific wind speed values: 7, 10, 13 and 20 m/s. These operation points, which are also analyzed by Sørensen et al. [109], are of importance here because they span the entire operation range of the wind turbine including flow regimes for attached flow (7 m/s), stall onset (10-13 m/s) and fully detached flow (20 m/s). A simulation case is set up for each one of the wind speeds and for each one of the blade models.



(a) Angle of attack.



(b) Lift coefficient.



(c) Drag coefficient.

Figure 6.14: Aerodynamic coefficients at 20 m/s.

All simulations are run from an initialization point in which the flow speed is set to the inlet velocity magnitude; for this reason, the computational time needed for the stabilization of the transient solution depends on the inlet flow speed, this parameter determines the time it takes for initial transient vortices to be transported downstream to the pressure outlet by the action of convection. The torque time history is shown in Figure 6.15 for the cases involving the reference blade; revealing at least two important facts: first, the stabilization time decreases as the inlet wind speed increases and second, the stabilization of the integral torque comes accompanied by oscillations as the wind speed increases towards stall onset and deep stall. The same kind of behavior is observed for the simulations with the coupled blade, shown in Figure 6.16.

Initial transients are disregarded from the mentioned time history plots, but the long term stabilization of torque is assumed as an indicator of convergence or more precisely, stabilization of the transient solution. The net mass flow rate residuals for the fluid flow solution are monitored in a similar way, and besides stabilizing much more rapidly, i.e. before a flow time of 1 s, the values stabilize around 1×10^{-4} kg/s.

The data transfer process between structural and fluid flow solvers is governed by the System Coupling GUI and a revision of the mapping diagnostics for the blade surface, where information is being interpolated from one solution to the other, is made to ensure that most of the node and element locations where information is being sourced and transferred into is being identified and used by the data transfer processes. The percentage of mapped nodes, elements and surface area is above 99% for the data transfers of both pressure and displacement, which is expected due to the almost identical geometries used in the structural and fluid flow solutions. The diagnostics on the convergence of the coupling procedure itself are also observed during the general solution, to ensure identical rms residual change in data transfers between source and target locations at the end of each coupling step.

The postprocessing of CFD solutions for the co-simulation cases on the reference and coupled blades included an estimation of the pressure coefficient at different blade-wise locations from static pressure distributions around the perimeter of the blade cross sections. The results are presented in Figure 6.17, and comprise three different wind speeds and the two blade structures of the reference and coupled cases respectively. The estimation of the static pressure coefficient (C_p) uses the local dynamic pressure, and this is computed with an approximation of the relative wind speed as a function of both the radius and the free-stream wind speed. Because of the induced velocities in the axial and tangential directions, the tangential and free-stream wind speed are actually different from ωr and V_∞ respectively, however assuming negligible induction for this exercise is a fair simplification, justified on the fact that $C_p \approx 1$ for the stagnation point of almost all cases.

Because of the increase in twist angle towards the blade root and the corresponding increase in angle of attack, it is often at inner blade stations that the flow behavior is less regular and starts showing indications of flow separation. This seems to be the case of the C_p distributions at $r = 1.17$ m, which show the largest difference between the suction and pressure side and the most steep pressure gradient for the suction side, where C_p is mostly negative; in addition this blade station blends the shape of the S809 airfoil with the circular cross section at the root, which makes it relatively thicker with respect to the shape of the remaining sections.

At 7 m/s the differences in C_p distributions are hardly noticeable, except for the innermost blade station of the coupled blade (Figure 6.17b) which reveals a more benign pressure gradient at the suction side for $\bar{x} > 0.4$. Other than that, the pressure peaks at the suction side remain placed at the same location for all the blade stations, in both the reference and coupled blade scenarios. The location of the stagnation points shows no change between coupled and reference blade cases but there is an increase in the x coordinate with smaller radial position; this is expected due to the increase in angle of attack for inner blade stations.

At 13 m/s there are more interesting features such as the greater spread in the stagnation points location; this is of course a result of the larger angles of attack, derived from the increased freestream wind speed. The pressure gradients for the sections at $r = 1.17$ m and $r = 3.05$ m reveal an important difference as the coupled blade shows a more gradual increase in static pressure for $\bar{x} > 0.4$ in comparison with the reference blade, in which a steep increase in pressure can be observed right after $\bar{x} = 0.6$. The second interesting element is the broad shape of the pressure peaks at the suction side for the blade stations at $r = 1.17$ m and $r = 3.05$ m; the plateau shape for $r = 1.17$ m

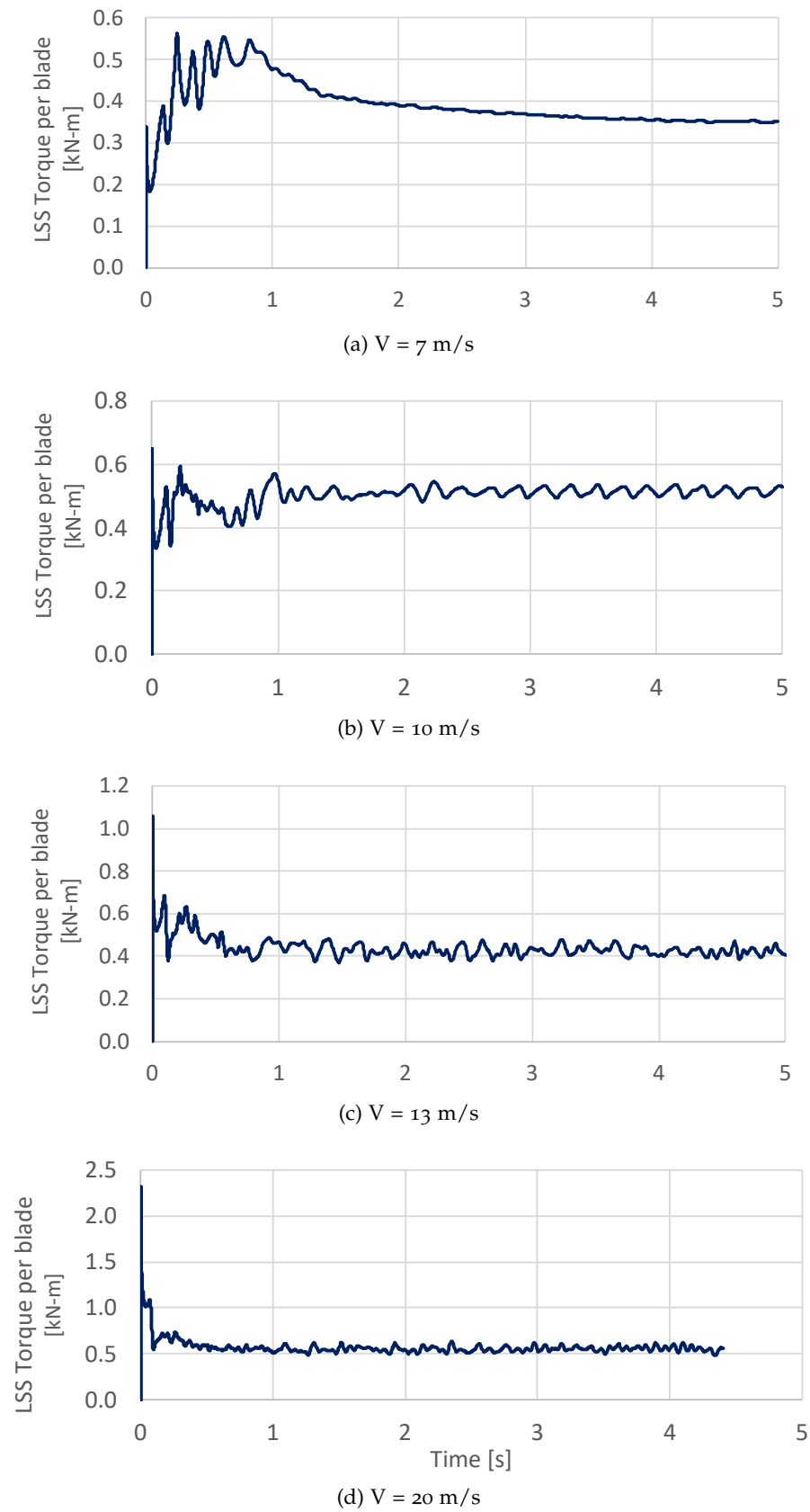


Figure 6.15: Torque convergence history for the reference blade.

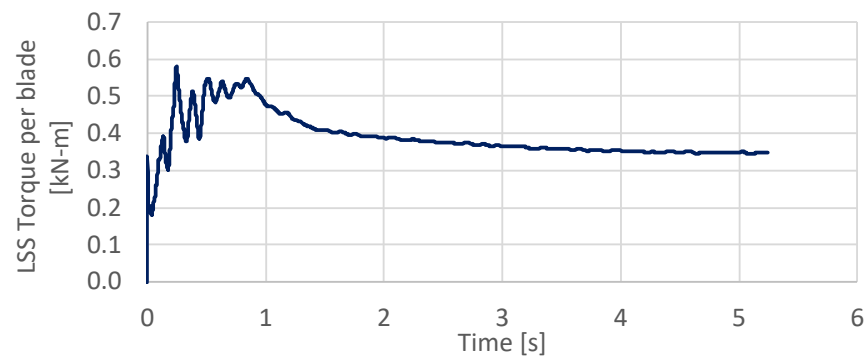
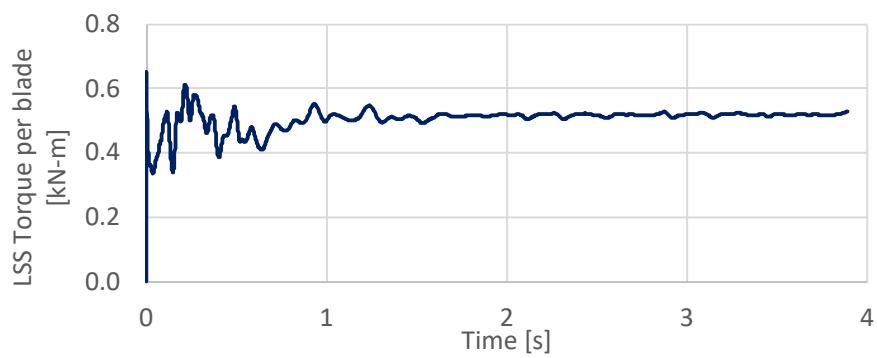
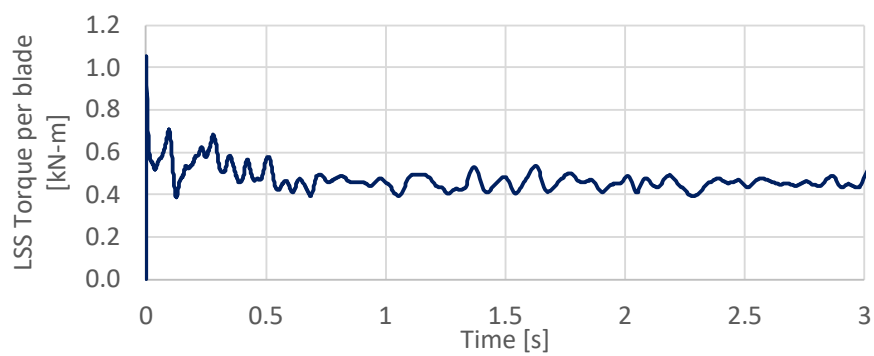
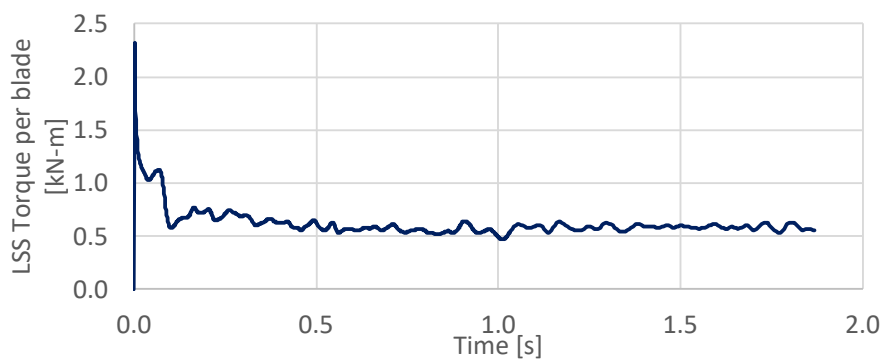
(a) $V = 7 \text{ m/s}$ (b) $V = 10 \text{ m/s}$ (c) $V = 13 \text{ m/s}$ (d) $V = 20 \text{ m/s}$

Figure 6.16: Torque convergence history for the coupled blade.

right after the initial peak may hint at separation phenomena close to the leading edge. For $r = 3.05$ m there is a secondary peak instead of a plateau indicating perhaps the continuation of an irregular flow pattern over the suction surface of the blade. It is curious that the station at $r = 1.92$ m, placed in between the aforementioned locations, shows little relation with the adjacent C_p distributions. This inconsistency might point to a variation in the flow patterns in the radial direction. In fact, radial flow is one of the characteristics of the fluid flow around a wind turbine blade that is neglected in the BEM analysis, but becomes clear with the use of a 3-D FVM solution of the fluid domain.

At 20 m/s the C_p distribution for the innermost blade section shows greater separation between suction and pressure side profiles, and the pressure gradient for the suction side appears to be slightly softer and to start further away from the leading edge for the coupled blade in comparison with the reference blade. This situation occurs between $\bar{x} = 0.4$ and $\bar{x} = 0.6$ and can be observed in Figure 6.17f; with the lower limit marking the approximate position for the maximum thickness and thus, the threshold from which flow separation due to adverse pressure gradients forms. The C_p distributions for the remaining blade sections remain relatively uniform along the blade and between the reference and coupled blade cases. Interestingly, the pressure gradients at the intermediate and external blade sections are moderate, with no abrupt variations beyond $\bar{x} = 0.4$ regardless of the blade structural configuration. Considering the higher freestream wind speed for this case and the resulting higher magnitudes in the distribution of α , it is very likely that the blade is operating under separated flow conditions to some degree along most of its span.

The postprocessing of static pressure distribution is followed by a similar treatment of shear stress over the blade sections, with the goal of obtaining the necessary inputs for estimating the normal and tangential force coefficients per unit length on each one of the analyzed blade sections. At this point it is important to bear in mind that the normal and tangential names refer to the components of aerodynamic force that are normal and tangential to the chord line of each section, instead of the force components for a blade element in a reference plane oriented with the blade rotation plane and the rotation axis. The full set of data is presented in Figure 6.18 and is assembled from three different sources: the experimental results, which are actually an estimation from the measurements of the NREL Phase VI experiment, the computations with the current simplified framework (BEM and static deflection profiles) and, the computations from the current robust simulation framework (2-way FSI). Three wind speed magnitudes are considered and, for each plot, the direct comparison between reference and coupled blade structures is presented, for both the simplified and robust simulation frameworks.

From a general perspective, the apparent accuracy of the present computations offers mixed results, matching the experimental measurements in some cases better than others. The results at 7 m/s illustrate this initial impression very well; on one hand, the normal force coefficients appear to match relatively well to the experimental values and, on the other, the tangential force coefficients are quite different from the experiment for both prediction methods. At 13 m/s the results are more balanced, since the match between numerical and experimental results improves for both the normal and tangential force coefficients. At this intermediate wind speed, the experimental results

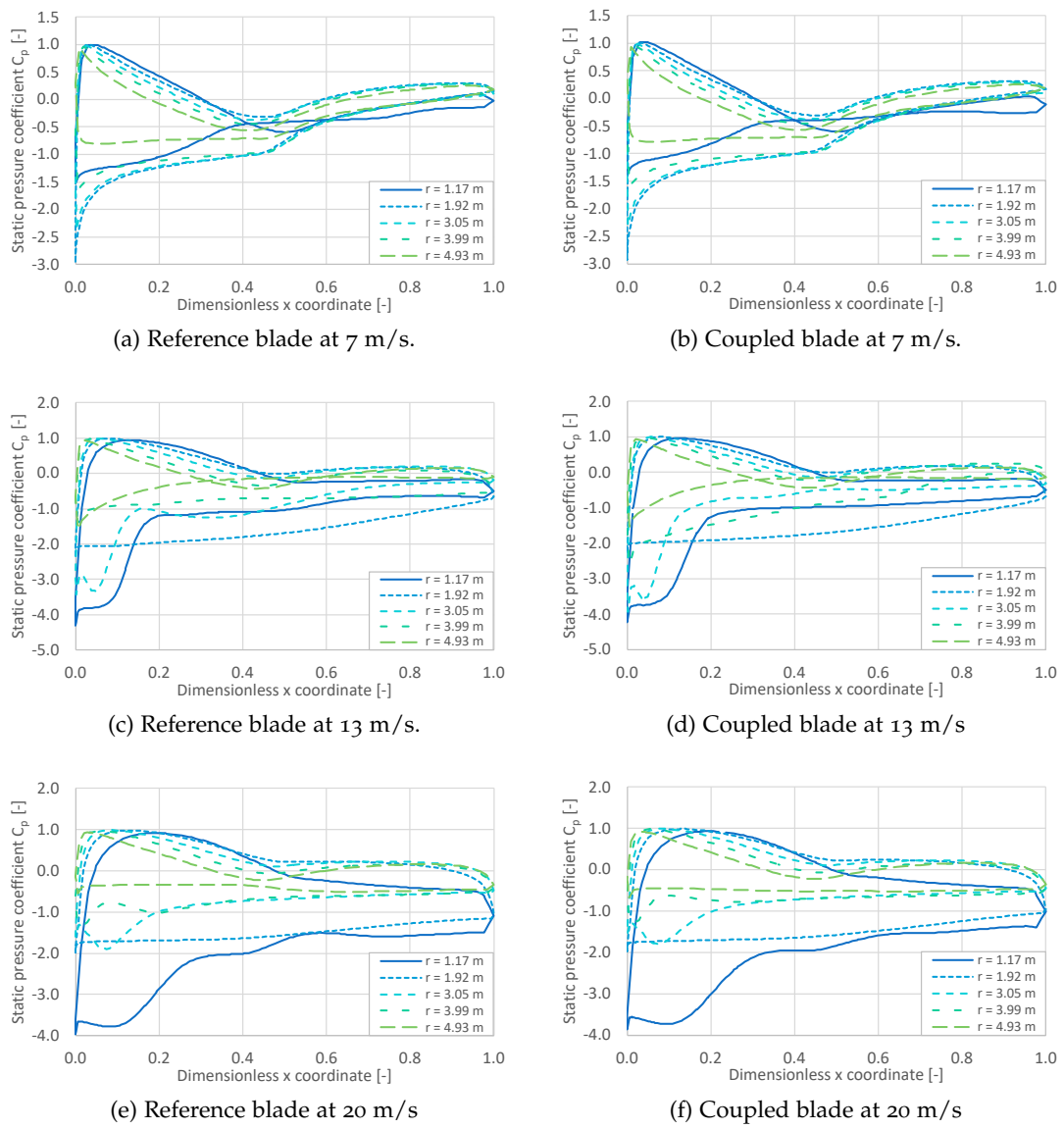


Figure 6.17: Pressure coefficient distributions for the robust framework co-simulations.

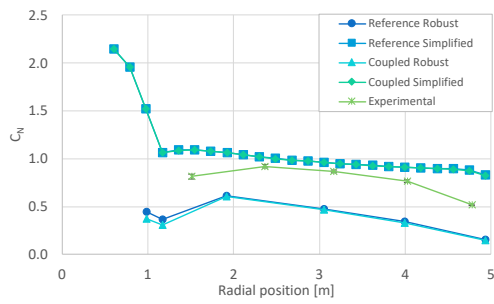
are characterized by a non-monotonic variation, this feature is replicated by the robust simulation framework, although, in both cases the comparison of a continuous profile is being represented in 5 locations only; in contrast, the more spatially resolved simplified framework reveals a gradual variation for both coefficients, which despite being non-monotonic for the tangent force, remains smooth and continuous for the mid and outboard blade sections.

At 20 m/s the results are notably positive even though each simulation framework outperforms the other depending on the predicted coefficient. The normal force coefficient in Figure 6.18e is clearly better predicted by the simplified simulation framework, matching the experimental data for most of the mid and outboard blade sections. Despite underpredicting normal force coefficients, the robust simulation framework outperforms the simplified one at the prediction of the tangential forces, despite the visible differences between the reference and the coupled blade structure.

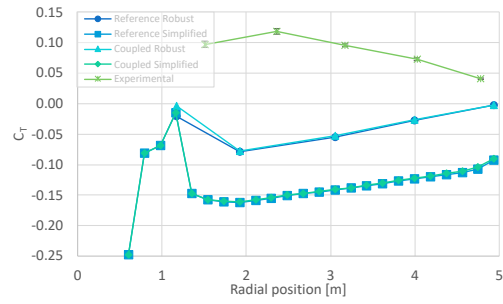
The difference between reference and coupled blades throughout the different simulation cases is less noticeable for the scenarios with a wind speed of 7 m/s which is expected given the known dependency of the bend-twist coupling mechanism on the wind speed magnitude. At 20 m/s the differences in normal and tangential coefficients are evident but not substantially. Given the steady nature of the simulations performed with the simplified simulation framework and the involved BEM treatment of the flow, the respective results are more regular and consistent with the expected behavior of the blade as a function of wind speed. The results of the robust simulation framework differ in that there is not a consistent difference between the sets of results for the reference and coupled blades. It is important to consider that these simulations are unsteady and are very likely to involve detached flow conditions at wind speeds of 13 m/s and 20 m/s; for this reason, the resulting aerodynamic loads are oscillatory and the presented coefficients give only a glimpse of the latest instant in the time history of the solution. A long-term time average is not shown as the postprocessing of the aerodynamic coefficients would require the solution for the entire flow field to be stored for a sufficiently large amount of time steps; computer storage constraints make this impossible for the current work. Additionally, because normal and tangential forces are linear combinations of lift and drag for a given angle of attack, the interpretation of the effect of coupling on the behavior of aerodynamic forces is not as intuitive as it is when the comparison focuses directly on lift and drag, as is the case for the results of C_l and C_d discussed earlier in this chapter.

Seven locations along the blade length are used for sampling vertical displacement along the z -axis and torsional rotation in the longitudinal or y -axis (See Figure 6.3). The radial positions at which the structural solution is being sampled is derived from the sections used to determine the laminate drop-offs according to Chapter 5. This way of defining the sampling positions aims to simplify the handling of the blade mesh in Ansys[®], as the definition of the virtual nodes at which data is recovered requires the use of partition boundaries of features in the blade geometry.

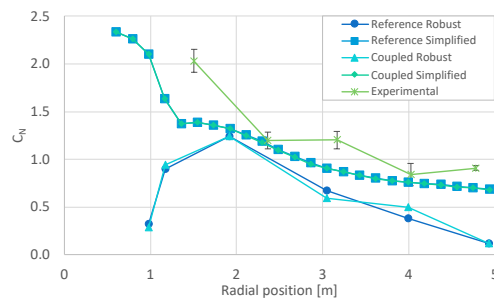
Figures 6.19a and 6.19b show flap-wise or out-of-plane displacement in the negative z direction. At a first glance, the results reveal the typical deformation profile for a cantilever beam and indicate also that displacement magnitude increases in direct proportion to wind speed. The latter statement is somewhat expected for a constant angular speed machine. There is also a hint of non-linearity with respect to wind speed when the displacements for outboard blade stations are inspected; for instance the re-



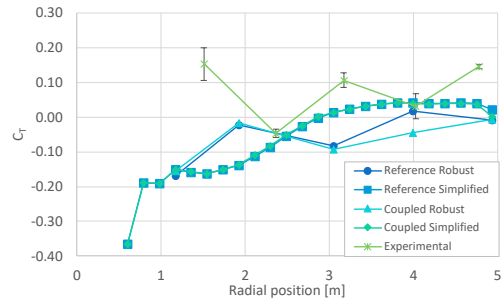
(a) Normal force coefficient at 7 m/s.



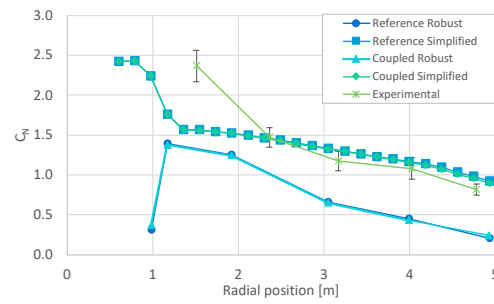
(b) Tangential force coefficient at 7 m/s.



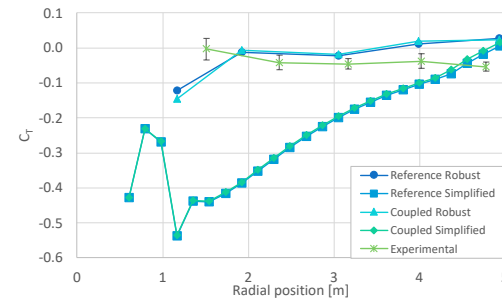
(c) Normal force coefficient at 13 m/s.



(d) Tangential force coefficient at 13 m/s.



(e) Normal force coefficient at 20 m/s.



(f) Tangential force coefficient at 20 m/s.

Figure 6.18: Blade-wise distributions of normal and tangential force coefficients.

sults at 10 m/s and 13 m/s seem to be mutually clustered and more separated from the results at 7 m/s or 20 m/s. This behavior raises some questions but is not new at all since it has been already reproduced in similar analysis, for instance the work of Lee et al. [45]. From the work of Section 4.2 it is clear that aerodynamic instabilities associated to flow detachment from the blades is responsible for non-linear behavior of rotor torque. Furthermore, the flow conditions responsible for stall between 10 m/s and 13 m/s, as in this range the torque curves reach their peak values before decreasing at higher wind speeds; in consequence the non-linear aerodynamic loads experienced at wind speeds around peak torque are the most likely cause of non-linear deflections at the very same wind speeds.

When comparing the magnitude for maximum displacement, which happens at the tip of the blade ($r = 5.029$ m) and at 20 m/s, the coupled blade results show a larger magnitude by approximately 6.6 mm. Despite aiming for flap-wise bending stiffness as close as possible to the one from the experimental blade, the reference blade model implementation is slightly stiffer between the inner and midboard blade sections, as can be observed when comparing Figure 5.4b to Figure 5.7b.

The torsional displacement for the reference blade model, shown in Figure 6.19c, reveals a relatively weak coupling between flap-wise bending and torsional displacements since the magnitude of blade section rotations is of the order of 1×10^{-2} degrees. The rotation angle has a non-monotonic variation while it appears to increase. The maximum rotation, at least among the set of sampling locations, is observed at the fifth probe location counted from the blade root ($r = 3.013$ m), this happens for all wind speeds. It is likely that the aerodynamic force applied at a distance from the elastic axis of the blade is responsible, at least partially, for the observed rotation in the reference blade. When defining the laminate groups for the reference blade, an analysis with classical lamination theory shows that the bend-twist coupling terms in the force and moment resultants for the considered laminates in rectangular plates are exactly zero. Even though the laminates in the reference blade have no bend-twist coupling, the blade geometry is more complicated than a rectangular flat plate, therefore material based coupling cannot be ruled out of the reference blade model. Assuming thin plate theory, an order 1×10^{-2} change in angle of attack should result in an order 1×10^{-3} change in lift coefficient, therefore aerodynamic forces should be insensitive to the amount of coupling seen in the reference model.

When observing the results for the blade structure with bend-twist coupling in Figure 6.19d an evident contrast arises with respect to the reference blade. First, the bend-twist coupling increases the order of magnitude in blade rotation to 1×10^{-1} , this happens for all wind speeds in the middle and outer blade sections. The displacement profile for the coupled blade is similar to the profiles observed in Figure 6.9 which were predicted with the 1-way FSI approximation. At $r = 1.257$ m, where the third sampling point is located, the rotational displacement profile shows a steep change in slope, most likely due to the marked change in thickness as the core plies of the blade root meet the transition area between the cylindrical and airfoil shapes.

The prediction of torque values from the FSI analysis of the reference and coupled blades is presented in Figure 6.20 along with the experimental values at each corresponding wind speed. The shape of the torque curves for the reference and coupled blade are relatively close to each other, with the torque of the latter being slightly higher than the torque of the former, and more notably at 13 and 20 m/s. This in-

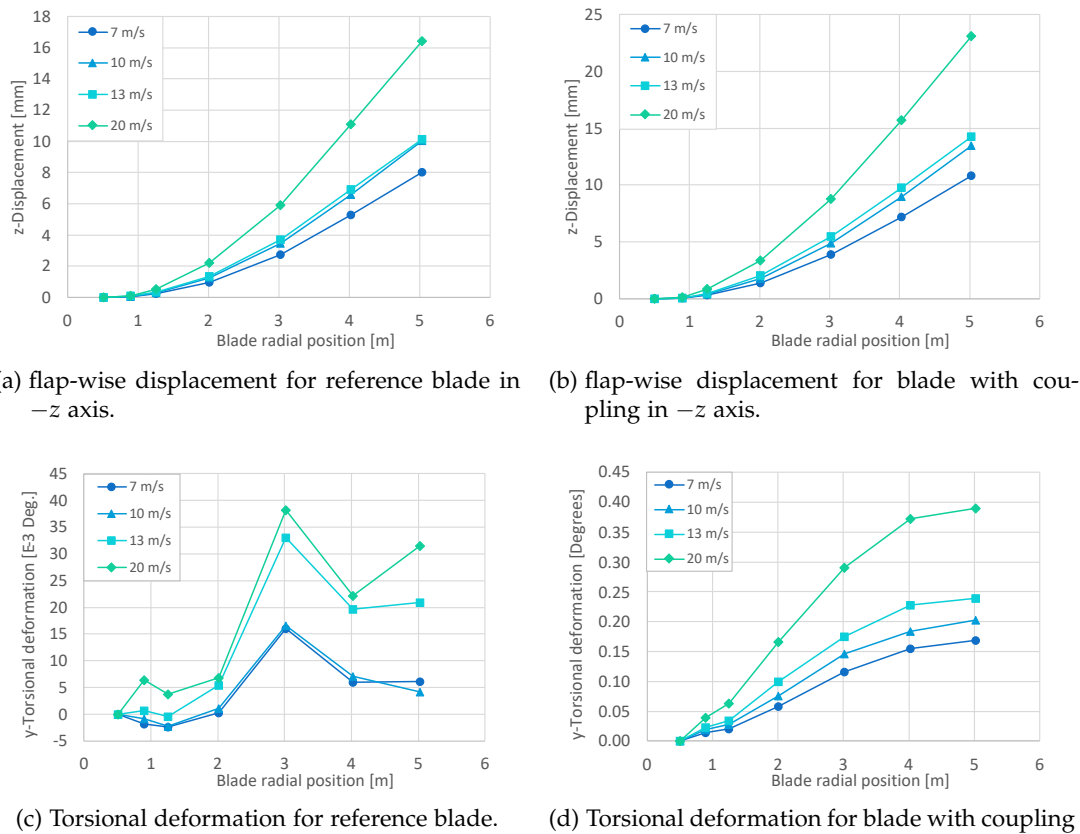


Figure 6.19: Structural responses for reference and coupled blade.

indicates that the pitch towards feather via bend-twist coupling has a positive effect in increasing the amount of torque delivered by the rotor; with the increase being stronger at higher wind speeds. From the data of the reference and coupled series of Figure 6.20 it is also evident that the numerical calculations with the robust simulation framework result in torque underpredictions with respect to the experimental data published in the sequence S measurement campaign (NREL Phase VI experiment [1]).

The discrepancy between numerical results and experimental data is even more notorious at 10 and 13 m/s, two wind speeds at which the prevailing separation and stall effects heavily determine the aerodynamics around the blade. This is a critical issue in the prediction of rotor loads for fixed pitch wind turbines which is not being taken into consideration in the mathematical model of Ansys[®] Fluent. Flow separation and its role on stall behavior cannot be predicted with the present $k-\omega$ SST turbulence model, and this is one of the main limitations of the robust simulation framework. Furthermore the CFD mesh has a resolution constraint from the computational resource which limits the mesh size to less than 4 million cells while the mesh deformation procedure puts an extra constraint on the wall adjacent element size and slenderness due to element quality considerations; in consequence, a wall adjacent mesh resolution with $y^+ \approx 30$ is the best possible result. An additional set of simulations on the fluid flow solver for steady state flow and no blade deformation are carried out, this time using a much more finely resolved mesh, allowing for $y^+ \approx 2$ in the near wall region.

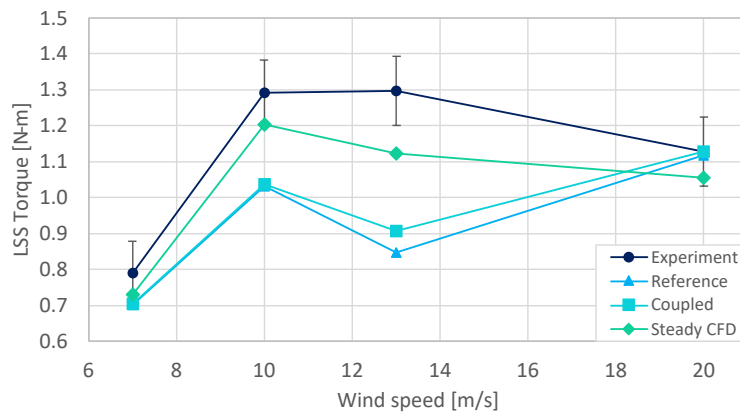


Figure 6.20: Low speed shaft torque at different wind speeds.

The results for this round of simulations are closer to the experimental results as Figure 6.20 shows, but this is true for wind speeds of 10 and 13 m/s.

Besides providing an overview of torque predictions with respect to the experimental data, the predictions in blade root bending moments are also included. The objective of assessing the performance of the blade from a structural point of view, contemplates the analysis of the flap-wise and edge-wise bending moments. The flap-wise bending moment is perhaps the most critical for the structural integrity of the blade root assembly; it is dominated by the bending action of the thrust force which has contributions from both drag force and a component of lift force at every section of the blade. The prediction of flap-wise bending moment from the robust simulation framework is shown in Figure 6.21, revealing two main outcomes: the results are close to the experimental measurements, at least within the error boundaries and the action of bend-twist coupling is stronger at the higher wind speeds.

The edge-wise bending moment results are shown in Figure 6.22 along with experimental data and their associated error. An underestimation of moment is observed for all wind speeds except at 20 m/s; nevertheless, the standard deviation of experimental edge-wise bending moment is relatively large, at least with respect to other measured quantities such as shaft torque. Again, following the expected dependency of bend-twist coupling strength and free-stream wind speed, the results for the coupled blade begin deviating from the reference values for the cases at 10, 13 and 20 m/s.

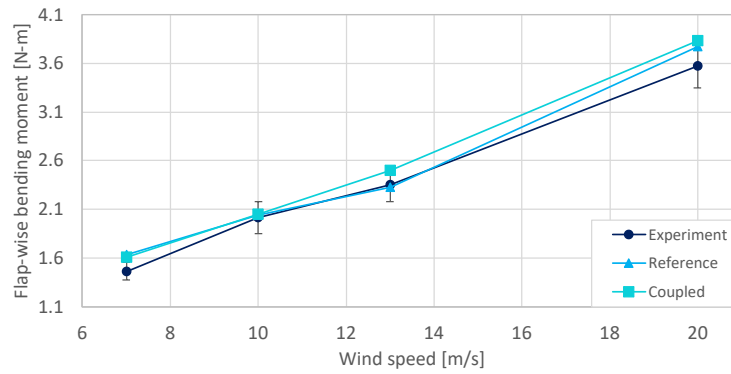


Figure 6.21: Flap-wise bending moment at the blade root.

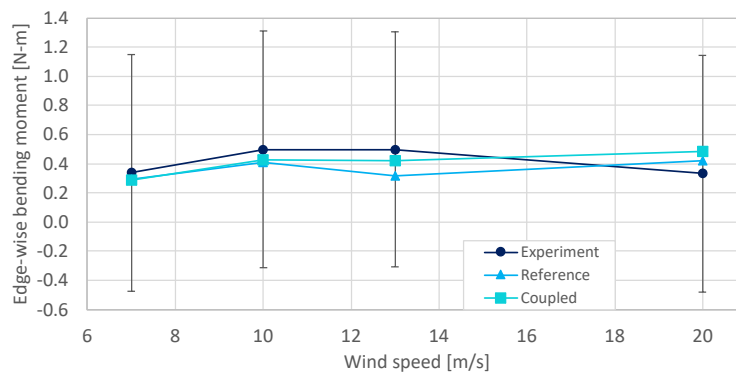


Figure 6.22: Edge-wise bending moment at the blade root.

A second part of the comparative analysis is performed using an implementation of the [BEM](#) model including dynamic induction, stall delay and dynamic stall effects as described in [Chapter 4](#). The aerodynamic solution provided by the [BEM](#) model is now interacting with a very simple approach to the blade deformation which consists in an interpolation of the blade local torsion as a function of radial position and free-stream wind speed, using as an input the results from the 1-way [FSI](#) analysis (see [Figure 6.9](#)). Two sets of data are initially generated for the comparison of the reference blade and the coupled blade, these are a set curves of thrust versus wind speed and, a set of curves of power versus wind speed. Since the [NREL](#) Phase VI wind turbine is a constant speed machine, the mechanical power is computed as the product between torque and angular speed.

According to [Figure 6.23](#) bend-twist coupling, as implemented for the present model, seems to have a small effect on the rotor integral thrust force. The reduction in thrust force, which is a desirable scenario from a load mitigation point of view, is barely noticeable and mostly at higher wind speeds at which the bend-twist coupling effect is already known to provide a stronger response in torsional displacement. Putting load magnitudes aside for a moment, it is also evident that the implemented coupling does not increase loads in the axial direction, therefore, the design of other components

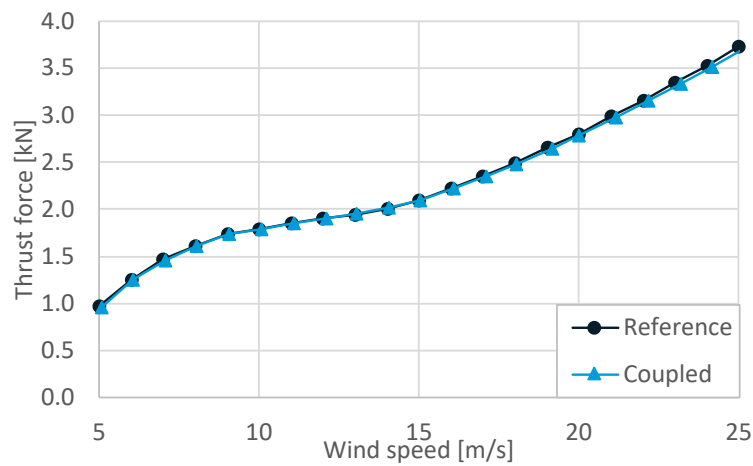


Figure 6.23: Thrust curve comparison

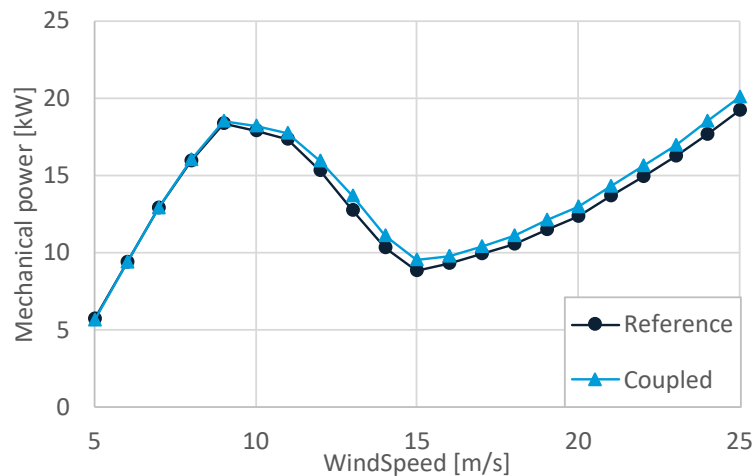


Figure 6.24: Power curve comparison

such as the tower and foundations would not be impacted from the use of a blade with bend-twist coupling.

By observing the power curve predictions from Figure 6.24 one can immediately see a different scenario, as the power for the bend-twist coupling blade is consistently higher than the reference power for a broader range of the operating envelope. For wind speeds beyond 10 m/s, the bend twist coupling is effective in increasing rotor torque by inducing a local torsion into the feather position along the blade. When pitching the blade into feather, the angle of attack tends to decrease and even though lift can be decreased as well, the reduction in drag forces might be significant enough as to result in an overall torque gain.

When it comes to power or torque increments due to bend-twist coupling, both the robust and simplified simulation frameworks give consistent results with respect to each other. The percentual increments that are shown side-to-side in Table 6.3 indicate that both simulation strategies give similar predictions of the torque increment due to the coupled blade structure. In more detail, the results at 7, 13 and 20 m/s are relatively close to each other whereas the torque increment at 10 m/s shows the largest discrepancy out of all four wind speed cases. Despite existing discrepancies, the simplified

V [m/s]	Simplified framework torque [N-m]			Robust framework torque [N-m]		
	Reference	Coupled	Increment (%)	Reference	Coupled	Increment (%)
7	1710.3	1713.5	0.2	702.4	705.6	0.5
10	2374.8	2409.8	1.5	1032.7	1036.0	0.3
13	1689.9	1810.1	7.1	846.7	906.0	7.0
20	1639.1	1719.9	4.9	1117.4	1128.9	1.0

Table 6.3: Torque prediction comparison between the proposed simulation frameworks.

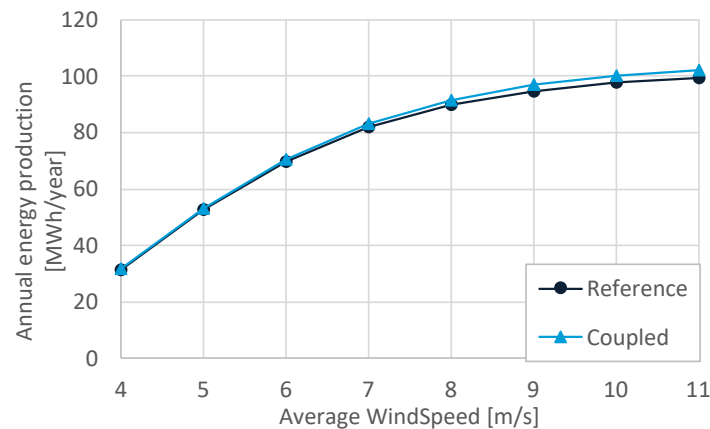


Figure 6.25: AEP curve comparison.

simulation framework is surprisingly close to the results from the robust framework at wind speeds that have been known for the adverse flow regimes, i.e. 13 m/s and 20 m/s; however, the fact that the simplified simulation framework imposes a torsional displacement as a function of wind speed and blade position from linear interpolations must not be overlooked; this is a significant assumption compared with the strongly coupled 2-way FSI from the robust simulation framework.

Perhaps a more global perspective can be given by considering the effect of the coupling through composite material configuration on the AEP of the rotor, at least considering mechanical energy only. For this purpose the wind resource is represented by a Rayleigh probability distribution and a set of average wind speeds ranging from 4 m/s to 11 m/s. The results in Figure 6.25 show that the maximum AEP for the reference blade is happens at 11 m/s with 99.2 MWh whereas for the coupled blade the maximum AEP at the same average wind speed is 102.2 MWh. The increment in AEP due to bend-twist coupling is relatively small at wind speeds from 4 to 7 m/s, but grows at higher wind speeds, reaching a 1.5% improvement at 7 m/s and a 3% improvement at 11 m/s. At higher wind speeds the AEP curve appears to flatten, and the power increments grow more slowly, reaching 3.5% at 14 m/s.

6.5 EXTREME WIND LOADING

After the introduction of the extreme wind model in Section 6.1 and the adoption of the reference wind speed for a Class III small wind turbine, two simulations are performed

on the reference and coupled wind turbine blades, following the set up for the normal operation torque curves and considering the following aspects: 1) the velocity inlet boundary condition is set to the extreme wind magnitude with recurrence period of one year, $V_{e1} = 39.4$ m/s and 2) Assuming a parked condition, the angular velocity is set to zero. Because of the much greater inlet wind speed, the solution in the robust simulation framework tends to stabilize faster, well before 1 second of flow time.

The structural response of the blades in terms of flap-wise displacement and torsion is shown in Figure 6.26, revealing familiar profiles to the ones observed for the normal operation cases. Torsional displacement for instance, is characterized by a relatively small order of magnitude (1×10^{-2}) and a non-monotonic increase along the radius in the case of the reference blade. The torsional displacement of the blade with bend-twist coupling has a defined tendency to increase with the radial position and reaches a maximum of about 0.64° at the tip of the blade. The nature of the case from an aerodynamic perspective is in essence the same of a flat plate normal to the flow, since the blade is not rotating and much of its length is placed at an almost 90° orientation with respect to the freestream wind; it is for this reason that drag force, instead of lift, can be expected to be the dominant load driving the deformation of the blade. It is also sound to expect that the aerodynamic moment acting on the blade along its longitudinal axis (y -direction for reference in Figure 6.3) is partially responsible for the torsional displacement adding to the coupling induced rotation; this is a very likely scenario, as drag force exerts a normal pressure on the blade in the same direction as the flap-wise deflection.

Further analysis on the main aerodynamic moments and forces acting on the blade indicates that the effect of bend-twist coupling in the aerodynamics of the blade is not detrimental to the load state of the blade. The magnitudes of the three bending moments and the magnitudes of tangential and axial force acting on the static blade are organized in Table 6.4 to highlight the relative change for the coupled blade with respect to the reference structure.

	Flap-wise moment [N-m]	Edge-wise moment [N-m]	Torsional moment [N-m]	Axial Force [N]	Tangential force [N]
Reference Blade	-7214.36	1375.69	288.44	-2525.57	-545.92
Coupled Blade	-7235.30	1429.58	286.52	-2530.76	-562.32

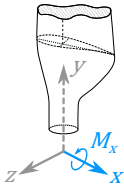
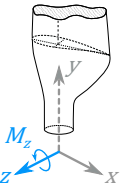
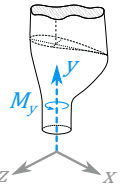
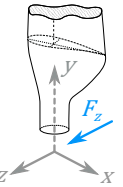
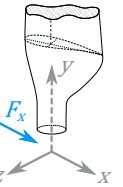






Table 6.4: Load analysis at the blade root

One of the most important loads is the bending flap-wise moment because it plays an important role on the cost of the blade to hub attachment. As result of the coupling, this load is increased by 0.3% with respect to the baseline blade. The axial force,

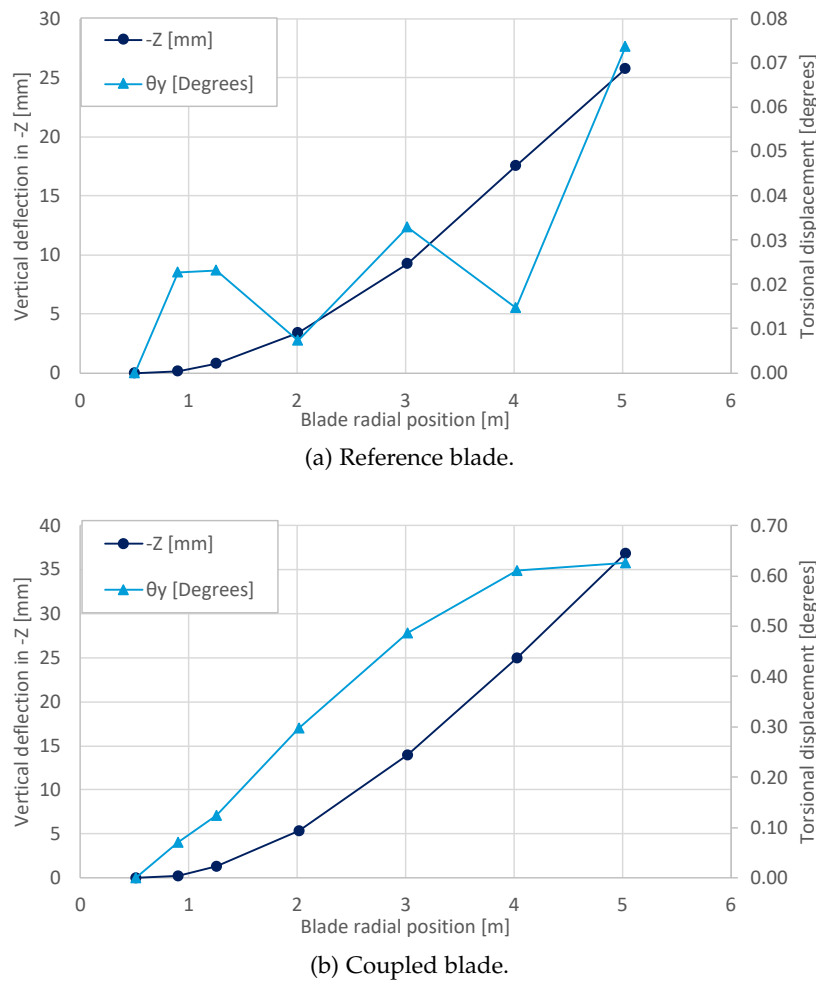


Figure 6.26: Flap-wise and torsional displacement for the EWM.

generated mainly by drag due to the blade static position, sees an equally small increase of about 0.2% with respect to the corresponding value for the reference blade. An observed 3.9% increase in edge-wise moment is consistent with the 3% increase in tangential force and both outcomes are a consequence of the observed torsional displacement from Figure 6.26b which decreases the angle of attack through a pitch action towards feather, specially for the blade tip region. By reducing the angle of attack along the blade length, some degree of lift force may contribute to the aerodynamic force resultant since not only the inboard region of the blade but other sections near the tip are likely to be in a deep stall flow condition as opposed to the normal flow scenario; in consequence, an increase of about 16 N in tangential force is experienced.

CONCLUSIONS

An actuation mechanism for regulating rotor power has been proposed and analyzed with numerical simulation by two different approaches: a simplified simulation framework, with BEM modeling of rotor aerodynamics and a pseudo-coupling between the aerodynamics and the steady analysis of blade deformation and, a robust simulation framework for 2-Way FSI analyses considering 3D FVM modeling of the aerodynamics and a 3-D modeling of the composite structure.

The simulation of fluid-structure interaction is performed at two levels of complexity, but capable of considering transient phenomena from either approach. The robust simulation framework offers the most general modeling of the involved phenomena: non-linear aerodynamics, including the effects of turbulence and blade rotation and, non-linear structural behavior, considering the anisotropic properties of a composite material structure. The source of experimental measurements considers a fixed speed rotor for all campaigns, therefore a constant angular speed is set for all the numerical analysis in order to establish a direct comparison between predicted and real behavior. This is a substantial simplification, that eliminates the need for additional simulation of the generator internal dynamics into the coupled framework. The same can be said of the simplified simulation framework which can still reproduce transient variations in angular speed as well as free-stream wind speed and blade deformations.

An ideal distribution of bend-twist coupling has been proposed by a simple exercise of determining the sensitivity of blade tip rotation to the orientation of off-axis fibers for the blade with a coupled structure. The behavior of tip rotation revealed a well-defined variation with a clear peak value for fibers placed at a 20° with respect to the blade longitudinal axis. This information is used to propose a blade structure that successfully undergoes a torsional deflection along its longitudinal axis in response to an aerodynamic load. This exercise is performed at the same time that the flexural and torsional stiffnesses of the original blade are maintained as close as possible to the levels of the experimental blade; the resulting blade structures are the result of a trial and error study on the proposed blade structures since the experimental blade structure is not specified beyond a series of spanwise distributed mechanical properties. The main analysis of the coupled blade structure, other than the 2-way FSI studies in the robust simulation framework, are condensed into a series of steady-state, 1-way interaction simulations that demonstrate the efficacy of the coupled composite structure, with 20° fibers, for inducing a rotation of increasing magnitude as the freestream wind speed is increased from the cut-in value to the cut-out value.

The robust analysis of the coupled blade structure is accompanied by a twin analysis under the same operating conditions but, considering the reference blade structure. This reference blade is made also of composite materials and, because of the natural location of the elastic axis through the blade, there is a small amount of rotation with magnitudes of the order of 1×10^{-2} . The results of both analyses are compared to find out that the use of bend-twist coupling as a mechanism for passive blade torsion can induce a positive change in the resulting annual energy production, with a 3% increase

considering a Rayleigh distribution with an average wind speed of 11 m/s. This results are obtained by a torsion towards the feather position, which decreases the angle of attack and in consequence results in an increased L/D ratio whenever the associated change in drag outweighs the change in lift. Because lift is reduced, a secondary consequence of the proposed actuation mechanism is a reduction of the total thrust force over the rotor blades for most of the wind speeds within the operation range, particularly between 15 and 25 m/s at which the total thrust force sees a reduction of about 0.35%. Despite the fact that a more substantial reduction in thrust force would be a highly desirable scenario, the modest change observed here is still favorable because it suggests that the improvement in rotor torque and hence power comes at no cost from the point of view of the thrust loading which eventually impacts the cost of the entire turbine assembly.

The feasibility of a blade with bend-twist coupling is demonstrated from a structural point of view from the analysis of blade root loads under extreme wind conditions with a 39.4 m/s wind speed in parked conditions. As a consequence of the bend-twist coupling, the flapwise bending moment increases by 0.3% and the axial force increases by 0.2%, both of these magnitudes are dominated by drag forces acting on the blade due to its orientation at very high angles of attack, i.e. 80°-90°. Edgewise bending moment and side forces are most likely caused by lift, these experience increments of 3.9% and 3% respectively, and have generally smaller magnitudes than their axial counterparts, for instance a 1 to 5 ratio between flapwise and edgewise bending moments. These results evidence a negligible increase in the critical blade loads when bend-twist coupling is implemented as a part of the structure.

AERODYNAMIC MODELING

The modeling of the aerodynamic loads acting on the rotor blades is a very sensible part within an [FSI](#) analysis and its application to a wind turbine rotor blade brings additional challenges into the table. The high Reynolds number over the outer portion of the blade means that turbulence is to be considered whereas the rotational motion of the blades cause radial flow and the departure of sectional aerodynamic coefficients from the theoretical 2D values. The first effort to tackle these issues is performed as an implementation of a [BEM](#) model with a proposed correction for three-dimensional flow effects which proves to accurately predict mechanical torque with an error no greater than 11.5% and the flapwise bending moment with an error no greater than 13.6%. This is a fundamental step to be able to predict aerodynamic loads with an acceptable accuracy but in a short computational time, which is the main goal of the simplified simulation framework.

The [FVM](#) analysis used for the robust simulation framework includes a separate validation step from the main studies on the wind turbine blade; this is done on an industrial fan blade with a thin plate section geometry. The validation case for the [CFD](#) analysis shows favorable results for the fluid flow stand alone solutions and for the coupled problem but reveals discrepancies for the analysis of the [NREL](#) Phase VI wind turbine blade. These discrepancies between predicted and experimental torque arise at high wind speeds which is consistent with the difficulties encountered by other authors addressing the analysis of wind turbine operation in stall conditions.

The resolution of the near wall mesh and its role on the turbulence modeling of the near wall flow properties is perhaps the crux of the fundamental issue on the discrepancies between the CFD validation case and the analysis of the wind turbine blade. The blade from the validation case is prone to operate under leading edge separation conditions because of the thin plate geometry and the small leading edge radius, therefore, the solution might be less sensitive to the y^+ than in a case with attached flow, which would justify the good results despite the coarse mesh used to discretize the condenser fan blade. In contrast, the analysis of the wind turbine blade involves the geometry of thick airfoil with a relatively large leading edge radius that ensure partial operation with fully attached flow conditions. Because of the influence of the near wall flow solution on the overall prediction of shear-stresses and therefore of friction drag, the analysis of the wind turbine may be more sensitive to the wall y^+ . The computational time restrictions place a direct constraint over the near wall mesh resolution; because wall y^+ is limited above a value of 30, there may be a poor prediction of the flow conditions around the wind turbine blade at some operating conditions.

APPROACH TO FLUID-STRUCTURE INTERACTION

Judging the magnitude of blade tip transverse displacements with respect to the total length, the case can be assumed lineal from a structural point of view, which is adequately described by the modeling in composite materials as demonstrated by the validation case of a bend-twist coupled D-spar. The information transfer processes from the robust simulation framework is carried out with no difficulties because of the nearly identical geometries between fluid and solid meshes, additionally, the element size on both sides of the mesh ensure that profile preserving and conservative data transfers are carried out successfully depending on the interpolated variable. The third aspect of the FSI analysis is the aerodynamic modeling, which as discussed earlier, presents important challenges when applied to the analysis of a wind turbine.

The largest discrepancy from the results obtained with the robust simulation framework are attributed to the aerodynamic modeling and its difficulty in predicting the flow properties under separated flow. It is for the torque predictions where the robust simulation framework presents the most significant discrepancies with respect to the experimental data; however, despite of the error in the reference blade torque prediction, the increment in torque due to bend-twist coupling appears to be consistent with the results from the simplified simulation framework.

In fact the direct comparison of torque increment due to bend-twist coupling between the robust and simplified simulation frameworks, show that the correct prediction of torque when the blade experiences a rotation due to flapwise bending is consistent in terms of relative percentage for the different wind speeds at which the analysis is performed.

APPROACH TO BEND-TWIST COUPLING

What could be regarded as the central analysis of this work, the estimation of change in annual energy production due to bend-twist coupling, is performed with the simplified simulation framework because it offers the possibility of computing full torque and power curves for the entire wind speed operational envelope. Due to computational time constraints the robust simulation framework analyses are limited to four wind speed cases. Despite this limitation, the improvement in torque due to bend-twist coupling can reach up to 3% considering an average wind speed of 11 m/s, the analysis on the flapwise bending moment and total rotor thrust show that there is little increment in these critical loads and, the one to one comparison of torque increase for the robust and simplified frameworks are consistent with each other as discussed earlier.

The way in which bend-twist coupling is incorporated into the present blade structure follows a relatively simple methodology dependent on material anisotropy to induce structural coupling, the most important task in this procedure is perhaps the definition of the angle orientation for the reinforcement fibers inside the composite materials. Despite the fact that 20° fiber off-axis angles have been defined in a direct and simplistic way from a sensitivity analysis, the results show that material based bend-twist coupling effectively increases torque, especially for wind speeds above 13 m/s. This is contrary to the expectations to observe a more substantial increase at low wind speeds and a consequence of the observed impact of drag forces on bending at high and very high wind speeds. Nevertheless, the increase in rotor torque for wind speeds below 10 m/s is evidenced from the robust simulation framework (1.5%) and from the simplified simulation framework (0.3-0.5%).

The resulting increases in torque are substantial despite the simplicity of the wind turbine blade, consisting of outer shells as the main and only load carrying members. This consideration for the structural concept is proposed mainly to preserve the typical architecture of small wind turbine blades, which usually have no internal components. The main outcome is the demonstration of an attractive improvement in power output that has little structural complexity provided that composite material manufacture is considered as a part of the reference blade.

BIBLIOGRAPHY

- [1] MM Hand, DA Simms, LJ Fingersh, DW Jager, JR Cotrell, S Schreck, and SM Larwood. Unsteady aerodynamics experiment phase vi: wind tunnel test configurations and available data campaigns. Technical report, National Renewable Energy Lab., Golden, CO.(US), 2001. (Cited on pages [viii](#), [2](#), [70](#), [73](#), [96](#), [100](#), and [129](#).)
- [2] K Hayat and S K Ha. Load mitigation of wind turbine blade by aeroelastic tailoring via unbalanced laminates composites. *Composite Structures*, 128:122–133, 2015. doi: 10.1016/j.compstruct.2015.03.042. (Cited on pages [viii](#), [7](#), [8](#), [16](#), [18](#), and [103](#).)
- [3] John N. Bertin and Russell M. Cummings. *Aerodynamics for Engineers-6th ed.* Pearson, 2014. (Cited on pages [viii](#), [27](#), and [28](#).)
- [4] Satish Kumar Chimakurthi, Steve Reuss, Michael Tooley, and Stephen Scampoli. ANSYS Workbench System Coupling: A state-of-the-art computational framework for analyzing multiphysics problems. *Engineering with Computers*, 34:385–411, 2018. (Cited on pages [viii](#), [56](#), [57](#), and [58](#).)
- [5] M F G Serra and M C van Schoor. Aeroelastic tailoring of a horizontal axis wind turbine. *Wind Engineering*, 19(4):193–207, 1995. URL <https://www.scopus.com/inward/record.uri?eid=2-s2.0-0029413765&partnerID=40&md5=833950c2872201438c37c09e51d56f65>. (Cited on pages [viii](#) and [60](#).)
- [6] ANSYS, Inc. System coupling user’s guide, release 2021 r2, 2021. (Cited on pages [viii](#), [59](#), [60](#), and [61](#).)
- [7] C H Ong, J Wang, and S W Tsai. Design, manufacture and testing of a bend-twist d-spar. In *37th Aerospace Sciences Meeting and Exhibit*, pages 43–52, 1999. (Cited on pages [xi](#), [4](#), [79](#), [80](#), and [81](#).)
- [8] John H Chujutalli, Guilherme Pimenta da Silva, and Segen F Estefen. Determination of the geometric and material properties of the nrel phase vi wind turbine blade. *Marine Systems & Ocean Technology*, 16(2):69–83, 2021. (Cited on pages [xi](#), [97](#), [98](#), and [100](#).)
- [9] Don Lobitz and Paul Veers. Aeroelastic behavior of twist-coupled HAWT blades. In *1998 ASME Wind Energy Symposium*, Reston, Virginia, jan 1998. American Institute of Aeronautics and Astronautics. doi: 10.2514/6.1998-29. URL <http://arc.aiaa.org/doi/10.2514/6.1998-29>. (Cited on pages [4](#), [13](#), [14](#), and [109](#).)
- [10] T D Ashwill, P S Veers, J Locke, I Contreras, D Griffin, and M D Zuteck. Concepts for adaptive wind turbine blades. In *Wind Energy Symposium*, pages 56–69, 2002. (Cited on page [4](#).)

- [11] P S Veers, T D Ashwill, H J Sutherland, D L Laird, D W Lobitz, D A Griffin, J F Mandell, W D Músiel, K Jackson, M Zuteck, A Miravete, S W Tsai, and J L Richmond. Trends in the design, manufacture and evaluation of wind turbine blades. *Wind Energy*, 6(3):245–259, 2003. doi: 10.1002/we.90. (Cited on pages 4 and 11.)
- [12] D A Griffin, D Berry, M D Zuteck, and T D Ashwill. Development of prototype carbon-fiberglass wind turbine blades: Conventional and twist-coupled designs. In *42nd AIAA Aerospace Sciences Meeting and Exhibit*, pages 1–12, 2004. (Cited on page 5.)
- [13] T D Ashwill. Passive load control for large wind turbines. In *51st AIAA/ASME/ASCE/AHS/ASC Structures, Structural Dynamics, and Materials Conference 18th AIAA/ASME/AHS Adaptive Structures Conference 12th*, 2010. (Cited on page 5.)
- [14] Don W Lobitz. Ramifications of aeroelastic analysis approximations as blade designs approach stability boundaries. In *42nd AIAA Aerospace Sciences Meeting and Exhibit*, pages 203–210, 2004. (Cited on pages 5 and 108.)
- [15] A Maheri, S Noroozi, C Toomer, and J Vinney. A simple algorithm to modify an ordinary wind turbine blade to an adaptive one. In *European Wind Energy Conference*, volume 2, pages 1195–1202, 2006. (Cited on pages 5, 15, 16, and 18.)
- [16] R Thresher and A Laxson. Advanced wind technology new challenges for a new century. In *European Wind Energy Conference & Exhibition 2006*, volume 3, pages 2543–2551, 2006. (Cited on page 6.)
- [17] R F Nicholls-Lee and S R Turnock. Enhancing performance of a horizontal axis tidal turbine using adaptive blades. In *OCEANS 2007-Europe*, 2007. doi: 10.1109/oceanse.2007.4302437. (Cited on pages 6, 16, and 18.)
- [18] M Capuzzi, A Pirrera, and P M Weaver. A novel adaptive blade concept for large-scale wind turbines. Part I: Aeroelastic behaviour. *Energy*, 73:15–24, 2014. doi: 10.1016/j.energy.2014.06.044. (Cited on pages 6 and 18.)
- [19] M Capuzzi, A Pirrera, and P M Weaver. A novel adaptive blade concept for large-scale wind turbines. Part II: Structural design and power performance. *Energy*, 73:25–32, 2014. doi: 10.1016/j.energy.2014.04.073. (Cited on pages 6 and 18.)
- [20] M Capuzzi, A Pirrera, and P M Weaver. Structural design of a novel aeroelastically tailored wind turbine blade. *Thin-Walled Structures*, 95:7–15, 2015. doi: 10.1016/j.tws.2015.06.006. (Cited on pages 7, 10, 16, and 18.)
- [21] M T Herath, A K L Lee, and B G Prusty. Design of shape-adaptive wind turbine blades using Differential Stiffness Bend-Twist coupling. *Ocean Engineering*, 95:157–165, 2015. doi: 10.1016/j.oceaneng.2014.12.010. (Cited on pages 7 and 14.)
- [22] F Zahle, C Tibaldi, C Pavese, M K McWilliam, J.P.A.A. Blasques, and M H Hansen. Design of an Aeroelastically Tailored 10 MW Wind Turbine Rotor. In *Journal of Physics: Conference Series*, volume 753, 2016. doi: 10.1088/1742-6596/753/6/062008. (Cited on pages 7, 10, 15, 16, and 18.)

- [23] A R Stäblein, C Tibaldi, and M H Hansen. Using pretwist to reduce power loss of bend-twist coupled blades. In *34th wind energy symposium*, 2016. (Cited on pages 7, 15, and 16.)
- [24] J Saverin, J Peukert, D Marten, G Pechlivanoglou, C O Paschereit, and D Greenblatt. Aeroelastic simulation of multi-MW wind turbines using a free vortex model coupled to a geometrically exact beam model. In *J. Phys. Conf. Ser.*, volume 753, 2016. doi: 10.1088/1742-6596/753/8/082015. (Cited on pages 8, 13, and 16.)
- [25] S Scott, M Capuzzi, D Langston, E Bossanyi, G McCann, P M Weaver, and A Pirrera. Effects of aeroelastic tailoring on performance characteristics of wind turbine systems. *Renewable Energy*, 114:887–903, 2017. doi: 10.1016/j.renene.2017.06.048. (Cited on pages 8, 9, 15, 16, and 18.)
- [26] O Atalay and A Kayran. Load Reduction in Wind Turbines with Bend-Twist Coupled Blades without Power Loss at Underrated Wind Speeds. In *Journal of Physics: Conference Series*, volume 1037, 2018. doi: 10.1088/1742-6596/1037/4/042015. (Cited on pages 9, 15, 16, and 18.)
- [27] T Bagherpour, X M Li, D I Manolas, and V A Riziotis. Modeling of material bend-twist coupling on wind turbine blades. *Composite Structures*, 193:237–246, 2018. doi: 10.1016/j.compstruct.2018.03.071. (Cited on page 9.)
- [28] R Riva, M Spinelli, L Sartori, S Cacciola, and A Croce. Stability analysis of wind turbines with bend-twist coupled blades. In *Journal of Physics: Conference Series*, volume 1037, 2018. doi: 10.1088/1742-6596/1037/6/062014. (Cited on page 9.)
- [29] Ö Şener and A Kayran. Structural performance and power production of wind turbine systems with bend-twist coupled blades in underrated wind conditions. In *2018 Wind Energy Symposium*, page 1242, 2018. doi: 10.2514/6.2018-1242. (Cited on page 9.)
- [30] X Zhou, K Huang, and Z Li. Effects of bend-twist coupling on flutter limits of composite wind turbine blades. *Composite Structures*, 192:317–326, 2018. doi: 10.1016/j.compstruct.2018.02.071. (Cited on page 9.)
- [31] E Ferede, M Abdalla, F Gandhi, G van Bussel, and J Dillinger. Aeroelastic optimization of composite wind turbine blades using variable stiffness laminates. In *AHS International-73rd Annual Forum Proceedings*, pages 3023–3039, 2017. (Cited on page 10.)
- [32] S M Barr and J W Jaworski. Optimization of tow-steered composite wind turbine blades for static aeroelastic performance. *Renewable Energy*, 139:859–872, 2019. doi: 10.1016/j.renene.2019.02.125. (Cited on pages 10, 15, 16, and 18.)
- [33] M Masoudi and K Pope. Numerical predictions on fluid-structure bend-twist coupling of wind turbine blades. *International Journal of Mechanical Engineering and Robotics Research*, 8(4):506–510, 2019. doi: 10.18178/ijmerr.8.4.506-510. (Cited on page 10.)

- [34] W Miao, C Li, Y Wang, B Xiang, Q Liu, and Y Deng. Study of adaptive blades in extreme environment using fluid-structure interaction method. *Journal of Fluids and Structures*, 91, 2019. doi: 10.1016/j.jfluidstructs.2019.102734. (Cited on pages 10 and 16.)
- [35] H Aa Madsen, F Zahle, F Meng, T Barlas, F Rasmussen, and RT Rudolf. Initial performance and load analysis of the LowWind turbine in comparison with a conventional turbine. In *Journal of Physics: Conference Series*, volume 1618, page 032011. IOP Publishing, 2020. (Cited on pages 10 and 18.)
- [36] Giannis P Serafeim, Dimitris I Manolas, Vasilis A Riziotis, and Panagiotis K Chaviaropoulos. Lightweight optimal rotor design of a 10mw-scale wind turbine using passive load control methods. In *Journal of Physics: Conference Series*, volume 1618, page 022061. IOP Publishing, 2020. (Cited on page 11.)
- [37] Ang Li, Mac Gaunaa, Georg Raimund Pirrung, Néstor Ramos-García, and Sergio González Horcas. The influence of the bound vortex on the aerodynamics of curved wind turbine blades. In *Journal of Physics: Conference Series*, volume 1618, page 052038. IOP Publishing, 2020. (Cited on page 11.)
- [38] P Shakya, M R Sunny, and D K Maiti. A parametric study of flutter behavior of a composite wind turbine blade with bend-twist coupling. *Composite Structures*, 207:764–775, 2019. doi: 10.1016/j.compstruct.2018.09.064. URL <https://www.scopus.com/inward/record.uri?eid=2-s2.0-85054194039&doi=10.1016%7Cj.compstruct.2018.09.064&partnerID=40&md5=0430db505019890cede449eb1520c9bc>. (Cited on page 11.)
- [39] Praveen Shakya, Mohammed Rabius Sunny, and Dipak Kumar Maiti. Time domain flutter analysis of bend-twist coupled large composite wind turbine blades: a parametric study. *Mechanics Based Design of Structures and Machines*, pages 1–23, 2020. (Cited on page 11.)
- [40] D L Laird, F C Montoya, and D J Malcolm. Finite element modeling of wind turbine blades. In *43rd AIAA Aerospace Sciences Meeting and Exhibit*, pages 9–17, 2005. (Cited on pages 11 and 12.)
- [41] A Maheri, S Noroozi, C Toomer, and J Vinney. Single-step versus coupled-aero-structure simulation of a wind turbine with bend-twist adaptive blades. In *proc. European Wind Energy Conference EWEC*, volume 1, pages 440–445, 2006. (Cited on page 11.)
- [42] A Maheri, S Noroozi, and J Vinney. Combined analytical/FEA-based coupled aero structure simulation of a wind turbine with bend-twist adaptive blades. *Renewable Energy*, 32(6):916–930, 2007. doi: 10.1016/j.renene.2006.04.007. (Cited on page 11.)
- [43] A Maheri, S Noroozi, and J Vinney. Application of combined analytical/FEA coupled aero-structure simulation in design of wind turbine adaptive blades. *Renewable Energy*, 32(12):2011–2018, 2007. doi: 10.1016/j.renene.2006.10.012. (Cited on page 11.)

- [44] Alireza Maheri, Siamak Noroozi, Chris A. Toomer, and John Vinney. WTAB, a computer program for predicting the performance of horizontal axis wind turbines with adaptive blades. *Renewable Energy*, 31(11):1673–1685, 2006. ISSN 09601481. doi: 10.1016/j.renene.2005.09.023. (Cited on page 11.)
- [45] Kyoungsoo Lee, Ziaul Huque, Raghava Kommalapati, and Sang-Eul Han. Fluid-structure interaction analysis of nrel phase vi wind turbine: Aerodynamic force evaluation and structural analysis using fsi analysis. *Renewable Energy*, 113:512–531, 2017. (Cited on pages 11, 30, 71, and 128.)
- [46] J Paquette, D Laird, D T Griffith, and L Rip. Modeling and testing of 9 m research blades. In *44th AIAA Aerospace Sciences Meeting and Exhibit*, volume 19, pages 14569–14581, 2006. (Cited on page 12.)
- [47] V A Fedorov, N Dimitrov, C Berggreen, S Krenk, K Branner, and P Berring. Investigation of structural behaviour due to bend-twist couplings in wind turbine blades. In *ICCM International Conferences on Composite Materials*, 2009. (Cited on page 12.)
- [48] L I Lago, F L Ponta, and A D Otero. Analysis of alternative adaptive geometrical configurations for the NREL-5MW wind turbine blade. *Renewable Energy*, 59: 13–22, 2013. doi: 10.1016/j.renene.2013.03.007. (Cited on page 12.)
- [49] M. O.L. Hansen, J. N. Sørensen, S. Voutsinas, N. Sørensen, and H. Aa Madsen. State of the art in wind turbine aerodynamics and aeroelasticity. *Progress in Aerospace Sciences*, 42(4):285–330, 2006. ISSN 03760421. doi: 10.1016/j.paerosci.2006.10.002. (Cited on page 13.)
- [50] V Fedorov and C Berggreen. Bend-twist coupling potential of wind turbine blades. In *Journal of Physics: Conference Series*, volume 524, 2014. doi: 10.1088/1742-6596/524/1/012035. (Cited on page 14.)
- [51] A R Stäblein. Analysis and design of bend-twist coupled wind turbine blades. In *MARE-WINT: New Materials and Reliability in Offshore Wind Turbine Technology*, pages 67–80. Springer, Cham, 2016. doi: 10.1007/978-3-319-39095-6_5. (Cited on page 18.)
- [52] PJ Couturier, L Mailly, D Molitor, and Q Wang. On the importance of the beam reference line. In *Journal of Physics: Conference Series*, volume 1618, page 052054. IOP Publishing, 2020. (Cited on page 17.)
- [53] M.O.L. Hansen. *Aerodynamics of Wind Turbines*. Earthscan, London, 2008. (Cited on pages 23, 67, and 72.)
- [54] A. H. van Zuijlen. *Fluid-structure interaction simulations: efficient higher order time integration of partitioned systems*. PhD thesis, Technische Universiteit Delft, Delft-the Netherlands, November 2006. (Cited on pages 30 and 51.)
- [55] A.H. van Zuijlen, A. de Boer, and H. Bijl. Higher-order time integration through smooth mesh deformation for 3d fluid-structure interaction simulations. *Journal of Computational Physics*, 224(1):414–430, 2007. (Cited on page 30.)

- [56] Y. Bazilevs, M.C. Hsu, I. Akkerman, S. Wright, K. Takizawa, B. Henicke, T. Spielman, and T.E. Tezduyar. 3D simulation of wind turbine rotors at full scale. Part I: Geometry modeling and aerodynamics. *International journal for numerical methods in fluids*, 65(1-3):207–235, 2011. (Cited on page 30.)
- [57] Y. Bazilevs, M.C. Hsu, J. Kiendl, R. Wüchner, and K.U. Bletzinger. 3D simulation of wind turbine rotors at full scale. Part II: Fluid–structure interaction modeling with composite blades. *International Journal for numerical methods in fluids*, 65(1-3): 236–253, 2011. (Cited on page 30.)
- [58] Y. Bazilevs, K. Takizawa, T. E. Tezduyar, M. Hsu, N. Kostov, and S. McIntyre. Computational wind-turbine analysis with the ale-vms and st-vms methods. *Numerical Simulations of Coupled Problems in Engineering*, pages 355–386, 2014. (Cited on page 30.)
- [59] ANSYS, Inc. Ansys[®] fluent theory guide, release 2021 r2, 2021. (Cited on pages 31, 32, and 63.)
- [60] J.H. Ferziger and M. Perić. *Computational methods for fluid dynamics*. Springer, Berlin (Germany), 2002. (Cited on pages 32 and 37.)
- [61] Chae M Rhie and Wei-Liang Chow. Numerical study of the turbulent flow past an airfoil with trailing edge separation. *AIAA journal*, 21(11):1525–1532, 1983. (Cited on page 32.)
- [62] Florian R. Menter. Zonal two equation $k-\omega$ turbulence models for aerodynamic flows. In *23rd fluid dynamics, plasmadynamics, and lasers conference*, page 2906, 1993. (Cited on pages 33 and 36.)
- [63] Florian R. Menter. Two-equation eddy-viscosity turbulence models for engineering applications. *AIAA journal*, 32(8):1598–1605, 1994. (Cited on pages 33 and 84.)
- [64] ANSYS, Inc. Ansys[®] Mechanical APDL Theory Reference, Release 2021 R2, 2021. (Cited on pages 37, 39, 40, 42, 60, and 82.)
- [65] Nathan M Newmark. A method of computation for structural dynamics. *Journal of the engineering mechanics division*, 85(3):67–94, 1959. (Cited on page 40.)
- [66] H. M. Hilber, T. J. R. Hughes, and R. L. Taylor. Improved numerical dissipation for time integration algorithms in structural dynamics. *Earthquake Engineering & Structural Dynamics*, 5(3):283–292, 1977. (Cited on page 40.)
- [67] G.R. Liu and S.S. Quek. *The finite element method: A practical course*. Butterworth-Heinemann, Oxford, 2003. (Cited on page 42.)
- [68] ANSYS, Inc. ANSYS Mechanical APDL Element Reference, release 14.0, 2011. (Cited on page 42.)
- [69] Eric Reissner. The effect of transverse shear deformation on the bending of elastic plates. *American Society of Mechanical Engineers*, 12:A68–A77, 1945. (Cited on page 42.)

- [70] R.D. Mindlin. Influence of rotatory inertia and shear on flexural motions of isotropic elastic plates. *Applied Mechanics*, 18:31–38, 1951. (Cited on page 42.)
- [71] J. N. Reddy. *Mechanics of laminated composite plates and shells: Theory and analysis-2nd ed.* CRC Press, Boca Raton, 2004. (Cited on pages 44 and 45.)
- [72] A. de Boer, A. H. van Zuijlen, and H. Bijl. Comparison of conservative and consistent approaches for the coupling of non-matching meshes. *Computer Methods in Applied Mechanics and Engineering*, 197(49-50):4284–4297, 2008. (Cited on pages 52, 53, and 54.)
- [73] Amin Totounferoush, Frédéric Simonis, Benjamin Uekermann, and Miriam Schulte. Efficient and scalable initialization of partitioned coupled simulations with precice. *Algorithms*, 14(6):166, 2021. (Cited on page 52.)
- [74] J. R. Cebal and R. Löhner. Conservative load projection and tracking for fluid-structure problems. *AIAA journal*, 35(4):687–692, 1997. (Cited on page 54.)
- [75] R. Löhner. Fluid-structure interaction using a loose coupling algorithm and adaptive unstructured grids. *AIAA-95-2259*, 1995. (Cited on page 54.)
- [76] ANSYS, Inc. Ansys[®] fluent user’s guide, release 2021 r2, 2021. (Cited on page 64.)
- [77] J. G. Schepers and H. Snel. Dynamic inflow: yawed conditions and partial span pitch control. Technical report, Energy Research Centre of the Netherlands, 1995. (Cited on page 67.)
- [78] H. Snel and J. G. Schepers. Joint investigation of dynamic inflow effects and implementation of an engineering method. Technical report, Energy Research Centre of the Netherlands, 1995. (Cited on page 67.)
- [79] Stig Øye. Unsteady wake effects caused by pitch angle changes. Technical report, Technical University of Denmark, 1986. (Cited on pages 67, 78, and 79.)
- [80] D. L. Pitt and D. A. Peters. Theoretical prediction of dynamic-inflow derivatives. In *Sixth European Rotorcraft and Powered Lift Aircraft Forum*, Bristol, United Kingdom, 1980. (Cited on pages 67, 78, and 79.)
- [81] C Lindenburg. Investigation into rotor blade aerodynamics. Technical report, Energy research Centre of the Netherlands (ECN) Wind Energy publication, ECN-C-03-025, 2003. (Cited on pages 68, 70, 74, and 75.)
- [82] Zhaohui Du and Michael S. Selig. A 3-D stall-delay model for horizontal axis wind turbine performance prediction. In *1998 ASME Wind Energy Symposium*, pages 9–19, Reno, Nevada, 1998. (Cited on pages 69, 70, 74, and 75.)
- [83] Maintained by A2e Data Archive and Portal for U.S. Department of Energy, Office of Energy Efficiency and Renewable Energy. Atmosphere to Electrons (A2e). uae6/uae6.z07.00., . DOI: 10.21947/1483810, Accessed: 30 01 2023. (Cited on pages 70, 73, and 77.)

- [84] Ijaz Fazil Syed Ahmed Kabir and E. Y.K. Ng. Insight into stall delay and computation of 3D sectional aerofoil characteristics of NREL phase VI wind turbine using inverse BEM and improvement in BEM analysis accounting for stall delay effect. *Energy*, 120:518–536, 2017. ISSN 03605442. (Cited on page 70.)
- [85] H Snel, R Houwink, J Bosschers, WJ Piers, G JW Van Bussel, and A Bruining. Sectional prediction of sd effects for stalled flow on rotating blades and comparison with measurements. 1993. (Cited on page 70.)
- [86] P. K. Chaviaropoulos and M. O.L. Hansen. Investigating three-dimensional and rotational effects on wind turbine blades by means of a quasi-3d navier-stokes solver. *Journal of Fluids Engineering, Transactions of the ASME*, 122(2):330–336, 2000. ISSN 1528901X. doi: 10.1115/1.483261. (Cited on page 70.)
- [87] S.-P. Breton, F N Coton, and G Moe. A study on rotational effects and different stall delay models using a prescribed wake vortex scheme and NREL phase VI experiment data. *Wind Energy*, 11(5):459–482, 2008. (Cited on pages 70 and 71.)
- [88] M N Hamlaoui, A Smaili, and H Fellouah. Improved BEM Method for HAWT Performance Predictions. In *2018 International Conference on Wind Energy and Applications in Algeria, ICWEAA 2018*, 2019. (Cited on page 70.)
- [89] W Zhong, W Z Shen, T Wang, and Y Li. A tip loss correction model for wind turbine aerodynamic performance prediction. *Renewable Energy*, 147:223–238, 2020. (Cited on page 71.)
- [90] R Lanzafame and M Messina. BEM theory: How to take into account the radial flow inside of a 1-D numerical code. *Renewable Energy*, 39(1):440–446, 2012. (Cited on pages 71 and 74.)
- [91] X Tang, X Huang, S Sun, and R Peng. Wind turbine power curve prediction with consideration of rotational augmentation effects. volume 161, 2016. (Cited on page 71.)
- [92] James L. Tangler. The nebulous art of using wind-tunnel airfoil data for predicting rotor performance. *2002 ASME Wind Energy Symposium*, 257(December 2001):190–196, 2002. ISSN 1095-4244. (Cited on pages 71 and 74.)
- [93] M. H. Hansen, M. Gaunaa, and H. A. Madsen. A Beddoes-Leishman type dynamic stall model in state-space and indicial formulations. Technical report, Risø National Laboratory, Roskilde, Denmark, 2004. (Cited on page 72.)
- [94] Maintained by A2e Data Archive and Portal for U.S. Department of Energy, Office of Energy Efficiency and Renewable Energy. Atmosphere to Electrons (A2e). uae6/uae6.z08.00., . DOI: 10.21947/1483813, Accessed: 30 01 2023. (Cited on page 77.)
- [95] Maintained by A2e Data Archive and Portal for U.S. Department of Energy, Office of Energy Efficiency and Renewable Energy. Atmosphere to Electrons (A2e). uae6/uae6.z09.00., . DOI: 10.21947/1483815, Accessed: 30 01 2023. (Cited on page 77.)

- [96] Maintained by A2e Data Archive and Portal for U.S. Department of Energy, Office of Energy Efficiency and Renewable Energy. Atmosphere to Electrons (A2e). uae6/uae6.z16.00., . DOI 10.21947/1481776, Accessed: 30 01 2023. (Cited on page 77.)
- [97] Cheng-Huat Ong and Stephen W. Tsai. Design, manufacture and testing of a bend-twist D-Spar. Technical report, Sandia National Laboratories, Albuquerque, New Mexico, 1999. (Cited on pages 80 and 81.)
- [98] Christian D Peters, Sybrand J van der Spuy, Daniel NJ Els, and Jörg Kuhnert. Aerodynamic damping of an oscillating fan blade: Mesh-based and meshless fluid structure interaction analysis. *Journal of Fluids and Structures*, 82:173–197, 2018. (Cited on pages 81, 82, 83, 84, 85, and 86.)
- [99] Christian Dietrich Peters. *Aerodynamic damping of an oscillating fan blade: Numerical fluid structure interaction analysis*. PhD thesis, Stellenbosch: Stellenbosch University, 2017. (Cited on pages 83, 84, 85, and 86.)
- [100] Friedrich Wilhelm Riegels. *Aerodynamische Profile. Aerofoil Sections. Results from Wind-tunnel Investigations. Theoretical Foundations... Translated... by DG Randall*. Butterworths, 1961. Translation by D.G. Randall. (Cited on pages 83 and 84.)
- [101] Nico Raymond Basson. *Investigating the effect of aerodynamic damping on an axial flow fan blade*. PhD thesis, Stellenbosch: Stellenbosch University, 2015. (Cited on page 85.)
- [102] Kyoungsoo Lee, Ziaul Huque, Raghava Kommalapati, and Sang-Eul Han. Evaluation of equivalent structural properties of NREL phase VI wind turbine blade. *Renewable Energy*, 86:796–818, 2016. (Cited on page 97.)
- [103] Robert M. Jones. *Mechanics of composite materials*. Taylor & Francis, Philadelphia, PA, 1999. (Cited on page 98.)
- [104] Daniel Laird and Thomas Ashwill. Introduction to NuMAD - a numerical manufacturing and design tool. In *1998 ASME Wind Energy Symposium*, page 60, 1998. (Cited on page 98.)
- [105] Jonathan C. Berg and Brian R. Resor. Numerical manufacturing and design tool (NuMAD v2.0) for wind turbine blades: User’s guide. <https://www.osti.gov/biblio/1051715-numerical-manufacturing-design-tool-numad-v2-wind-turbine-blades-user-guide>, 2012. Accessed: 2022-07-13. (Cited on page 100.)
- [106] International Electrotechnical Commission. IEC 61400-2 wind turbines—part 2: Small wind turbines, 2013. (Cited on page 105.)
- [107] J. G. Holierhoek. *Aeroelastic design of wind turbine blades*. Woodhead Publishing Limited, 2013. ISBN 9780857094261. doi: 10.1533/9780857097286.1.150. URL <http://dx.doi.org/10.1533/9780857097286.1.150>. (Cited on pages 108 and 109.)

- [108] Don W Lobitz. Aeroelastic stability predictions for a mw-sized blade. *Wind Energy: An International Journal for Progress and Applications in Wind Power Conversion Technology*, 7(3):211–224, 2004. (Cited on pages [108](#) and [109](#).)
- [109] Niels N Sørensen, JA Michelsen, and Scott Schreck. Navier–Stokes predictions of the NREL Phase VI rotor in the NASA Ames 80 ft× 120 ft wind tunnel. *Wind Energy: An International Journal for Progress and Applications in Wind Power Conversion Technology*, 5(2-3):151–169, 2002. (Cited on page [119](#).)